Analysis of Cardiac Motion Using MRI and Nonrigid Image Registration

Raghavendra Chandrashekara

A dissertation submitted in partial fulfillment

of the requirements for the degree of

Doctor of Philosophy

of the

University of London

October 2004

Department of Computing

Imperial College London

Abstract

In recent years, significant progress has been made in the care and treatment of patients with cardiovascular diseases, the major cause of death in the world. Principal among the developments which have improved the outlook for patients is the development of *magnetic resonance imaging* (MRI) technology. The ability to obtain high resolution cine volume images easily and safely has made it the preferred method for diagnosis of cardiovascular diseases. MRI is also unique in the respect that noninvasive markers can be introduced directly into the tissue being imaged (MR tagging) during the image acquisition process. By tracking the motion of the tag markers the deformation field in the heart can be reconstructed. Although MRI is starting to be used more frequently for cardiovascular examinations, quantitative analysis of the images acquired is hindered by the absence of automated tools.

The work presented in this thesis describes the development of nonrigid image registration techniques to track the motion of the heart in MR images. We extend an existing nonrigid image registration algorithm based on 3D B-splines for its application to cardiac motion analysis. The deformation field is reconstructed by registering a sequence of images taken during the contraction of the heart to reference images taken at the start of the cardiac cycle. Because the motion of the heart is three-dimensional, both short- and long-axis images of the heart are used to reconstruct the deformation field in the heart. We also compare transformation models which describe the motion of the heart in a Cartesian coordinate system to a model which describes the motion in a cylindrical coordinate system. A registration algorithm using a 4D B-spline motion model is also developed for representing the motion of the heart continuously over time. We also construct and investigate the use of a statistical motion model for cardiac motion analysis. We develop two different types of statistical motion model, a time-dependent motion model and time-independent

motion model. The algorithms developed are evaluated on both synthetic data and data acquired from patients and volunteers.

In the final chapter of this thesis we summarize and make conclusions on the work presented and discuss directions for future work.

Acknowledgements

First and foremost I would like to thank my supervisor, Dr. Daniel Rueckert, for his encouragement, enthusiasm and support throughout the course of my research. The time he has spent on helping me to develop my skills as a researcher has meant a lot to me, and I hope that his scientific rigour and standards are reflected in the work presented.

I would also like to thank Dr. Raad Mohiaddin from the Royal Brompton and Harefield NHS Trust, London for his valuable input and acquiring the many MR data sets used in this thesis.

Sincere thanks also go to Dr. Wiro Niessen of the Image Sciences Institute, University Medical Center Utrecht and Dr. Reza Razavi of Guy's and St. Thomas' Hospital, London for agreeing to be my examiners.

I would also like to thank my colleagues and friends in the VIP group for their help and support over the course of my research. I would like to especially thank Maria, Anil, Gerardo, Dimitrios, and Paul for agreeing to be scanned many times and also for the numerous discussions on both research and non-research related matters.

Finally, I would like to thank my family for their love and support in all my endeavours.

Contents

List of Figures

14

List of Tables

Chapter 1

Introduction

According to recent *World Health Organization* (WHO) estimates, 16.7 million people die in the world every year because of *cardiovascular diseases* (CVDs) [114]. This makes CVDs the greatest cause of death in the world. With the development of novel imaging techniques, such as *magnetic resonance imaging* (MRI), clinicians and researchers now have the tools necessary to monitor and assess the progression of CVDs so that effective procedures for the care and treatment of patients can be devised. In this chapter we review the basic anatomy and function of the heart, the various diseases which can affect the heart and the main imaging techniques that have been developed for diagnosing patients with CVDs.

1.1 The Anatomy and Structure of the Heart

The cardiovascular system [20, 78] is comprised of the heart and blood vessels whose function is to circulate blood around the body. They act as a transport system delivering oxygen from the lungs and nutrients from the gastrointestinal tract to the cells of the body. The heart (figure 1.1) consists of two pumps lying side by side which pump in phase with each other. Each pump has an atrium and a ventricle as shown in the figure. The *right atrium* receives venous blood from the body and passes it through into the the *right ventricle* (RV) where it is pumped to the lungs
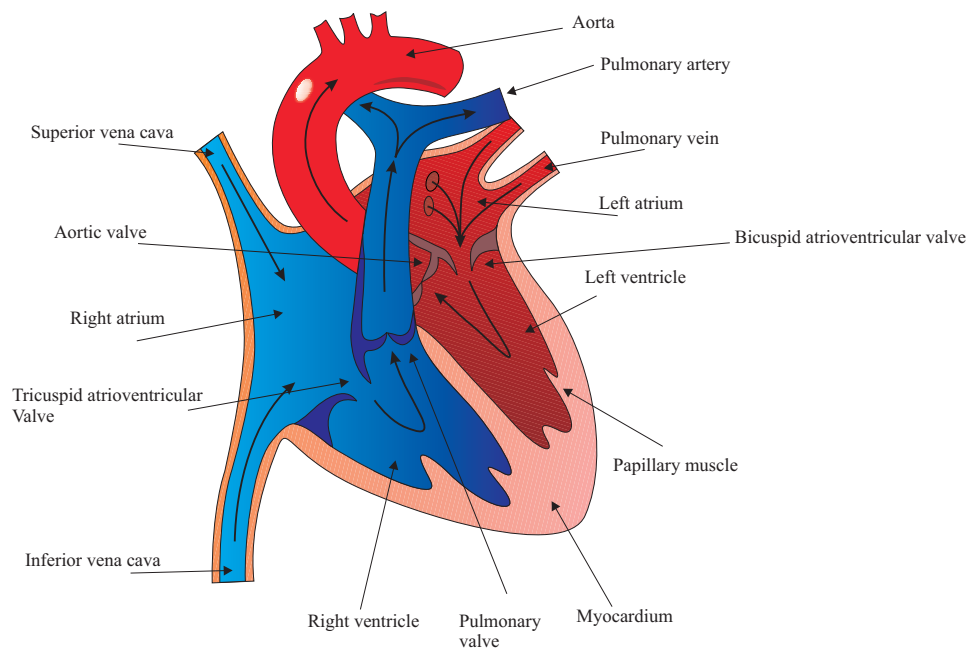
Figure 1.1: The heart consists of two pumps lying side by side. The arrows show the direction of blood flow in the two sides. This figure has been adapted from figure 13.3 in Bray *et al* [20].

(pulmonary circulation) for oxygenation. At the same time the *left atrium* receives oxygenated blood from the lungs and the *left ventricle* (LV) pumps it out to the rest of the body (systemic circulation).

The four chambers of the heart are separated from each other and the rest of the body by four sets of valves. The bicuspid (or mitral) and tricuspid *atrioventricular* (AV) valves separate the left and right atria and ventricles respectively, while the aortic valve separates the LV from the aorta, and the pulmonary valve separates the RV from the pulmonary artery. Thin chords called the *chordae tendineae* are attached to the atrioventricular valves and projections of the ventricular muscles known as the papillary muscles. During ventricular contraction the papillary muscles tense and prevent the valves from inverting into the atrium.

1.1.1 The Cardiac Cycle

Venous blood returning to the heart from the rest of the body, flows continuously from the superior and inferior vena cava into the right atrium, while oxygenated

blood from the lungs enters the left atrium through the pulmonary veins. When the pressure in the atria exceeds the pressure in the ventricles, the AV valves open and the blood enters the ventricles. When the ventricles are about 80% full, the atria contract and propel more blood into the ventricles completing ventricular filling. This stage, where ventricular filling takes place, is known as diastole.

After a very short pause ($\sim$ 0.1 s) the ventricles contract. This stage is known as systole. As the ventricles contract the pressure in the ventricles increases rapidly and exceeds the atrial pressure, causing the AV valves to close. Simultaneously the papillary muscles contract so that the AV valves do not revert back into the atria. The continued contraction raises the ventricular pressure beyond the pressure in the aorta and the pulmonary artery. This causes the pulmonary and aortic valves to open and blood is ejected at low pressure from the RV into the pulmonary circuit and from the LV into the systemic circuit. When the pressure in the ventricles falls below that in the pulmonary artery and the aorta, the pulmonary and aortic valves close. When the ventricular pressure falls below the atrial pressure, the AV valves open and the ventricles start to refill with blood again and the cycle repeats.

1.1.2   The Electrical Activation of the Heart

The myocardium (the heart muscle) is comprised of muscle cells called myocytes. These are typically 10–20μm in diameter and 50–100μm in length. The junction between adjacent myocytes, called the intercalated disc, allows electrical impulses to be transmitted from cell to cell making the myocardium act like an electrically continuous sheet.

The contraction of the heart is initiated by the *sino-atrial* (SA) node and acts as a pacemaker, dictating the rate of beating of the heart (figure 1.2). The node is composed of myocytes which generate an action potential roughly once every second that excites the adjacent atrial work cells and causes a wave of depolarization to travel across the two atria and initiates atrial systole.
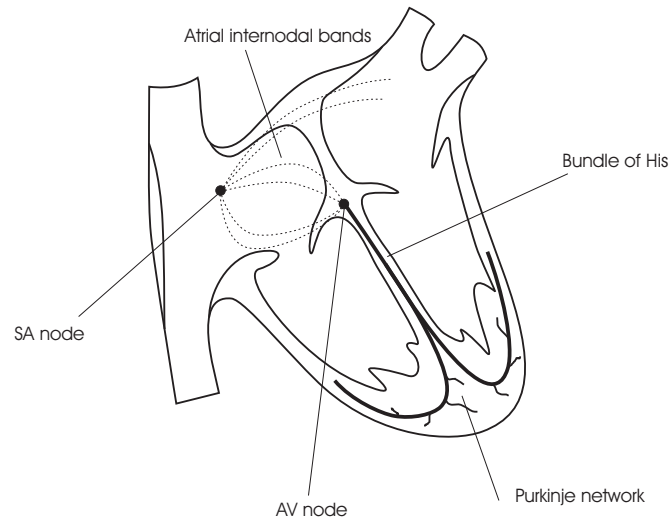
Figure 1.2: The cardiac conduction system (adapted from figure 13.5 in Bray *et al* [20]).

The electrical impulse then reaches the *atrioventricular* (AV) node in the atrial septum (the wall separating the two atria). The impulse is delayed by the AV node allowing the atria to finish contracting before the ventricles are activated.

The electrical impulse then travels down a narrow bundle of conduction fibers called the *bundle of His* which separates into two parts, one activating the LV of the heart and the other the RV. The bundle of His terminates in the Purkinje network, located in the subendocardium, which distributes the electrical impulse rapidly to the work cells of the myocardium.

1.1.3   The Coronary Circulation

The heart receives the energy it needs from the coronary circulation (figure 1.3), which consists of five main arteries: the *left main coronary artery* (LEFT MAIN), the *right coronary artery* (RCA), the *left anterior descending artery* (LAD), the *left circumflex artery* (CIRC), and the *posterior descending artery* (PDA). The RCA and the LEFT MAIN arise from the aorta, while the LAD and CIRC arise from the LEFT MAIN when it splits into two. The PDA arises from the RCA in approximately 90% of the human population and from the CIRC in approximately 10% of the population.
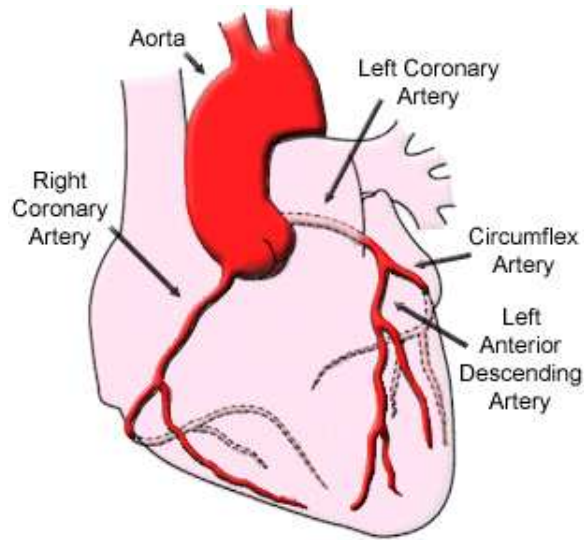
Figure 1.3: The coronary circulation (from [161]).

The blood flow from the coronary arteries reaches the myocardium by vessels which penetrate the walls of the ventricles. This means that the endocardial regions of the heart are very vulnerable to cell death, or infarction, if coronary artery occlusion occurs. This is especially the case with the LV which has a much thicker wall than the RV. Occlusion of the LEFT MAIN is much more serious than occlusion of any one of the other arteries since this blocks off all of the blood supply to the LV.

1.2 Cardiovascular Diseases

Table 1.1 shows a percentage breakdown of the deaths due to CVDs in the USA [3]. In both the USA and Europe, the greatest proportion of deaths resulting from CVDs are due to *coronary heart disease* (CHD) [3, 136]. Atherosclerosis of the coronary arteries can lead to occlusion or narrowing of the arteries. This results from the build up of fatty deposits in the artery walls and restricts the supply of oxygen to the muscles of the heart. One of the consequences are abnormalities in the motion of the ventricular walls which results in a loss of cardiac function. Atherosclerosis of the coronary arteries affects the LV to a greater extent because of its larger size and greater demand for energy.

Type of CVD	Percentage of deaths
Coronary heart disease	54
Stroke	18
Congestive heart failure	6
High blood pressure	5
Diseases of the arteries	4
Other	13

Table 1.1: Percentage breakdown of deaths due to CVDs [3].

1.2.1 Coronary Heart Disease

The heart needs an unrestricted supply of substrates from the coronary circulation, notably oxygen, to meet its energy demands. It cannot tolerate ischemia, which results from coronary occlusion. Coronary occlusion is followed, almost immediately, by a loss of function, and within hours, by cell death. The main symptoms of coronary artery disease are angina, acute myocardial infarction and heart failure and in some cases arrhythmias.

1.2.1.1 Angina

An imbalance between cardiac energy demands and energy supply causes angina pectoris (literally meaning a strangling in the chest). The main symptoms felt are pain in the left chest, upper body and at the sites of old scars and injuries.

When the symptoms of coronary occlusive disease do not change the patient is said to have stable angina pectoris. Stable angina often decreases in severity over weeks and months because of the development of collateral vessels and enlargement of partially occluded coronary arteries.

1.2.1.2 Acute Myocardial Infarction

This occurs when coronary flow is reduced so severely as to cause cell death in a part of the heart. Most clinical infarctions involve the LV; RV infarction does occur but it is usually less important than infarction of the LV. The endocardium is especially vulnerable to coronary occlusion because the major coronary arteries

penetrate the LV from its epicardial surface. In addition the energy expenditure by the endocardium is greater than that of the epicardium largely because of the higher tension developed in the inner layers of the ventricle. For these reasons, endocardial cells die sooner than those of the epicardium after a coronary occlusion. One consequence is that severe, but not total restriction of coronary flow can cause a subendocardial infarction where necrosis is confined to the endocardium.

1.2.1.3 Arrhythmias

Coronary artery disease changes the cellular structure of the myocardium and alters the propagation of electrical impulses in the heart causing arrhythmias. In some, lethal arrhythmias are the terminal event in patients whose hearts have undergone severe and progressive failure, while other patients can die suddenly within the first few minutes of the occurrence of a severe acute myocardial infarction.

Ventricular Ectopic Beats Myocytes present in the myocardium may occasionally fire before the SA node. This triggers an extra beat known as an ectopic beat. If the trigger is located in the ventricle then the resulting wave of depolarization is ill synchronized because the excitation has not been distributed through the His-Purkinje system. The resulting ill coordinated contraction fails to eject blood properly from the heart.

Heart Block Ischaemic heart disease can also cause the AV node, main bundle, or one of the bundle branches to not transmit electrical signals properly. This can result in a slowing of conduction from the AV node to ventricular myocardium (first-degree heart block), an intermittent failure of excitation to pass from the atria to the ventricles (second-degree heart block), or complete failure of electrical transmission from the atria to the ventricles (third-degree heart block).

Pathological Tachycardias Abnormal myocardial conduction pathways can cause a wave of excitation to travel in a never-ending circle or spiral. Myocytes emerging

from a period of excitation are re-excited by the return of the electrical wave (a process called re-entry). Re-entry mechanisms are responsible for tachycardias and for maintining fibrillation.

Atrial Fibrillation   Multiple local re-entry circuits within the atrial wall can cause an uncoordinated, repetitive excitation of myocytes. The resulting movement of the wall becomes less effective in ejecting blood. A chief danger is the formation of a blood clot or thrombus in a stagnant region of the atrium which can embolize.

Ventricular Fibrillation   Multiple local re-entry circuits can also cause fibrillation in the ventricles resulting in an ineffective rippling motion of the walls. With no cardiac output death can follow in minutes.

Ultimately, the state of the myocardial tissue has a direct effect on the cardiac function and can be categorized into the following depending on the extent to which it has been damaged by coronary occlusion [50]:

Normal Normal myocardium with normal perfusion.

Ischemic Results when the oxygen being supplied to the myocardium is insufficient to meet its demands.

Stunned Where perfusion is near normal but where contractile function is abnormal (occurs after periods of ischemia).

Hibernating Myocardium which has had its microstructure altered due to chronic hypoperfusion resulting in loss of contractile function.

Infarcted Myocardium which has become fibrotic due to total coronary occlusion. Infarcted tissue has little chance of recovery.

Being able to distinguish between these states can help clinicians identify those patients who will most benefit from treatment as well as the best course of treatment.

1.2.2   Stroke

Stroke is a CVD which affects the arteries leading to and within the brain. A strokes occurs when a blood vessel carrying the oxygen and nutrients to a part of the brain is blocked by a clot or ruptures. The part of the brain which is affected can die because of the lack of blood flow and the consequences can be devastating. The patient may become paralyzed in addition to the loss of language skills and vision. Stroke can be treated, if the warning signs are detected early enough, by drugs or surgical intervention.

1.2.3   Diseases of the Arteries

1.2.3.1   Atherosclerosis

Atherosclerosis is the name given to the process of the buildup of fatty substances, cholesterol, cellular waste products, calcium and other substances in the inner lining of an artery. The buildup, called a plaque, reduces the blood flow through the artery and causes it lose its elasticity. Most of the damage caused by a plaque occurs when it becomes fragile and ruptures. The plaque can travel to a different part of the body and block a blood vessel that feeds the heart (causing a heart attack) or the brain (causing a stroke).

Atherosclerosis is a slow and complex disease that starts at childhood and progresses into adulthood. It is thought that damage to the innermost layer of the artery (the endothelium) causes the formation of the plaque.

The effects of atherosclerosis in the coronary arteries can be treated with the use of medication which reduces the amount of energy needed by the heart. In other cases surgical procedures such as balloon dilation or a bypass operation may be necessary. The arteries may also be cleaned at the time of surgery (endarterectomy) although this procedure is only used in treatment of the cartoid arteries and is rarely used for other arteries.

1.2.3.2 Kawasaki Disease

Kawasaki disease is a childhood disease (80 % of people with Kawasaki disease are under the age of 5) which predominantly affects boys and children of Asian ancestry. It is thought that the disease is caused by a infectious agent such as a virus. It affects the coronary arteries and the muscles of the heart. The walls of the coronary arteries can become weakened resulting in two dangers: A blood clot can form in the weakened area blocking the artery and causing a heart attack, or, in a few rare cases, an aneurysm may form which ruptures. Other changes including the inflammation of the heart (myocarditis) or the sac surrounding the heart (pericarditis), arrhythmias, and abnormal functioning of the heart valves may also occur. Most problems usually resolve themselves in a few weeks and no lasting damaging occurs.

Although the cause of Kawasaki disease is unknown some medicines such as aspirin, which prevents the formation of blood clots, can be taken to prevent the effects of the disease. Another medication, intravenous gamma globulin, is also given to decrease the risk of developing coronary artery abnormalities, but it must be given in the early stages of the disease.

1.2.4 Congestive Heart Failure

Congestive heart failure is a chronic disease and is the result of a weakening of the heart muscles from an underlying cause such as clogged arteries, high blood pressure, or a defect in the muscular walls or valves. It can involve either the LV, the RV, or both. However it commonly occurs in the LV first. Systolic failure occurs when the LV loses its ability to contract resulting in its inability to properly pump blood out of the heart. If the muscles of the LV become too stiff then the LV loses its ability to relax (diastolic failure). Blood flow may "back up" causing fluid to leak into the lungs (pulmonary edema) and the reduced blood flow also causes fluid to build up in tissues throughout the body (edema). The excess fluid build up explains the term congestive.

Increased fluid pressure as a result of LV failure is transferred through the lungs to the right side of the heart ultimately damaging the RV and its ability to pump. When this occurs blood is not pumped properly to the lungs causing blood to back up into the veins and results in a swelling of the legs and ankles.

Congestive heart failure can be treated by taking medications to improve circulation and help strengthen the muscle's pumping action. If the heart has lost significant pumping capacity then surgery may become necessary. A coronary artery bypass surgery can help to increase the blood flow to the heart but in severe cases a heart transplant may be the only option.

1.2.5   High Blood Pressure

High blood pressure is often called the "silent killer" as no symptoms are shown in a person suffering from this CVD. Untreated it can lead to stroke, heart attack, heart failure, or kidney failure. Medications are available which can help to reduce and control high blood pressure but it is a lifelong disease which cannot be cured. Proper choice of diet, exercise, and lifestyle choices (such as quitting smoking) can also help to control high blood pressure.

1.2.6   Congenital Heart Disease

Children are sometimes born with defects or abnormalities in the heart referred to as cardiac anomalies. The defects are primarily seen in the malformation of the valves, the septum and the narrowing of the arteries leading from the heart.

1.2.6.1   Arterial Defects

Aortic Stenosis   Aortic stenosis results from the obstruction of the blood flow between the LV and the aorta. It occurs because of muscular obstruction of the aortic valves or because of aortic narrowing immediately above the valve. The most common abnormality seen is the presence of only two leaflets in the aortic valve

rather than the normal three. The leaflets are also commonly thicker and less pliable then the leaflets in the normal aortic valve. The ventricular wall becomes thicker because of the greater amount of work that it must do to eject blood. This is known as left ventricular hypertrophy. A narrowing of the aorta known as coarctation of the aorta is also seen sometimes in addition to a bicuspid aortic valve.

Interrupted Aortic Arch (IAA)   The aorta leaves the heart and ascends into the chest to give off blood vessels to the arms and the head. It then arches and turns downward to the lower half of the body. *Interrupted aortic arch* (IAA) is the absence or discontinuation of a portion of the aortic arch. With this defect not all parts of the body are able to receive oxygen-rich blood from the left side of the heart.

Patent Ductus Arteriosus (PDA)   The ductus arteriosus is a connection between the aorta and the pulmonary artery and is present in all babies before birth. It usually closes on its own in the first 15 hours of life. When it does not close the formation is called a *patent ductus arteriosus* (PDA). In newborns a drug called Indomethacin can be given which constricts the walls of the PDA and help to close it. The potential side effects of the drug sometimes necessitates surgery.

Pulmonary Valvar Stenosis   Pulmonary valvar stenosis is an obstruction between the right ventricle and pulmonary arteries caused by a muscular obstruction, obstruction at the pulmonary valve itself, or a narrowing of the artery above the valve. Similar to aortic stenosis the RV must work harder to pump blood to the lungs and so the muscles of the RV become much thicker to compensate for the extra work needed.

Total Anomalous Pulmonary Venous Return (TAPVR)   *Total anomalous pulmonary venous return* (TAPVR) is rare malformation which occurs when the pulmonary veins do not connect to the left atrium but instead drain abnormally

into the right atrium. An *atrial septal defect* (ASD) also occurs with a TAPVR and is the only source of blood flow from the lungs into the left atrium.

Transposition of the Great Arteries   Transposition of the great arteries is an anomaly in which the aorta arises from the RV and the pulmonary artery arises from the LV. This creates a situation in which the systemic and pulmonary circulations are in parallel rather than in series. Unless there is some location where the oxygenated and unoxygenated blood can mix (for example at a ventricular septal defect, an atrial septal defect, or a patent ductus arteriosus) none of the organs will receive any oxygen.

Truncus Arteriosus   A baby with a truncus arteriosus has only one great blood vessel leaving the heart. The great vessel is connected to both the LV and the RV and usually has between two to five leaflets. A ventricular septal defect is also usually present.

1.2.6.2   Valvular Defects

Ebstein's Anomaly   Ebstein's anomaly occurs when the tricuspid valve is malformed. Two of the valve leaflets are displaced downward into the right ventricle and third is elongated and may be adherent to the wall chamber. The valve leaks blood into the right atrium when the RV contracts and as a result the chamber becomes enlarged.

Tricuspid Atresia   Tricuspid atresia is the disease name given when the valve between the right atrium and the right ventricle does not form. Blood returning from the body must travel through an atrial septal defect into the left side of the heart before it can enter the RV.

1.2.6.3 Septal Defects

One of the most common congenital defects is the formation of holes in the septum separating the four chambers of the heart. These can occur in the regions separating the atria or the ventricles.

Atrial Septal Defect (ASD) An *atrial septal defect* (ASD) allows blood to flow from the left to the right atrium. Untreated, this can lead to pulmonary hypertension (high blood pressure in the lungs), congestive heart failure (weakening of the heart muscle), atrial arrhythmias (abnormal beating of the heart) and an increased risk of stroke.

Ventricular Septal Defect (VSD) *Ventricular septal defect* (VSD) is the term used when a hole forms in the septum separating the ventricles. The size of the hole determines to a large extent the need for surgery as small holes usually close on their own.

Atrioventricular Septal Defect (AVSD) *Atrioventricular septal defects* (AVSDs) occur most commonly in infants with Down syndrome. The defect is the result of the failure of the formation of heart structures that arise from an embryonic structure called the endocardial cushions which are responsible for the separating the central parts of the heart near the tricuspid and mitral valves. Surgery is necessary to correct this severe structural defect and prevent congestive heart failure.

1.2.6.4 Single Ventricle Defects

Single ventricle defects are used to describe a group of defects which have the common feature that only one of the ventricles is of normal size.

Hypoplastic Left Heart Syndrome (HLHS) In *hypoplastic left heart syndrome* (HLHS) the left side of the heart is severely underdeveloped. The RV of the heart

does the work of the LV by pumping the oxygenated blood that enters the RV through an atrial septal defect.

1.2.7   Rheumatic Heart Disease/Rheumatic Fever

Rheumatic heart disease is an inflammatory disease caused by a streptococcal infection and affects many of the bodies connective tissues, especially those of the heart, joints, brain and skin. Damage to the valves of the heart can be prevented by treatment using penicilin or other antibiotics once the first signs of rheumatic fever are detected.

1.3   Cardiac Imaging

As we have discussed in the previous section, the heart can be affected by numerous diseases which diminish its ability to pump blood out to the rest of the body. To be able to assess the efficacy of a particular course of treatment, images of the heart must be acquired first so that various functional parameters can be measured. In this section we briefly review the imaging methods used for diagnosing the heart. A more detailed description of the imaging methods can be found in Webb [173] or Suetens [158].

1.3.1   Ultrasound

Ultrasound (US) is an important imaging modality for diagnosing the heart as it is relatively inexpensive, safe, noninvasive and is portable enough that diagnoses can be made at the bedside. The basic principle on which US imaging relies on is the fact that sound energy waves generated by a transducer and which travel through an object are scattered by structures present in the object. The reflected signals and their intensities can be detected and processed to reconstruct images of the structures in the object.

In addition to visualizing anatomy, US imaging can also be used to assess function through measurements of blood flow velocities and myocardial velocities (Doppler imaging).

1.3.1.1 Conventional Ultrasound Imaging

Data acquisition for conventional US imaging is done in three different ways. In the simplest form of US imaging, based on the pulse-echo principle, the transducer is used as a receiver immediately after the transmission of a pulse. This is called A-mode (amplitude) imaging. This yields a measurement of the strength of signals reflected in the body as function of depth. In B-mode (brightness) US a linear array of transducers simultaneously scans a plane through a body and produces a 2D image of the reflected signal. If a rapid sequence of B-mode scans is repeated over time then the motion of a structure within the body can be measured as the positions of the reflective structures in the body change with respect to the position of the transducer. This is know as M-mode imaging (for motion). It is used extensively in cardiac and fetal cardiac imaging.

1.3.1.2 Doppler Imaging

Doppler US is based on the Doppler effect. The frequency of the reflected US waves is altered if the reflecting object is moving (the reflected frequency becomes higher if the object is moving towards the transducer and lower if the object is moving away from the transducer). This change in frequency can be used to measure how fast the object is moving. A recent application of Doppler US is the measurement of strain and strain rate in the tissue being imaged [76, 50]. The strain rate can be estimated by calculating the spatial gradients of the measured velocities and these can be integrated over time to obtain the strain in the tissue.

The main limitation of US imaging is the difficulty in obtaining high quality images. In conventional 2D US a mental image of the structure and motion of the heart is formed from multiple 2D acquisitions oriented in different directions. This

can lead to incorrect diagnoses as the images formed are subjective and depend on the observer. Additionally, follow up procedures are difficult to perform since the position of the transducer cannot be accurately reproduced from examination to examination.

Recent developments in 3D echocardiography [52] have the potential to provide real-time 3D visualizations of the structure of the heart and overcome some of the limitations of conventional 2D ultrasound.

1.3.2   X-Ray Computed Tomography

X-Ray *computed tomography* (CT) can be used to produce cross-sectional images of the body representing the X-Ray attenuation properties of the tissue being imaged. Thin X-Ray beams are used to the scan the field of view in a either a parallel or cone-beam configuration. This yields line attenuation measures for all possible angles of the X-Ray beams with respect to the body being imaged and are used to reconstruct the X-Ray attenuation at each point of the slice being scanned.

3D images can be obtained using spiral or sequential CT. Additionally, as CT is based on the attenuation of X-Rays as they pass through the body, contrast agents can be used to visualize blood vessels and identify tumors because of the different levels of contrast uptake in the tumours in comparison to the surrounding tissue.

The cardiac applications of X-Ray CT are in the evaluation of aortic disease, cardiac masses, and pericardial disease. The main advantage of X-Ray CT is the high resolution and good tissue contrast in the 3D images which can be acquired. But this advantage has to be weighed against the potentially harmful effects of the radiation dose given to the subject being imaged.

1.3.3   Nuclear Medicine Imaging

In nuclear medicine imaging a tracer molecule (a molecule containing an unstable radioactive isotope) is administered to the patient. The molecule is taken up by

the organs of the body as part of its normal metabolic processes. Measurements of gamma ray photons emitted by the tracer are then used to reconstruct maps of the concentration of the tracer in the body over time. Two types of imaging can be performed depending on the tracer molecule used.

1.3.3.1 SPECT

Single photon emission computed tomography (SPECT) relies on the emission of gamma ray photons from the radionuclide used. The most important single photon tracer is ^{99m}Tc, which is a metastable daughter product of the decay of ^{99}Mo, and decays to ^{99}Tc by emitting a single photon of 140 keV with a half-life of 6 hours.

The photons emitted are detected using a scintillation crystal coupled to a photomultiplier tubes. As the source of the emitted photons is an unknown distribution the gamma ray photons must be collimated with a mechanical collimator (a thick lead plate with cylindrical holes). The line information obtained can then be used to reconstruct the distribution of the tracer molecule in the body.

SPECT is used to assess the location and extent of ischemia and infarction in the heart resulting from coronary heart disease. SPECT imaging provides 3D density maps of blood perfusion in the myocardium. In a stress-rest study two perfusion maps of the myocardium are taken from the patient, one while the patient is at rest and one while the patient is exercising (under stress). Ischemic, infarcted, and normal tissue can be detected by comparison of the stress-rest images:

Normal If the intensity distributions in the perfusion maps are normal in both the stress and rest images then the state of the myocardium is normal.

Ischemic If the intensity distribution in the stress perfusion map is low but normal in the rest perfusion map then the myocardium is ischemic.

Infarcted If the intensity distributions in both the stress and rest maps are low then the myocardium is infarcted.

1.3.3.2 PET

In *positron emission tomography* (PET) imaging a tracer molecule containing a radionuclide such as ^{18}F is used. ^{18}F decays by emitting a positron and has a half-life of 109 minutes. The emitted positron very quickly ($\sim 10^{-9}$ seconds), and within a few millimeters of its origin, meets an electron and is annihilated producing two photons of 511 keV which travel in opposite directions.

No collimation is required in PET imaging as information about the origin of emission can be deduced from the fact that it must lie on the line joining the positions at which the photons are detected as well as the difference in times at which they are detected. PET is also more sensitive than SPECT as no photons are absorbed by a lead collimator during imaging but a PET scanner is also about four times more expensive to operate than a SPECT scanner.

Two areas of clinical application have emerged for PET imaging. Firstly, it can be used to detect, localize, and describe coronary artery disease; and secondly it can be used to identify injured but viable myocardium in a similar way to SPECT.

1.3.4   Magnetic Resonance Imaging

MRI [84, 104] of our bodies is possible because hydrogen atoms contained in the water and fat molecules of our organs possess an intrinsic spin ($\frac{1}{2}$) and an associated nuclear magnetic dipole moment, μ. When a body is placed in a strong constant magnetic field, $\mathbf{B}_0$, the nuclear magnetic dipole moments present in the body align themselves either in direction $\mathbf{B}_0$, or in the direction opposite to $\mathbf{B}_0$, while precessing about the direction of $\mathbf{B}_0$, as shown in figure 1.4. The precessional frequency is related to the strength of the applied magnetic field by the Larmor equation

$$\omega_0 = \gamma ||\mathbf{B}_0|| \tag{1.1}$$
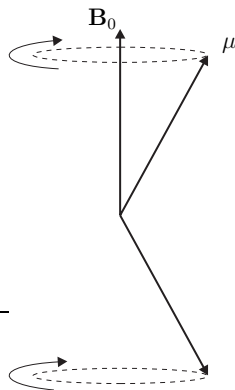
Figure 1.4: When an object containing hydrogen atoms is placed in a strong magnetic field $\mathbf{B}_0$ the nuclear magnetic dipole moments align themselves either in the direction of $\mathbf{B}_0$ or in the direction opposite to $\mathbf{B}_0$ while precessing at the same time about $\mathbf{B}_0$.

where γ is called the gyromagnetic ratio and for hydrogen atoms is equal to 42.57 MHz/T. There is a small excess in the number of magnetic dipole moments which are aligned in the direction of the $\mathbf{B_0}$ field and this results in a measurable macroscopic magnetization $\mathbf{M}$ which is equal to the sum of the microscopic nuclear magnetic dipole moments. Because the precessing nuclear magnetic dipole moments have random phases the transverse (the transverse plane is defined as the plane perpendicular to the $\mathbf{B}_0$ field, and the longitudinal direction is defined as the direction of the $\mathbf{B}_0$ field) components of the dipole moments sum to zero and $\mathbf{M}$ points in the same direction as the $\mathbf{B}_0$ field.

When an oscillating magnetic field in the form of a *radio-frequency* (RF) pulse, $\mathbf{B}_1$, with the frequency of oscillation equal to ω_0 and perpendicular to $\mathbf{B}_0$ is applied on the object, the magnetization is tipped away from $\mathbf{B_0}$. This results in a measurable transverse magnetization and a loss in longitudinal magnetization. But once the $\mathbf{B}_1$ field is switched off the magnetization recovers its thermal equilibrium value (called longitudinal relaxation or $T1$ relaxation), with a simultaneous loss in transverse magnetization due to nuclear interactions (called transverse relaxation or $T2$ relaxation) and the nonuniformity of $\mathbf{B}_0$ ($T2^*$ relaxation). By Faraday's law of induction, the rotating magnetization induces an electrical current in RF receiver coils placed in the scanner. This transient response, called a *free-induction decay* (FID),

of the spin system after the pulse excitation is dependent on a number of factors including the flip angle (the angle made by $\mathbf{M}$ with $\mathbf{B}_0$), the total number of spins in the sample, the magnetic field strength, and the magnetic field inhomogeneity.

To image a single plane in the body only nuclei within that plane are excited. This is achieved with magnetic field gradients, which alter the precessional frequencies of the nuclei within the sample along the direction of the gradient, so that when an RF pulse is applied only nuclei whose precessional frequencies match the oscillation frequency of the RF pulse resonate and generate a signal. To locate the signal within the imaged plane two further magnetic field gradients are used, one to encode the horizontal position (frequency encoding), and one to encode the vertical position (phase encoding). Thus, the spatial location of nuclei generating the detected signal is encoded in the signal itself. It can be shown that the signal detected is equivalent to the Fourier transform of the desired image [158, 91] and measuring the FID signals generated due to the perturbation of the spin system by the RF pulses allows the Fourier space to be sampled. An inverse Fourier transform applied on the raw data collected produces an image slice in the body.

As water and fat have different $T1$ and $T2$ relaxation times this fact can be used to generate contrast between the tissues in the body. It is also possible to perform angiography by taking the difference between two images which give different weights to the blood in the images but the same weight to other tissue in the images.

1.3.4.1   Imaging Sequences

The RF pulses and gradient fields can be applied in innumerable ways to generate contrast in the images acquired or to increase image acquisition speed [103, 158]. The spin echo sequence consists of a slice selective 90° pulse followed by one or more 180° refocusing pulses. This sequence can be used to generate $T1$-weighted, $T2$-weighted, or proton density images.

Gradient echo sequences such as the *fast low angle shot* (FLASH) sequence overcome the relatively large imaging times of the spin echo pulse sequences by not using

the 180° refocusing pulses and using a flip angle smaller than 90°. Gradient echo pulse sequences are primarily used for fast 2D and 3D acquisition of $T1$-weighted images. *Echo-planar imaging* (EPI) is a modification of Fourier imaging in which all experiments necessary to reconstruct the image of an entire plane are performed within a single FID. Other fast imaging sequences such as *turbo spin echo* (TurboSE), *half-Fourier acquisition with single-shot turbo spin echo* (HASTE), and spiral imaging have also been developed.

1.3.4.2 Flow Measurement

Phase Contrast MR It has been known for a long time (even before the proper development of MRI) that NMR signals are sensitive to flow and motion [169]. Measured phase changes induced in the transverse magnetization of moving spins in a spatially varying magnetic field can be used to compute the velocities of the moving spins. The total phase shift, ϕ, induced between excitation and measurement is given by [158]

$$\phi = \int_0^t \gamma \mathbf{G}(t).\mathbf{r}(t)\,dt \tag{1.2}$$

where $\mathbf{G}$ is the gradient field applied between times 0 and t and $\mathbf{r}$ is the path followed by the moving spin. Expanding $\mathbf{r}$ in terms of a Taylor series about $t = 0$

$$\mathbf{r}(t) = \mathbf{r}(0) + \left.\frac{d\mathbf{r}}{dt}\right|_{t=0} t + \cdots + \left.\frac{d^l\mathbf{r}}{dt^l}\right|_{t=0} \frac{t^l}{l!} + \cdots \tag{1.3}$$

and substituting into equation 1.2 we obtain

$$\phi = \mathbf{r}_0.\mathbf{m}_0 + \mathbf{v}_0.\mathbf{m}_1 + \mathbf{a}_0.\mathbf{m}_2 + \cdots + \tag{1.4}$$

where

$$\mathbf{r}_0 = \mathbf{r}(0) \tag{1.5}$$

$$\mathbf{v}_0 = \left.\frac{d\mathbf{r}}{dt}\right|_{t=0} \tag{1.6}$$

$$\mathbf{a}_0 = \left.\frac{d^2\mathbf{r}}{dt^2}\right|_{t=0} \tag{1.7}$$

are the position, velocity, and acceleration of the moving spins at time $t = 0$ and

$$\mathbf{m}_l = \int_0^t \gamma \mathbf{G}(t) \frac{t^l}{l!} \, dt \tag{1.8}$$

is the l-th order moment of the gradient waveform. The first term in equation 1.4 is related to how the spatial positions of the spins are encoded in a MR pulse sequence and at the time of measurement (the echo time) is equal to 0. Assuming that higher order terms can be ignored we see that the phase shift is proportional to the velocity. This result can be used to measure the velocities of moving spins in a voxel by voxel basis [123].

1.3.4.3 Magnetic Resonance Angiography

In the *Time-of-Flight* (TOF) pulse sequence a gradient-echo pulse sequence is used to alter the longitudinal magnetization vectors in an imaging slice. The magnetization vectors of stationary spins are made very small, an effect known as saturation, while moving spins are unaffected. If a blood vessel passes through the imaging plane it appears as a bright vessel in the image while all other stationary tissue remains dark. The TOF pulse sequence is used to perform MR angiography.

Alternatively 3D MR angiography can be performed by using a contrast agent (such as gadolinium chelate) which alter the $T1$ and $T2$ relaxation times of blood.

1.3.4.4 Magnetic Resonance Tagging

Myocardial tissue in the body can be labelled by altering its magnetization properties which is persistent even in the presence of motion. By measuring the motion of the labelled tissue, deformation fields in the myocardium can be reconstructed. Magnetic resonance tagging was first proposed by Zerhouni *et al* [181] as a means of non-invasively introducing markers within the myocardium of the LV. The technique relies on the perturbation of the magnetization in the myocardium by using a sequence of RF saturation pulses before the acquisition of images using conventional imaging. Because the myocardium retains knowledge of the perturbation in the magnetization the motion of the myocardium can be tracked during systole. Recent reviews of MR tagging are given in [137] and [10].

Tagging Pulse Sequences The *SPAatial Modulation of Magnetization* (SPAMM) pulse sequence was developed by Axel and Dougherty [12, 11], which consists of two nonselective (a nonselective pulse is one that is designed to excite all the spins in the sample) RF pulses separated by a magnetic field gradient pulse. In the frame of reference rotating with the $\mathbf{B}_1$ field generated by the first RF pulse, the effect of the pulse is to flip the longitudinal magnetization onto the transverse plane creating a transverse magnetization. The phase of the transverse magnetization is the same everywhere in the sample. The gradient pulse spatially modulates the phase of the transverse magnetization along the direction of the gradient. When the second RF pulse is applied, the magnetization vectors are tipped on to the transverse plane again, creating a modulation in the longitudinal magnetization.

The effect of the SPAMM pulse sequence is to produce a series of hypointense stripes in the images acquired. Two sequences of stripes can be produced forming a grid pattern as shown in figure 1.5.

$$\xrightarrow{\quad\text{ed}\qquad\qquad\text{ms}\qquad\qquad\text{es}\qquad} t$$
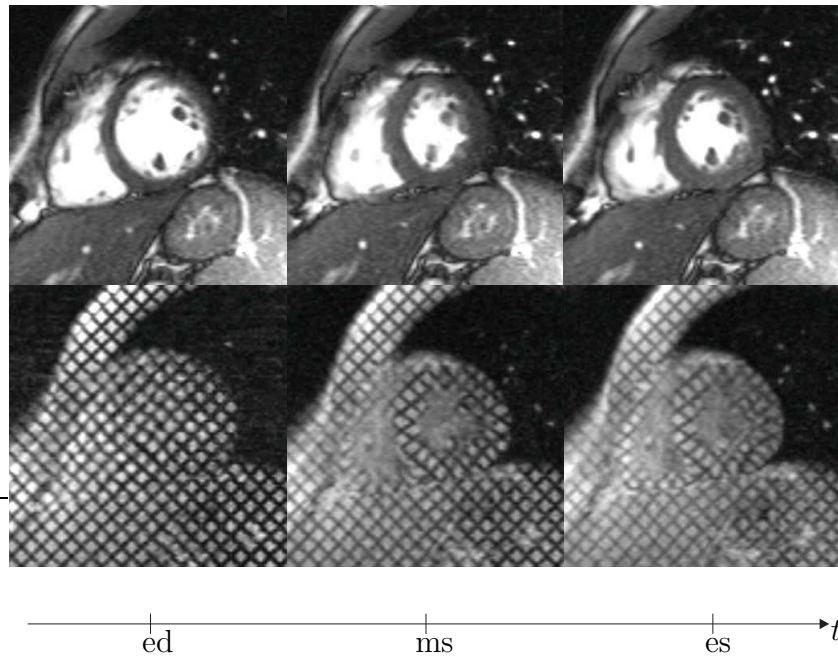
Figure 1.5: The top row shows a sequence of short-axis mid-ventricular untagged images taken from a normal healthy volunteer at three different points in the cardiac cycle, end-diastole (ed), mid-systole (md), and end-systole (es). The bottom row shows the corresponding set of SPAMM images.

1.3.4.5 Perfusion

Blood perfusion in tissues can be evaluated by using a a contrast agent such as gadolinium chelate which is intravenously injected into the patient. The contrast agent decreases the $T1$ and $T2$ relaxation times of the blood, while extravascular protons are not affected. The contrast produced can be used to measure the activity of the capillary network permeating the myocardial tissue.

1.3.5 Imaging Planes

As the heart is continuously in motion it is necessary to acquire images in multiple orientations so that an accurate diagnosis can be made. It is common to define, orient, and display the heart using the long-axis of the left ventricle and selected planes at 90° angles relative to the long-axis. The imaging planes used are shown in figure 1.6 and some example images are shown in figure 1.7. Other factors which also make cardiac imaging challenging are patient motion, respiration, and

41
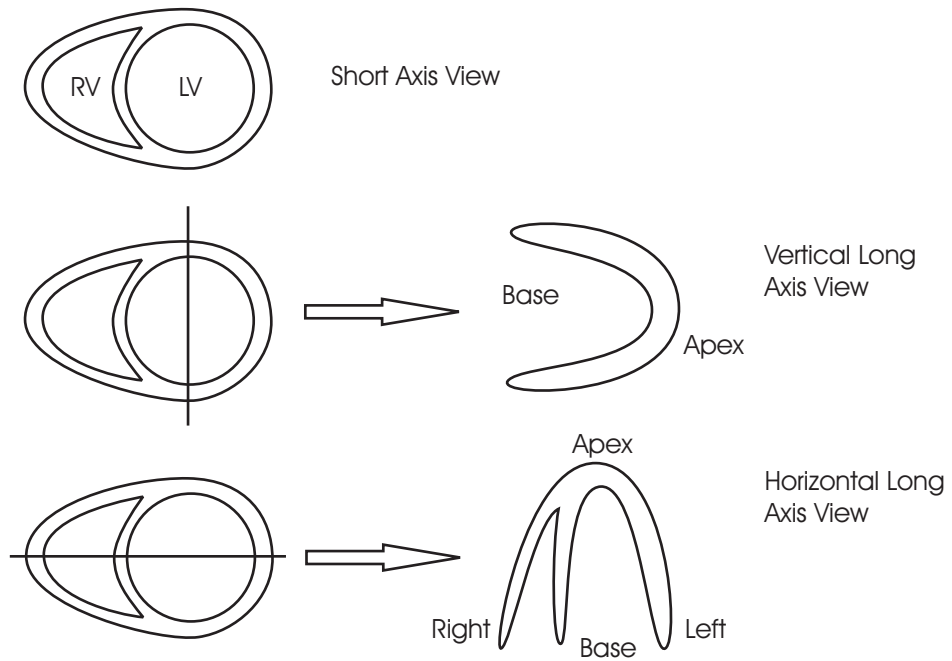
Figure 1.6: The cardiac imaging planes [23].

Figure 1.7: The images from left to right show respectively short-axis, horizontal long-axis and vertical long-axis views of the heart.

the anisotropic resolution of the images acquired. Typically, the in-plane resolution is much higher than the through-plane resolution as shown in figure 1.8.

1.4 Contributions

Although a wealth of data can be collected about the anatomy and physiology of the heart it is only in recent years, with the development of sufficient computational power and novel methods for image analysis, that the full potential of cardiovascular imaging has begun to be realized. It is also clear that MRI is becoming the modality
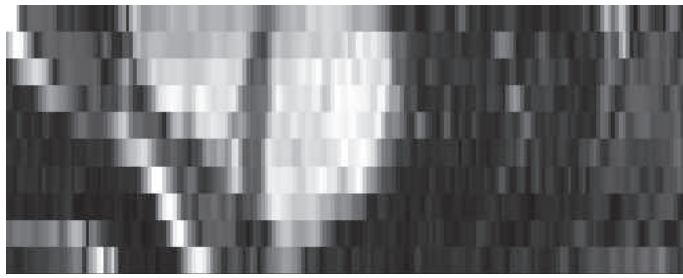
Figure 1.8: This figure shows a simulated long-axis view of the heart which has been obtained by stacking a set of short-axis images. As can be seen the through-plane resolution is lower than the in-plane resolution.

of choice for cardiovascular image analysis as it has a number of advantages over other imaging techniques. It is safe, noninvasive, and 3D and 4D images with high spatial and temporal resolution of the anatomy and physiology of the heart can be acquired in arbitrary orientations. Additionally, the acquisition protocols developed for MRI enable blood flow and motion to be measured non-invasively, and among them MR tagging can be used to measure myocardial deformation. However, MR tagging is still not used routinely in the clinical environment as the amount of post-processing required to extract meaningful functional parameters is too prohibitive to be useful clinically. Additionally, no fully automatic method for the extraction of deformation fields from tagged MR images yet exists.

The focus of the research presented in this thesis is the use of nonrigid image registration techniques for cardiac motion analysis. The work presented makes four main contributions to the analysis of tagged MR images and are contained in chapters 4–7:

- A technique for cardiac motion tracking in tagged MR images of the LV is developed using nonrigid image registration and a transformation model based on free-form deformations. To reconstruct the full four dimensional motion field within the heart, short-axis and long-axis images of the heart are used. The images taken during the cardiac cycle are registered to a set of reference images taken at end-diastole to recover the deformation field within the myocardium of the heart. The proposed method is validated using a cardiac

motion simulator and strain patterns from a group of normal volunteers are derived to show the viability of the method for clinical use.

- We then extend the registration technique presented to use a cylindrical free-form deformation model of cardiac motion. The cylindrical free-form deformations are able to model more closely the radial thickening, circumferential twisting, and longitudinal contraction of the heart. We compare this method with the method based on ordinary free-form deformations and derive strain patterns from a group of normal volunteers.

- A 4D image registration algorithm for cardiac motion tracking is then developed. The technique is based on the registration of two 4D image sequences to each other, one in which the heart is moving and the other in which the heart is stationary. The algorithm uses a 4D free-form deformation to model the motion of the heart and allows the computation of deformation parameters at arbitrary time instants in the cardiac cycle thus making comparison of strain patterns across different subjects easier.

- Finally, a statistical model of the cardiac motion in a group of normal volunteers is constructed. To build this statistical model the motion fields in the hearts of a group of 17 volunteers are transformed into a common coordinate system so that an objective comparison of the motion fields can be made. A *principal component analysis* (PCA) of the motion fields is then performed to derive the major modes of variation in the motion fields across the subjects. Two different types of PCA are performed, a time-dependent PCA and a time-independent PCA. The free-form deformation model used for tracking the motion of the heart is then reparameterized in terms of the major modes of variation in the deformation fields. The ability of the statistical deformation model to track the motion of the heart is then evaluated.

1.5　Overview of Thesis

Chapters 2 and 3 contain the introductory and background material on cardiac image analysis. Chapter 2 reviews the methods that have been developed for motion estimation in cardiac images and chapter 3 reviews the methods that have been developed for cardiac image registration.

The methods and algorithms that have been developed during our research are presented in the subsequent chapters. In chapter 4 we develop a method for cardiac motion tracking using nonrigid image registration and free-form deformations. In chapter 5 we extend the method presented in chapter 4 to use free-form deformations based in a cylindrical coordinate system. In chapter 6 a 4D B-spline registration algorithm for tracking the motion of the heart is developed and in chapter 7 a statistical motion model for cardiac motion tracking is presented.

Finally, in chapter 8, we summarize the work presented in this thesis and discuss future work.

Chapter 2

Cardiac Motion Analysis

The ultimate objective of clinicians and researchers working in the field of cardiac image processing and analysis is to build useful and efficient tools for the diagnosis and treatment of patients with CVDs. Since it is common for large amounts of data to be generated in a single imaging session, the manual analysis of the images acquired is too time consuming to be useful in a clinical setting and is subject to intra- and inter-observer variability. It is also likely that further development of imaging technologies will only increase the amount of data made available for use and so the need for highly automated tools to aid in the extraction and analysis of clinically useful functional parameters will only increase. Also, an increasing amount of attention has been focussed on the estimation of local deformation parameters, such as strain, from cardiac images as it is believed that investigating the mechanical effects of diseases such as cardiomyopathy and ischemia can lead to improved methods for the treatment of patients with CVDs.

Although the motion of the heart is complex, three different components can be distinguished in a normal motion: radial thickening, longitudinal shortening, and apico-basal twisting. Regional variations can also be seen in the motion and strain patterns in a normal heart—the lateral part of the heart moves more significantly than the septum and transmural differences in the strain distribution are also seen [111]. CVDs affect the normal motion patterns seen in the heart. For exam-

ple, the reduction in blood flow to the myocardium resulting from coronary artery disease changes the mechanical properties of the heart muscle. One of earliest signs seen is the decreased contractility of the myocardium. Infarcted regions of the heart permanently lose their ability to contract and these can also be detected from motion studies. Detection of abnormal motion patterns and their evolution over time can be invaluable in determining those who will benefit most from available treatments as well as monitor their recovery.

In general, the sequence of processes involved in the functional analysis of cardiac images can be divided into four main stages as shown in figure 2.1.

Imaging To image the heart successfully is a challenging endeavor. Not only is the image acquisition made difficult by the intrinsic beating motion of the heart itself but the breathing motion of the patient must also be accounted for. Furthermore, motion estimation is made difficult in many modalities (such as US, PET, and SPECT) as there are no clearly distinguishable anatomical features in the walls of the heart. In these imaging modalities only simple measures of contractility such as the radial contraction or radial thickening of the ventricular walls can be estimated. Ideally we would like to be able to construct a 4D model (3D spatial and 1D time) to properly estimate various functional parameters. To construct such a model, 3D image sequences must be acquired covering the entire heart for the whole of the cardiac cycle. The number and quality of the images that can be acquired depend on the imaging modalities used and these have their own unique characteristics and limitations as described in chapter 1. Thus, the model that can be built and the parameters that can be derived from it depend directly on the imaging modality or modalities chosen.

Feature Extraction and Model Construction After the images are acquired specific features such as surfaces and contours related to the geometry of the heart are extracted. These features are used to construct the spatio-temporal
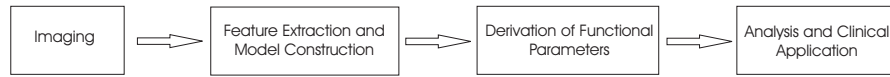
Figure 2.1: A block diagram showing the sequence of steps taken in extracting functional parameters from cardiac images.

models of the heart. Most researchers have concentrated on building models for just the LV as it is larger than the RV and, because of its greater demand for energy, is also more susceptible to CHD. Information about the internal structure of the heart, such as the muscle fiber orientations that can be obtained from diffusion tensor MRI [71], can also be incorporated with the geometrical information extracted to enhance the predictive capabilities of the model built.

Derivation of Functional Parameters from Model The models are then used to estimate specific global and local parameters of interest to the clinician.

Analysis and Clinical Application Finally, the parameters extracted are used by clinicians to assess the functioning of the heart. To aid in this analysis, visualization tools can be used to determine whether the extracted parameters fall within normal limits.

A significant amount of progress has been made in the development of methods for the functional analysis of cardiac images and an extensive review has been made by Frangi *et al* [56]. In this chapter we review the computational methods that have been developed for the measurement of functional parameters using the imaging modalities described in the previous chapter with a particular emphasis on cardiac motion analysis.

2.1 Feature Extraction and Model Construction

To derive global parameters of cardiac function the endocardial and epicardial contours need to be extracted. Many segmentation algorithms have been developed

for this purpose, each tailored to the specific problems encountered when using a particular imaging modality. US images are perhaps the most difficult images to segment because the boundaries of the LV are not clearly visible due to the noise present in the images. Several steps are usually necessary to group detected edges into the contours of the LV based on geometrical and spatiotemporal constraints [90, 18, 177, 174, 172]. The extracted contours can then be used to construct parametric B-spline surfaces of the LV cavity so that global parameters of cardiac function can then be estimated [177].

A number of generic methods have been adapted for contour detection and can applied to X-Ray CT, PET, SPECT, and MR images in which the contours of the LV can be clearly delineated. Neural networks [40], fuzzy C-means clustering [19], and model-based techniques [80] have been used in gated PET and SPECT images.

Active shape models [37, 38] and active appearance models [35, 36] which incorporate prior knowledge about the shape and appearance of the LV into the segmentation algorithm have also been used successfully to segment the contours of the LV in both US and cardiac MR images [74, 110, 109, 79]. Recently Lorenzo-Valdés *et al* [94] have developed atlas-based segmentation of the LV using image registration.

2.2 Functional Parameters

Functional parameters used to assess cardiac function can be classed into two different categories: global and local functional parameters. Global measures of cardiac function describe the overall ability of the heart to deliver blood to the rest of the body, while local functional parameters are used to assess regional dysfunction in the heart which is determined by the state of the myocardial tissue (section 1.1.3).

2.2.1 Global Functional Parameters

Global functional parameters assess the overall performance of the ventricles in their ability to eject blood. The *left ventricular volume* (LVV), *left ventricular mass*

(LVM), *stroke volume* (SV), *ejection fraction* (EF) and *cardiac output* (CO) have all been used to assess the performance of the LV [56].

Left Ventricular Volume (LVV) LVV is defined to be the volume enclosed by the LV. Volume-time curves of the left-ventricular cavity can provide information about the global contractility of the myocardium.

Left Ventricular Mass (LVM) LVM is the mass of the LV and is equal to the volume of the myocardium, V_m, multiplied by the density of the myocardium, $\rho_m = 1.05\,\text{g/cm}^3$:

$$\text{LVM} = V_m\rho_m \tag{2.1}$$

This quantity can be used to assess the excessive development of the myocardium of the LV (hypertrophy) which can also result in a loss of function.

Stroke Volume (SV) SV is defined as the volume ejected during systole and is equal to the difference between the *end-diastolic volume* (EDV) and the *end-systolic volume* (ESV):

$$\text{SV} = \text{EDV} - \text{ESV} \tag{2.2}$$

Ejection Fraction (EF) The EF is defined as the ratio of the SV to the EDV:

$$\text{EF} = \frac{\text{SV}}{\text{EDV}} \times 100\% \tag{2.3}$$

Cardiac Output (CO) The CO is the amount of blood ejected from the LV per minute and is equal to the SV multiplied by the *heart rate* (HR):

$$\text{CO} = \text{SV} \times \text{HR} \tag{2.4}$$

Although global functional parameters can be used to determine the abnormal functioning of the heart they do not indicate which regions of the heart have reduced contractile function. Moreover, for some patients, global functional parameters fall

within normal limits even though the wall motion may be abnormal. For example, patients suffering from hypertensive left ventricular hypertrophy may have normal EF while circumferential and longitudinal shortening are depressed [82, 118]. Measuring local functional parameters can help to detect areas of the myocardium which have been damaged because of reduced blood flow.

2.2.2 Local Functional Parameters

The motion of the heart can be characterized in terms of its contraction in the radial, circumferential and longitudinal directions, the wall thickening, the apico-basal twist of the myocardium, as well as the strain in the myocardium.

2.2.2.1 Radial, Circumferential and Longitudinal Contraction

In assessing the radial, circumferential, and longitudinal contraction motion parameters, a coordinate system is chosen that is defined with respect to the geometry of the heart. For example, to assess motion parameters in the LV (figure 2.2), the z-axis or the long-axis of the LV is defined to be the line joining the apex to the midpoint of the base of the LV (usually taken to be the midpoint of the mitral valve leaflets). The planes perpendicular to the long-axis then define the short-axis planes. The radial, circumferential, and longitudinal contraction are then defined by the vectors $\mathbf{u}_r$, $\mathbf{u}_\theta$, and $\mathbf{u}_z$, as shown in figure 2.2.

2.2.2.2 Apico-basal Twist

There is a gradient in the rotation angle of the myocardium of the LV about the long-axis as it contracts. This is due to the helically oriented muscle fibers in the LV [62]. When viewed from base to apex, the base is seen to rotate in a clockwise direction while the apex is seen to rotate in an anticlockwise direction. Torsion in the LV reduces the transmural myocardial strain and reduces oxygen demand during systole. When muscle cells die systolic LV torsional deformation is delayed
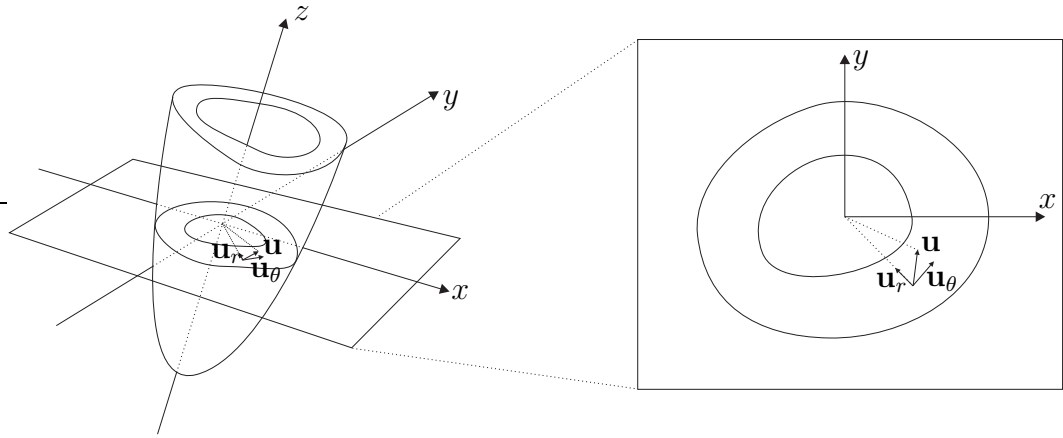
Figure 2.2: Local motion parameters in the LV are measured in a coordinate system which is defined with respect to the geometry of the LV.

and decreased, impairing the beneficial effects of torsional deformation [163], while in patients suffering from pressure overload due to aortic stenosis the torsion is significantly increased and diastolic apical untwisting is prolonged compared with those of normal subjects [153].

2.2.2.3   Strain

When an object is deformed, internal forces are produced within the body which tend to return the object to its undeformed state. These forces are related directly to the amount of stretching or deformation that the body is made to undergo. Strain is a quantity which measures the load placed on the body by measuring the amount of deformation of the body. In one dimension the strain can be defined in a number of ways. For example, in figure 2.3, which shows the deformation of a 1D object, the material point A with position x initially, moves to the position $q(x)$ in the deformed state; and the material point B with position $x + dx$ initially, moves to the position $q(x + dx)$. Then, one way of defining the strain is as the ratio of the extension of

the element $\overrightarrow{AB}$ to its original length

$$E \quad = \quad \frac{||\overrightarrow{AB}_{\mathrm{def}}|| - ||\overrightarrow{AB}||}{||\overrightarrow{AB}||} \tag{2.5}$$

$$= \quad \frac{q(x + dx) - q(x) - dx}{dx} \tag{2.6}$$

$$= \quad \frac{dq}{dx} - 1 \tag{2.7}$$

where $\overrightarrow{AB}_{\mathrm{def}}$ is the vector between the material points A and B in the deformed state. In terms of the displacement of points in the object, $u(x) = q(x) - x$, the strain is:

$$E = \frac{du}{dx} \tag{2.8}$$

The strain can also be defined as the ratio of the difference between the squares of the lengths of the element $\overrightarrow{AB}$ in its deformed and undeformed states to the square of the length of the element in its undeformed stated

$$E \quad = \quad \frac{1}{2} \frac{||\overrightarrow{AB}_{\mathrm{def}}||^2 - ||\overrightarrow{AB}||^2}{||\overrightarrow{AB}||^2} \tag{2.9}$$

$$= \quad \frac{1}{2} \frac{(q(x + dx) - q(x))^2 - dx^2}{(dx)^2} \tag{2.10}$$

$$= \quad \frac{1}{2} \left[\left(\frac{dq}{dx} \right)^2 - 1 \right] \tag{2.11}$$

which in terms of the displacement, u, is:

$$E = \frac{du}{dx} + \frac{1}{2} \left(\frac{du}{dx} \right)^2 \tag{2.12}$$

The two definitions of strain given in equations 2.8 and 2.12 become equivalent to each other when the deformation is very small.

In three dimensions (figure 2.4), where $\mathbf{x} = (x_1, x_2, x_3)$ and $\mathbf{q} = (q_1, q_2, q_3)$, it is mathematically more convenient to consider the squares of the elements $||\overrightarrow{AB}||$ and
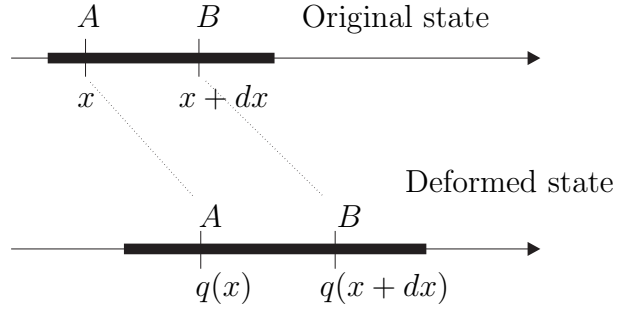
Figure 2.3: The deformation of an object in 1D.

$||\overrightarrow{AB}_{\text{def}}||$ in finding a suitable definition for the strain:

$$||\overrightarrow{AB}_{\text{def}}||^2 - ||\overrightarrow{AB}||^2 \quad = \quad ||\mathbf{q}(\mathbf{x}+d\mathbf{x}) - \mathbf{q}(\mathbf{x})||^2 - ||d\mathbf{x}||^2 \tag{2.13}$$

$$= \quad \sum_i \sum_j \frac{\partial q_i}{\partial x_j} dx_j \sum_k \frac{\partial q_i}{\partial x_k} dx_k - dx_i\, dx_i \tag{2.14}$$

Rewriting $\mathbf{q}(\mathbf{x})$ in terms of the displacement field $\mathbf{u}(\mathbf{x}) = (u_1, u_2, u_3)$

$$\mathbf{q}(\mathbf{x}) = \mathbf{x} + \mathbf{u}(\mathbf{x}) \tag{2.15}$$

equation 2.14 becomes:

$$||\overrightarrow{AB}_{\text{def}}||^2 - ||\overrightarrow{AB}||^2 = \sum_i \sum_j \left(\frac{\partial u_i}{\partial x_j} + \frac{\partial u_j}{\partial x_i} + \sum_k \frac{\partial u_k}{\partial x_i} \frac{\partial u_k}{\partial x_j} \right) dx_i\, dx_j \tag{2.16}$$

The strain is defined from this equation as:

$$E_{ij} = \frac{1}{2} \left(\frac{\partial u_i}{\partial x_j} + \frac{\partial u_j}{\partial x_i} + \sum_k \frac{\partial u_k}{\partial x_i} \frac{\partial u_k}{\partial x_j} \right) \tag{2.17}$$

$\mathbf{E} = \{E_{ij}\}$ is called the Lagrangian strain tensor and it behaves like a symmetric tensor of rank 2. When the displacement field $\mathbf{u}$ is very small the third term in equation 2.17 vanishes and we obtain another measure of strain, $\mathbf{e} = \{e_{ij}\}$, called Cauchy's infinitesimal strain tensor:

$$e_{ij} = \frac{1}{2} \left(\frac{\partial u_i}{\partial x_j} + \frac{\partial u_j}{\partial x_i} \right) \tag{2.18}$$
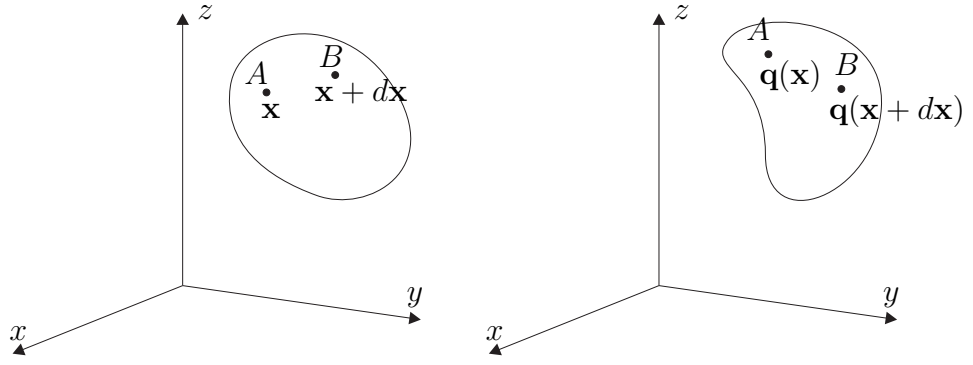
Figure 2.4: This figure shows the deformation of an object. The point $\mathbf{x}$ moves to the position $\mathbf{q}(\mathbf{x})$, and the point $\mathbf{x} + d\mathbf{x}$ moves to the position $\mathbf{q}(\mathbf{x} + d\mathbf{x})$.

The diagonal elements in $\mathbf{E}$ and $\mathbf{e}$ are called the *normal* strains, and the off-diagonal elements are called the *shear* strains.

We can compute the strain in a particular direction by using the transformation law for tensors. If $\mathbf{R}$ is the rotation matrix which transforms the components of a position vector measured in the coordinate system with Cartesian axes xyz into a coordinate system with the Cartesian axes $x'y'z'$, then the components of the strain tensor measured in the $x'y'z'$ coordinate system are given by

$$E'_{ij} = \sum_\alpha \sum_\beta R_{i\alpha} R_{j\beta} E_{\alpha\beta} \tag{2.19}$$

where R_{ij} is the element of matrix $\mathbf{R}$ with row i and column j.

Figure 2.5 shows a coordinate system, $x'y'z'$, in which the x'-axis points in the radial direction, $\mathbf{e}_r$, the y'-axis points in the circumferential direction, $\mathbf{e}_\theta$, and the z'-axis points in the same direction as the z-axis, $\mathbf{e}_z$. Using equation 2.19 the radial strain is given by

$$E_{\mathbf{e}_r} = E'_{11} = \mathbf{e}_r^T \mathbf{E} \mathbf{e}_r \tag{2.20}$$

where $\mathbf{e}_r^T = [\cos\theta, \sin\theta, 0]$. In general, the strain in a particular direction, $\mathbf{u}$, is given by

$$E_{\mathbf{u}} = \mathbf{u}^T \mathbf{E} \mathbf{u} \tag{2.21}$$

which is a scalar value.
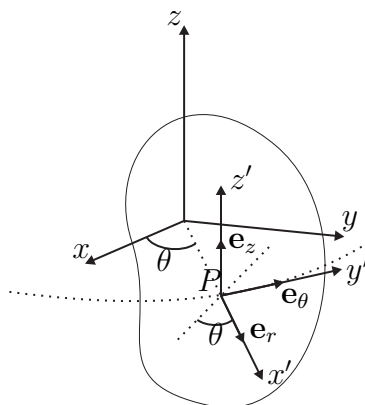
Figure 2.5: To compute the strain tensor at the point P in a coordinate system whose axes x', y', and z' are aligned in the directions $\mathbf{e}_r$, $\mathbf{e}_\theta$, and $\mathbf{e}_z$ we can use the transformation law for tensors.

Strain Visualization   A common way to visualize strains in a particular region of interest is by using contour or color maps. Another way of visualizing strains is with the use of tensor ellipsoids. Since the strain tensor, E, is a symmetric tensor, a coordinate system can be found in which E take the form a diagonal matrix. The rotation matrix which transforms into this coordinate system is given by $\mathbf{R}_P$ in which the column vectors are equal to the the eigenvectors of $\mathbf{E}$. The diagonal components of the strain tensor in this coordinate system are called the principal strains and are equal to the eigenvalues of $\mathbf{E}$. The eigenvectors point in the principal strain directions. At each point in the region of interest an ellipsoid can be drawn whose axes point in the directions of the eigenvectors of the strain tensor and whose lengths are proportional to the eigenvalues.

Figure 2.6 shows a visualization of a synthetic displacement field using an arrow plot and the corresponding strain field using tensor ellipsoids.

2.3   Motion Analysis using Ultrasound

As there are no clear landmarks in the ventricular walls, true 4D motion estimation from US images is not possible. Nevertheless, the relatively low cost of US and the ability to acquire images from the bedsides of critically ill patients have attracted a significant amount of attention in the literature for the estimation of
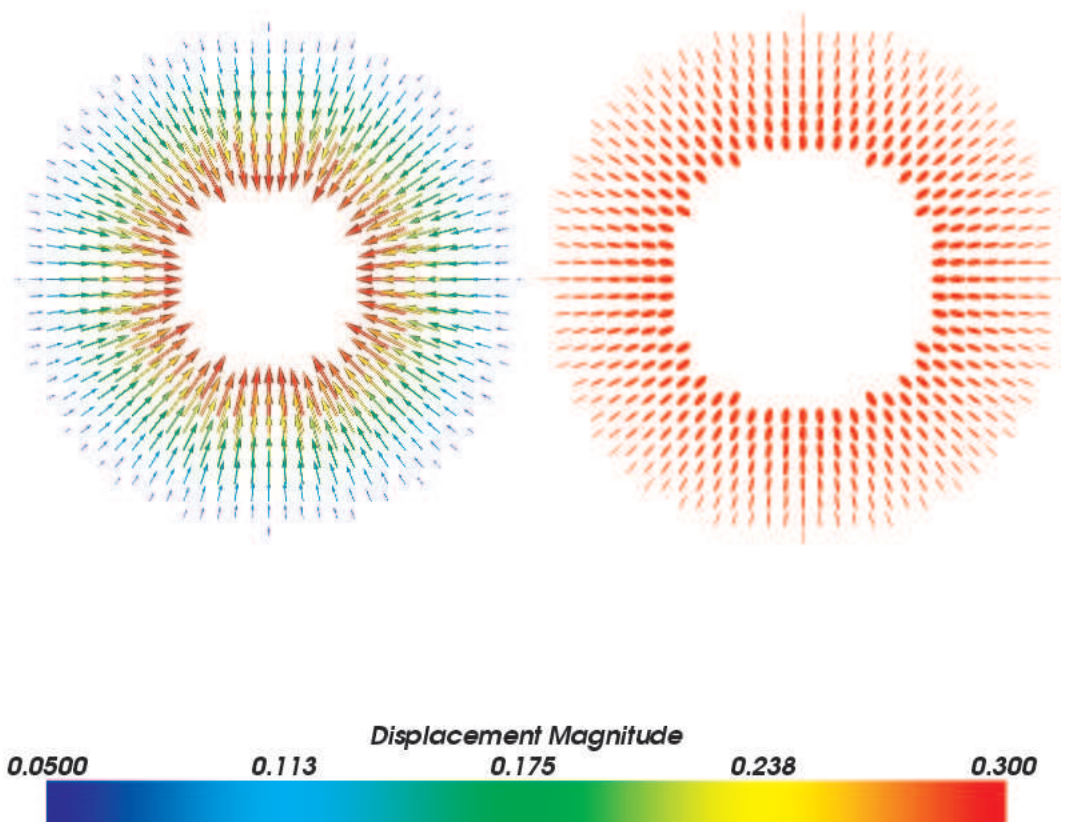
Figure 2.6: The figure on the left shows an arrow plot of a radially symmetric displacement field. The figure on the right shows a plot of the corresponding strain field using tensor ellipsoids.
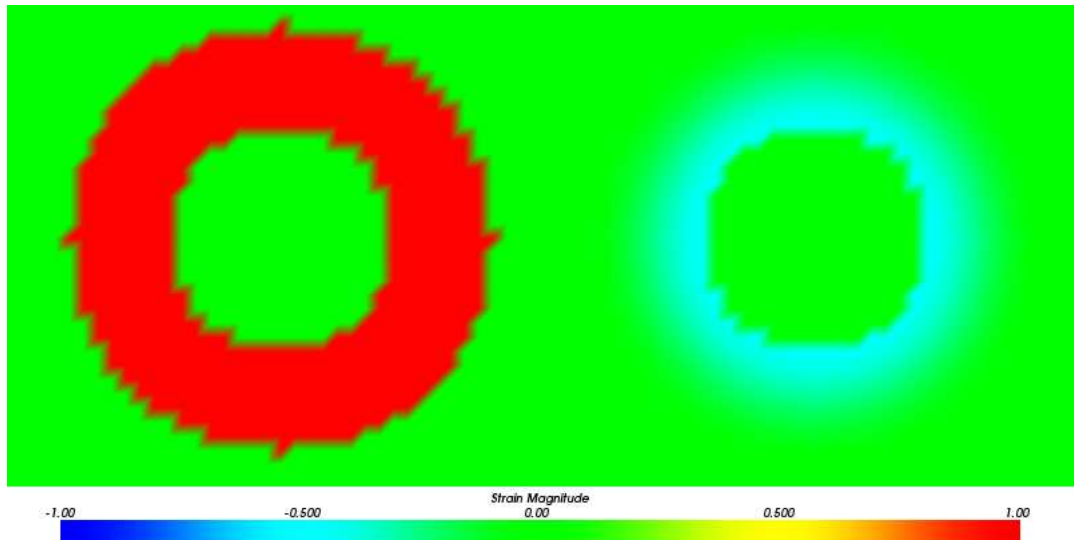
Figure 2.7: A plot of the radial (left) and circumferential strains (right) generated by the displacement field shown in figure 2.6.

motion parameters from US images.

Because of the noise present in the US images some researchers have concentrated on finding only the boundaries of the LV and estimated local deformation parameters from the contours extracted. Tseng *et al* [165] used 4D knowledge-based snakes and a *continuous distance transform neural network* (CDTNN) to detect the endocardium of the LV in US images acquired using transesophageal echocardiography. Other methods based on level sets [39] and active contours [60] have also been proposed for contour tracking. Common to all of these methods, the epicardium is not as easy to track because of the poor contrast between it and the background.

Papademetris *et al* [120] relied on operator intervention and correction of a semi-automatic algorithm for the detection of endocardial and epicardial surfaces. Corresponding points on the surfaces detected in the image sequence were then mapped to each other using an algorithm which tried to minimize the differences in principal curvatures between the surfaces [151]. They then used a biomechanical model of the LV which incorporated prior knowledge of the muscle fiber orientations to obtain a dense estimate of the deformation field within the myocardium.

There is some evidence that the speckle patterns generated from scattering by underlying tissue elements in echocardiographic image sequences are temporally

correlated. Some researchers have investigated the possibility of reconstructing the deformation field in the myocardium by tracking the motion of the speckle during the cardiac cycle. Mailloux *et al* [97] assumed that the interframe velocity field could be locally described by a set of linear equations. The linearity of the optical flow field was introduced into the optical flow formulation of Horn and Schunck [70] and used to estimate the deformation of the LV wall in 2D echocardiographic image sequences. A more general method using deformable meshes and block matching has also been suggested for tracking speckle patterns [178] but has yet to be applied for heart images.

The assumption that the motion of the underlying tissue is strongly coupled to the motion of the speckle patterns becomes false when the tissue scattering structures which generate the speckle patterns move in a nonuniform way. This results in speckle decorrelation and is the greatest difficulty encountered when tracking speckle patterns. Other problems such as noise, through-plane motion, and speckle motion artifacts resulting from the image formation process itself also make motion estimation from US images challenging.

2.4   Motion Analysis using PET and SPECT

Wall motion analyses can also be performed on PET and SPECT, although the poor resolution of the images acquired imply that dense estimates of deformation parameters are not possible. Simple numerical scores can be assigned to segments of the heart to classify the type of motion motion exhibited in a particular region of the myocardium. For example, 1 = normal wall motion, 2 = hypokinesis (diminished endocardial wall motion and thickening), 3 = akinesis (no endocardial movement or wall thickening), and 4 = dyskinesis (outward excursion of the wall during systole). Such numerical indices have been used by human observers to grade wall motion abnormalities in *electrocardiographically* (ECG) gated PET images [67, 145, 176]. Similar studies have also been conducted in gated SPECT images [168, 15, 2, 1, 89].

2.5 Motion Analysis using MRI

Unique to MRI is the ability to measure displacements and velocities of material points in the myocardium. Two different methods can be used to quantify myocardial kinematics—*phase contrast MRI* (PC-MRI) and *magnetic resonance tagging.*

2.5.1 Phase Contrast MR

The main difficulty associated with motion estimation from cine phase contrast MR images is the accumulation of errors which results when the measured velocities are integrated over time to track the motion of a material point. This is particularly true near borders of the LV. Other difficulties also result from the spatially dependent phase offsets caused by eddy currents.

To overcome some of these difficulties Zhu and Pelc [182] computed motion trajectories from cine PC-MRI images by modeling the the periodic motion of the heart as composed of Fourier harmonics and integrating the material velocity of the tracked point in the frequency domain. They then extended the method using a spatio-temporal finite element mesh model [184] in which the nodes of the finite element mesh were characterized by the Fourier harmonics. This allowed a smooth transition from a coarse but highly reproducible model to a perfect spatiotemporal representation (at the expense of reduced reproducibility). Meyer *et al* [108] integrated information from the LV contours as well as the velocity data into a deforming mesh to track the myocardium over time. The mesh was guided by a Kalman filter in which the cardiac motion was modeled as being temporally smooth and cyclical when there was low confidence in the contour and velocity data. Other similar methods to estimate strain have also been suggested [183].

A virtual tagging framework has been proposed by Masood *et al* [105]. Velocity measurements made during the cardiac cycle are used to deform an artificial tag grid imposed on the heart muscle. The differences between the velocities computed from the deforming virtual tag grid and the true velocities measured during the scanning

are minimized in a least squares sense. The deformation of the virtual tag grid can then be used to compute the strain in the myocardium.

2.5.2 Magnetic Resonance Tagging

The main difficulty associated with the MR tagging is the loss of contrast between tags due to longitudinal (T1) relaxation so that the entire cardiac cycle cannot be tracked with a single set of images. Fischer *et al* [53] proposed a method called *Complementary SPAtial Modulation of Magnetization* (CSPAMM) to reduce the effects of tag fading by acquiring two sets of images in which the tagging grids in the first set of images is the negative of the tagging grids in the second set and subtracting one from the other. As the two sets of images are acquired sequentially the image acquisition time is correspondingly increased.

Other methods to improve the tagging contrast and resolution have also been proposed including the *Delays Alternating with Nutations for Tailored Excitations* (DANTE) tagging sequence [112] as well as hybrid methods utilizing *Steady-State Free Precession* (SSFP) [66] and spiral MR imaging sequences [143]. Radial geometries for tag patterns [13, 152] have also been developed for the characterization of myocardial motion patterns but their clinical usefulness has, to date, not been fully investigated.

A second difficulty associated with the reconstruction of motion fields using tagged MR images is that of through-plane motion. This is depicted in figure 2.8 which shows the deformation of the LV that takes place between two times in the cardiac cycle, $t = 0$ and $t = n\tau$, where n is the frame number and τ is the time interval between the frames.

As can be seen in the figure the imaging volume defined by the MR scanner coordinate system is stationary whereas the heart moves continuously in three dimensional space due to the respiratory motion of the subject being imaged as well as the intrinsic beating motion of the heart itself. It follows that the tissue that
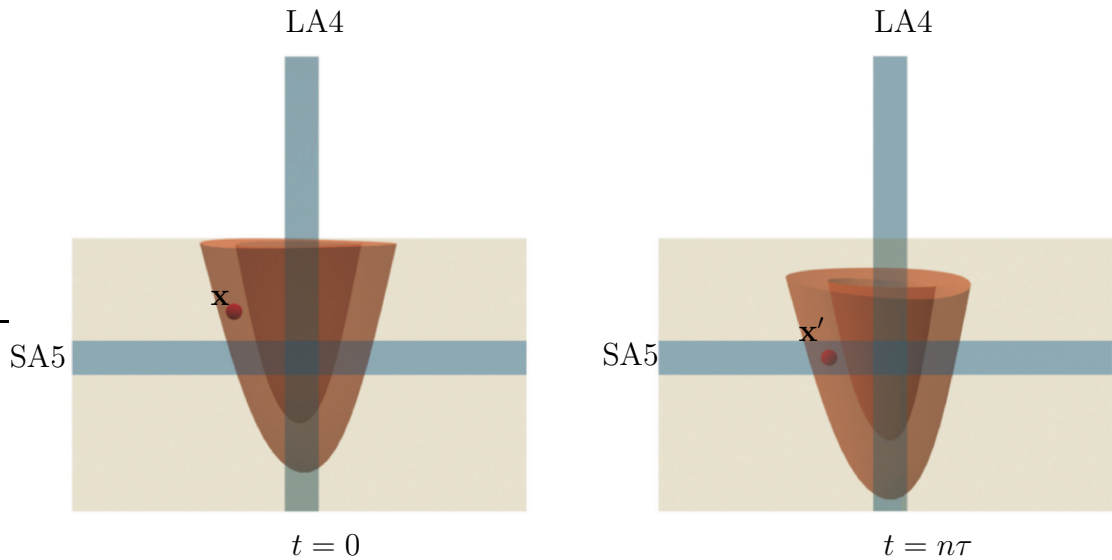
Figure 2.8: This figure shows the deformation of the LV that takes place between times $t = 0$ and $t = n\tau$.

is imaged at a particular time will not be the same as the tissue that is imaged in subsequent times. So to accurately reconstruct the deformation field in the myocardium a contiguous set of slices must be acquired covering the whole of the LV. Moreover, as the tagging patterns are two-dimensional, to estimate the complete 3D motion of the heart over time tagged MR images in two different directions need to be acquired (usually the short-axis (SA) and long-axis (LA) directions). In this way the true three-dimensional motion of the heart can be estimated.

To overcome the problem of through-plane motion induced by respiratory motion breath-hold cine MRI [107] can be used, but care must be taken to coach the volunteer to have a consistent breathing pattern so that the position of the heart at end-expiration is the same across the multiple breath-holds needed for 3D imaging. To account for the motion of the heart itself, slice-following [154] can be used in conjunction with breath-hold methods. Recently, Ryf *et al* [144] have extended the CSPAMM method to produce 3D dimensional tag patterns thus reducing the complexity of deformation field reconstruction from multiple sets of SA and LA tagged MR images.

2.5.2.1 Motion Tracking Methods

A general trend seen in the literature relating to tagged MR image analysis is the separation of the task of tag localization or tag displacement measurement with that of deformation field reconstruction: Usually the tags are localized in an initial step and then a transformation or deformation model is fitted to the measured displacements. In the following we describe the various methods which have been developed for tagged MR image analysis.

Active Contour Models The most popular method for tracking tag stripes in SPAMM [12, 11] MR images is through the use of active contour models or snakes [77]. A snake is defined to be a curve or a surface which minimizes an energy functional. In 2D a snake is a curve

$$\mathbf{x}(s) = [x(s), y(s)], s \in [0, 1] \tag{2.22}$$

that minimizes an energy functional of the form

$$E = \int_0^1 \frac{1}{2}[\alpha||\mathbf{x}'(s)||^2 + \beta||\mathbf{x}''(s)||^2] + E_{\text{ext}}(\mathbf{x}(s)) \, ds \tag{2.23}$$

where $\mathbf{x}'(s)$ and $\mathbf{x}''(s)$ are, respectively, the first and second derivatives of $\mathbf{x}(s)$ with respect to s, α and β are weighting parameters that control the snake's tension and rigidity respectively and are associated with the internal energy of the snake, and $E_{\text{ext}}(\mathbf{x}(s))$ is an external energy function derived from the image data. The external energy term is chosen to be a function which attracts the snake to features of interest in the images—the epicardial and endocardial contours of the LV or the dark stripes defining the tagging grid in tagged MR images.

Two difficulties are encountered when using snakes. The first difficulty stems from the fact that an external energy function, designed to attract the snake towards

edges in the image, is usually derived from the gradient of the image intensity:

$$E_{\text{ext}} = -|\nabla I(x, y)|^2 \qquad (2.24)$$

This means that if the snake is initialized to lie in a relatively homogeneous region of the image then no forces will exist to drive the snake towards features of interest. The second difficulty arises when the image forces are not sufficiently strong enough to drive the active contour towards concave features of interest in the images. *Gradient vector flow* (GVF) flow fields have been suggested by Xu and Prince [175] to overcome these difficulties.

Amini *et al* [7, 4] used B-snakes and coupled B-snake grids (a B-snake is an active contour parameterized by B-spline functions) to track the motion of the myocardium in radial and SPAMM tagged MR images. The B-snake grids were optimized by finding the minimum intensity locations in the tagged MR images. A dense displacement field was then interpolated by calculating a smooth warp based on continuity and intersection constraints. As the authors have noted, their method is limited to 2D analyses of the motion field within the myocardium as cardiac through plane motion is neglected. A specific imaging protocol consisting of a series of short-axis SPAMM tagged MR images lying along the corresponding tag planes in a set of parallel-tagged long-axis images has also been suggested for the analysis of cardiac motion [5]. The intersections of the tag planes, which were modeled as a series of B-spline surfaces, defined a set of points called myocardial beads which could then be visualized as the heart contracted during its cycle. A 4D extension has also been developed by Huang *et al* [72].

Active contour models were also used by Young *et al* [180] where a weighted combination of energy potentials related to the internal energy of the deforming grid, the energy of the tagged image itself and the energy of user interactions was minimized using a modified gradient descent technique. The displacements obtained were then fitted to a finite element model to calculate deformation indices.

Park *et al* [121, 122] defined a new class of deformable models parameterized by functions which captured the local shape variation of the LV such as the contraction and axial twist. Again the SPAMM tag pattern was tracked using active contour models and the displacement data obtained was fitted with the deformable models. The main advantage of this method was that the parameter functions were few in number, intuitive, and allowed quantitative analyses to be made easily.

Specific packages have also been designed for the measurement of tag displacements. Kumar and Goldgof [83] used energy minimizing active contour models to track a SPAMM grid in tagged MR images, while Guttman *et al* [64] have designed a package called "findtags" which uses a series of image processing steps to find the myocardial contours and tags in parallel and radial tagged MR images. The contours are found by using a morphological closing operator to remove tags in the myocardium followed by the minimization of a nonlinear combination of local cost functions. The tags were then detected using template matching based on expected tag profiles from a tagged spin-echo imaging equation. The package also uses a *graphical user interface* (GUI) to help users to adjust incorrectly detected contours and tags.

These packages have been used by various researchers to both validate and fit specific models of the LV that reflect its geometry. O'Dell *et al* [113] used a truncated series expansion in prolate spheroidal coordinates to fit tag displacement measurements and reconstruct the motion field within the myocardium from a set of orthogonal parallel planar tagged MR images. Declerck *et al* [43] also used orthogonal parallel planar tagged MR images, but the motion of the myocardium was modeled using a four-dimensional (4D) planispheric transformation. Again, in an initial step, "findtags" was used to make measurements of tag displacements. The advantage of using a 4D planispheric transformation is that it is continuous both in space and time. Denney and Prince [159] used an estimation theoretic approach modeling the measurement noise in tracking tags with a white random process. Using smoothness and incompressibility constraints, they were able to estimate the motion field within
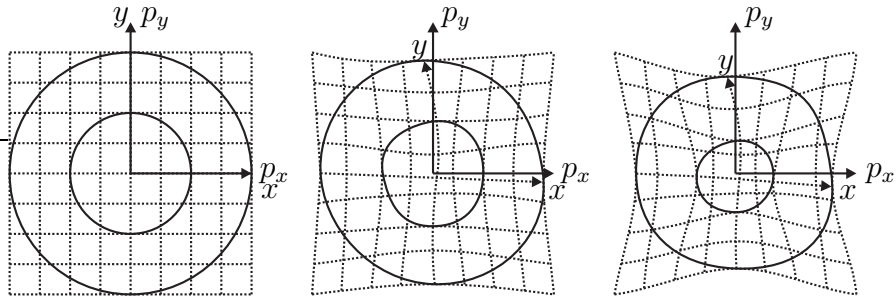
Figure 2.9: The dotted lines show the deformation of the material coordinate system with respect to the Cartesian coordinate system.

the myocardium using a Fisher estimation framework. A number of the methods discussed in the above paragraphs have been compared in Declerck *et al* [44].

Optical Flow Methods Optical flow methods [70] have also been used for tracking tag patterns in tagged MR images. Figure 2.9 shows an 2D object that is deforming as time progresses. The image on the left in the figure shows two coordinate systems xy and $p_x p_y$ whose origins are at the center of the object initially. $p_x p_y$ is a Cartesian coordinate system which is fixed in space at time $t = 0$. The xy coordinate system is fixed to the object and deforms with the object as time progresses as shown in the images in the middle and to the right in figure 2.9. The coordinates of points measured with respect to the xy coordinate system refer to single particle in the object's material. We call the xy coordinate system the material coordinate system and the points referred to, with respect to this coordinate system, as material points.

Suppose we take a sequence of images of the deforming object. Let the intensity distribution in the image sequence be given by a function $I(\mathbf{p}, t)$ where $\mathbf{p} = [p_x, p_y]^T$ and let the deformation of the object be described by a function $\mathbf{q}(\mathbf{x}, t) = [q_x(x, y, t), q_y(x, y, t)]^T$ which takes a point $\mathbf{x} = [x, y]^T$, measured in the material coordinate system at time $t = 0$, and gives the position that it has moved to at time t in the $p_x p_y$ coordinate system.

The image intensity of a material point in the image sequence is given by

66

$I(\mathbf{q}(\mathbf{x}, t), t)$. Differentiating I with respect to t while keeping $\mathbf{x} = [x, y]^T$ constant

$$\left(\frac{\partial I}{\partial t}\right)_{\mathbf{x}} = \nabla_q I.\dot{\mathbf{q}} + \left(\frac{\partial I}{\partial t}\right)_{\mathbf{q}} \tag{2.25}$$

where

$$\nabla_q I = \left[\left(\frac{\partial I}{\partial q_x}\right)_{q_y, t}, \left(\frac{\partial I}{\partial q_y}\right)_{q_x, t}\right]^T \tag{2.26}$$

and

$$\dot{\mathbf{q}} = [\dot{q}_x, \dot{q}_y]^T = \left[\left(\frac{\partial q_x}{\partial t}\right)_{x, y}, \left(\frac{\partial q_y}{\partial t}\right)_{x, y}\right]^T \tag{2.27}$$

is the velocity field.

In conventional optical flow [70] the rate of change of the image intensity of a material point is assumed to be zero. This assumption does not hold true in tagged MR images as the contrast between the tags decays, due to T1 relaxation, during the cardiac cycle.

A number of methods have been proposed to model this variation in contrast. The variable brightness optical flow (VBOF) method of Prince and McVeigh [131, 132] used a model of the imaging process to estimate the variation in the brightness of material points in the myocardium as it undergoes deformation. The image taken at time t was modeled as the sum of an untagged image, $I_0(\mathbf{q}, t)$, and an image, $I_T(\mathbf{q}, t)$, due to the tag pulse sequence

$$I(\mathbf{q}, t) = I_0(\mathbf{q}, t) + I_T(\mathbf{q}, t) \tag{2.28}$$

where

$$I_0(\mathbf{q}, t) = D_0(\mathbf{x})e^{-T_E/T_2(\mathbf{x})}\left(1 - e^{-T_R/T_1(\mathbf{x})}\right) \tag{2.29}$$

$$I_T(\mathbf{q}, t) = D_0(\mathbf{x})e^{-T_E/T_2(\mathbf{x})}(\xi(\mathbf{x}) - 1)\left(e^{-t/T_1(\mathbf{x})} - e^{-T_R/T_1(\mathbf{x})}\right) \tag{2.30}$$

and D_0 is the spin density, T_1 is longitudinal relaxation time, T_2 is the transverse relaxation time, T_E is the echo time, and $\xi(\mathbf{x})$ is the cosine of the magnetization tip angle at $\mathbf{x}$ needed to produce the tag pattern.

A solution to equation 2.25 was obtained by regularizing the velocity field, $\dot{\mathbf{q}}$, to be smooth and using a variational framework in which the following integral

$$
\begin{aligned}
S \;=\; & \alpha^2 \iint \left(\frac{\partial \dot{q}_x}{\partial x}\right)^2 + \left(\frac{\partial \dot{q}_x}{\partial y}\right)^2 + \left(\frac{\partial \dot{q}_y}{\partial x}\right)^2 + \left(\frac{\partial \dot{q}_y}{\partial y}\right)^2 dx\,dy + \\
& \iint \left(\nabla_q I.\dot{\mathbf{q}} + \left(\frac{\partial I}{\partial t}\right)_{\mathbf{q}} - \left(\frac{\partial I}{\partial t}\right)_{\mathbf{x}}\right) dx\,dy
\end{aligned}
\tag{2.31}
$$

was minimized at each time instant. In the above equation, α is a regularization constant which provides a tradeoff between the smoothness of the velocity field and the noise present in the image sequences. The deformation of the object was then estimated by integrating the velocity fields obtained over time.

The key difficulty with the VBOF method is that it requires prior knowledge of the longitudinal and transverse relaxation parameters, the proton density, and the tagging pattern itself over the entire field of view at end-diastole. Additionally, to estimate the material time derivative of the image intensity, $(\partial I/\partial t)_{\mathbf{x}}$, requires knowledge of the reference map, $\mathbf{x}(\mathbf{q})$, at each time instant. If the model of the imaging process is not sufficiently accurate then the errors in the estimated velocity fields will accumulate causing errors in the reference maps ultimately degrading the performance of VBOF to below that of conventional OF methods as time progresses.

Because of the difficulties in estimating the imaging parameters, Gupta and Prince [63] used a local linear transformation model to take account of the brightness variation in the tagged MR images. The linear transformation was approximated using the spin-echo tagging equation from MR physics. Although the method requires less knowledge of the MR imaging parameters it is still dependent on an appropriate approximation of the longitudinal relaxation parameter of the imaged tissue.

Dougherty *et al* [51] circumvented the problem of the modeling the brightness variation of tagged MR images by preprocessing the images with a series of Laplacian filters [21] to reduce the intensity variation and enhance edges in the images. A Laplacian pyramid representation was computed for each frame and the motion

field between two successive time frames was estimated by minimizing a sum of squares difference measure of image similarity using a Gauss-Newton optimization technique.

The optical flow methods discussed above have been developed for motion estimation from 2D images and further development is needed before they can be applied to 3D images.

HARP *HARmonic Phase* (HARP) MRI [115, 116] is a recent technique which can be used to derive strain patterns directly from tagged MR images without the need for feature extraction. The method is based on the fact that the Fourier transforms of SPAMM images contain a number of distinct spectral peaks. Using a bandpass filter to extract a peak in the Fourier domain yields a complex harmonic image, consisting of a harmonic magnitude image which describes the change in heart geometry as well as the image intensity changes, and a harmonic phase image which describes the motion of the tag pattern in the myocardium. The advantage of HARP imaging is that it can be used to directly calculate the strain from the images.

An image taken immediately after the application of a 2D SPAMM tag pattern at time $t = 0$ can be represented by

$$I(\mathbf{x}) = I_0(\mathbf{x})s(\mathbf{x}; \mathbf{w}_1, \alpha_1, \theta_1)s(\mathbf{x}; \mathbf{w}_2, \alpha_2, \theta_2) \tag{2.32}$$

where I is the image that would have been produced without the application of the tag pattern and s is a modulation function which represents the tag pattern:

$$s(\mathbf{x}; \mathbf{w}, \alpha, \theta) = \cos^2(\alpha) + \sin^2(\alpha)\cos(\mathbf{w}^T\mathbf{x} + \theta) \tag{2.33}$$

The parameters in the above equation are the gradient strength and direction, $\mathbf{w}$, the tip angle, α, and a fixed phase shift, θ, controlling the position of the tag pattern.

Rewriting equation 2.33 as

$$I(\mathbf{x}) = \sum_{i=0}^{4} D_i(\mathbf{x}; \alpha_1, \alpha_2) \cos(\mathbf{w}_i^T \mathbf{x} + \theta_i) \tag{2.34}$$

where the functions D_i can be obtained by expanding equation 2.32 using equation 2.33, and $\mathbf{w}_0 = \mathbf{0}$, $\mathbf{w}_3 = \mathbf{w}_1 + \mathbf{w}_2$, $\mathbf{w}_4 = \mathbf{w}_1 - \mathbf{w}_2$, $\theta_0 = 0$, $\theta_3 = \theta_1 + \theta_2$ and $\theta_4 = \theta_1 - \theta_2$.

The images taken at a later time, t, as a function of the spatial position can be represented as

$$I(\mathbf{q}, t) = \sum_{i=0}^{4} D_i(\mathbf{x}(\mathbf{q}(\mathbf{y}), t); \alpha_1, \alpha_2) \cos(\mathbf{w}_i^T \mathbf{x}(\mathbf{q}(\mathbf{y}), t) + \theta_i) \tag{2.35}$$

where $\mathbf{x}(\mathbf{q}, t)$ is the reference map at time t and $\mathbf{y}$ are the image coordinates. $\mathbf{y}$ is related to $\mathbf{q}$ by

$$\mathbf{q}(\mathbf{y}) = y_1 \mathbf{h}_1 + y_2 \mathbf{h}_2 + \mathbf{q}_0 \tag{2.36}$$

where $\mathbf{h}_1$ and $\mathbf{h}_2$ are the directions of the horizontal and vertical axes in the image and $\mathbf{q}_0$ is the origin of the image

In equation 2.35 we see that the image taken at time t is equal to the sum of a constant image and four images modulated by cosine functions. The Fourier transform of $I(\mathbf{q}, t)$ contains a number of spectral peaks at the locations $\mathbf{w}_i$ (a synthetic example is given in figure 2.10). Each peak corresponds to one of the cosine functions in equation 2.35 and taking the inverse Fourier transform of one of these peaks yields a magnitude and an angle image which contain information about the geometry and motion of the LV.

Recently, Pan *et al* [119] developed a 3D motion tracking technique based on HARP. Their method used a mesh model, built using SA and LA images, representing a collection of material points inside the LV wall.

Fourier transform

Magnitude image   Angle image
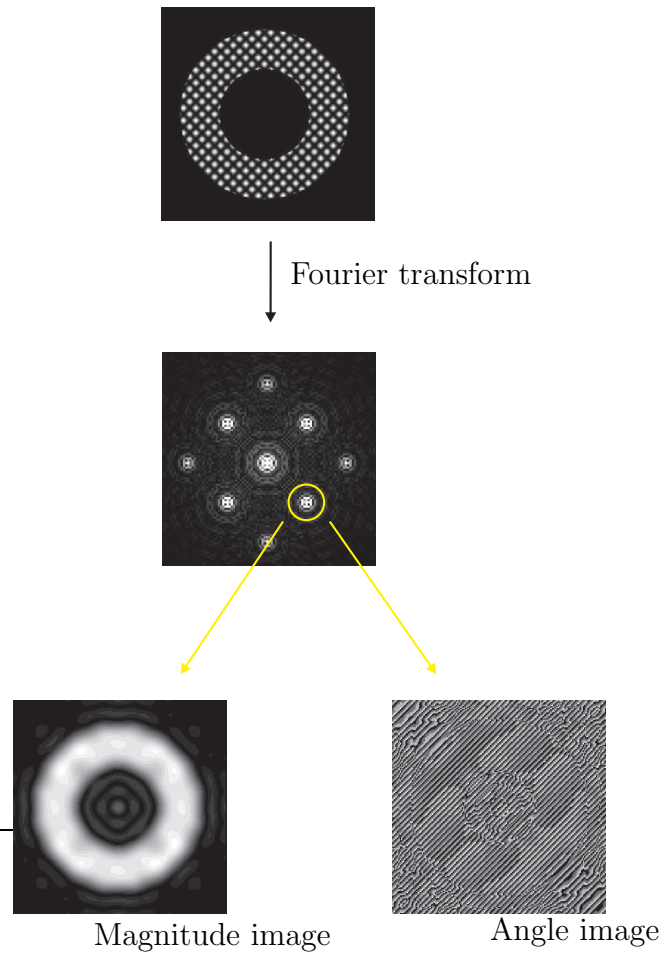
Figure 2.10: The Fourier transform of a SPAMM tagged MR image contains a number of spectral peaks in the Fourier domain. Taking the inverse Fourier transform of a single peak in the Fourier domain yields a magnitude and an angle image which contain information about the geometry and motion of the LV.

2.6   Validation

Since there is no agreed gold standard for the extraction of the deformation field in the myocardium researchers have taken three different approaches to the validating their work. Each has its own advantages and disadvantages. Existing approaches are based on

Validation with a cardiac motion simulator Amini *et al* [7, 4, 5], Huang *et al* [72], O'Dell *et al* [113], Denney and Prince [159], Prince and McVeigh [132], Gupta and Prince [63], Osman *et al* [115, 116]

Validation with a phantom Young *et al* [180], Dougherty *et al* [51].

Validation with a human observer Kumar and Goldgof [83], Ozturk and McVeigh [117].

Of the three methods, validation using a cardiac motion simulator is the most popular. The advantage of using a motion simulator is that the motion fields generated in the images are known exactly and can be compared easily with the proposed algorithm for motion tracking. The disadvantage of this approach is that a simplified model of the cardiac motion and the imaging process is used and does not completely take into account the difficulties encountered in clinical practice.

The type of motion which can be generated with a phantom are even more simpler than the ones that can be generated using a motion simulator. This is because of the difficulty in constructing the model and controlling it during its operation. The advantage of using a phantom is that no assumptions need to be made regarding the imaging process.

The final method used for validation is to manually track the motion of the myocardium in volunteer data using graphical tools written specifically for that purpose. This method has the advantage of testing the motion tracking on real images. The disadvantage of this method is that only in-plane displacements can be

measured at a finite number of points in the myocardium. Furthermore, no ground truth for quantities such as strain can be obtained in this way.

2.7   Summary

A summary of the work done on tagged MR image analysis is given in table 2.1. Researchers have predominantly used a grid tag pattern to reconstruct deformation fields as two components of the 3D motion field can be measured from a single image. However, complete 3D reconstruction of motion fields requires the acquisition of additional images in which the tag planes are perpendicular to the grid tag pattern, and this has been the focus of more recent research. Further work still needs to be done on using optical flow methods for 3D motion reconstruction.

The work presented in this thesis aims to overcome some of the problems encountered in cardiac motion analysis by using image registration techniques. The advantage of using image registration techniques is that no feature extraction needs to be performed. Additionally the transformation model used in the registration algorithm can be used to compute directly the deformation parameters of interest thus removing the extra step needed for model construction. In the following chapter we review the image registration techniques that have been developed and their application to cardiac image analysis.

Authors	Tagging Method	2D/3D	Tag Localization	Motion Reconstruction	Validation
Amini *et al* [7, 4]	radial & grid	2D	ACM	thin-plate splines	motion simulator
Amini *et al* [5]	grid	3D	ACM	B-spline surfaces	motion simulator
Young *et al* [180]	grid	3D	ACM	finite-element model	gel phantom
Park *et al* [121, 122]	grid	3D	ACM	deformable models	none
Kumar & Goldgof [83]	grid	2D	ACM	thin-plate splines	manual tracking
Guttman *et al* [64]	radial & parallel	2D	ACM/TM	none	none
O'Dell *et al* [113]	parallel	3D	ACM/TM	series expansion	motion simulator
Declerck *et al* [43]	parallel	3D	ACM/TM	planispheric transformation	none
Denney & Prince [159]	parallel	3D	ACM/TM	Fisher estimation framework	motion simulator
Prince & McVeigh [132]	grid	2D	OF	velocity fields	motion simulator and phantom
Gupta & Prince [63]	grid	2D	OF	velocity fields	motion simulator
Dougherty *et al* [51]	grid	2D	OF	velocity fields	gel phantom
Osman *et al* [115, 116]	grid	2D	–	HARP	motion simulator

Table 2.1: This table summarizes the work which has been done in tagged MR image analysis. The abbreviations used in the table are: 2-dimensional/3-dimensional (2D/3D), active contour models (ACM), template matching (TM), optical flow (OF), harmonic phase (HARP).

Chapter 3

Cardiac Image Registration

Patient diagnosis frequently involves the use of information available from images taken using different imaging modalities. For example, MR images reveal information about the proton density in a particular region of the body (the anatomy), whereas PET images are used to evaluate biological processes by measuring concentrations of positron-emitting radioisotopes in living tissue (the physiology). Before a clinician can make any interpretations based on the complementary information available in the images, the images must be aligned so that points in one image can be related to points corresponding to the same anatomical locations in the second image. Images acquired at different time points may also need to be aligned. This is necessary, for example, if the effects of a surgical procedure need to be evaluated.

The process of determining the transformation $\mathbf{T}(\mathbf{x})$ which maps points in an image $R(\mathbf{x})$ defined over a domain $\mathbf{x} \in V_R$ to their corresponding positions in the image $S(\mathbf{x})$ defined over a domain $\mathbf{x} \in V_S$ is called image registration (as shown in figure 3.1). The transformation which registers the images is found by optimizing a similarity measure, $\mathcal{C}$, derived from features in the image or the intensities of voxels in the images.

A schematic diagram of a voxel-based image registration algorithm and its main components are shown in figure 3.2. The inputs to the registration algorithm are a fixed image, a moving image and an initial transform estimate that needs to be
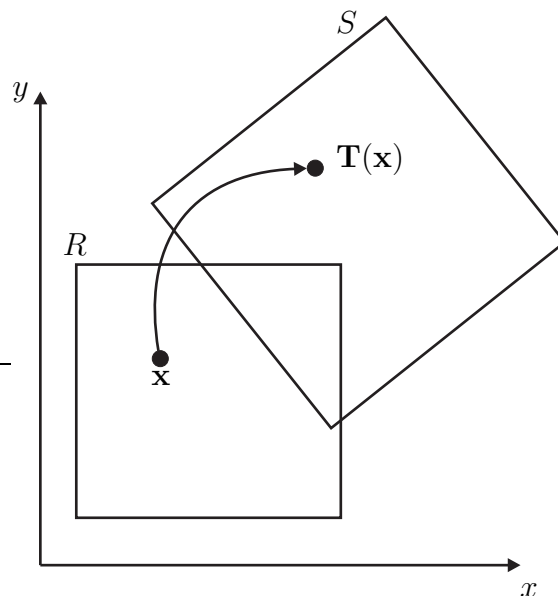
Figure 3.1: The transformation $\mathbf{T}(\mathbf{x})$ transforms the point $\mathbf{x}$ in the image R into its corresponding position in the image S.

optimized. During the registration, points in the fixed image are mapped into the moving image before the similarity measure or metric is evaluated. As the mapped points will not lie exactly on the discrete grid positions defining the moving image, an interpolator is needed to estimate the voxel intensities at those points.

In this chapter we review image registration methods that have been developed for cardiac image analysis. General reviews and introductions to image registration methods can be found in Maurer and Fitzpatrick [22], Fitzpatrick *et al* [54], and Hill *et al* [68], while Maintz and Viergever [98], who cite a large number of papers, have classified registration algorithms according to nine different criteria. We begin by looking at the different types of transformations used to register images.

3.1   Transformation Types

The transformation types used in registration problems can be classified broadly into two different types: those that preserve the straightness of lines and those that do not. Rigid, affine, and perspective transformations (which preserve the straightness of lines) are appropriate for the alignment of images containing static structures such
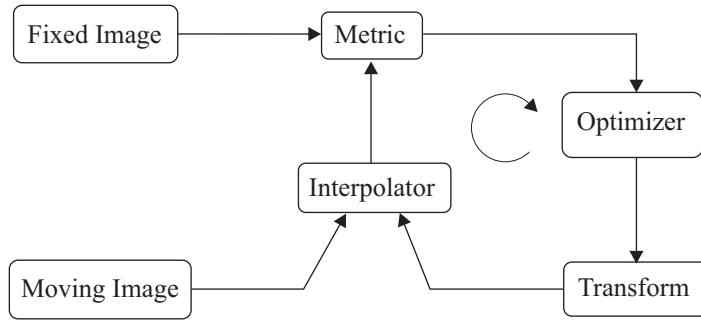
Figure 3.2: The main components in a voxel-based image registration algorithm are the input images, the interpolator, the metric, and the optimizer (adapted from figure 8.2 in [73]). The inputs to the registration algorithm are the fixed and moving images. The transformation which registers the moving image to the fixed image is found by optimizing a similarity measure. Because the image intensities are usually only defined on a grid of positions an interpolator is needed to interpolate the image intensities at nongrid locations.

as bone or external rigid objects introduced into the body to aid in the registration process (such as stereotactic markers). Curved transformations are used to register images of objects which change in shape over time such as the internal organs of the body. They are also used register images of organs which show anatomical variability across a number of different subjects.

3.1.1 Rigid Transformations

A rigid transformation applied to an object preserves distances and angles between points in the object. In 3D, a rigid transformation maps a point with position vector $\mathbf{x} = [x, y, z]^T$ to another point with position vector $\mathbf{x}' = [x', y', z']^T$. It can be defined by the following equation:

$$\mathbf{x}' = \mathbf{R}\mathbf{x} + \mathbf{t} \tag{3.1}$$

which in matrix form is

$$\begin{bmatrix} x' \\ y' \\ z' \end{bmatrix} = \begin{bmatrix} r_{00} & r_{01} & r_{02} \\ r_{10} & r_{11} & r_{12} \\ r_{20} & r_{21} & r_{22} \end{bmatrix} \begin{bmatrix} x \\ y \\ z \end{bmatrix} + \begin{bmatrix} t_x \\ t_y \\ t_z \end{bmatrix} \tag{3.2}$$

where $\mathbf{R} = \{r_{ij}\}$, $i, j \in \{0, 1, 2\}$ is a 3×3 orthogonal rotation matrix describing the rotational component of the transformation, and $\mathbf{t} = [t_x, t_y, t_z]^T$ is a displacement vector describing the translational component of the transformation. Two convenient ways for parameterizing the rotational component of the transformation are through Euler angles or quaternions [69].

3.1.2   Affine Transformations

An affine transformation is one which includes scale and shear components as well as rotation and translation components:

$$\mathbf{x}' = \mathbf{A}\mathbf{x} + \mathbf{t} \tag{3.3}$$

In matrix form

$$\begin{bmatrix} x' \\ y' \\ z' \end{bmatrix} = \begin{bmatrix} a_{00} & a_{01} & a_{02} \\ a_{10} & a_{11} & a_{12} \\ a_{20} & a_{21} & a_{22} \end{bmatrix} \begin{bmatrix} x \\ y \\ z \end{bmatrix} + \begin{bmatrix} t_x \\ t_y \\ t_z \end{bmatrix} \tag{3.4}$$

where $\mathbf{A} = \{a_{ij}\}, i, j \in \{0, 1, 2\}$ is a 3×3 matrix which describes the scale, shear, and rotation components of the transformation while $\mathbf{t}$ describes the translation component of the transformation. In contrast to rigid transformations the matrix $\mathbf{A}$ is not necessarily an orthogonal matrix.

3.1.3   Perspective Transformations

Perspective transformations have the form

$$\mathbf{x}' = \frac{d}{\mathbf{x} . \widehat{\mathbf{p}}} \mathbf{x} \tag{3.5}$$

where the origin is the focal point of the projection rays emanating from the objects of interest, $\widehat{\mathbf{p}}$ is the direction of the normal vector of the projection plane, and d is

the distance of the origin from the projection plane. The projection plane is defined by the equation:

$$\mathbf{x}.\widehat{\mathbf{p}} = d \tag{3.6}$$

Perspective transformations are used to model the imaging process that generate the 2D projection images in imaging modalities such as endoscopy, laparascopy, microscopy, and direct video acquisition.

3.1.4   Spline-Based Transformations

The rigid, affine, and perspective transformations preserve the straightness of lines and cannot model the change in shape of an object which has undergone local deformation in the images being registered. To model this deformation, correspondences between points in the object must be found in the two views of the object for all points of interest. In practice point correspondences can only be found for a finite number of locations, $\mathbf{x}_i$, in the object, such as at the intersections of surface or line features in the images being registered. The transformation field at all other points must be interpolated from the displacements at $\mathbf{x}_i$.

Spline-based transformations use blending functions located at the points $\mathbf{x}_i$ (called the control points) to compute the transformed positions of all other points. The blending functions used can have global or local support.

3.1.4.1   Thin-Plate Spline Transformations

A class of transformations which can be used to model the nonrigid deformation of objects is based on thin-plate spline surfaces. If an infinitely large thin sheet of metal is displaced vertically at a fixed number of points $\mathbf{x}_i = [x_i, y_i]^T$ by differing amounts f_i, then the function which gives the displacement, f, of the sheet of metal at all other points $\mathbf{x} = [x, y]^T$ in such a way that the bending energy

$$E = \iint \left(\left(\frac{\partial^2 f}{\partial x^2} \right)^2 + 2 \left(\frac{\partial^2 f}{\partial x \partial y} \right)^2 + \left(\frac{\partial^2 f}{\partial y^2} \right)^2 \right) dx \, dy \tag{3.7}$$

is minimized, is described by the thin-plate splines

$$f(x,y) = a_0 + a_x x + a_y y + \sum_{i=0}^{N-1} w_i U(||\mathbf{x}_i - \mathbf{x}||) \tag{3.8}$$

where

$$U(r) = r^2 \ln r^2 \tag{3.9}$$

and the coefficients a_0, a_x, a_y, and w_i in the above equations can be found by solving a set of linear equations as shown in [17].

Warping functions in 2D or 3D can be defined by specifying two or three sets of displacements respectively at each of the points $\mathbf{x}_i$. In this case the thin-plate spline transformations have the form

$$\mathbf{x}' = \mathbf{A}\mathbf{x} + \sum_{i=0}^{N-1} \mathbf{w}_i U(||\mathbf{x}_i - \mathbf{x}||) \tag{3.10}$$

where $\mathbf{A}$ is a matrix describing the affine component of the transformation and the $\mathbf{w}_i$ are coefficient vectors which sum to $\mathbf{0}$ and weight the radial basis functions $U(r)$ given by:

$$U(r) = \begin{cases} r^2 \ln r^2 & \text{in 2D} \\ r & \text{in 3D} \end{cases} \tag{3.11}$$

Thin-plate spline transformations have been used to characterize bone shapes in terms of principal warps [17], and also for registration tasks [61].

3.1.4.2 Free-Form Deformations

A 3D free-form deformation [149] is defined over a region Ω

$$\Omega = \{[x,y,z]^T : x_{\min} \le x < x_{\max}, y_{\min} \le y < y_{\max}, z_{\min} \le z < z_{\max}\} \tag{3.12}$$

by placing a regular grid of $(n_x + 1) \times (n_y + 1) \times (n_z + 1)$ control points over the region and specifying the displacement vectors at each control point of the grid. If

the positions of the control points are given by

$$\mathbf{x}_{i,j,k} = \mathbf{x}_0 + i\delta_x\widehat{\mathbf{u}} + j\delta_y\widehat{\mathbf{v}} + k\delta_z\widehat{\mathbf{w}} \tag{3.13}$$

where $\widehat{\mathbf{u}}$, $\widehat{\mathbf{v}}$, $\widehat{\mathbf{w}}$ are the unit basis vectors used to define a local coordinate system in the grid, δ_x, δ_y, δ_z are the control point spacings in the x-, y-, z-directions respectively, and $i \in \{0, 1, \ldots, n_x\}$, $j \in \{0, 1, \ldots, n_y\}$, $k \in \{0, 1, \ldots, n_z\}$, then the transformed position, $\mathbf{x}'$, of a point, $\mathbf{x}$, is given by

$$\mathbf{x}' = \mathbf{x} + \sum_i \sum_j \sum_k f_{i,j,k}(\mathbf{x})\mathbf{d}_{i,j,k} \tag{3.14}$$

where the $\mathbf{d}_{i,j,k}$ are the displacement vectors at each control point.

One choice for the blending functions $f_{i,j,k}$ are the symmetric B-spline functions of order n which are defined by the equation

$$\beta^n(x) = \sum_{j=0}^{n+1} \frac{(-1)^j}{n!} \binom{n+1}{j} (x - j + (n+1)/2)^n \mu(x - j + (n+1)/2) \tag{3.15}$$

where $\mu(x)$ is the step function

$$\mu(x) = \begin{cases} 0 & \text{for } x < 0 \\ 1 & \text{for } x \geq 0 \end{cases} \tag{3.16}$$

and are plotted in figure 3.3 for $n = 0, 1, 2, 3$.

The symmetric cubic B-spline functions are commonly used and ensure that $\mathbf{x}'$ can be differentiated twice with respect to $\mathbf{x}$. They can be obtained from equa-
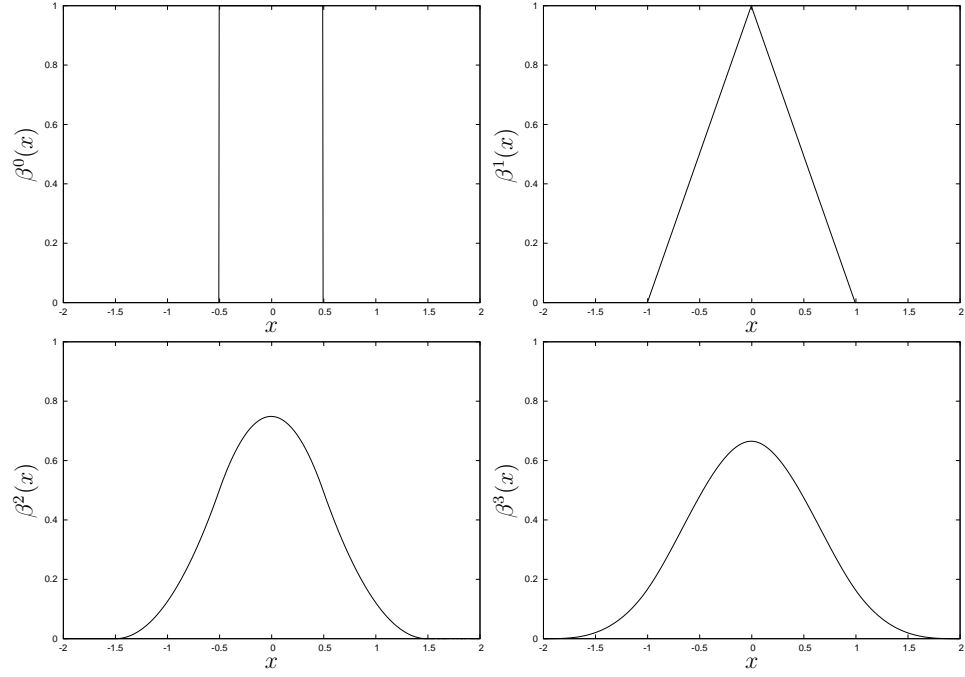
Figure 3.3: The B-spline functions of order $n = 0, 1, 2, 3$.

tion 3.15 by setting $n = 3$:

$$
\beta^3(x) =
\begin{cases}
(2 + x)^3/6 & \text{for } -2 \leq x < -1 \\
(4 - 6x^2 - 3x^3)/6 & \text{for } -1 \leq x < 0 \\
(4 - 6x^2 + 3x^3)/6 & \text{for } 0 \leq x < 1 \\
(8 - 12x + 6x^2 - x^3)/6 & \text{for } 1 \leq x < 2 \\
0 & \text{otherwise}
\end{cases}
\tag{3.17}
$$

The free-form deformation is then obtained by setting

$$
f_{i,j,k}(\mathbf{x}) = \beta^3\left(\frac{x - x_{i,j,k}}{\delta_x}\right) \beta^3\left(\frac{y - y_{i,j,k}}{\delta_y}\right) \beta^3\left(\frac{z - z_{i,j,k}}{\delta_z}\right)
\tag{3.18}
$$

and is given by

$$
\mathbf{x}' = \mathbf{x} + \sum_{i=0}^{n_x} \sum_{j=0}^{n_y} \sum_{k=0}^{n_z} \beta^3\left(\frac{x - x_{i,j,k}}{\delta_x}\right) \beta^3\left(\frac{y - y_{i,j,k}}{\delta_y}\right) \beta^3\left(\frac{z - z_{i,j,k}}{\delta_z}\right) \mathbf{d}_{i,j,k}
\tag{3.19}
$$

where $[x_{i,j,k}, y_{i,j,k}, z_{i,j,k}]^T = \mathbf{x}_{i,j,k}$.
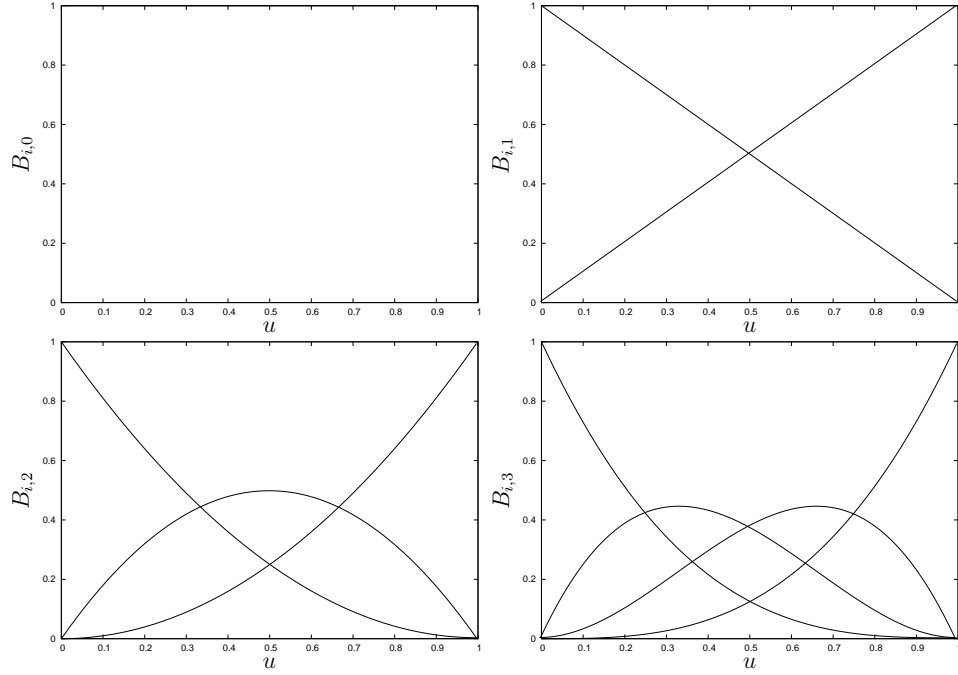
Figure 3.4: The Bernstein polynomials for $n = 0, 1, 2, 3$.

Another choice for the blending functions are the Bernstein polynomials

$$B_{i,n}(u) = \binom{n}{i} u^i (1-u)^{n-i} \tag{3.20}$$

which are plotted in figure 3.4 for $n = 0, 1, 2, 3$. In this case the free-form deformation is obtained by setting

$$f_{i,j,k}(\mathbf{x}) = \binom{n_x}{i}(1-s)^{n_x-i}s^i\binom{n_y}{j}(1-t)^{n_y-j}t^j\binom{n_z}{k}(1-u)^{n_z-k}u^k\mathbf{d}_{i,j,k} \tag{3.21}$$

where $s, t, u \in [0, 1]$ and are such that:

$$\mathbf{x} = \mathbf{x}_0 + sn_x\delta_x\widehat{\mathbf{u}} + tn_y\delta_y\widehat{\mathbf{v}} + un_z\delta_z\widehat{\mathbf{w}} \tag{3.22}$$

Free-form deformations have been used to model the nonrigid deformation of breast tissue [142], the heart, and the brain. They have also been used in the computer graphics field for morphing 2D images [86] and also for deforming 3D geometrical models [149] using Bernstein polynomials.

3.1.5 Physical Models of Deformation

3.1.5.1 Elastic Models

The deformation of objects can also be modeled directly using physical models of the forces acting within it. In elastic media the Navier-Stokes equilibrium equations for linear elasticity

$$\mu\nabla^2\mathbf{u} + (\lambda + \mu)\nabla(\nabla.\mathbf{u}(\mathbf{x})) + \mathbf{F}(\mathbf{x}) = \mathbf{0} \quad \forall x \in V_R \quad (3.23)$$

give the displacement field $\mathbf{u}(\mathbf{x})$ arising from the internal forces, $\mathbf{F}$, acting on the body, where λ and μ are Lamé coefficients and are related to the elastic properties of the medium.

The external force $\mathbf{F}$ is chosen to match corresponding regions in each image of the registration. Bajcsy and Kovačič [14] chose a force derived from the local correlation of the intensities in the images.

3.1.5.2 Viscous Fluid Models

Large deformations are sometimes necessary to register images, especially for intersubject or atlas-to-subject registration tasks. Registration algorithms which use regularization terms to ensure the smoothness of the transformations tend to penalize large deformations.

Viscous fluid models [33] allow for large deformations of objects while maintaining the transformations to be smooth. They are governed by the Navier-Stokes partial differential equation

$$\mu\nabla^2\mathbf{v} + (\lambda + \mu)\nabla(\nabla.\mathbf{v}) + \mathbf{F}(\mathbf{x}) = \mathbf{0} \quad (3.24)$$

where $\mathbf{v}$ is the instantaneous velocity of a material point at position $\mathbf{x}$ at time t, μ and λ are viscosity constants, and F is the force per unit volume acting on the body.

3.2 Similarity Measures

To register two images a measure of the degree of alignment of the images is required, which can be based on point, surface or intensity features present in the images. For point and surface based methods some preprocessing is required to extract the features of interest before the registration can be performed.

3.2.1 Point Based Methods

Point-based registration relies on the identification of corresponding sets of points $\{\mathbf{x}_i : i \in \{0, 1, \ldots, N\}\}$ and $\{\mathbf{y}_i : i \in \{0, 1, \ldots, N\}\}$, in the target and source images respectively. The points $\mathbf{x}_i$ and $\mathbf{y}_i$ can be external markers introduced into the image by rigid structures such as stereotactic frames or markers placed on the skin, or they can be anatomical features present in the images themselves. The points can be located manually or, if they are clearly discernible, with an automatic algorithm.

Alignment is achieved by minimizing the distance between the points $\mathbf{x}_i$ and the transformed points $\mathbf{T}(\mathbf{y}_i)$.

$$\mathcal{C} = \sum_i w_i^2 ||\mathbf{x}_i - \mathbf{T}(\mathbf{y}_i)||^2 \tag{3.25}$$

where the w_i are weighting coefficients that measure the degree of confidence to which the point features have been located.

For rigid transformations a least squares fitting procedure can be used [9]. Methods also exist for rigid transformations with isotropic and nonisotropic scaling, perspective transformations, and spline based transformations [54].

3.2.2 Surface Based Methods

Surface-based image registration is achieved by finding the transformation which aligns corresponding surface features present in the images being registered. Surfaces in an image can be represented by a polygonal model (for example as a col-

lection of triangles), through implicit equations, or in a parametric form. If the contrast between the boundary of a surface and the background is sufficient then a contour extraction algorithm such as the marching cubes algorithm [92] will generate a triangulation of the surface. The number of triangles generated increases with the dimensions of the image and for large images it may be necessary to run a decimation algorithm to reduce the number of triangles in the surface [148].

Intuitively, the similarity between two surfaces can be estimated by measuring the distance between corresponding points in the two surfaces. If we denote the two surfaces to be registered by R (the fixed surface) and S (the moving surface), and a set of points on the surface S by $\{\mathbf{y}_i\}$, then a measure of similarity between these two surfaces is given by

$$\mathcal{C} = \sqrt{\sum_{i=1}^{N} w_i^2 ||\mathbf{x}_i - \mathbf{T}(\mathbf{y}_i)||^2} \tag{3.26}$$

where w_i is a weight assigned to the point $\mathbf{y}_i$ and controls the degree to which that point affects the computed similarity measure, and $\mathbf{x}_i$ is the closest point on the surface R which corresponds to $\mathbf{T}(\mathbf{y}_i)$. Pelizarri *et al* [124] used the intersection of the line joining the centroid of the surface R with the transformed points $\mathbf{T}(\mathbf{y}_i)$ to define the closest points, $\mathbf{x}_i$. This was called the "head and hat" algorithm as the registration process could be visualized as the fitting of the point set $\{\mathbf{y}_i\}$ (the hat) to the surface R (the head).

The distance between a point and a surface can be precomputed using Euclidean distance transforms [42] but at the cost of reduced accuracy since the surfaces need to be converted into discrete binary representations.

The *iterative closest point* (ICP) algorithm [16] decomposes the surfaces being registered into point sets: the fixed surface point set and the moving surface point set. The algorithm works by iteratively finding points on the moving surface point set which are closest to the points in the fixed surface point set, registering the two point sets together (using a point-based registration algorithm), and applying the

resulting transformation to the moving surface point set.

3.2.3   Intensity Based Methods

The voxel intensities in an image can be used to directly measure the similarity between two images. The main attraction of intensity based methods is that no prior feature extraction is necessary.

3.2.3.1   Sum of Squared Differences

If the images to be registered differ only by Gaussian noise then it can be shown that the optimal similarity measure is the *sum of squared differences* (SSD) of the intensities of the voxels in the two images [170]. The sum of squared differences between two images being registered is given by

$$\mathcal{C}_{\text{SSD}} = \sum_i [R(\mathbf{x}_i) - S(\mathbf{T}(\mathbf{x}_i))]^2 \quad \forall i \text{ such that } \mathbf{T}(\mathbf{x}_i) \in V_S \qquad (3.27)$$

where V_S is the spatial region covered by the image S.

3.2.3.2   Correlation Coefficient

If the intensities of corresponding voxels in the images to be registered are linearly related then it can be shown that the optimal measure of image similarity is the correlation coefficient between the voxel intensities [170]

$$\mathcal{C}_{\text{CC}} = \frac{\sum_i [R(\mathbf{x}_i) - \langle R \rangle][S(\mathbf{T}(\mathbf{x}_i)) - \langle S(\mathbf{T}(\mathbf{x}_i)) \rangle]}{\{\sum_i [R(\mathbf{x}_i) - \langle R \rangle]^2 \sum_i [S(\mathbf{T}(\mathbf{x}_i)) - \langle S(\mathbf{T}(\mathbf{x}_i)) \rangle]^2\}^{1/2}}$$
$$\forall i \text{ such that } \mathbf{T}(\mathbf{x}_i) \in V_S \qquad (3.28)$$

where $\langle R \rangle$ is the mean intensity of voxels in image R and $\langle S(\mathbf{T}(\mathbf{x}_i)) \rangle$ is the mean intensity of the voxels in the transformed image $S(\mathbf{T}(\mathbf{x}_i))$.

3.2.3.3 Mutual Information

Mutual information (MI) is an entropy based measure of the similarity between two images and is not dependent on the specific functional relationship between the intensity distributions in the pair of images being registered, making it particularly suitable for cross-modality image registration.

The entropy of a discrete random variable, X, is defined by

$$H(X) = -\sum_x f_X(x) \log f_X(x) \qquad (3.29)$$

where $f_X(x) = \mathbb{P}(\{X = x\})$ is the probability that the random variable X takes the value x. The entropy of X is a measure of the uncertainty in the value that X will take when it is measured. The more evenly distributed $f_X(x)$ is, the larger the uncertainty or entropy.

Similarly, for a pair of discrete random variables, X and Y, the joint entropy $H(X, Y)$ is defined by

$$H(X,Y) = -\sum_x \sum_y f_{X,Y}(x,y) \log f_{X,Y}(x,y) \qquad (3.30)$$

which is a measure of the uncertainty in the values that X and Y will both take when they are measured.

From these definitions the mutual information, $I(X;Y)$, between a pair of discrete random variables, X and Y, is defined by [41]

$$I(X;Y) = \sum_x \sum_y f_{X,Y}(x,y) \log \frac{f_{X,Y}(x,y)}{f_X(x) f_Y(y)} \qquad (3.31)$$

where $f_{X,Y}(x,y)$ is the joint probability mass function of the random variables X, and Y. $I(X,Y)$ is a measure of the distance (the Kullback-Leibler distance) between

the two probability mass functions $p_{X,Y}(x, y)$ and $q_{X,Y}(x, y)$ defined as

$$p_{X,Y}(x, y) = f_{X,Y}(x, y) \tag{3.32}$$

$$q_{X,Y}(x, y) = f_X(x)f_Y(y) \tag{3.33}$$

For example, in the special case when X and Y are independent then $p_{X,Y}(x, y) = q_{X,Y}(x, y) = f_{X,Y}(x, y) = f_X(x)f_Y(y)$ and $I(X;Y) = 0$. Thus, the mutual information can be viewed as a measure of the independence of the two variables X and Y.

$I(X, Y)$ can also be written as [41]

$$I(X;Y) = H(X) + H(Y) - H(X, Y) \tag{3.34}$$

$$= H(X) - H(X|Y) \tag{3.35}$$

$$= H(Y) - H(Y|X) \tag{3.36}$$

where the conditional entropy $H(Y|X)$ is defined as

$$H(Y|X) = -\sum_x \sum_y f_{X,Y}(x, y) \log f_{Y|X}(y|x) \tag{3.37}$$

and similarly for $H(X|Y)$.

Equation 3.35 can be interpreted as saying that there is a reduction in the uncertainty of X due to the knowledge of Y. Similarly, equation 3.36 can be interpreted as saying that there is a reduction in the uncertainty of Y due to the knowledge of X.

If the intensities of the voxels in the images to be registered are viewed as being generated by two random variables X and Y then mutual information can be used as a measure of similarity if we assume that the images are registered when the mutual information between the intensities of the images is maximized. The use of mutual information as an image similarity measure was proposed independently by

Viola [170] and Collignon *et al* [34].

The probability density functions of X and Y can be estimated using histograms. For example if the range of intensities corresponding to the random variable X are $[X_{\min}, X_{\max}]$, they can be grouped into N bins each of fixed width X_w

$$X_w = \frac{X_{\max} - X_{\min}}{N} \tag{3.38}$$

The bins are labelled $B_{X,0}, B_{X,1}, \ldots, B_{X,N-1}$ and the corresponding range of intensities are $[X_{\min}, X_{\min} + X_w), [X_{\min} + X_w, X_{\min} + 2X_w), \ldots, [X_{\min} + (N-1)X_w, X_{\min} + NX_w]$. The probability density function of X is then estimated by taking a certain number of random samples in the image and incrementing the count of the corresponding bin. The probability that a voxel lies within a particular range of intensities is then given by dividing the number of voxels in the corresponding bin by the total number of samples taken.

The limited number of samples taken in estimating the probability density functions of X and Y can lead to errors in the computation of the mutual information. To help make a more stable estimate of the mutual information histogram smoothing techniques such as Parzen windowing [162] can be used.

3.2.3.4 Normalized Mutual Information

The estimation of the probability distributions of the image intensities in the fixed and moving images are dependent on the amount of image overlap. In certain cases it is possible for the images to become increasingly misaligned while the mutual information increases because of a decrease in image overlap. Studholme *et al* [156], suggested the use of a normalized measure of mutual information

$$N(X;Y) = \frac{H(X) + H(Y)}{H(X,Y)} \tag{3.39}$$

which was empirically found to be less sensitive to the amount of image overlap.

Although mutual information based measures have been used successfully for many image registration tasks, it discards all spatial information and thus decreases its robustness. To overcome this problem extensions have been proposed which make use of gradient information [128] and the co-occurrence matrices of neighboring voxels' intensities [138]. A recent review of image registration algorithms based on mutual information is given in Pluim *et al* [129].

3.3   Cardiac Applications

A recent review of image registration methods for cardiac images acquired using different imaging modalities is given in Mäkelä *et al* [99]. Image registration plays a crucial role in many stages of the functional analysis of cardiac images. We review some of the main applications of image registration for cardiac image analysis in the following subsections.

3.3.1   Motion Correction

To compensate for the motion of the heart induced by the breathing of the patients during MR image acquisition, several slice tracking methods have been developed. Manke *et al* [102] used fast rigid and affine image registration techniques to model the respiratory motion of the heart from low-resolution 3D images. The motion parameters obtained from the registration were then used to correct for motion in coronary MR angiography examinations.

Regional myocardial blood flow can be measured using PET but techniques such as these require greater time than a single breath hold to acquire images, and so models of respiratory motion have also been used to reduce blurring due to respiratory motion. Motion correction in Turkington *et al* [166] was achieved using a simple translational model with correlation being used to measure the degree of similarity between the image frames, while a 4D affine model of respiratory motion was used by Klein *et al* [81] to correct for motion in gated PET images using a least

squares difference voxel similarity measure.

A difficulty encountered when using intensity based measures for registration of PET images is the considerable variation in intensities due to the first-pass of the contrast agent. Delzescaux *et al* [47], rather than use intensity information to effect registration, used the contour of the LV, RV and myocardium to build several registration models. These were then registered to the image sequences acquired by using a generalization of the distance map [101].

McLeish *et al* [106] have built a statistical model of the motion of the heart by registering images taken at different time points in the breathing cycle to a template image taken at exhalation. Such a model can be used for motion correction during scanning.

3.3.2   Image Fusion

Before the complementary information available from different imaging modalities such as PET, SPECT, and MRI can be used, the images must be registered to each other.

Registration of PET and SPECT images to MR images is a common application of image registration as it provides a means for the detection of ischemic and infarcted regions of the myocardium (section 1.3.3). Because of the much lower resolution of PET/SPECT images it is common for some feature extraction to be done on the PET/SPECT images before registration is performed.

Mäkelä *et al* [100] used surface and point-based registration methods to fuse data from MR and PET images and *magnetocardiography* (MCG) data. Declerck *et al* [46] developed a method for comparison of rest and stress blood perfusion SPECT images with a template of normal blood perfusion map by using an affine transformation to register the rest and stress perfusion images to each other and a local spline transformation to map the template to the stress image. The ICP algorithm was used by Santarelli *et al* [146] to fuse MR and PET images and functional information

which can be extracted from MR images have also been combined with coronary vasculature visible in CT angiography data to assess coronary artery disease [157].

3.3.3 Atlas and Statistical Shape Model Construction

Prior information about the shape and average intensities of cardiac structures can be used to aid in the analysis of cardiac MR images. To do this the variation in the images arising from the different image acquisition parameters must be removed by aligning the images into a common coordinate system.

Frangi *et al* [57] constructed statistical shape models of the LV, RV and myocardium by first aligning a set of manual segmentations of the cardiac structures into a common coordinate system using the global registration algorithm of Studholme *et al* [155]. As the images to be registered were labelled structures, two different voxel similarity measures were introduced, the *label consistency* and the κ statistic. The label consistency measured how many of the labels in the images being registered mapped onto each other; and the κ statistic, frequently used in biomedical research, measured the agreement between the classifications of the cardiac structures in the images during registration. A dense set of landmarks were then defined on the atlas using the marching cubes algorithm [92] and the nonrigid registration algorithm of Rueckert *et al* was used to propagate the landmarks into the segmented images after alignment. A *principal component analysis* (PCA) on the positions of the landmarks was then performed to derive a statistical model of the shape variability of the cardiac structures.

Lotjonen *et al* constructed a four chamber statistical shape model of the heart from multiple short-axis and long-axis images of the heart by registering segmented images of the chambers from a number of volunteers.

Perperidis *et al* [125] developed a 4D registration algorithm for the spatio-temporal alignment of cardiac image sequences acquired from different subjects so that comparisons of cardiac function could be made between them. Their transfor-

mation model, $\mathbf{T}(\mathbf{x}, t)$, mapped points in a 4D image $I(\mathbf{x}, t)$ into their corresponding positions in a reference 4D image. The transformation was decomposed into a spatial and temporal part, each of which was affine in nature. To register two image sequences a similarity measure based on normalized mutual information (NMI) was maximized. Because the motion of the heart cannot be completely described by an affine transformation, an extended algorithm was presented in [126] which used a free-form deformation to model the motion of the heart.

3.3.4   Segmentation

Before global quantitative measures such as the EF can be estimated the cardiac structures (LV, RV, and myocardium) must be first segmented. In some cases segmentation is also required in an initial step before deformation parameters can be extracted in the myocardium. Some researchers have investigated the use of image registration to aid in the segmentation of cardiac structures. The advantage of using image registration is that prior information about both the shape and intensities of structures in the heart can be made use of.

Lelieveldt *et al* [88] constructed models of the thorax using *constructive solid geometry* (CSG) modeling techniques where the individual structures within the CSG model were represented by fuzzy implicit surfaces. This model was then used to segment thoracic MRI images by using the boundaries of the fuzzy implicit surfaces and the tissue-air transitions in the MRI images to define an energy function which was minimal when the model was registered to the MRI images.

Lorenzo-Valdés *et al* [94] used a population-specific atlas, constructed using the method of Frangi *et al* [57], and a subject-specific atlas constructed by registering all images taken during the cardiac cycle to the end-diastolic time frame to segment 4D cardiac MR images. The end-diastolic image was segmented by registering the population-specific atlas to the subject-specific atlas. The segmentations were then propagated to all other time frames by registering the segmented subject-specific

atlas to all other time frames. A 4D probabilistic atlas was constructed in [95] to segment cardiac structures using the EM algorithm [48] and 4D Markov random fields.

3.3.5 Motion Analysis

Image registration techniques have also been applied for cardiac motion tracking. Petitjean *et al* [127] proposed the use of a generalized information-theoretic measure [130] called exclusive f-information to register successive image pairs in a tagged MR image sequence. Ledesma-Carbayo *et al* [85] computed the displacement field in 2D sequences of US images by registering each frame in the sequence to a reference image taken at end-diastole using a SSD measure of image alignment.

3.4 Summary

In contrast to other organs in the body, the heart is continuously in motion, making registration of cardiac images a challenging task. No single method exists which can solve all problems encountered in cardiac image registration. Nonelastic registration methods have been used primarily for motion compensation and image fusion applications; and elastic registration algorithms have been used to correct for the variability in the anatomy of the heart both in time (for tasks such as segmentation) and across different subjects (for atlas construction).

Although some work has been done on using image registration for motion field reconstruction in cardiac images, the advantages of using such an approach as well as the difficulties encountered have not been fully investigated. In the following chapters we investigate the use of image registration for cardiac motion analysis.

Chapter 4

Analysis of 3D Myocardial Motion in Tagged MR Images Using Nonrigid Image Registration

One of the fundamental reasons limiting the widespread use of tagged MRI in the clinical environment is the lack of automated tools to aid in the extraction and analysis of the motion fields within the myocardium. A number of methods have been proposed in recent years to help with this task (section 2.5.2), but many need substantial manual intervention and user interaction, while others are limited to 2D motion analysis or require special imaging sequences. The main difficulties arise from the loss of contrast between tag stripes, due to T1 relaxation, as the heart contracts during its cycle, and the need to estimate through-plane motion.

In this chapter we propose a new method for the extraction and analysis of the deformation field within the myocardium based on nonrigid image registration. The registration algorithm we use is based on free-form deformations and the maximization of NMI [142], and was originally developed for the registration of contrast enhanced MR breast images for the detection of cancerous lesions. We have modified this algorithm in a way so that it may be used for the extraction and analysis of the full four-dimensional (4D) deformation field within the myocardium of the LV.

To do this we make use of both tagged SA and LA images of the LV.

The advantage of using this approach, firstly, is that tag localization and deformation field reconstruction are done simultaneously; and secondly, we have made no assumptions about the nature of the tag pattern used and so the algorithm will be applicable to images with radial, parallel or grid tag patterns.

In section 4.1 we describe the nonrigid registration algorithm and how it is used to recover the deformation field within the myocardium. In section 4.2 validation results using a cardiac motion simulator and experiments conducted on volunteer data are presented. Finally, section 4.3 summarizes our work. The main contributions of this chapter are the modifications which have been made to the registration algorithm of Rueckert *et al* [142], namely the use of a weighted sum of NMI as a similarity measure and the corresponding changes to the optimization algorithm. The work presented in this chapter has been published in [25], [26], and [29].

4.1 Registration of Tagged MR Images

In a normal healthy adult the left ventricle undergoes a number of different types of deformation as it pumps blood out to the body [8]. Not only does the myocardium thicken as the LV contracts but it also undergoes a twisting motion. It is also known that the base of the LV moves approximately 10 mm from base to apex during systole [113]. Since the imaging planes defined in an MR scanning session are stationary with respect to the coordinate system of the scanner, this results in a problem for the tracking of material points within the myocardium—not all points will stay within a single plane during the cardiac cycle. Thus, to fully reconstruct the deformation field within the myocardium, we need to acquire multiple-slice SA and LA images of the LV.

Figure 4.1 shows a typical configuration of imaging planes which could be used to reconstruct the deformation field within the myocardium. The figure shows a series of short-axis planes $(SA_1, SA_2, \ldots, SA_8)$ and a series of long-axis planes

$(LA_1, LA_2, \ldots, LA_7)$ which define an imaging volume enclosing the LV. A set of SA and LA images are also shown, to the right in the figure, corresponding to one of the SA imaging planes and one of the LA imaging planes throughout the cardiac cycle.

Consider a material point P in the myocardium at a position $\mathbf{x} = [x, y, z]^T$ at time $t = 0$ (corresponding to end-diastole) that moves to another position $\mathbf{x}'$ at time $t = i\tau$ where τ is the time interval between two consecutive time frames and i is the frame number (figure 4.2). The problem, simply stated, is to find the transformation $\mathbf{T}$ for all time frames, n, such that:

$$\mathbf{T}(\mathbf{x}, n\tau) = \mathbf{x}' \tag{4.1}$$

We propose to represent $\mathbf{T}$ using a series of free-form deformations [87] as described in the next subsection.

4.1.1 Combined nonrigid registration of SA and LA images

The algorithm used to calculate the transformation $\mathbf{T}(\mathbf{x}, t)$ is based on the non-rigid registration algorithm of Rueckert *et al* [142]. In their paper, registration was achieved by optimizing a cost function measuring the similarity between two images as well as the smoothness of the deformation needed to align the images. The similarity measure used is based on NMI and is particularly suited for application to tagged MR images since it is not dependent on changes in intensity in the images, as is the case in our application. Although the transformation model is a hierarchical one consisting of a global affine transformation and a local transformation (defined by a free-form deformation (FFD)), the motion of the heart is predominantly nonrigid, so we focus on the local transformation. The cost function used in the registration algorithm is the sum of two terms:

$$\mathcal{C}_{\mathbf{T}} = -\mathcal{C}_{\text{similarity}}(A, \mathbf{T}(B)) + \lambda \mathcal{C}_{\text{smooth}}(\mathbf{T}) \tag{4.2}$$
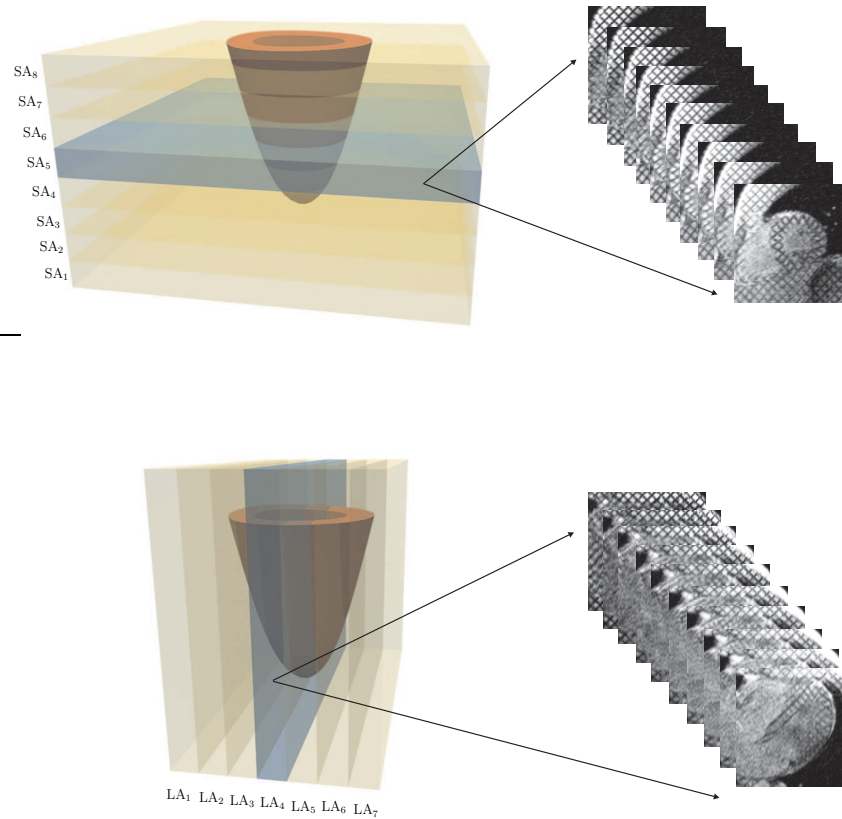
Figure 4.1: A typical configuration of imaging planes required to fully reconstruct the deformation field consists of both short-axis (SA) planes as well as long-axis (LA) planes. The images on the right show the corresponding set of tagged MR images for the SA_5 and LA_4 imaging planes.
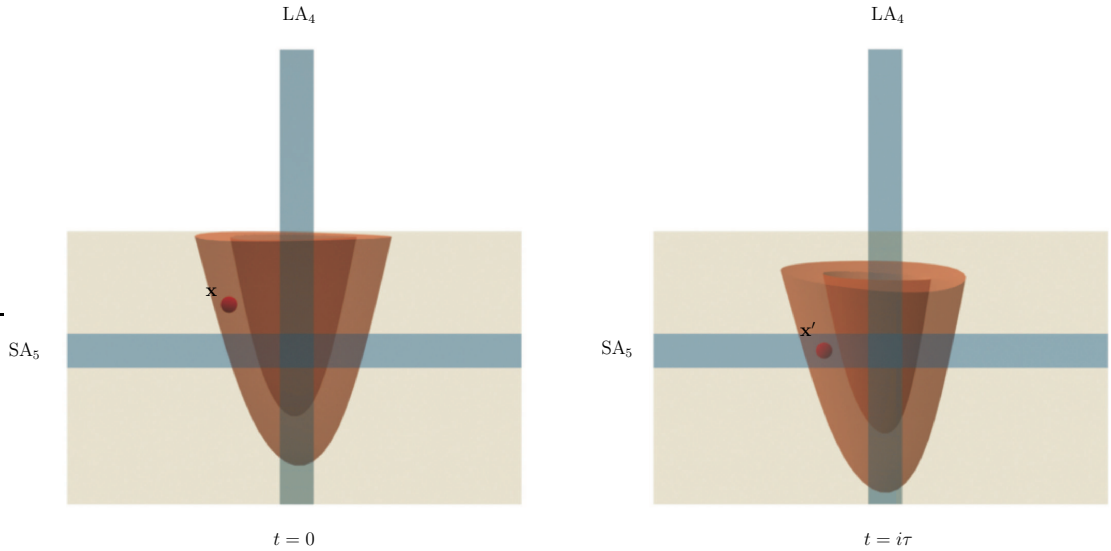
Figure 4.2: To reconstruct the deformation field within the myocardium we must relate points in the myocardium from images taken at time $t = 0$ (end-diastole) to their corresponding positions in images taken at a later time $t = i\tau$. This figure also shows that the myocardium moves through the imaging planes as the LV contracts (as can be seen from the relative positions of the material point indicated by the red circle).

The first term, $\mathcal{C}_{\text{similarity}}(A, \mathbf{T}(B))$, is a measure of the similarity between the images being registered where A and B are the images being registered and $\mathbf{T}(B)$ is the image B transformed so that it is aligned with image A. The second term is measure of the smoothness of the transformation and is the 3D counterpart of the the 2D bending energy of thin sheet of metal. It is given by

$$\mathcal{C}_{\text{smooth}} = \frac{1}{V} \iiint \left[\left(\frac{\partial^2 \mathbf{T}}{\partial x^2} \right)^2 + \left(\frac{\partial^2 \mathbf{T}}{\partial y^2} \right)^2 + \left(\frac{\partial^2 \mathbf{T}}{\partial z^2} \right)^2 \right] dx\, dy\, dz \qquad (4.3)$$

where V is the volume over which the transformation is defined. As the motion of the heart is small between time frames we have found that the regularization term can be omitted by setting $\lambda = 0$.

To apply the algorithm in [142] for motion tracking in cardiac MR images several modifications are necessary. In particular, the existing algorithm can only be applied to either SA or LA images which means that through-plane motion of the heart will not be accounted for. If only the SA images are used, then the output

from the registration algorithm will be a transformation in which the component perpendicular to the SA direction is zero. Similarly if only the LA images are used then the component of the output transformation in the direction perpendicular to the LA images will be zero. Moreover, the separate motion fields obtained from the SA and LA images cannot be combined to yield the correct motion field. Therefore, we have modified the registration algorithm and the voxel similarity measure to work with SA and LA images simultaneously, producing a single 3D motion field.

For the purposes of explanation we will assume that we have acquired a series of multiple-slice SA and LA images enclosing the whole of the LV and for the entire cardiac cycle as shown in figure 4.1. A volumetric free-form deformation (FFD) is defined, as in section 3.1.4.2, on a domain Ω by a mesh of $(n_x+1)\times(n_y+1)\times(n_z+1)$ control point displacement vectors Φ. The domain Ω corresponds to the volume of interest and includes both the short-axis image slices SA_j as well as long-axis image slices LA_j. The domain Ω defines a single coordinate system in which to perform the tracking of the LV throughout the cardiac cycle. The choice of the coordinate system in which to define the control point lattice is essentially arbitrary. This is because the directions in which the control points move in order to describe the deformation of the myocardium is independent of the orientation of the coordinate system in which the free-form deformation is defined. We have chosen a coordinate system whose x- and y-axes are aligned with the short-axis image planes, as this is the most natural coordinate system to work in.

To track the cardiac motion throughout multiple time frames we adopt a multi-level FFD as suggested by Schnabel *et al.* [147] where the transformation $\mathbf{T}$ is represented as the sum of a series of local FFDs

$$\mathbf{T}(\mathbf{x}, n\tau) = \mathbf{x} + \sum_{h=1}^{n} \mathbf{u}^h(\mathbf{x}) \qquad (4.4)$$

$$\mathbf{u}^h(\mathbf{x}) = \sum_{i=0}^{n_x} \sum_{j=0}^{n_y} \sum_{k=0}^{n_z} \beta^3\left(\frac{x - x_{i,j,k}}{\delta_x}\right) \beta^3\left(\frac{y - y_{i,j,k}}{\delta_y}\right) \beta^3\left(\frac{z - z_{i,j,k}}{\delta_z}\right) \phi_{i,j,k}^h \qquad (4.5)$$

where $\phi^h_{i,j,k}$ is the control point displacement vector at position $[x_{i,j,k}, y_{i,j,k}, z_{i,j,k}]^T =$ $\mathbf{x}_{i,j,k}$, and δ_x, δ_y, and δ_z are the control point spacings in the x-, y-, and z-directions respectively. The spacings between the control points Φ in the x- and y-directions are chosen to be approximately equal to the tag spacing, while the spacing in the z-direction is chosen to be equal to the distance between the SA slices. As we are concerned only with recovering the deformation field within the myocardium we need a segmentation of the myocardium at end-diastole. This we obtain by noting that although the SPAMM tag pattern is retained by the myocardium as the LV contracts, the tag pattern in the center of the LV is completely spoiled by the blood flowing within it. At the end of the cardiac cycle the configuration of the tag pattern has returned to the state it was in at end-diastole except for its absence within the blood pool. This fact allows us to segment the myocardium in the images taken at end-diastole by segmenting the image taken at the end of the cardiac cycle. The segmentation, which is obtained manually, is then overlaid on the images taken at end-diastole to define the myocardium at that time point. An example of how a mid-ventricular SA slice at end-diastole is segmented is shown in figure 4.3. A problem with this approach is that the final image in the sequence acquired may not correspond exactly with end-diastole. To help with the segmentation of the end-diastolic image and reduce the chance of errors during the motion field reconstruction untagged images may be acquired in addition to the tagged images.

A plane from the control point grid defining a local FFD is shown in figure 4.4 overlaid on a segmentation of the myocardium at end-diastole. Control point displacement vectors which cannot affect this field are marked as passive and not optimized. The bounding box, $\Omega_{i,j,k}$, of each control point position, $\mathbf{x}_{i,j,k}$, is defined as the volume in which the deformation field is affected when the displacement vector at that control point is modified and is given by

$$\Omega_{i,j,k} = \{(x,y,z) : x_{\min} \leq x < x_{\max}, y_{\min} \leq y < y_{\max}, z_{\min} \leq z < z_{\max}\} \qquad (4.6)$$
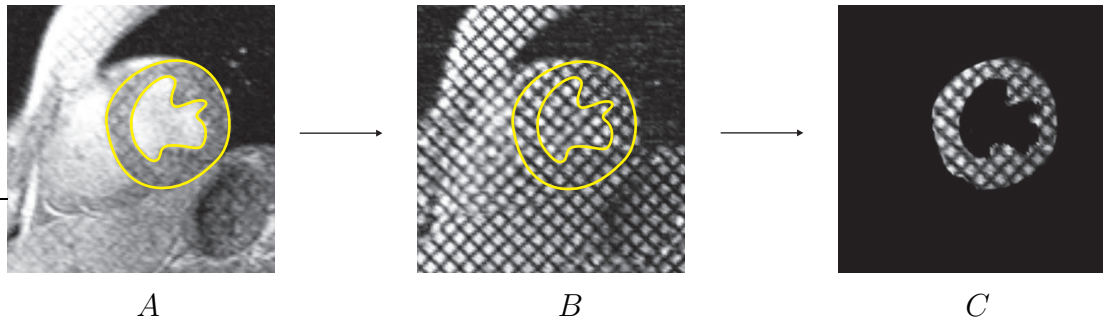
Figure 4.3: A mid-ventricular SA slice at end-diastole is segmented by first segmenting the image taken at the end of the cardiac cycle (A). The segmentation obtained is then overlaid on the end-diastolic image (B) to yield a segmentation of that image(C). The other SA and LA image slices are segmented in a similar way giving us the segmented SA and LA volume images at end-diastole.

where

$$
\begin{aligned}
x_{\min} &= x_{i,j,k} - 2\delta_x, \quad x_{\max} = x_{i,j,k} + 2\delta_x \\
y_{\min} &= y_{i,j,k} - 2\delta_y, \quad y_{\max} = y_{i,j,k} + 2\delta_y \\
z_{\min} &= z_{i,j,k} - 2\delta_z, \quad z_{\max} = z_{i,j,k} + 2\delta_z
\end{aligned}
\tag{4.7}
$$

The bounding box is used to mark those control points which cannot affect the deformation field in the myocardium as passive. For example, control point A, whose bounding box contains a part of the myocardium, is marked as active. Whereas, control point B, whose bounding box does not contain the myocardium at all, is marked as passive and not optimized during the registration process. Thus the blood pool, the right ventricle and other parts of the body are not considered during the registration process. This allows us to not only obtain more accurate results but also to perform the registration much more quickly.

4.1.1.1 Similarity Measure

To achieve registration between images a similarity measure based on the weighted sums of the NMI of the images being registered is used. As normalized mutual information is a statistical measure of the relationship between the intensities in two images and makes no assumption about their functional dependence it is robust to any intensity changes which occur over time.
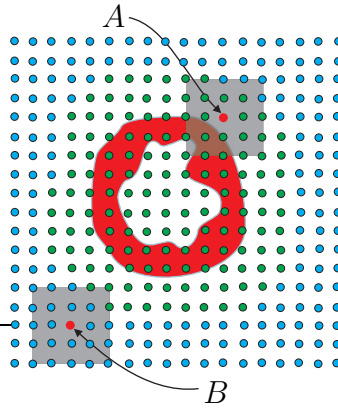
Figure 4.4: This figure shows a SA view of the heart segmented at end-diastole. Control points which cannot affect the deformation field in the myocardium are marked passive. For example control point B is marked as passive while control point A remains active.

The NMI between two images, A and B, is defined by (equation 3.39)

$$N(A; B) = \frac{H(A) + H(B)}{H(A, B)} \tag{4.8}$$

where $H(A)$ and $H(B)$ are the marginal entropies of the intensity distributions in images A and B respectively, and $H(A, B)$ is the joint entropy of the intensity distributions in the two images. To register the SA and LA images taken at time $t = n\tau$ to the images taken at time $t = 0$ we optimize a cost function which is based on the sum of the NMI [156] between the images being registered. Because the similarity measure is coupled to both the short- and long-axis image sets, we are able to recover the complete three-dimensional motion of the myocardium. This is because a single 3D transformation is optimized which must maximize both the similarity between the short- and long-axis images. Thus, the through plane motion that is present in the short-axis images is described by the transformation because of the presence of the long-axis images which it must also simultaneously register, and vice versa.

Since the SA and LA images typically contain different numbers of voxels, we weight the separate components of the NMI in the similarity measure according to the numbers of voxels in the myocardium in the segmented SA and LA images taken

at end-diastole $(t = 0)$

$$w_{\mathrm{S}} = \frac{N(\mathrm{S_{seg}})}{N(\mathrm{S_{seg}}) + N(\mathrm{L_{seg}})} \qquad (4.9)$$

$$w_{\mathrm{L}} = \frac{N(\mathrm{L_{seg}})}{N(\mathrm{S_{seg}}) + N(\mathrm{L_{seg}})} \qquad (4.10)$$

where $N(\mathrm{S_{seg}})$ and $N(\mathrm{L_{seg}})$ are the numbers of voxels in the myocardium in the segmented images taken at end-diastole. Thus, the similarity measure is given by

$$\mathcal{C}(\Phi) = w_{\mathrm{S}} \frac{H(\mathrm{S_{seg}}) + H(\mathbf{T}(\mathrm{S}_{n\tau}))}{H(\mathrm{S_{seg}}, \mathbf{T}(\mathrm{S}_{n\tau}))} + w_{\mathrm{L}} \frac{H(\mathrm{L_{seg}}) + H(\mathbf{T}(\mathrm{L}_{n\tau}))}{H(\mathrm{L_{seg}}, \mathbf{T}(\mathrm{L}_{n\tau}))} \qquad (4.11)$$

where the Φ are the parameters defining the local transformation, $\mathbf{T}$, $\mathrm{S_{seg}}$ and $\mathrm{S}_{n\tau}$ are the volume images formed by the SA slices at times 0 and $n\tau$ respectively, and $\mathrm{L_{seg}}$ and $\mathrm{L}_{n\tau}$ are the volume images formed by the LA slices. It is important to note that equation 4.11 only measures the similarity of the intensities of the SA and LA images between two time points. No extraction of features such as tag lines or intersections is used to calculate the optimal transformation.

4.1.1.2   Interpolation

To calculate the similarity measure (equation 4.11), we need to compute the NMI between the segmented short- and long-axis images (corresponding to time $t = 0$ at end-diastole) and the images (corresponding to a later time t) according to the current estimate of the free-form deformation. The contribution from the short-axis images which corresponds to the first term of the sum in equation 4.11 is calculated as follows: For each point, $\mathbf{x}$, in the segmented short-axis image we find its corresponding position, $\mathbf{T}(\mathbf{x}, n\tau)$, in the SA volume image at time $n\tau$, the intensity of the transformed point being $\mathrm{S}_{n\tau}(\mathbf{T}(\mathbf{x}, n\tau))$. Since $\mathbf{T}(\mathbf{x}, n\tau)$ will not fall directly onto a voxel location, the intensity at this location must be interpolated. For parallel, contiguous SA image slices (as used here), the tag planes at time $t = 0$ intersect the imaging plane at the same location for all slices and trilinear interpolation is an

appropriate interpolation scheme to use. The pairs of intensities are then stored in a two dimensional histogram which holds the joint probability distribution of voxel intensities in the two images. The NMI for the short axis images are then easily calculated from the joint probability distribution histogram.

The contribution from the long-axis images corresponding to the second term of the sum in equation 4.11 is calculated similarly. However, we must account for the fact that $\mathbf{T}(\mathbf{x}, n\tau)$ is defined relative to the SA planes. The positions of the voxels in the LA images are transformed into this coordinate system by using a rigid transformation, $\mathbf{R}_{\text{SA} \leftarrow \text{LA}}$, which maps points in the LA images to their corresponding positions in the SA coordinate system. This transformation is readily computed from the positions and orientations of the images stored in the DICOM headers of the images, thus the geometric relation between the SA and LA images is always known in the acquisition.

Figure 4.5 shows SA and LA views of the LV (for clarity we have used untagged images of the LV). The transformation which maps a point $\mathbf{x}$ expressed in homogeneous coordinates, $[x^{\text{LA}}, y^{\text{LA}}, z^{\text{LA}}, 1]^T$, from the LA coordinate system to the SA coordinate system is given by the rigid homogeneous transformation

$$\mathbf{R}_{\text{SA} \leftarrow \text{LA}} = \begin{pmatrix} \mathbf{e}_x^{\text{SA}}.\mathbf{e}_x^{\text{LA}} & \mathbf{e}_x^{\text{SA}}.\mathbf{e}_y^{\text{LA}} & \mathbf{e}_x^{\text{SA}}.\mathbf{e}_z^{\text{LA}} & (\mathbf{O}^{\text{LA}} - \mathbf{O}^{\text{SA}}).\mathbf{e}_x^{\text{SA}} \\ \mathbf{e}_y^{\text{SA}}.\mathbf{e}_x^{\text{LA}} & \mathbf{e}_y^{\text{SA}}.\mathbf{e}_y^{\text{LA}} & \mathbf{e}_y^{\text{SA}}.\mathbf{e}_z^{\text{LA}} & (\mathbf{O}^{\text{LA}} - \mathbf{O}^{\text{SA}}).\mathbf{e}_y^{\text{SA}} \\ \mathbf{e}_z^{\text{SA}}.\mathbf{e}_x^{\text{LA}} & \mathbf{e}_z^{\text{SA}}.\mathbf{e}_y^{\text{LA}} & \mathbf{e}_z^{\text{SA}}.\mathbf{e}_z^{\text{LA}} & (\mathbf{O}^{\text{LA}} - \mathbf{O}^{\text{SA}}).\mathbf{e}_y^{\text{SA}} \\ 0 & 0 & 0 & 1 \end{pmatrix} \tag{4.12}$$

We then transform this point by the free-form deformation to obtain the position of the deformed point. Finally, we transform the deformed point back to the long-axis coordinate system by using the inverse rigid transformation $\mathbf{R}_{\text{SA} \leftarrow \text{LA}}^{-1}$. The position of the point, $\mathbf{x}$, after it has been deformed, in the long-axis coordinate system is $\mathbf{R}_{\text{SA} \leftarrow \text{LA}}^{-1}(\mathbf{T}(\mathbf{R}_{\text{SA} \leftarrow \text{LA}}(\mathbf{x}), t))$.

As before the transformed point in the LA coordinate system will not necessarily
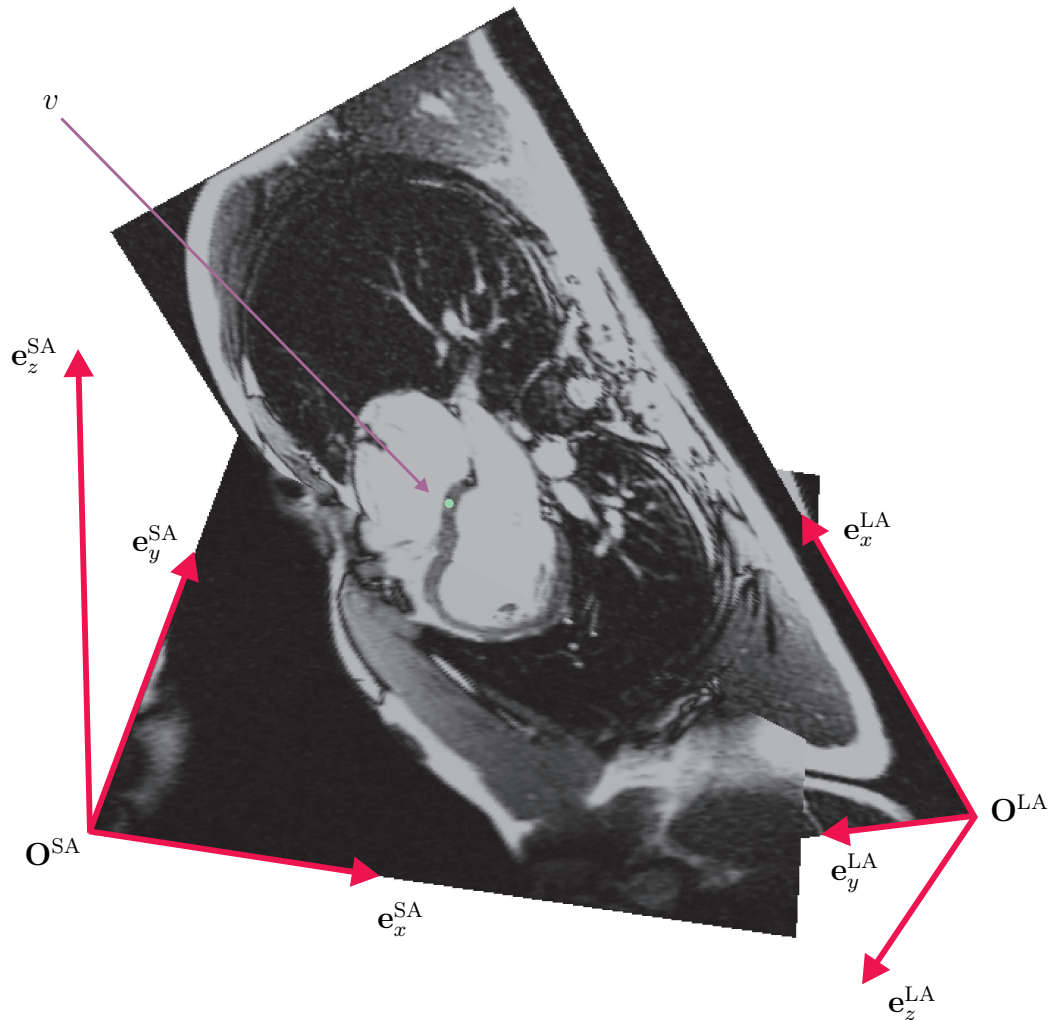
Figure 4.5: The xyz-coordinates of a point v in the LA coordinate system can be converted to the xyz-coordinates in the SA coordinate system by using the positions, and orientations of the SA and LA images stored in the DICOM headers of the images. For clarity, untagged images of the LV are shown in this figure.

lie exactly at the center of a voxel in the LA images and we need to interpolate the surrounding voxel intensities to obtain the LA voxel intensity at the transformed point. The interpolation is further complicated by the fact that some transformed points may lie entirely outside the LA imaging planes. There are three common configurations in which the LA planes are often acquired, and for each, an appropriate interpolation scheme must be chosen:

- Multiple LA images are acquired as a set of parallel contiguous slices (in a similar manner as the SA image slices). In this case trilinear interpolation can be used.

- Multiple LA images are acquired as a set of radial planes. Here trilinear interpolation cannot be used since the image planes are not contiguous and the distance between the LA planes varies in the radial direction of the LV. In this case, the interpolation of new intensities is difficult. One possible approach would involve a separate interpolation scheme for each LA plane in which the transformed point is projected onto the corresponding LA imaging plane and the new intensity is then calculated using bilinear interpolation. This approach is only correct if the deformed point has not moved by more than 1/2 the plane thickness in the direction perpendicular to the LA plane. Otherwise we would be extrapolating image intensities rather than interpolating them.

- Multiple sets of LA images are acquired in arbitrary orientations. This case is similar to the previous case where the LA images are acquired radially. For each set of LA images we can employ a separate interpolation scheme, either based on bilinear or trilinear interpolation depending on whether each set of LA images consists of one or more parallel contiguous slices. This interpolation scheme has been used for the simulator and volunteer data sets used in this chapter.

From the above it becomes apparent that the imaging protocol used dictates the interpolation scheme which can be used. The simplest and most accurate way

Registration Parameter	Value
No. of histogram bins	64
No. of iterations	20
No. of steps	8
Length of steps	15
ϵ	0.0001

Table 4.1: The parameters controlling the registration algorithm. The values given in the table were found empirically to give good registrations.

of recovering the motion field within the myocardium is to use a set of parallel and contiguous set of SA and LA image planes, but this choice may not always be available in the clinical environment where the cost and time taken to acquire the scans must also considered.

Once the intensities of the point $\mathbf{v}$ in its original and transformed positions, $L_0(\mathbf{v})$ and $L_{n\tau}(\mathbf{T}_{SA\leftarrow LA}^{-1}(\mathbf{T}(\mathbf{T}_{SA\leftarrow LA}(\mathbf{v}), n\tau)))$ respectively, have been found they are stored in a two dimensional histogram and used to calculate the NMI for the long-axis images. Finally, the contributions to the similarity measure (equation 4.11) are weighted by the number of voxels in the SA and LA images (equations 4.9 and 4.10).

4.1.2 Optimization Procedure

The optimization procedure used to maximize the similarity measure is an iterative gradient ascent technique similar to the one used by Rueckert *et al.* [142]. The difference in our case is that now we are trying to register both the short- and long-axis images with a single transformation. The gradient ascent optimization procedure used to optimize the control point displacement vectors for time $t = n\tau$ is shown in algorithm 1 and the parameters controlling the optimization are shown in table 4.1.

4.1.3 Summary of Motion Tracking Algorithm

The estimation of the deformation field $\mathbf{T}$ proceeds in a sequence of registration steps as shown in figure 4.6. In this figure, the symbols $S_{i\tau}$ and $L_{i\tau}$ represent the

Algorithm 1 The gradient ascent optimization procedure used to compute $\mathbf{u}^h(\mathbf{x})$
___
1: $L \leftarrow$ Maximum length of steps, $N \leftarrow$ Number of steps
2: **while** $N > 0$ **do**
3:      $I \leftarrow$ Number of iterations
4:      **while** $I > 0$ **do**
5:          Compute the gradient vector of the similarity measure

$$\nabla \mathcal{C} = \frac{\partial \mathcal{C}(\{\phi_{i,j,k}^h\})}{\partial \{\phi_{i,j,k}\}} \tag{4.13}$$

6:          **repeat**
7:              $\mathcal{C}_{\text{old}} \leftarrow$ Evaluate similarity measure
8:              **for all** control point displacement vectors $\phi_{i,j,k}^h$ **do**
9:

$$\phi_{i,j,k}^h \leftarrow \phi_{i,j,k}^h + L \left(\frac{\nabla \mathcal{C}}{||\nabla \mathcal{C}||} \right)_{i,j,k} \tag{4.14}$$

10:              **end for**
11:              $\mathcal{C}_{\text{new}} \leftarrow$ Evaluate similarity measure
12:          **until** $\mathcal{C}_{\text{new}} < \mathcal{C}_{\text{old}} + \epsilon$
13:          $I \leftarrow I - 1$
14:      **end while**
15:      $L \leftarrow L/2$, $N \leftarrow N - 1$
16: **end while**
___

volume images constructed from the SA and LA images respectively at time $t = i\tau$. To recover the deformation field at time $t = n\tau$ the SA and LA volume images at this time, $S_{n\tau}$ and $L_{n\tau}$, are registered to the segmented volume images of the myocardium at time $t = 0$, S_{seg} and L_{seg}, respectively.

After registering the volume images taken at time $t = \tau$ to the segmented volume images taken at $t = 0$ we obtain a *multi-level FFD* (MFFD) consisting of a single FFD representing the motion of the myocardium at time $t = \tau$. To register the volume images from $t = 2\tau$ a second level is added to the sequence of FFDs and then optimized to yield the transformation at time $t = 2\tau$. This process continues until all the volumes in the sequence are registered, as shown in figure 4.6, allowing us to relate any point in the myocardium at time $t = 0$ to its corresponding position throughout the sequence.
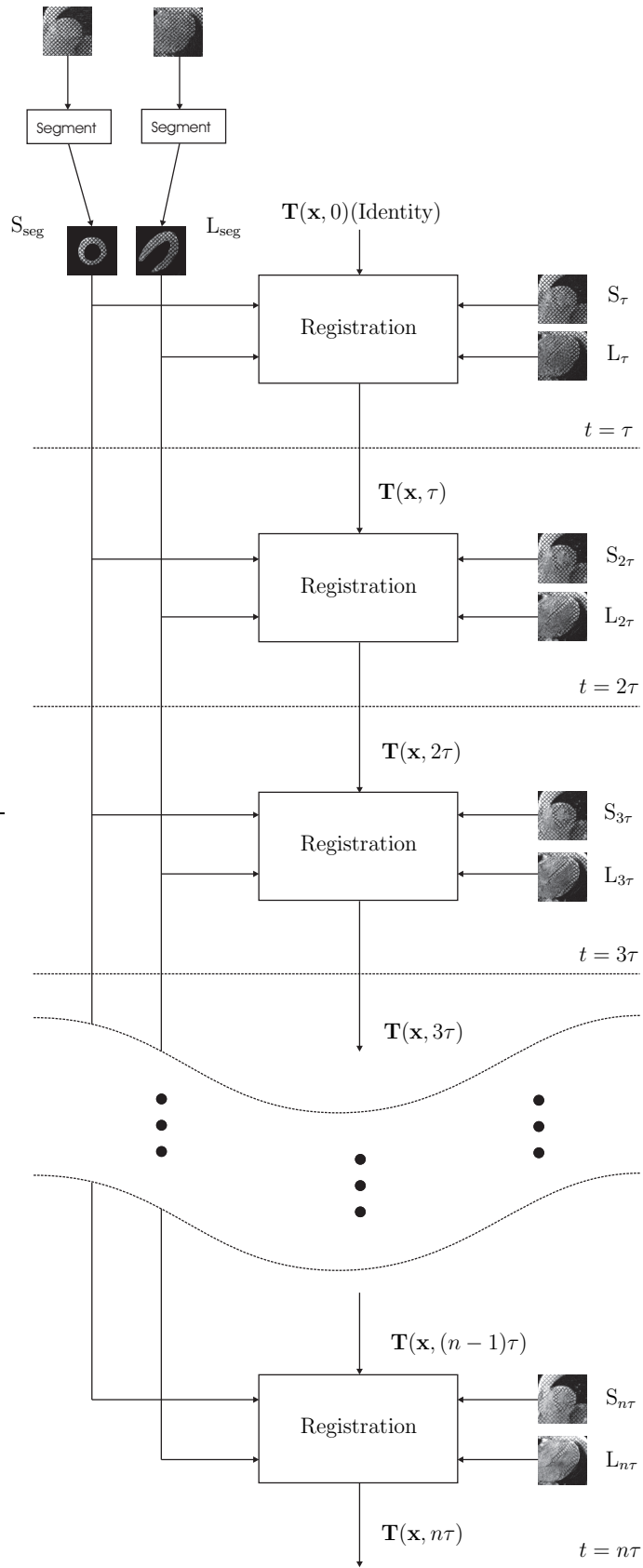
Figure 4.6: The SA and LA volume images, $S_{i\tau}$ and $L_{i\tau}$ respectively, taken at time $t = i\tau$ are registered simultaneously to their corresponding volume images taken at time $t = 0$ to recover the deformation field within the myocardium.

Parameter	Type of Motion
k_1	Radially dependent compression
k_2	Left ventricular torsion
k_3, k_4	Ellipticallization in LA and SA planes respectively
k_5, k_6, k_7	Shear in x, y, and z directions respectively
k_8, k_9, k_{10}	Rotation about x, y, and z axes respectively
k_{11}, k_{12}, k_{13}	Translation in x, y, and z directions respectively

Table 4.2: The 13 k-parameters controlling the cardiac motion simulator.

4.2 Results

4.2.1 Cardiac Motion Simulator Data

For the purposes of validation, a cardiac motion simulator as described in Waks *et al* [171] was implemented. The motion simulator is based on a 13-parameter model of left-ventricular motion developed by Arts *et al* [8] and is applied to a volume representing the LV that is modelled as a region between two confocal prolate spheres while the imaging process is simulated by a tagged spin-echo imaging equation [132]. The 13 parameters and the types of motion to which they correspond are shown in table 4.2. To compare how well the registration algorithm performed in reconstructing the deformation field, when the deformation field is known, nine sets of images were generated from the simulator showing three different types of nonrigid motion. Three sets of images, A_1, A_2, A_3, showing compressional motion were generated by varying k_1 as shown below:

$$k_1 = -0.01t \text{ where } t = 0, 1, \ldots, 9 \tag{4.15}$$

Gaussian noise with a mean of 0 and standard deviations, σ, of 8 and 16 were added to image sets A_2 and A_3 respectively. No noise was added to image set A_1. Another three sets of images, B_1, B_2, B_3, showing compressional and torsional motion were generated by varying k_2 in addition to k_1:

$$k_1 = -0.01t, \ k_2 = 0.01t \text{ where } t = 0, 1, \ldots, 9 \tag{4.16}$$

112

Parameter	Description	Value
λ_i	Inner radius	0.25
λ_o	Outer radius	0.60
δ/cm	Focal radius	4.00
D_0	Spin density	300.0
T_E/s	Echo time	0.03
T_R/s	Pulse repetition time	10.0
T_1/s	Longitudinal relaxation time	0.6
T_2/s	Transverse relaxation time	0.1
θ	Tip angle of tag pattern	45.0°
$\mathrm{SA}_x \times \mathrm{SA}_y \times \mathrm{SA}_z$	SA voxel sizes	$0.5 \times 0.5 \times 10$ mm
$\mathrm{LA}_x \times \mathrm{LA}_y \times \mathrm{LA}_z$	LA voxel sizes	$0.5 \times 0.78125 \times 6.4$ mm

Table 4.3: The parameter values used to generate the simulator image sets.

Similarly, Gaussian noise with a mean of 0 and standard deviations of 8 and 16 were added to image sets B_2 and B_3 respectively, while no noise was added to image set B_1. The final sets, C_1, C_2, C_3, showing ellipticallization, compressional, and torsional motion were generated by varying k_1, k_2, k_3 and k_4 according to:

$$k_1 = -0.01t, \ k_2 = 0.01t, \ k_3 = -0.01t, \ k_4 = -0.01t \quad \text{where } t = 0, 1, \ldots, 9 \quad (4.17)$$

Again, Gaussian noise with a mean of 0 and standard deviations of 8 and 16 were added to image sets C_2 and C_3 respectively. The images generated consisted of both SA and LA images. The SA slices were located at $z = -45, -35, \ldots, 45$ (in mm) with respect to the origin defined by the LV model [171]. Two sets of LA images were produced which were perpendicular to each other and also to the SA images. The two sets of LA image slices were located at positions $x = -16, -9.6, -3.2, 3.2, 9.6, 16$ (in mm) and $y = -16, -9.6, -3.2, 3.2, 9.6, 16$ (in mm) respectively.

Figures 4.7, 4.8, and 4.9 display some representative SA and LA slices, taken from the image sets in which no noise has been added, showing the deformation of the LV at three different time frames ($t = 0, 5, 9$). The model and imaging parameters used in generating the images are given in table 4.3. The tag spacing in all images was $20\pi/8$mm.

For each set of images, a transformation, $\mathbf{T}(\mathbf{x}, t)$, which gave the deformation of

(a) SA Images

(b) LA Images

Figure 4.7: The images shown in (a) and (b) are, respectively, SA ($z = 15.0$mm) and LA ($y = -3.2$mm) images taken from image set A_1 showing the deformation of the myocardium at time frames 0, 5, and 9.
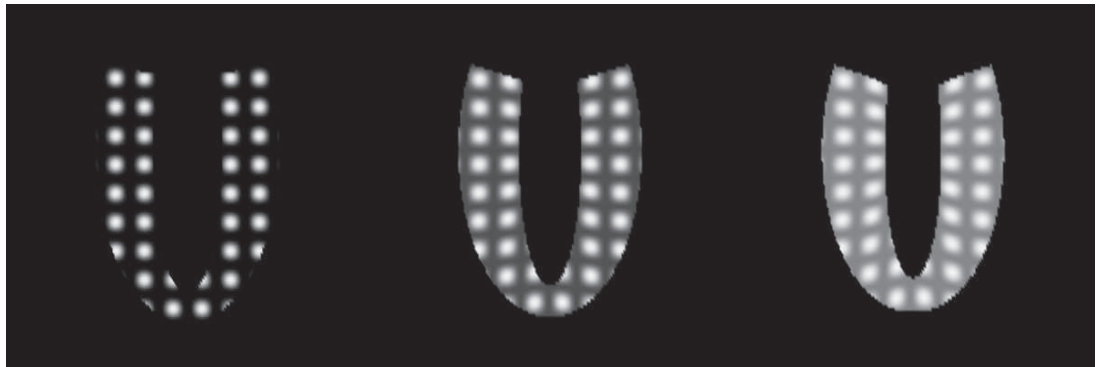
(a) SA Images

(b) LA Images

Figure 4.8: The images shown in (a) and (b) are, respectively, SA ($z = 15.0$mm) and LA ($y = -3.2$mm) images taken from image set B_1 showing the deformation of the myocardium at time frames 0, 5, and 9.
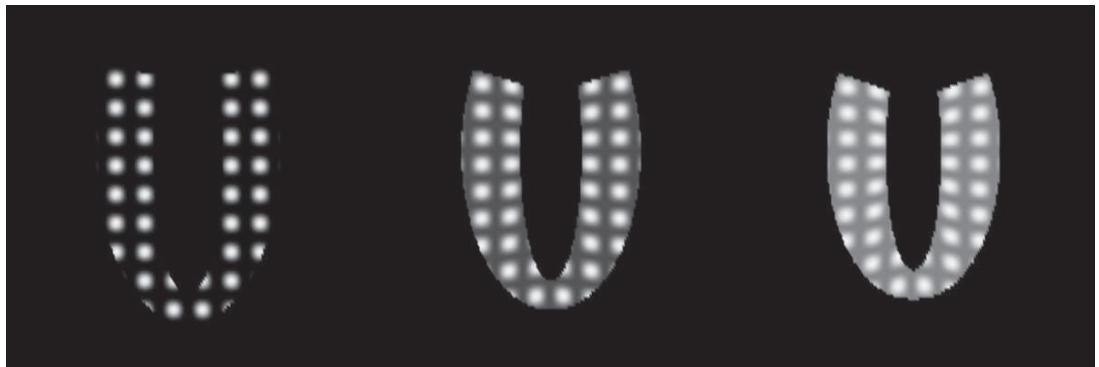
(a) SA Images

(b) LA Images

Figure 4.9: The images shown in (a) and (b) are, respectively, SA ($z = 15.0$mm) and LA ($y = -3.2$mm) images taken from image set C_1 showing the deformation of the myocardium at time frames 0, 5, and 9.

the model LV was calculated using the registration algorithm described in section 4.1 for all times t. The relative error, $\rho(t)$, in the displacement vectors of points in the LV estimated from the transformation $\mathbf{T}(\mathbf{x}, t)$ was then calculated. $\rho(t)$ is defined as

$$\rho(t) = \frac{1}{N} \sum_{\mathbf{x} \in \text{myo}} \frac{||\mathbf{u}_{\text{sim}}(\mathbf{x}, t) - \mathbf{u}(\mathbf{x}, t)||}{||\mathbf{u}_{\text{sim}}(\mathbf{x}, t)||} \times 100\% \qquad (4.18)$$

where $\mathbf{u}(\mathbf{x}, t) = \mathbf{T}(\mathbf{x}, t) - \mathbf{x}$ is the displacement estimated by the registration algorithm at position $\mathbf{x}$ and at time t, and $\mathbf{u}_{\text{sim}}$ is the true displacement calculated from the motion simulator. The summation is carried out over only those points that are in the myocardium, N being the total number of such points.

Figures 4.10(a), 4.10(b), 4.10(c) show the variation of the relative error, ρ, in the estimated displacements for the three different types of motion. Each of the figures shows that the relative error is the largest at time frame $t = 1$. ρ decreases between time frames $t = 1$ and $t = 6$ and remains relatively constant for later time frames. This is to be expected as the displacements of points in the myocardium at earlier time frames ($t < 4$) are of the order of the voxel size making an accurate estimate of the deformation field more difficult to obtain at these times than at later times ($t >= 4$) when the displacements are much larger than the voxel size. The addition of noise also decreases the accuracy of the estimated deformation fields especially at the start of the image sequences.

We also computed the *root mean square* (RMS) error, $\delta(t)$, in the estimated displacements. $\delta(t)$ is defined as

$$\delta(t) = \sqrt{\frac{1}{N} \sum_{\mathbf{x} \in \text{myo}} ||\mathbf{u}_{\text{sim}}(\mathbf{x}, t) - \mathbf{u}(\mathbf{x}, t)||^2} \qquad (4.19)$$

Figures 4.11(a), 4.11(b), 4.11(c) show plots of the variation of the RMS errors as a function of time for the three different types of motion. As can be seen the RMS error increases to a maximum of 0.3mm at $t = 9$ but remains below the voxel size. These results indicate that the motion of the myocardium can be tracked very well
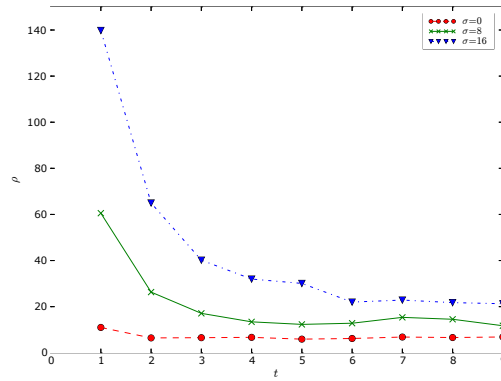
(a) Image set A
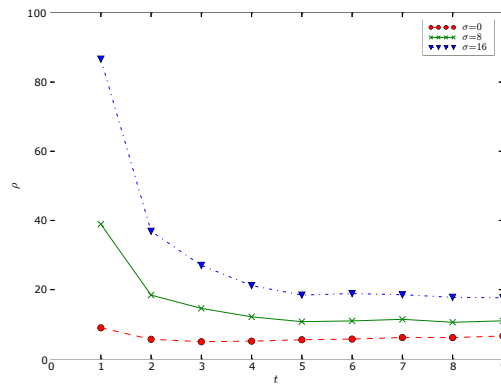
(b) Image set B
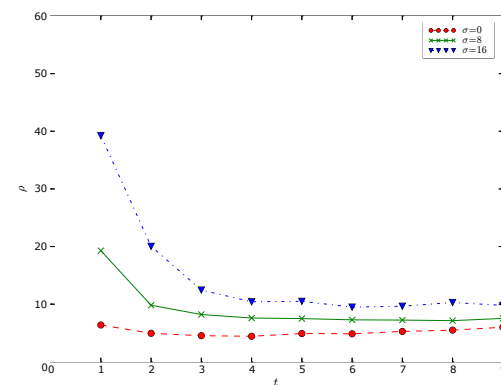
(c) Image set C

Figure 4.10: This figure shows the variation of the relative error in the estimated displacements for the three different types of motion generated from the LV simulator and for different amounts of Gaussian noise added to the images.

even when significant amounts of noise are added.

In addition to deformations, strains have been shown to be clinically useful indicators of abnormal cardiac function [111]. The Lagrangian strain (equation 2.17), at a particular position $\mathbf{x}$ and time instant t, can be expressed in matrix form as

$$\mathbf{E}(\mathbf{x}, t) = \frac{1}{2}(\mathbf{J}(\mathbf{x}, t) + \mathbf{J}^T(\mathbf{x}, t) + \mathbf{J}^T(\mathbf{x}, t)\mathbf{J}(\mathbf{x}, t)) \tag{4.20}$$

where $\mathbf{J}(\mathbf{x}, t)$ is the Jacobian matrix of the deformation field $\mathbf{u}(\mathbf{x}, t)$

$$\mathbf{J}(\mathbf{x}, n\tau) = \begin{bmatrix} \frac{\partial u_x(\mathbf{x}, n\tau)}{\partial x} & \frac{\partial u_x(\mathbf{x}, n\tau)}{\partial y} & \frac{\partial u_x(\mathbf{x}, n\tau)}{\partial z} \\ \frac{\partial u_y(\mathbf{x}, n\tau)}{\partial x} & \frac{\partial u_y(\mathbf{x}, n\tau)}{\partial y} & \frac{\partial u_y(\mathbf{x}, n\tau)}{\partial z} \\ \frac{\partial u_z(\mathbf{x}, n\tau)}{\partial x} & \frac{\partial u_z(\mathbf{x}, n\tau)}{\partial y} & \frac{\partial u_z(\mathbf{x}, n\tau)}{\partial z} \end{bmatrix} \tag{4.21}$$

and $u_x(\mathbf{x}, n\tau)$, $u_y(\mathbf{x}, n\tau)$, and $u_z(\mathbf{x}, n\tau)$ are the x-, y-, and z-components of the deformation field $\mathbf{u}(\mathbf{x}, n\tau)$. The deformation field at time $t = n\tau$ is

$$\begin{aligned} \mathbf{u}(\mathbf{x}, n\tau) &= \mathbf{T}(\mathbf{x}, n\tau) - \mathbf{x} & (4.22) \\ &= \sum_{h=1}^{n} \mathbf{u}^h(\mathbf{x}) & (4.23) \end{aligned}$$

Expressing $\mathbf{u}(\mathbf{x}, n\tau)$ in terms of $\mu_{i,j,k}^h$, $\nu_{i,j,k}^h$ and $\xi_{i,j,k}^h$, the x-, y-, and z-components of the control point displacement vectors at the positions $\mathbf{x}_{i,j,k}$ we obtain

$$\begin{aligned} u_x(\mathbf{x}, n\tau) &= \sum_{h=1}^{n} u_x^h(\mathbf{x}) \\ &= \sum_{h=1}^{n}\sum_{i=0}^{n_x}\sum_{j=0}^{n_y}\sum_{k=0}^{n_z} \beta^3\left(\frac{x - x_{i,j,k}}{\delta_x}\right)\beta^3\left(\frac{y - y_{i,j,k}}{\delta_y}\right)\beta^3\left(\frac{z - z_{i,j,k}}{\delta_z}\right)\mu_{i,j,k}^h \\ u_y(\mathbf{x}, n\tau) &= \sum_{h=1}^{n} u_y^h(\mathbf{x}) \\ &= \sum_{h=1}^{n}\sum_{i=0}^{n_x}\sum_{j=0}^{n_y}\sum_{k=0}^{n_z} \beta^3\left(\frac{x - x_{i,j,k}}{\delta_x}\right)\beta^3\left(\frac{y - y_{i,j,k}}{\delta_y}\right)\beta^3\left(\frac{z - z_{i,j,k}}{\delta_z}\right)\nu_{i,j,k}^h \end{aligned}$$
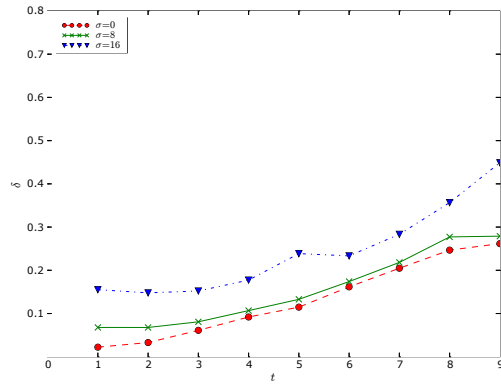
(a) Image set A
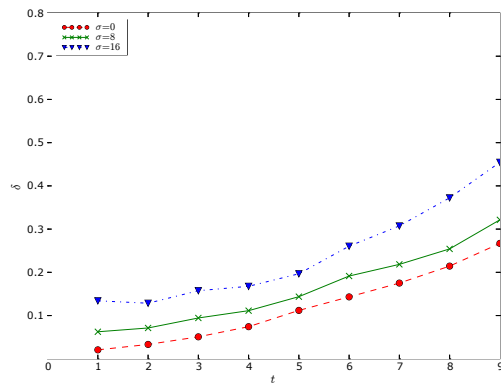
(b) Image set B
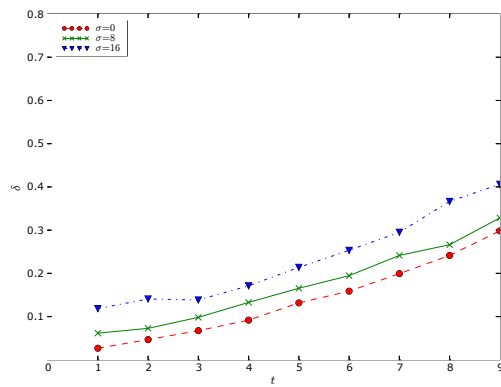
(c) Image set C

Figure 4.11: This figure shows the variation of the RMS error in the estimated displacements for the three different types of motion generated from the LV simulator and for different amounts of Gaussian noise added to the images.

$$u_z(\mathbf{x}, n\tau) = \sum_{h=1}^{n} u_z^h(\mathbf{x})$$

$$= \sum_{h=1}^{n}\sum_{i=0}^{n_x}\sum_{j=0}^{n_y}\sum_{k=0}^{n_z} \beta^3\left(\frac{x - x_{i,j,k}}{\delta_x}\right)\beta^3\left(\frac{y - y_{i,j,k}}{\delta_y}\right)\beta^3\left(\frac{z - z_{i,j,k}}{\delta_z}\right)\xi_{i,j,k}^h$$

The components of the Jacobian matrix of the deformation field can then be obtained from the above equations by finding the spatial derivatives of $u_x(\mathbf{x}, n\tau)$, $u_y(\mathbf{x}, n\tau)$ and $u_z(\mathbf{x}, n\tau)$. For example

$$\frac{\partial u_x(\mathbf{x}, n\tau)}{\partial y} = \sum_{h=1}^{n}\sum_{i=0}^{n_x}\sum_{j=0}^{n_y}\sum_{k=0}^{n_z}\beta^3\left(\frac{x - x_{i,j,k}}{\delta_x}\right)\frac{d\beta^3}{dv}\frac{dv}{dy}\beta^3\left(\frac{z - z_{i,j,k}}{\delta_z}\right)\mu_{i,j,k}^h$$

$$= \frac{1}{\delta_y}\sum_{h=1}^{n}\sum_{i=0}^{n_x}\sum_{j=0}^{n_y}\sum_{k=0}^{n_z}\beta^3\left(\frac{x - x_{i,j,k}}{\delta_x}\right)\frac{d\beta^3}{dv}\beta^3\left(\frac{z - z_{i,j,k}}{\delta_z}\right)\mu_{i,j,k}^h$$

where

$$v = \frac{y - y_{i,j,k}}{\delta_y} \tag{4.24}$$

and

$$\frac{d\beta^3}{dv} = \begin{cases} (2+v)^2/2 & \text{for } -2 \leq v < -1 \\ -(3v+4)v/2 & \text{for } -1 \leq v < 0 \\ (3v-4)v/2 & \text{for } 0 \leq v < 1 \\ -(3v^2 - 4v + 4)/2 & \text{for } 1 \leq v < 2 \\ 0 & \text{otherwise} \end{cases} \tag{4.25}$$

The other components of the Jacobian matrix can found similarly and substituted into equations 4.20 and 4.21 to obtain the strain.

To determine how accurately we could determine the strain distribution in the myocardium, simulated image sets showing a more realistic motion of the myocardium were generated using the k-parameter values given in figure 4 of [171] which were derived from a bead experiment on a dog heart [8]. A series of short- and long-axis images were generated for 10 equally spaced time instants between end-diastole and end-systole. These are plotted in figure 4.12. The parameter values from k_8 to k_{13} were set to 0 as these only control the rigid motion of the simulated

(a) k_1 (b) k_2 (c) k_3

(d) k_4 (e) k_5 (f) k_6

(g) k_7
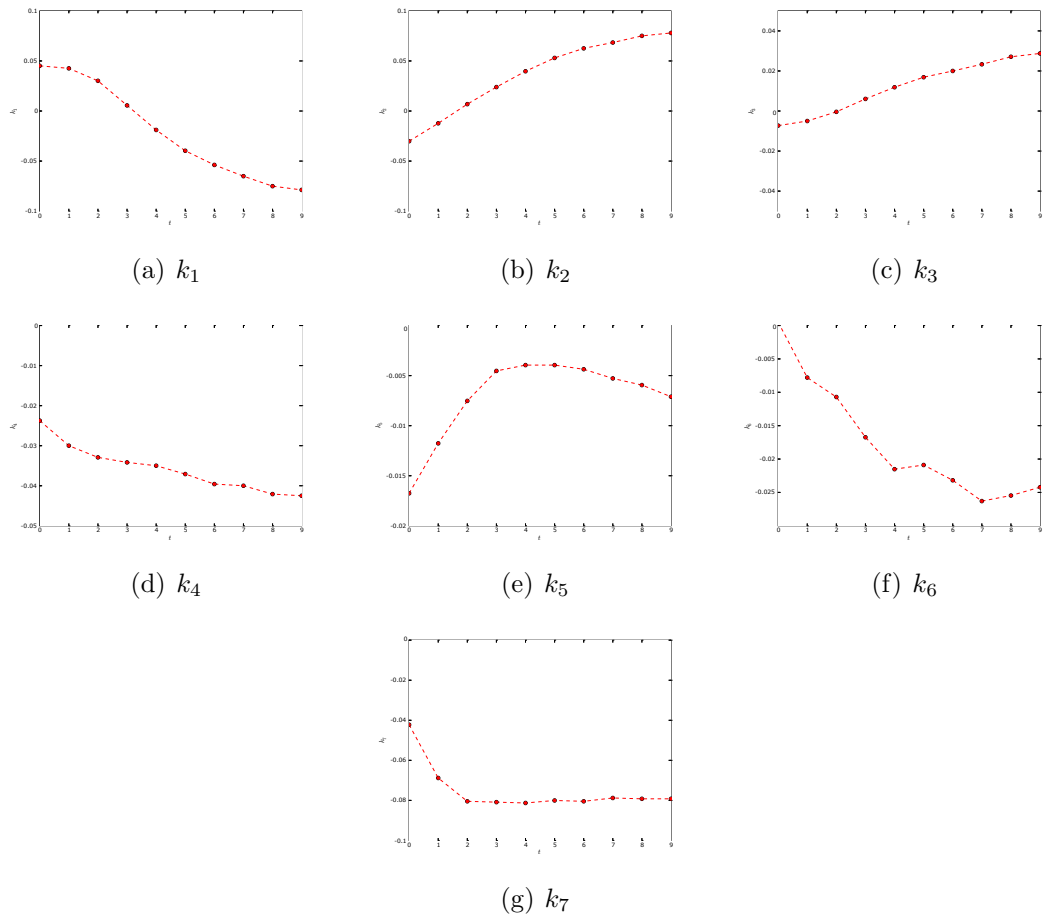
Figure 4.12: Plots showing the variation of the k-parameters of the LV simulators from end-diastole to end-systole obtained from a bead experiment on a dog [171, 8]. The data used to generate this plots were taken from figure 4 of [171].

LV. Figure 4.13 show representative SA and LA views of the generated images at time frames 0, 5, and 9. The model and imaging parameters used to generate the images were the same as those given in table 4.3 apart from the inner and outer radii, λ_i and λ_o, which were set to 0.35mm and 0.65mm respectively.

Figure 4.14 shows plots of the radial, circumferential, and longitudinal strain maps computed directly from the motion simulator for time $t = 9$. The three rows in the figure, from top to bottom, correspond to SA views of the LV at positions $z = -15$mm, $z = 5$mm, and 25mm respectively, and the three columns from left to right show the radial, circumferential, and longitudinal strains respectively. Figure 4.15 shows the corresponding strain maps computed from the method presented in this chapter, while figure 4.16 shows the differences between the true and
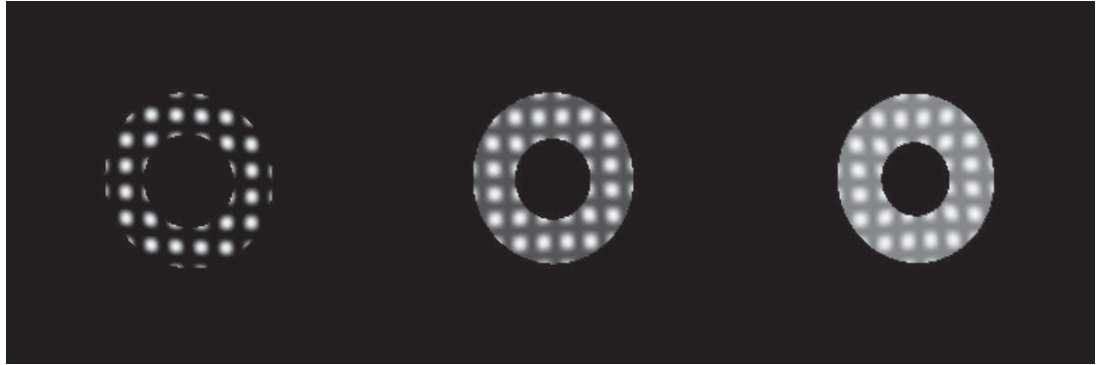
(a) SA Images

Figure 4.13: The images show in (a) and (b) are, respectively, SA ($z = 15.0$mm) and LA ($y = -3.2$mm) images taken from the simulated images generated using the k-parameter values given in figure 4.12.

estimated strain maps. As can be seen from a comparison of the radial and circumferential strain maps in the figures there is excellent agreement between the ones computed directly from the motion simulator and those computed using image registration. There is less of agreement between the longitudinal strain maps, particularly in the mid ventricular slice ($z = 5$mm). This is because the regional characteristics of the simulated displacement field have been effectively under-sampled with the imaging parameters chosen in table 4.3. Increasing the frequency of the tag spacing would reduce the under-sampling of the displacement field characteristics and thereby enable a much more accurate recovery of the strain maps. Additionally, increasing the resolution of the images used would also allow a more accurate estimate of the strain maps.

Finally, we visualized the strain maps computed from the motion simulator and the free-form deformations obtained from image registration using tensor ellipsoids (section 2.2.2.3). Figure 4.17 shows a tensor ellipsoid plot of the strain computed directly from the motion simulator and figure 4.18 shows the corresponding plot computed from the free-form deformations. The three SA slices shown in the two figures are at the same positions as those shown in figures 4.14 and 4.15. As can be seen from the two figures the principal strain directions computed from the free-form deformations agree very well with the true principal strain directions but the magnitude of the strain in the radial direction is underestimated by the free-form deformation in the endocardial regions. This indicates that the regional characteristics of the displacements field are more difficult to estimate in those regions with the chosen imaging parameters. To improve the strain estimates near the endocardium images with a smaller tag spacing would need to be used.

4.2.2 Human Data

Tagged MR data from 11 healthy volunteers was acquired with a Siemens Sonata 1.5 T scanner consisting of a series of SA and 0, 2, or 3 LA slices covering the whole of
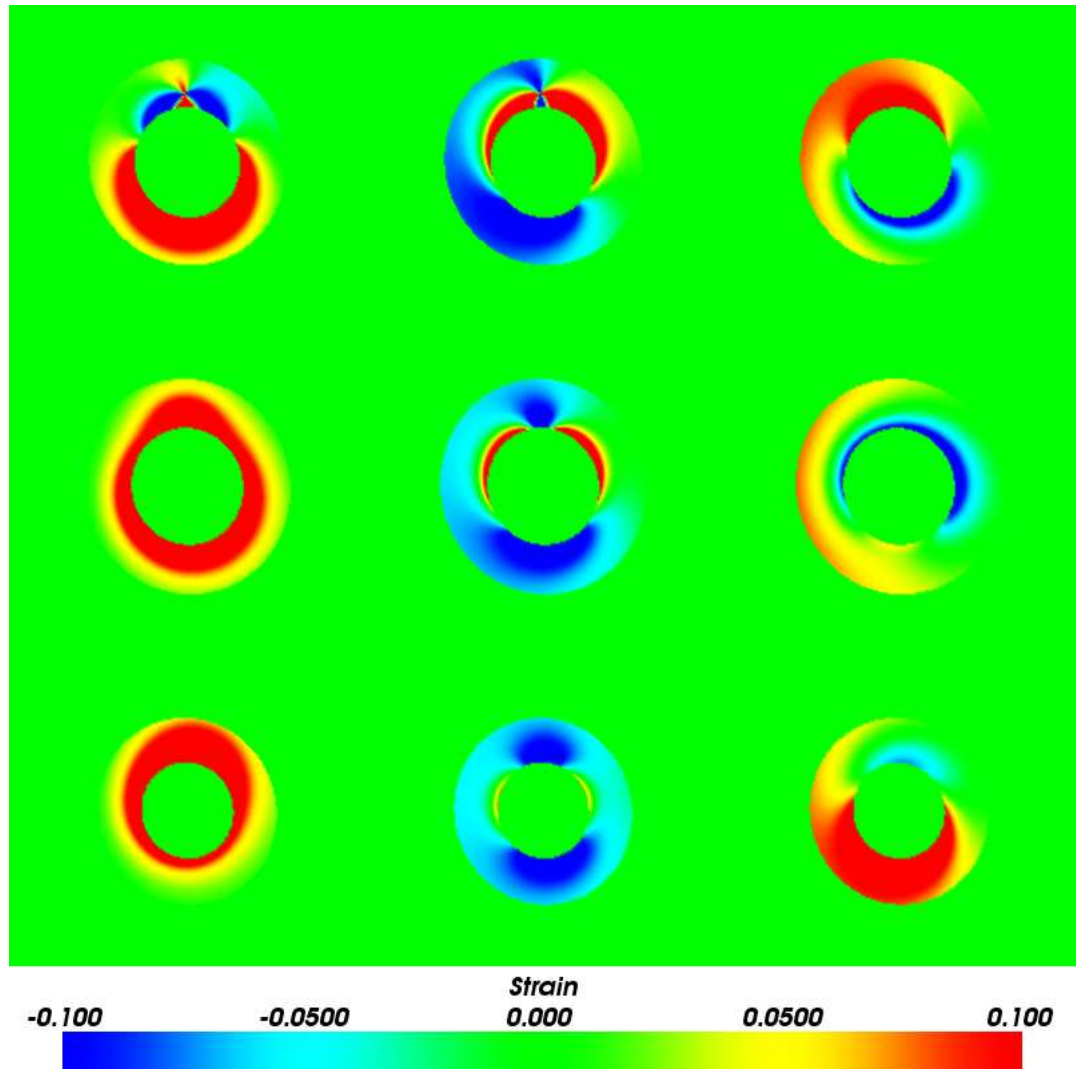
Figure 4.14: This figure shows plots of the radial, circumferential, and longitudinal strains in the myocardium computed directly from the motion simulator for the k-parameter values in figure 4.12 at time $t = 9$. The three rows from top to bottom show SA views of the strain maps at $z = -15$mm, $z = 5$mm, and $z = 25$mm respectively, and the three columns from left to right show the radial, circumferential, and longitudinal strains respectively.
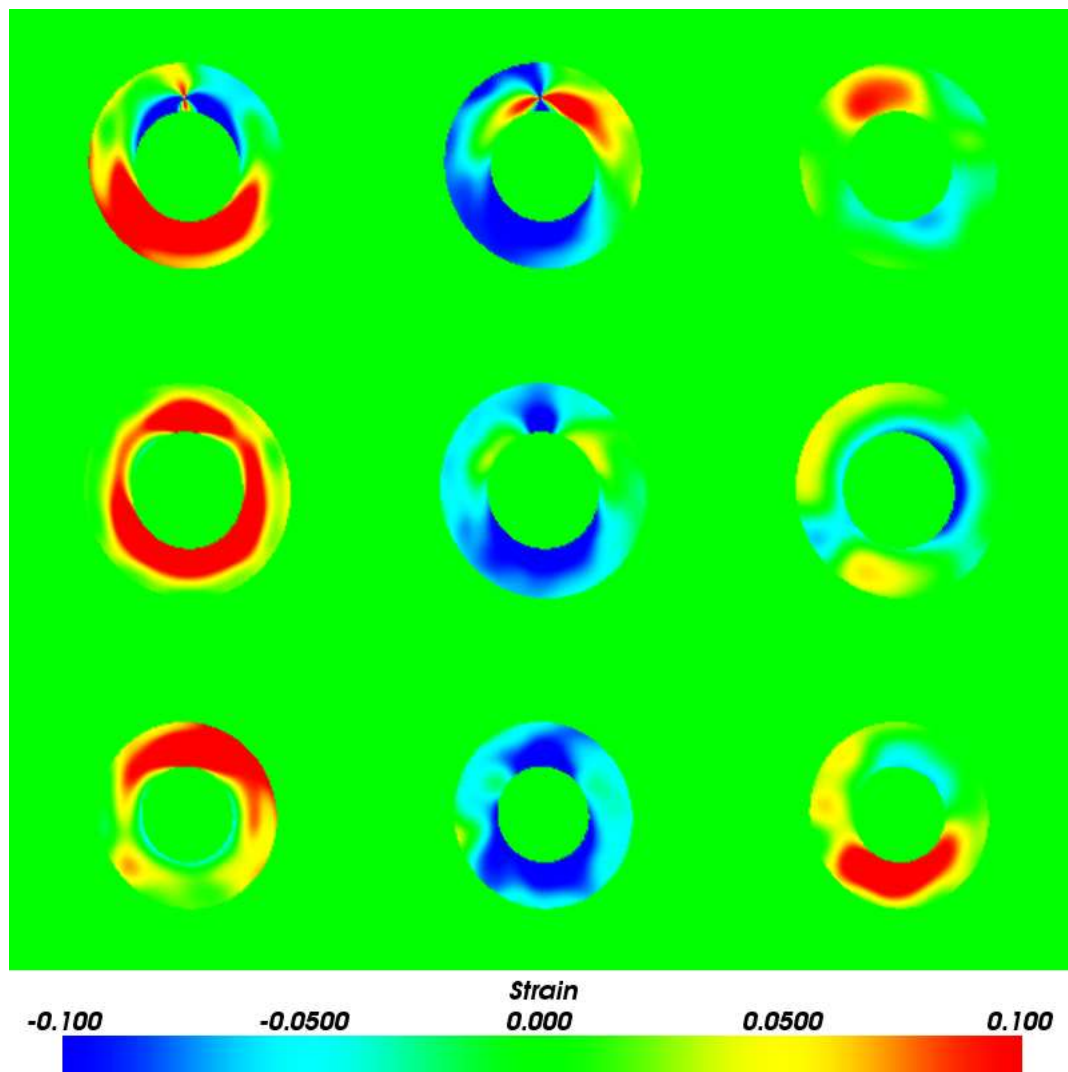
Figure 4.15: This figure shows plots of the radial, circumferential, and longitudinal strains in the myocardium computed from the free-form deformations obtained from the registration algorithm for the simulator images generated from the k-parameter values in figure 4.12. The strain maps shown here should be compared with the true strain maps in figure 4.14.
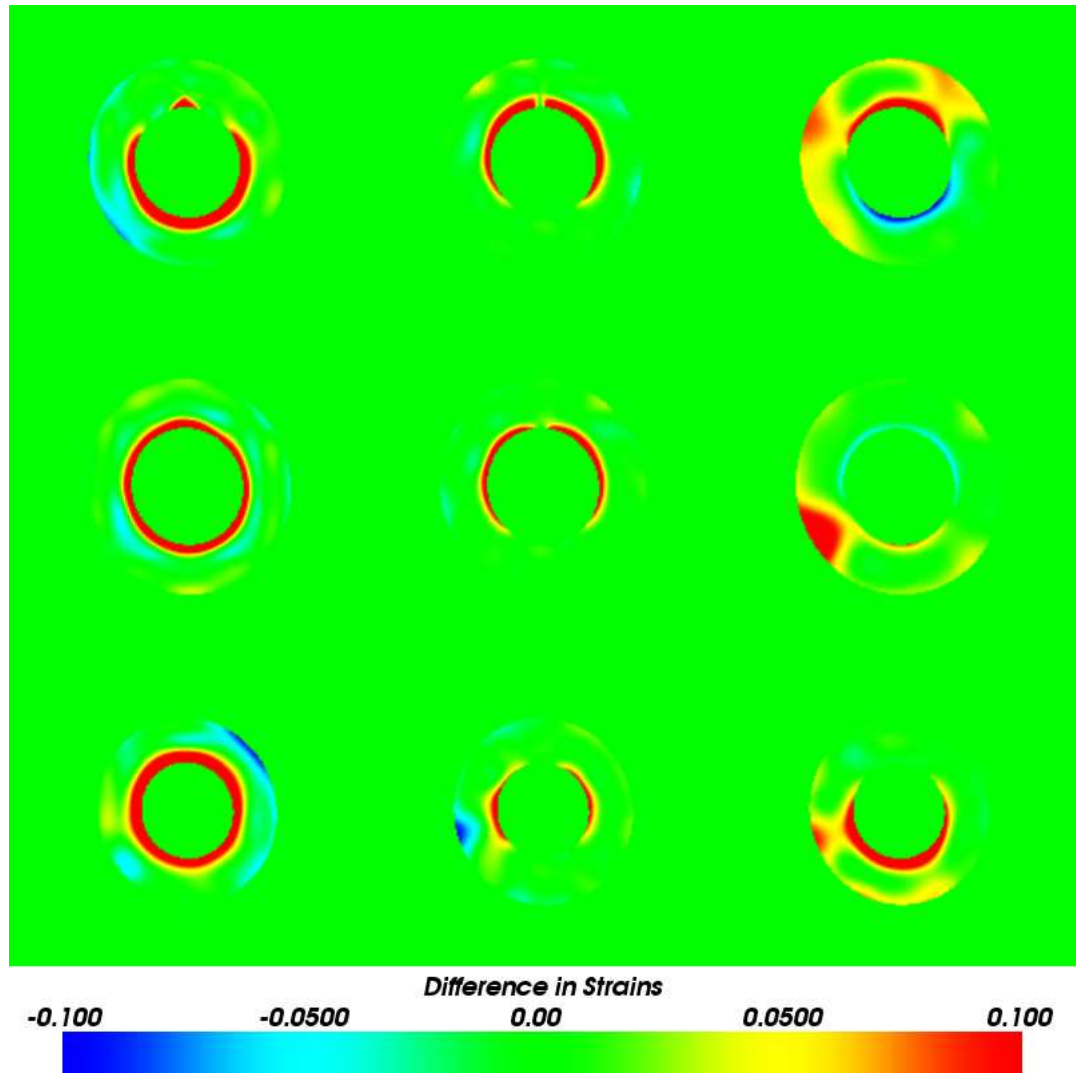
Figure 4.16: This figure shows the differences between the true (figure 4.14) and estimated (figure 4.15) strain maps.
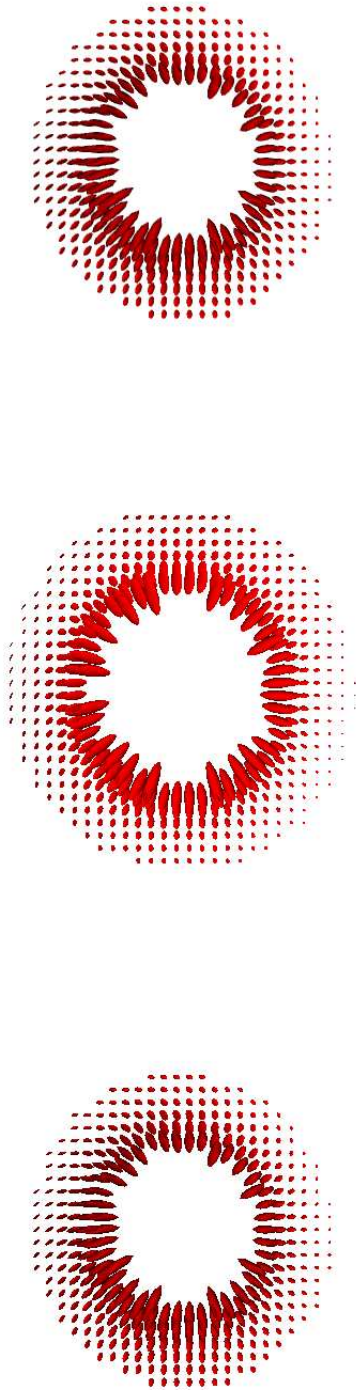
Figure 4.17: This figure shows plots of the strain in the myocardium computed directly from the motion simulator for the k-parameter values in figure 4.12 at time $t = 9$. The three rows from top to bottom show SA views of the strain maps at $z = -15$mm, $z = 5$mm, and $z = 25$mm respectively. The axes of the ellipsoids have been scaled by a factor of 10.
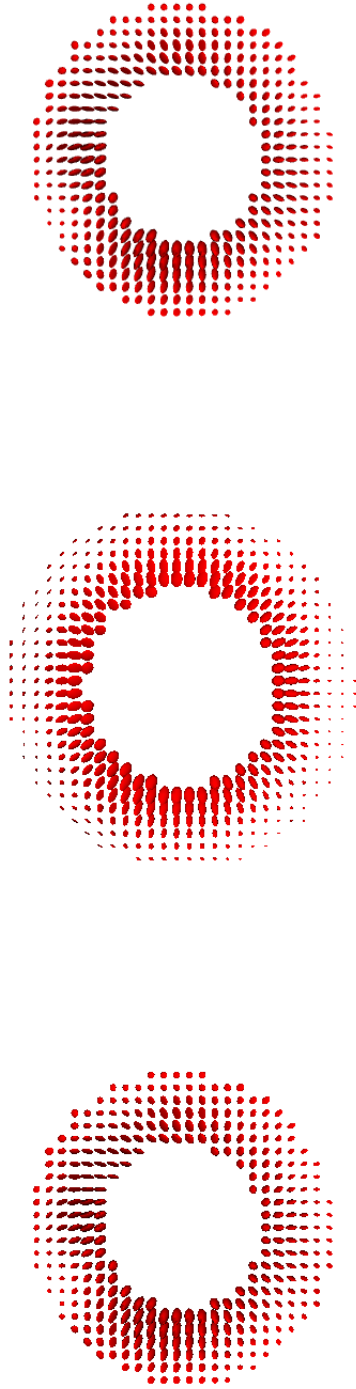
Figure 4.18: This figure shows plots of the strain in the myocardium computed from the free-form deformations obtained from the registration algorithm for the simulator images generated from the k-parameter values in figure 4.12. The strain maps shown here should be compared with the true strain maps in figure 4.17.
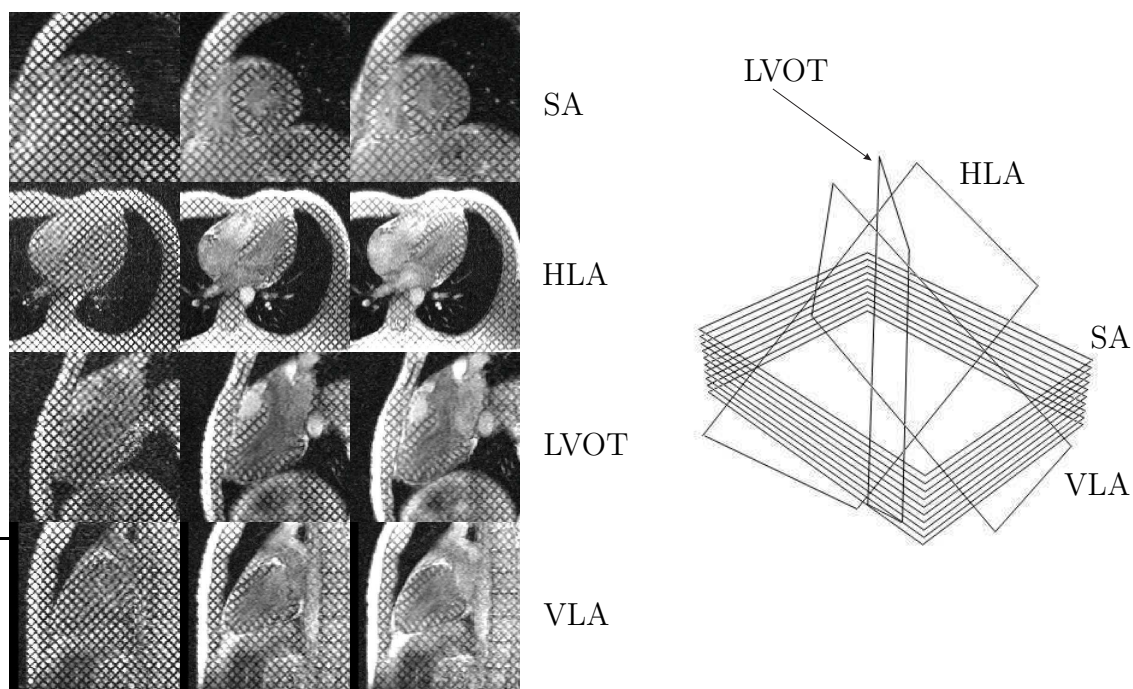
Figure 4.19: SA and LA images taken from a volunteer at three different times, end-diastole (left column), mid-systole (middle column), end-systole (right column). The top row shows SA images, and the next three rows show *horizontal long-axis* (HLA), *left ventricular out-flow tract* (LVOT), and *vertical long-axis* (VLA) images respectively. The orientation of the LA slices with respect to the SA slices is shown on the right.

the LV. For two of the volunteers no LA slices were acquired, for one volunteer 2 LA slices were acquired and for the remaining eight volunteers 3 LA slices were acquired. A cine breath-hold sequence with a SPAMM tag pattern was used with imaging being done at end expiration. The image voxel sizes were $1.40 \times 1.40 \times 7$mm, with the distance between slices being 10 mm, and 10–18 images were acquired during the cardiac cycle, depending on the volunteer. The images taken at end-diastole, mid-systole, and end-systole for one of the volunteers are shown in figure 4.19. The figure also shows the orientation of the LA images with respect to the SA images. The imaging parameters for this volunteer were a repetition time of 40 ms, an echo time of 4 ms, and a 15° flip angle.

The deformation field within the myocardium for each of the volunteers was constructed by using the method described in section 4.1. To assess how well the registration algorithm performed in tracking the motion of the myocardium for vol-

unteer data, tag-intersection points were detected manually by an observer in three different SA slices (apex, mid-ventricle and base) and one LA slice for all time frames between end-diastole and end-systole. The average number of intersection points which could be tracked in the LA slices was 17 compared to the average number in the SA slices which were 15, 22, and 19 in the apical, mid-ventricular, and basal slices respectively. The RMS error, $\delta(n\tau)$, between the in-plane displacements estimated from the registration algorithm and the true in-plane displacements as measured by the observer were then computed for each time frame n. $\delta(n\tau)$ for a particular SA or LA imaging plane is defined as

$$\delta(n\tau) = \frac{1}{N} \sum_i ||\mathbf{u}(\mathbf{x}_i, n\tau) - [\widehat{\mathbf{n}}.\mathbf{u}(\mathbf{x}_i, n\tau)]\, \widehat{\mathbf{n}} - \mathbf{t}(\mathbf{x}_i, n\tau)||^2 \qquad (4.26)$$

where $\mathbf{u}(\mathbf{x}_i, n\tau)$ is the estimated displacement of the i-th tag intersection point at time frame n, $\mathbf{t}(\mathbf{x}_i, n\tau)$ is the true in-plane displacement of the i-th tag intersection point at time frame n, $\widehat{\mathbf{n}}$ is the unit vector normal to the plane of interest, and N is the total number of tag intersection points. The results obtained are shown in figure 4.20. The figure shows that for most of the volunteers the RMS errors in the in-plane displacements were below the voxel size for most of systole. The minimum error in the estimated in-plane displacements were found to be in the mid-ventricular SA slices. This is because there is relatively little through-plane motion of the LV in this imaging plane in comparison to the horizontal HLA and basal slices. Additionally, the mid-ventricular region of the LV has been sampled to a greater extent than the other regions of the LV, as can be seen for one of the volunteers in figure 4.19, enabling a better estimate of the motion field in that region.

4.2.2.1   Visual Assessment of Motion Tracking

In the case of tagged MR images, a visual assessment of the registration can be obtained by using so-called "virtual tag grids". These virtual tag grids enable a
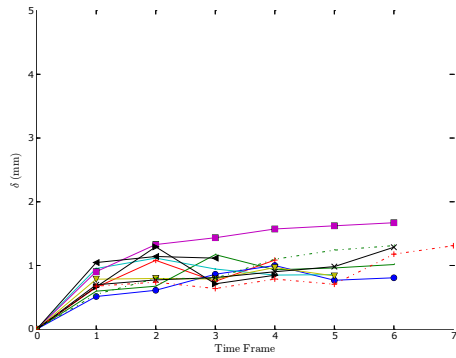
(a) Apical SA Slice
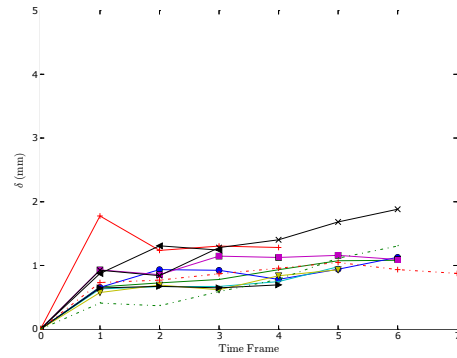
(b) Mid-ventricular SA Slice
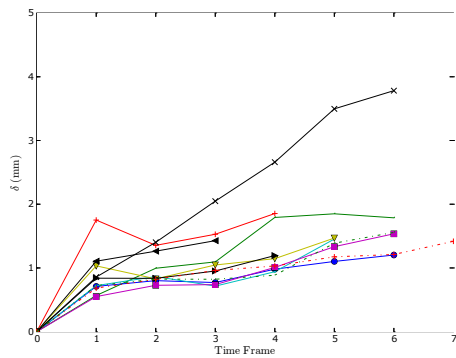
(c) Basal SA Slice
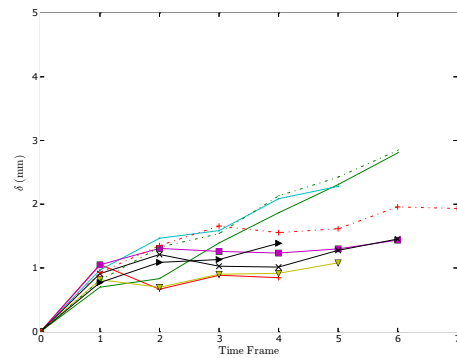
(d) Horizontal LA Slice

Figure 4.20: These graphs show the variation of the RMS error in the estimated in-plane displacements obtained from the registration algorithm as compared with the manual tracking of tag intersection points in different slices for the 11 volunteers.

qualitative understanding of how well the motion tracking in a sequence of tagged MR images has been achieved (figure 4.21). Virtual tag grids are placed on the tagged images by the user and deform with time according to the transformation $\mathbf{T}(\mathbf{x}, n\tau)$ computed from the registration algorithm. If the motion tracking has been performed accurately the virtual tag grids will follow the underlying tag pattern in the images and can be used to determine the validity of the nonrigid registration. As can be seen in figure 4.21, the virtual tag grids follow the underlying tag pattern in the images indicating the very good performance of the registration algorithm in recovering the deformation field in the myocardium.

In figures 4.22 and 4.23 the output transformation obtained from the registration algorithm was used to estimate the deformation of two tag planes which were perpendicular to the SA images at time $t = 0$. In figures 4.24 and 4.25 the deformation of two tag planes perpendicular to the LA image planes at $t = 0$ are shown. As can be seen in the figures the planes follow the underlying tag pattern. These results indicate a very good performance in the motion tracking.

In figure 4.26 we have produced a 3D arrow plot showing the motion of the myocardium. The figure clearly shows the contraction of the LV as well as its shortening in the longitudinal direction.

4.2.2.2 Derivation of Strain Parameters

To assess abnormal contractility in a particular region of the myocardium clinicians often use bullseye plots. In a bullseye plot the entire three-dimensional region of the LV is mapped onto a series of concentric rings on a two dimensional plane, with the inner most ring representing the apex of the LV, and the outer most ring representing the base of the LV. Within a particular region of the myocardium we can calculate the average value of the strain and assign it to the corresponding sector in the bullseye plot. The bullseye plot obtained can then be compared with the strain distribution in a normal subject to determine if there is any abnormal contractility resulting from coronary artery disease. To help with this task Cerqueira
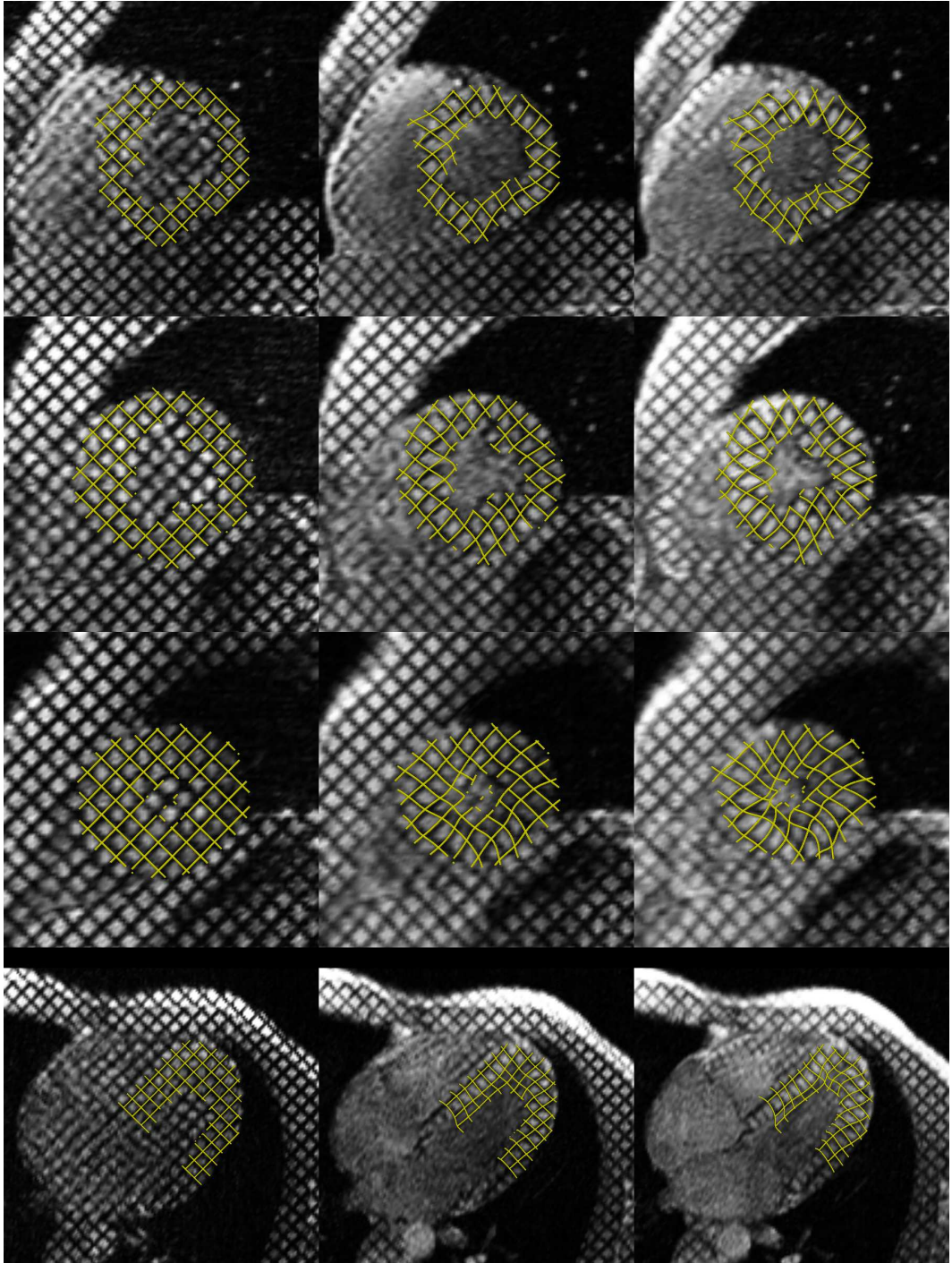
Figure 4.21: This figure shows a series of tagged images taken from one of the volunteers. A virtual tag grid has been placed on the tag pattern at end-diastole and allowed to deform with time according to the deformation field calculated. As time progresses the virtual tag grid can be seen to follow the underlying tag pattern and so we can say that the deformation field has been reconstructed accurately. The first three rows show basal, mid-ventricular, and apical SA images respectively. The fourth row shows a horizontal LA image. The first, second, and third columns correspond to end-diastole, mid-systole, and end-systole respectively. Animations of these virtual tag grids can be found on the accompanying CD.

Figure 4.22: This figure shows the estimated deformation of a tag plane which is perpendicular to the SA image planes at time $t = 0$. An animation of the deforming tag plane can be found on the accompanying CD.
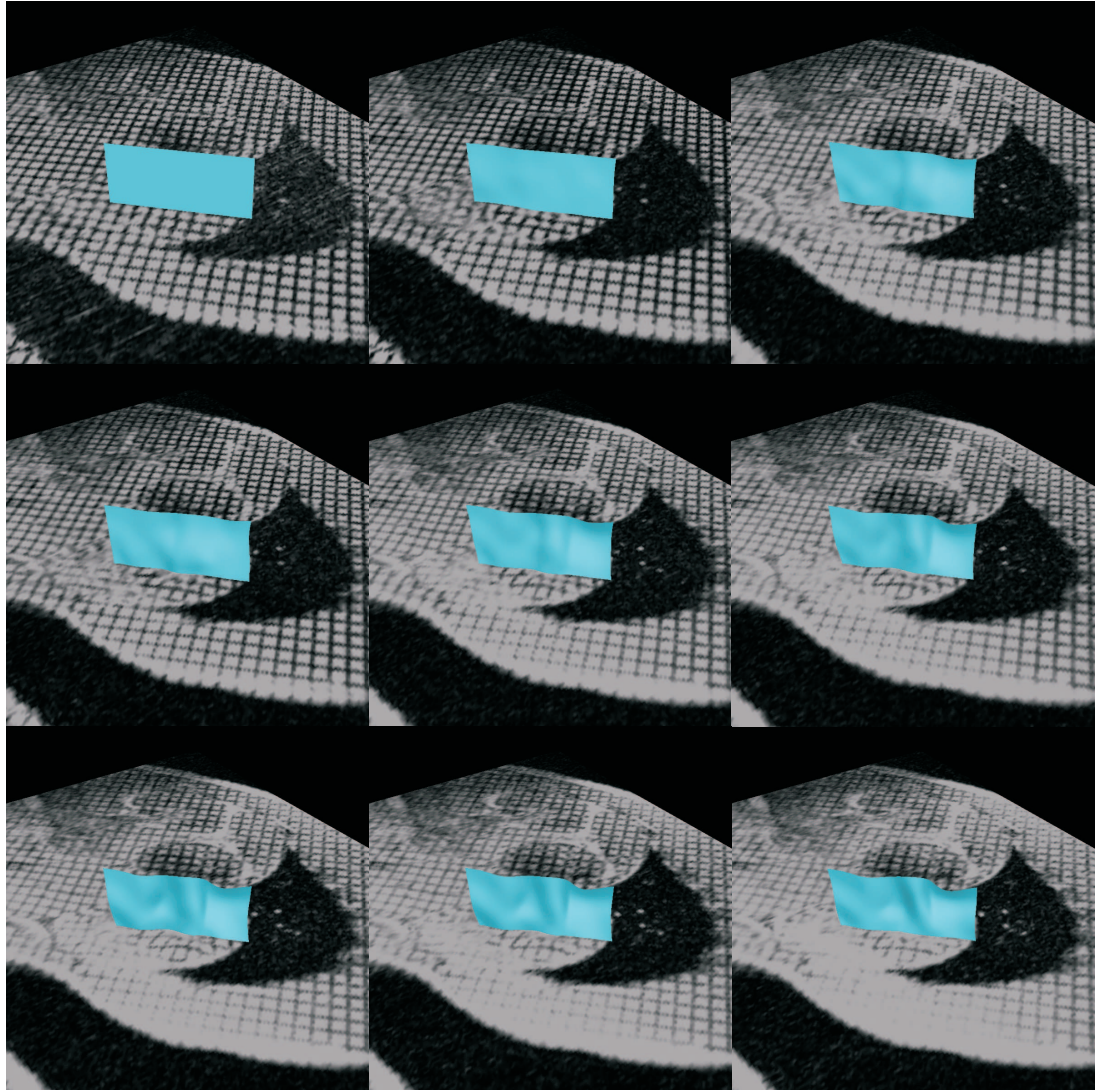
Figure 4.23: This figure shows the estimated deformation of a tag plane which is perpendicular to the SA image planes at time $t = 0$. An animation of the deforming tag plane can be found on the accompanying CD.
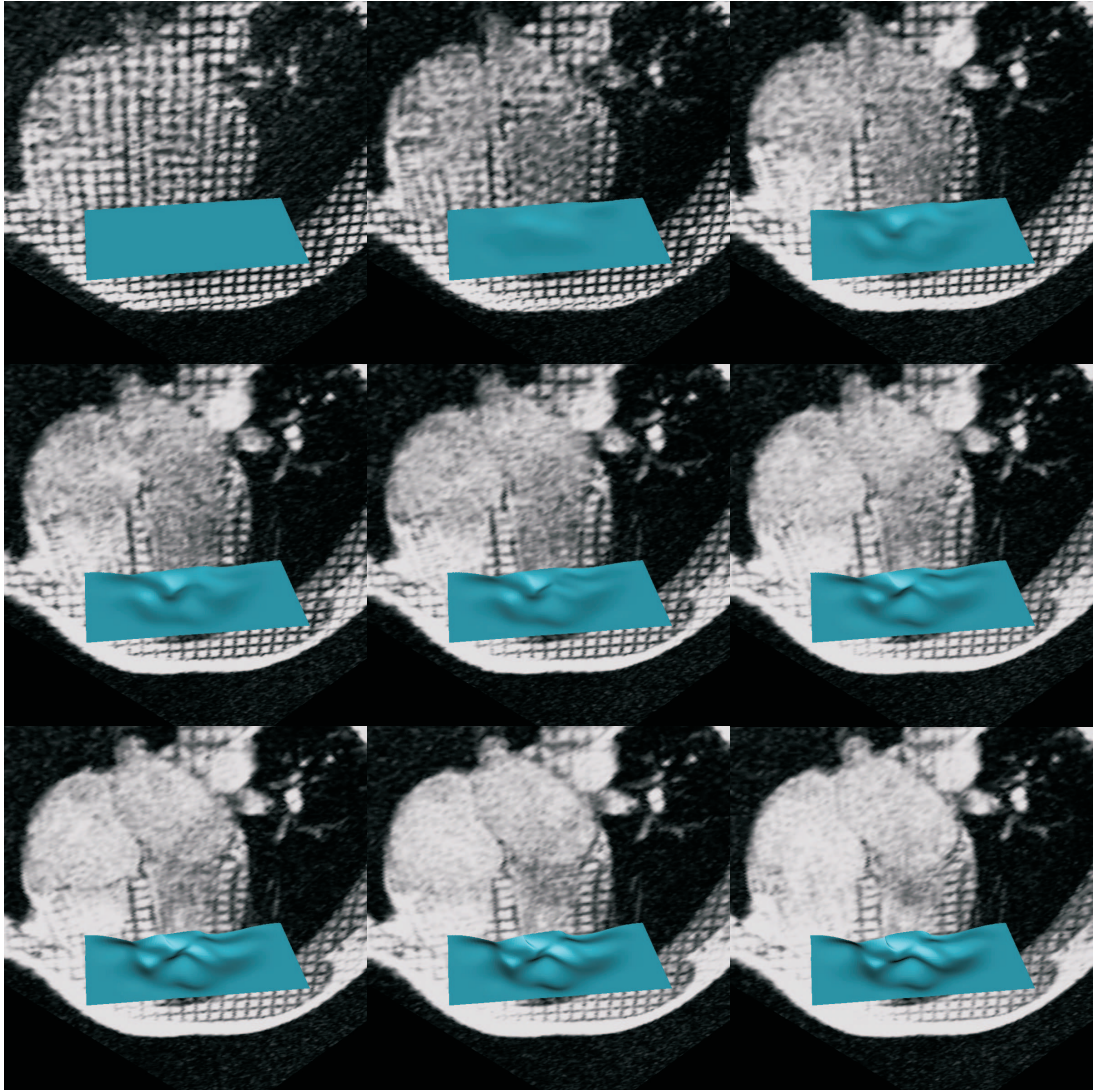
Figure 4.24: This figure shows the estimated deformation of a tag plane which is perpendicular to the LA image planes at time $t = 0$. An animation of the deforming tag plane can be found on the accompanying CD.
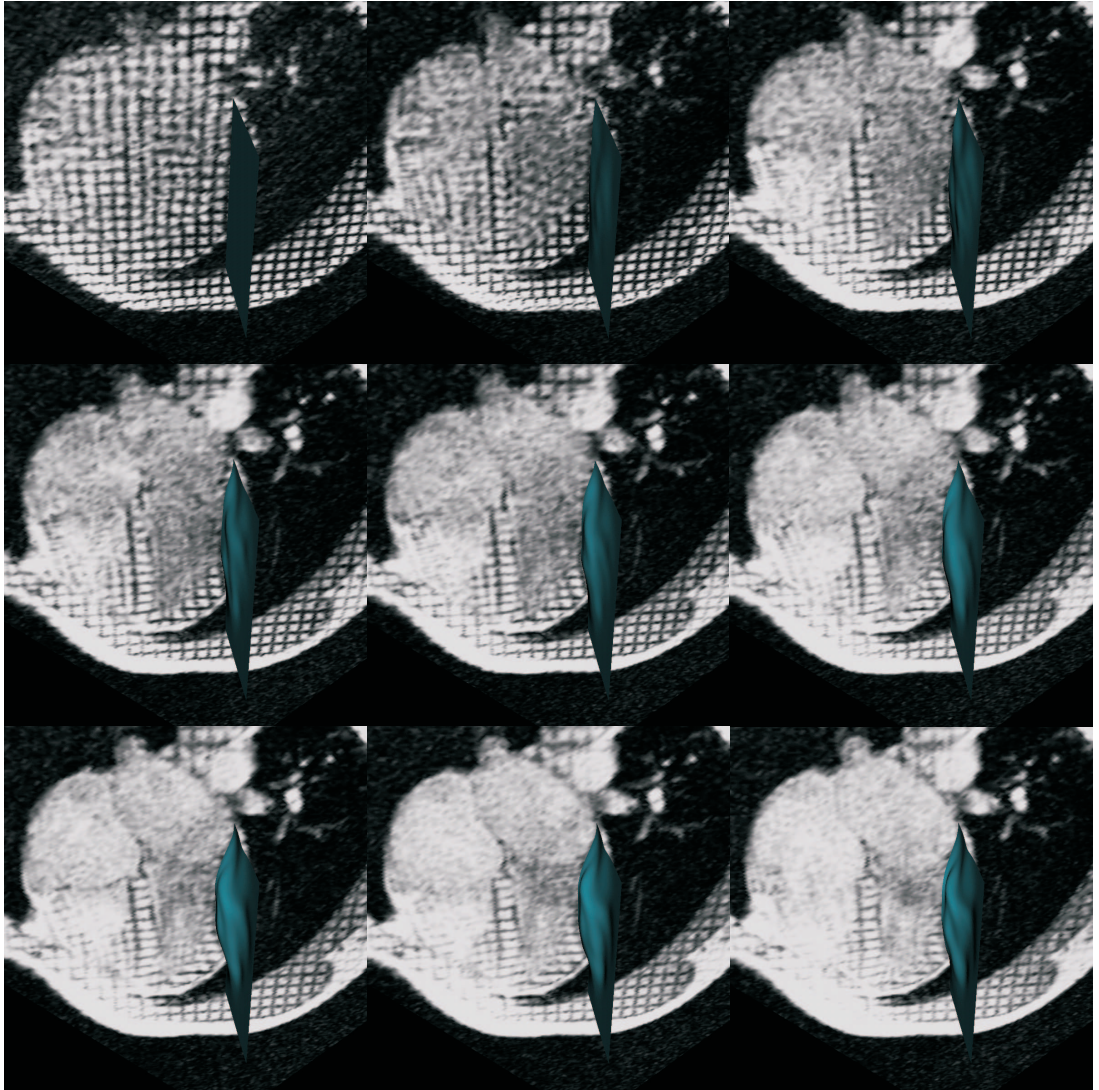
Figure 4.25: This figure shows the estimated deformation of a tag plane which is perpendicular to the LA image planes at time $t = 0$. An animation of the deforming tag plane can be found on the accompanying CD.
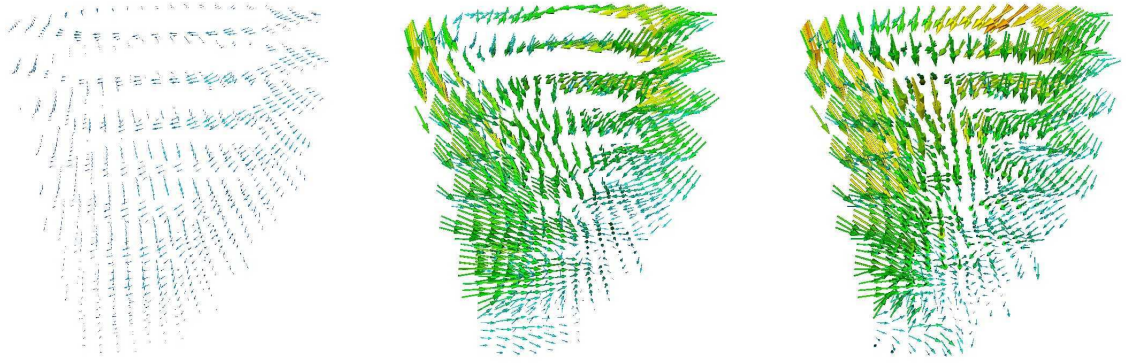
Figure 4.26: Arrow plots showing the motion of the myocardium from a normal volunteer. The images, from left to right correspond to end-diastole, mid-systole, and end-systole respectively.

et al [23] have recommended the assignment of individual segments to the three major coronary arteries as shown in figures 4.27(a) and 4.27(b), with the recognition that there is variability in the coronary artery blood supply to the different regions of the myocardium, especially for segment 17 which can be supplied by any of the three arteries.

Figure 4.28 shows bullseye plots of the average radial, circumferential, and longitudinal strains computed at end-systole for the 11 volunteers and figures 4.29, 4.30, and 4.31 show the variation of the radial, circumferential, and longitudinal strains with time for the volunteers. The horizontal axes in the strain-time plots have been rescaled to represent the percentage of the cardiac cycle from end-diastole to end-systole.

As can be seen from these plots the radial strain increases during systole over the entire myocardium reflecting the thickening of the myocardium in the radial direction. The radial strain is the greatest in the anterolateral region of the myocardium. The circumferential strain decreases during systole reflecting the shortening of the myocardium in the circumferential direction during systole. In addition the circumferential strain is also seen to increase slightly towards the apical region of the myocardium. Similar results have been reported by Moore *et al* [111], and Declerck *et al* [43]. There is larger variation in the computed longitudinal strain for the vol-

139

(a) Left ventricular segmentation

1	Basal anterior
2	Basal anteroseptal
3	Basal inferoseptal
4	Basal inferior
5	Basal inferoseptal
6	Basal anterolateral
7	Mid anterior
8	Mid anteroseptal
9	Mid inferoseptal
10	Mid inferior
11	Mid inferolateral
12	Mid anterolateral
13	Apical anterior
14	Apical septal
15	Apical inferior
16	Apical lateral
17	Apex

(b) Recommended names of segments

Figure 4.27: Bullseye plot showing the recommended names of the 17 myocardial segments in the LV and the assignment of the segments to the territories of the *left anterior descending* (LAD), *right coronary artery* (RCA), and the *left circumflex coronary artery* (LCX). Adapted from figures 4 and 5 of [23].
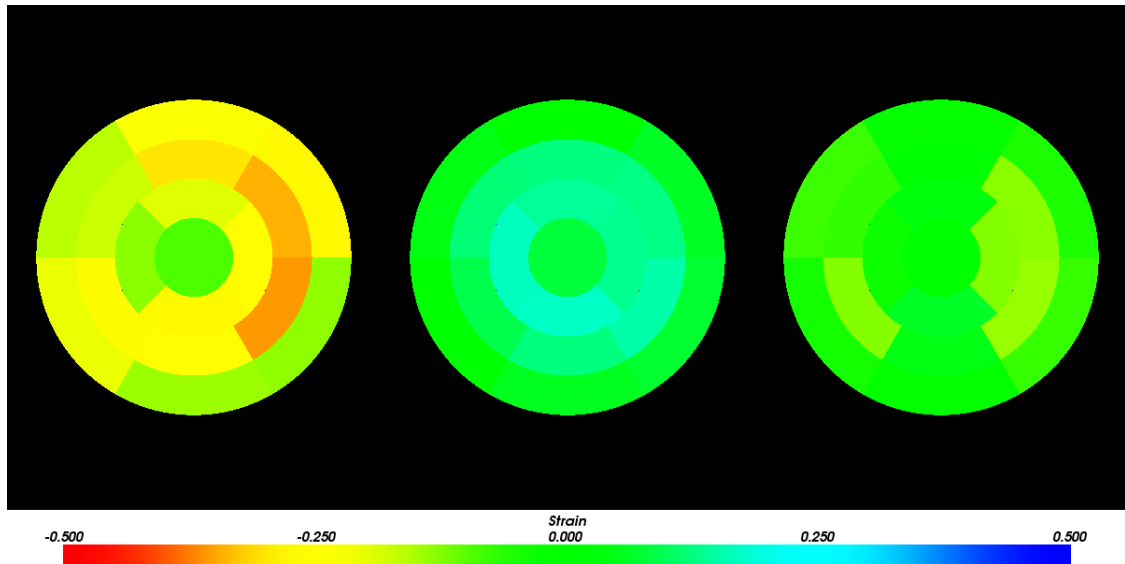
Figure 4.28: This figure (from left to right) shows bullseye plots of the average radial, circumferential, and longitudinal strains in the myocardium computed at end-systole for the 11 normal volunteers.

unteer subjects. In some regions of the heart the strain decreases during systole (for example the mid inferior and apical inferior regions of the LV), while in other regions there is no clear discernible pattern in the strain variation (for example the lateral regions of the heart). The longitudinal strain is the most difficult parameter to estimate because of the relatively small number of LA slices acquired in comparison with the number of SA slices acquired.

4.3 Summary

In this chapter we have presented a novel method for tracking the motion of the myocardium in the LV using nonrigid image registration. An existing nonrigid registration algorithm (Rueckert *et al* [142]) was used as the basis for the method presented in this chapter. To extract the 4D motion field in the myocardium from the multiple sets of SA and LA images acquired during the cardiac cycle, the SA and LA images taken during systole were registered to the corresponding segmented images taken at end-diastole. To achieve this registration the similarity measure used in [142] (and hence the interpolation procedure) was modified to use the weighted

(a) Basal Septal   (b) Basal Anterior   (c) Basal Lateral   (d) Basal Inferior

(e) Mid Septal   (f) Mid Anterior   (g) Mid Lateral   (h) Mid Inferior

(i) Apical Septal   (j) Apical Anterior   (k) Apical Lateral   (l) Apical Inferior
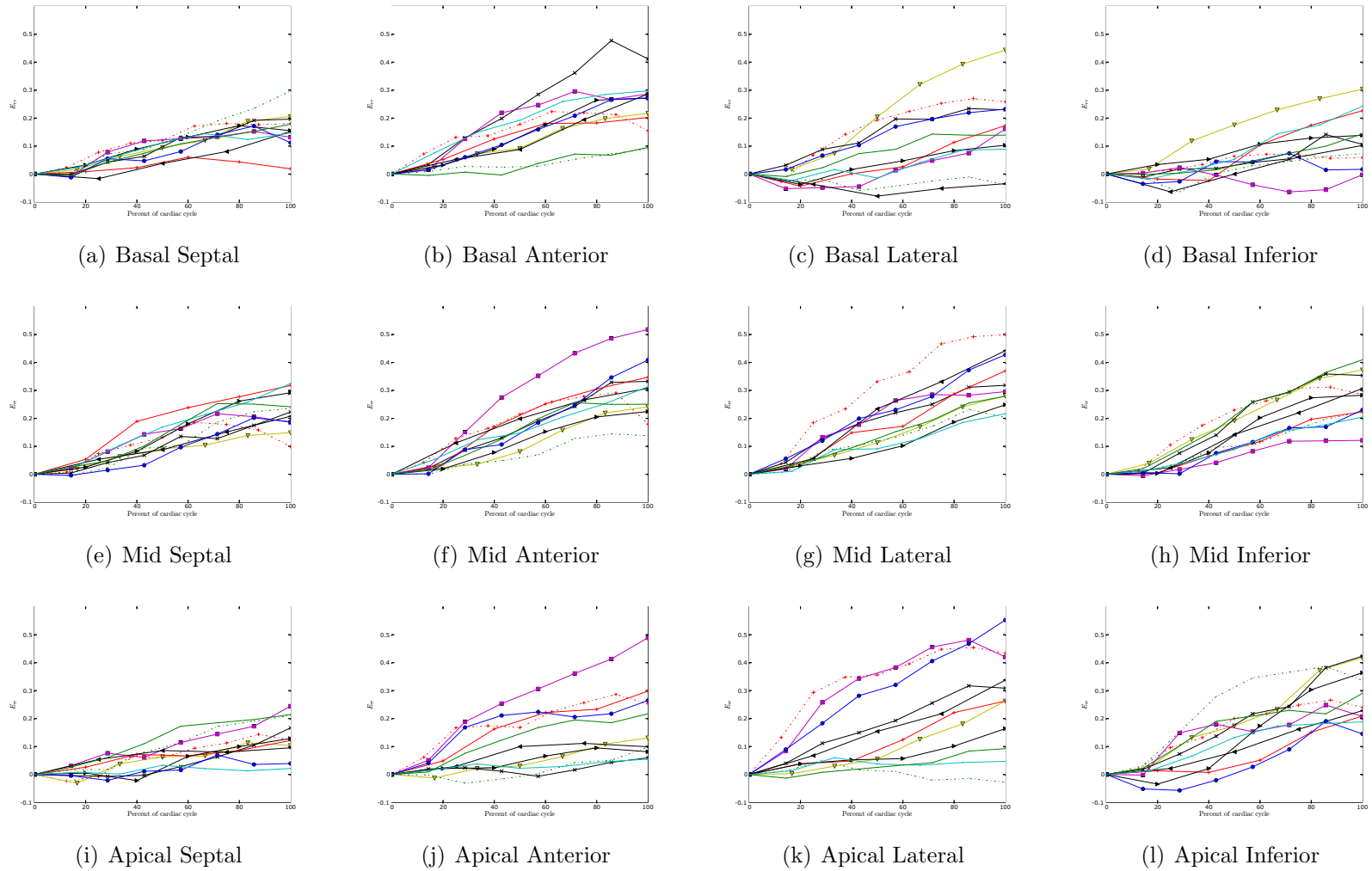
Figure 4.29: This figure shows plots of the radial strain in the different regions of the heart computed from the free-form deformations obtained from the registration algorithm for the 11 volunteers.

(a) Basal Septal   (b) Basal Anterior   (c) Basal Lateral   (d) Basal Inferior

(e) Mid Septal   (f) Mid Anterior   (g) Mid Lateral   (h) Mid Inferior

(i) Apical Septal   (j) Apical Anterior   (k) Apical Lateral   (l) Apical Inferior
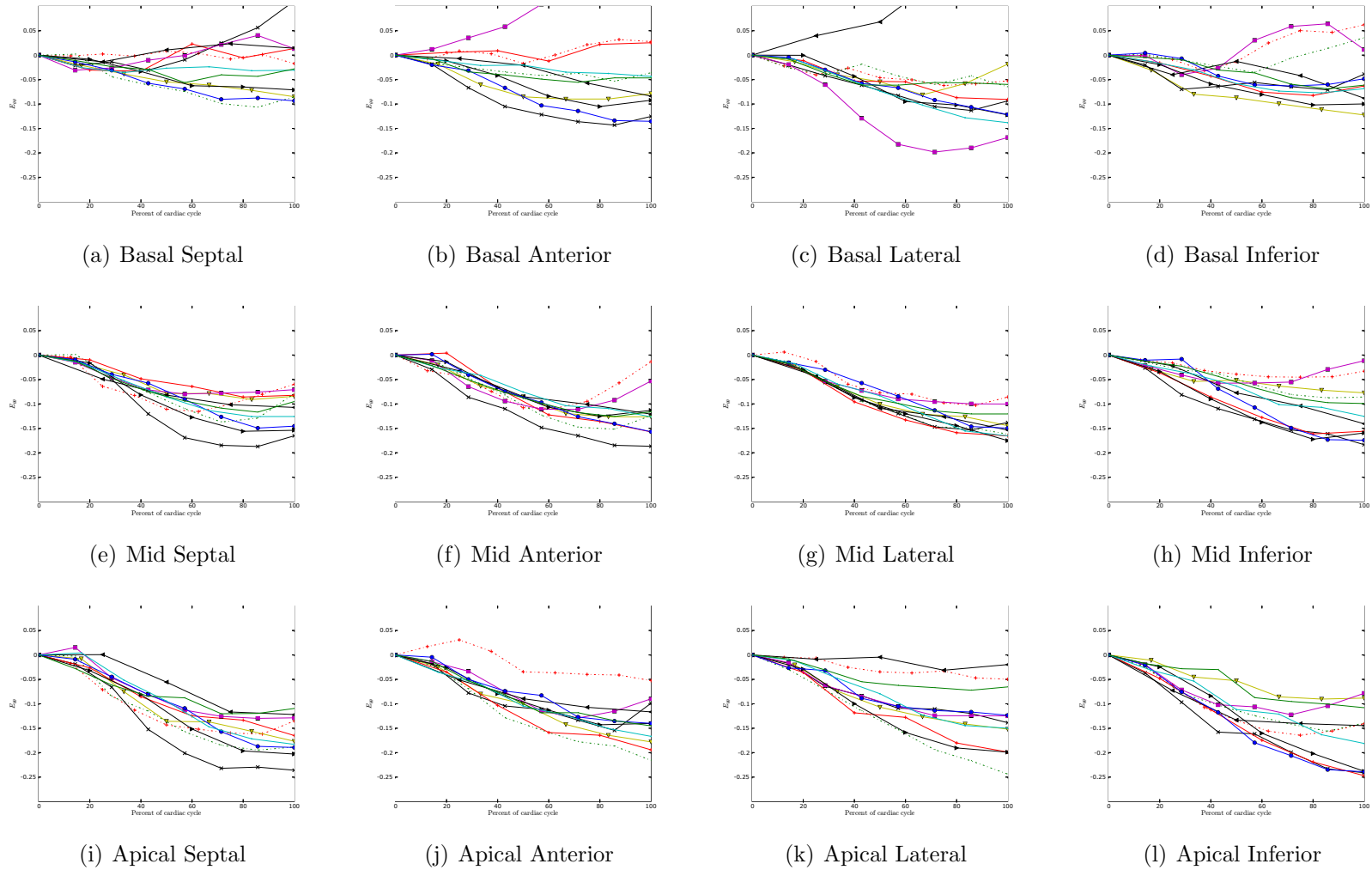
Figure 4.30: This figure shows plots of the circumferential strain in the different regions of the heart computed from the free-form deformations obtained from the registration algorithm for the 11 volunteers.

(a) Basal Septal   (b) Basal Anterior   (c) Basal Lateral   (d) Basal Inferior

(e) Mid Septal   (f) Mid Anterior   (g) Mid Lateral   (h) Mid Inferior

(i) Apical Septal   (j) Apical Anterior   (k) Apical Lateral   (l) Apical Inferior
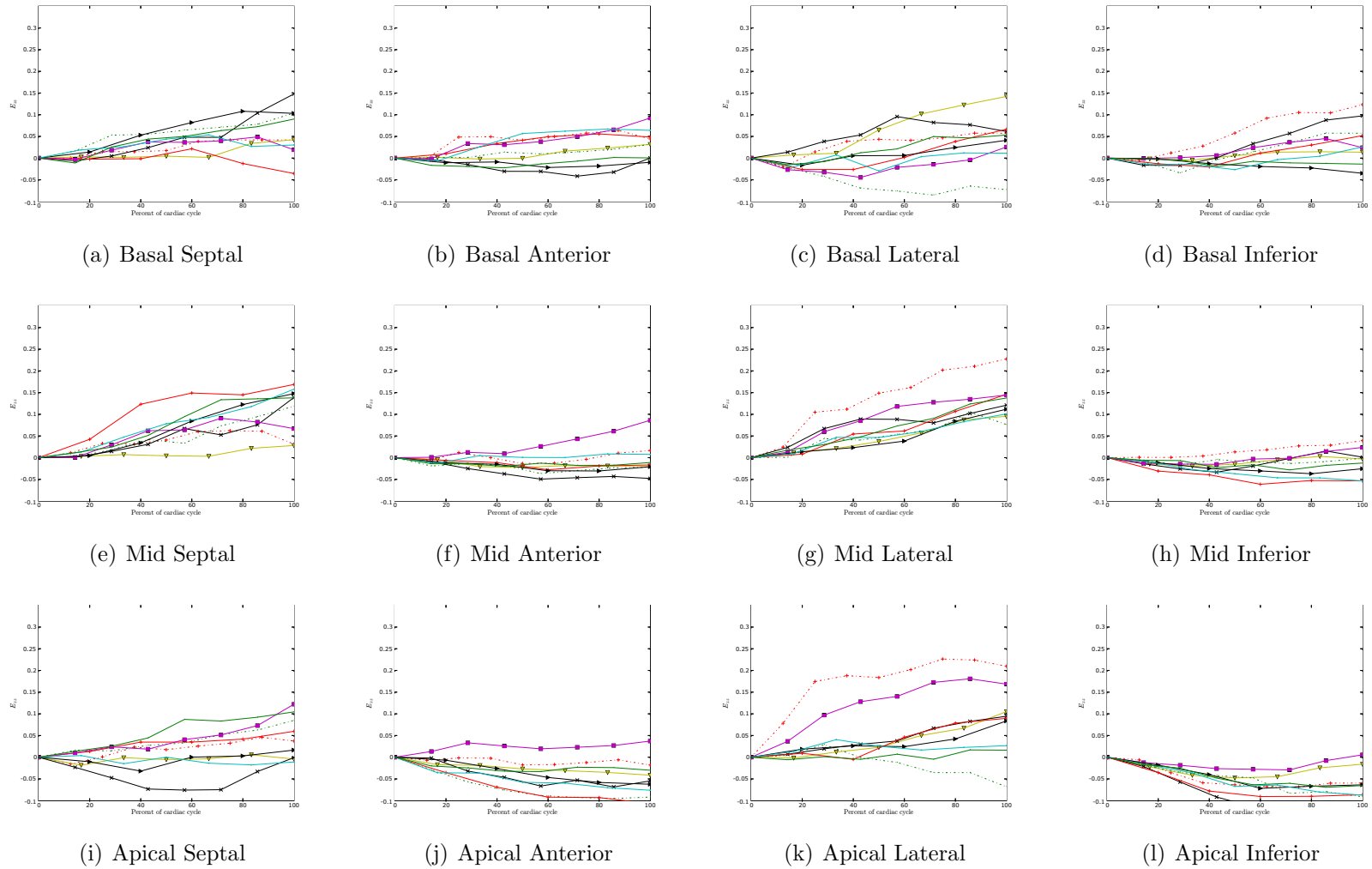
Figure 4.31: This figure shows plots of the longitudinal strain in the different regions of the heart computed from the free-form deformations obtained from the registration algorithm for the 11 volunteers.

sum of the NMI of the SA and LA images being registered. The modified similarity metric was maximized using a gradient ascent algorithm to simultaneously register the SA and LA images and extract the deformation field in the myocardium.

We evaluated our method using a cardiac motion simulator and found that the motion and strain fields computed using image registraton were very similar to the true motion and strain fields generated by the simulator. We also reconstructed the deformation field within the myocardium for 11 volunteers and showed that the RMS tracking error was below 2 mm for most parts of the cardiac cycle between end-diastole and end-systole.

The main advantage of the method proposed in this chapter, compared to the other methods available, is that tag localization and deformation field reconstruction are performed simultaneously. Thus, clinically relevant contractility parameters like circumferential or radial strain in the myocardium can be calculated directly from the transformation $\mathbf{T}(\mathbf{x}, t)$ obtained from the nonrigid registration algorithm. Another advantage is the fact that we have made no assumptions regarding the nature of the tag pattern in the acquired images; the presented algorithm will be able to cope with parallel, radial or grid tag patterns.

Although we have shown that image registration is a viable technique for cardiac motion tracking using tagged MR images, the transformation model used in the algorithm does not take into account the expected motion of the heart, namely the radial thickening, circumferential contraction, and the longitudinal contraction. In the following chapter we investigate the use of a cylindrical free-form deformation to reconstruct the deformation field in the myocardium of the LV. This is expected to improve the accuracy of the deformation field reconstruction.

Chapter 5

Analysis of Myocardial Motion and Strain Patterns Using a Cylindrical B-Spline Transformation Model

In the previous chapter we presented a method for the reconstruction of the motion field in the myocardium of the LV using a nonrigid image registration algorithm based on *free-form deformations* (FFDs). Although the results presented proved that the deformation field reconstructed was accurate enough for clinically useful parameters such as strains to be derived, the FFD model used was a generic transformation model and incorporated no prior information about the expected types of motion of the myocardium of the LV.

In this chapter we present a novel method for tracking the motion of the myocardium in tagged MR images of the heart using a nonrigid registration algorithm based on *cylindrical free-form deformations* (CFFDs) and the optimization of a cost function based on NMI. Our key idea is that the CFFDs models more closely the geometry and motion of the LV than the FFDs in Cartesian coordinates. In particular the displacement vectors at each control point defining the CFFDs are

described in terms of unit basis vectors, $\widehat{\mathbf{e}}_r$, $\widehat{\mathbf{e}}_\theta$, and $\widehat{\mathbf{e}}_z$, which are aligned with the radial, circumferential, and longitudinal directions respectively, and enable the radial thickening, circumferential contraction, and longitudinal contraction of the LV to be described in a more natural way.

This chapter is organized as follows. Section 5.1 presents a brief review of the coordinate systems used in describing the deformation of the LV. In section 5.2 the CFFDs are defined and our motion tracking algorithm is described. As in chapter 4, validation of our method has been performed by using a cardiac motion simulator [171] and tagged MR data acquired from a group of normal volunteers. These results are presented in section 5.3. Finally, in section 5.4, we summarize our work. The work presented in this chapter has been published in [28] and [27]

5.1 Coordinate Systems used in Cardiac Deformation Modelling

The primary reason for choosing a coordinate system different from a Cartesian coordinate system in describing the motion of the LV is to simplify the description of its shape and motion. In addition, choosing a coordinate system more closely related to the shape of the LV sometimes simplifies the decomposition of the motion into its radial, circumferential, and longitudinal parts, thus allowing the results of the deformation field reconstruction to be interpreted more easily. In the following three subsections we describe three commonly used coordinate systems to model the deformation of the LV beginning with the prolate spheroidal coordinate system.
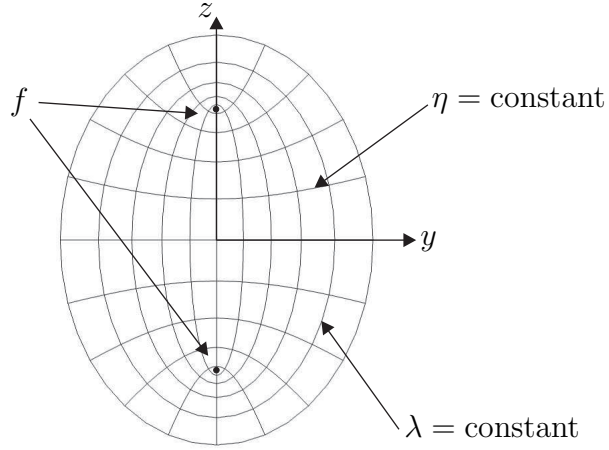
Figure 5.1: The prolate spheroidal coordinate system (the x-axis is not shown but is perpendicular to the page and points upwards). The focal points f are located at $[0, 0, -1]^T$ and $[0, 0, 1]^T$. The surfaces of constant λ and η resemble closely the surface shape of the LV.

5.1.1 Prolate Spheroidal Coordinate System

A point, (λ, η, ϕ), in the prolate spheroidal coordinate system (figure 5.1) has the following Cartesian coordinates

$$x = \delta \sinh \lambda \sin \eta \cos \phi \qquad (5.1)$$

$$y = \delta \sinh \lambda \sin \eta \sin \phi \qquad (5.2)$$

$$z = \delta \cosh \lambda \cos \eta \qquad (5.3)$$

where δ is a fixed parameter called the focal radius and is the distance from the origin to either focal point of the prolate sphere. As can be seen in figure 5.1 the surfaces of constant λ and η resemble the endocardial and epicardial surfaces of the LV enabling the shape of the LV to be described easily. The compact representation of the shape of the LV that can be obtained in the prolate spheroidal coordinate system has been utilized for building finite element models of the LV (Young *et al* [180, 179]). A problem which must often be dealt with when building such models is finding the optimal values of the LV surface radii and focal radius so that the the focal points

148

of the coordinate system do not lie too close to the apex of the LV as quantities of interest such as deformation parameters cannot be defined at these points. Prolate spheroidal coordinates have also been used for displacement field fitting by O'Dell *et al* [113].

5.1.2   Planispheric Coordinate System

The planispheric coordinate system has properties of both the cylindrical and spherical coordinate systems (Declerck *et al* [45, 43]). It is defined as shown in figure 5.2. Two points are chosen, $\mathbf{x}_C$ and $\mathbf{x}_B$, $\mathbf{x}_C$ being the center of the LV cavity and $\mathbf{x}_B$ the center of the base of the LV. For each point $\mathbf{x} = [x, y, z]^T$ a center point $\mathbf{x}_H$ is defined on the line segment joining $\mathbf{x}_C$ and $\mathbf{x}_B$ such that

$$\mathbf{x}_H - \mathbf{x}_C = (1 - \cos\theta)(\mathbf{x}_B - \mathbf{x}_C) \tag{5.4}$$

$\mathbf{x}_H$ and hence θ are found numerically using the Newton-Raphson method. The point $\mathbf{x}_H$ is chosen as the center of a spherical polar coordinate system and the spherical polar coordinates (r, θ, ϕ) of the point $\mathbf{x}$ are found. The planispheric coordinates (X, Y, R) are then given by

$$X = \frac{\theta}{\pi}\cos\phi \tag{5.5}$$
$$Y = \frac{\theta}{\pi}\sin\phi \tag{5.6}$$
$$R = \frac{r}{\sigma_r} \tag{5.7}$$

where σ_r is a normalization constant.

Declerck *et al* [45] defined a 4D transformation in this coordinate system to
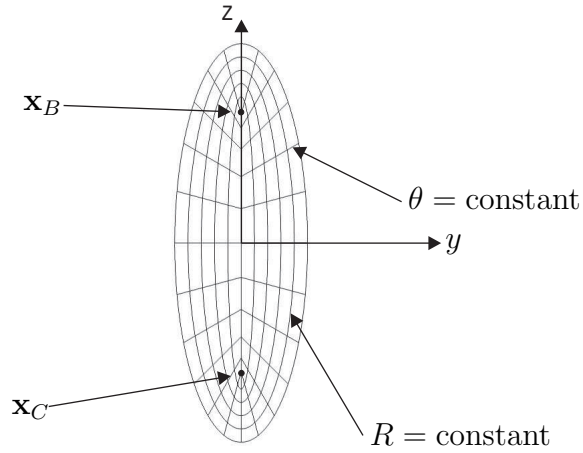
Figure 5.2: The planispheric coordinate system (the x-axis is not shown but is perpendicular to the page and points upwards). The center is located at $\mathbf{x}_C = [0, 0, -1]^T$ and the base is located at $\mathbf{x}_B = [0, 0, 1]^T$.

describe the motion of the LV using a system of linear equations

$$X' = a_0 X - a_1 Y + a_2 \tag{5.8}$$

$$Y' = a_1 X + a_0 Y + a_3 \tag{5.9}$$

$$R' = a_4 R + a_5 \tag{5.10}$$

where the a_i are continuous and differentiable functions of r, θ, ϕ, and t. In the above equations X' and Y' are transformed by a similarity transformation (a similarity transformation is a combination of rotation, uniform scaling, and translation components), and R' is related to R by an affine transformation. The main advantage of the planispheric transformation is the reduced number of parameters needed to define it enabling the motion of the LV to be decomposed into its radial, circumferential, and longitudinal components easily.

5.1.3 Cylindrical Coordinate System

A point (r, θ, z) in a cylindrical coordinate system has the following x- and y-coordinates in a Cartesian coordinate system (the z-coordinate remains unchanged)

$$x \;\; = \;\; r\cos\theta \tag{5.11}$$

$$y \;\; = \;\; r\sin\theta \tag{5.12}$$

Recently Deng and Denney [49] have used a cylindrical B-spline transformation model to compute the strain in the myocardium of the LV using tagged MR images. The difference between the approach presented in [49] and the one presented in this chapter is that Deng and Denney assume that the tag lines have been identified in each image in the sequence being analyzed by one of several previously published techniques [6, 65, 180]. So the cylindrical B-spline motion model is not used directly to estimate the motion of the myocardium during the cardiac cycle.

Of the three coordinate systems the planispheric and prolate-spheroidal coordinate systems most closely resemble the shape of the LV. We have chosen to investigate free-form deformations defined in a cylindrical coordinate system mainly because of the simplicity of their definition in this coordinate system. However, it must be stated that transformations defined using a prolate-spheroidal coordinate system or a planispheric coordinate system may also help to improve the accuracy of motion tracking using image registration.

5.2 Registration of Tagged MR Images

The technique presented in this chapter is a fully automated one that uses nonrigid image registration combined with a cylindrical free-form deformation (FFD) model to extract the motion field within the myocardium from tagged MR images. As in chapter 4, we take account of through-plane motion of the myocardium by using both short-axis (SA) and long-axis (LA) images of the LV to recover the complete

3D motion of the myocardium over time. The transformations obtained can be used to directly calculate various clinically relevant parameters like strain.

5.2.1   Definition of Cylindrical Free-Form Deformations

We define the transformation $\mathbf{T}(\mathbf{x}, t)$ which maps points in the myocardium at time $t = 0$ to their corresponding positions at time $n\tau$ using a series of cylindrical free-form deformations as described below. A cylindrical free-form deformation (CFFD) is defined on a domain Ω

$$\Omega = \{(r', \theta', z') : R'_{\min} \leq r' < R'_{\max}, 0 \leq \theta' < 2\pi, Z'_{\min} \leq z' < Z'_{\max}\} \tag{5.13}$$

corresponding to the volume of interest by a mesh of control points $(n_{r'} + 1) \times (n_{\theta'} + 1) \times (n_{z'} + 1)$, where $n_{r'} + 1$ is the number of control points in the radial direction, $n_{\theta'} + 1$ is the number of control points in the circumferential direction, and $n_{z'} + 1$ is the number of control points in the longitudinal direction. The cylindrical control point grid is aligned with the left ventricle by calculating the center of mass of the myocardium in the apical and basal short-axis image slices; the line joining the apex to the base then defines the LA of the left ventricle. A shearing and translation transformation, $\mathbf{S}$, is calculated which aligns this axis with the axis of the cylindrical control point grid. Thus, each $r'\theta'$-plane in the cylindrical coordinate system is aligned with a short-axis image plane. The shearing and translation transformation is given by the homogeneous transformation matrix

$$\mathbf{S} = \begin{bmatrix} 1 & 0 & -\frac{a_x - b_x}{a_z - b_z} & \frac{a_x b_z - a_z b_x}{a_z - b_z} \\ 0 & 1 & -\frac{a_y - b_y}{a_z - b_z} & \frac{a_y b_z - a_z b_y}{a_z - b_z} \\ 0 & 0 & 1 & -a_z \\ 0 & 0 & 0 & 1 \end{bmatrix} \tag{5.14}$$

where $\mathbf{a} = [a_x, a_y, a_z]^T$, and $\mathbf{b} = [b_x, b_y, b_z]^T$ represent the positions of the apex and the base of the left ventricle respectively. We calculate the coordinates of a

point, $\mathbf{x} = [x, y, z]^T$, in the myocardium in the cylindrical coordinate system by first multiplying $[x, y, z, 1]^T$ by $\mathbf{S}$ to obtain

$$
\begin{bmatrix} x' \\ y' \\ z' \\ 1 \end{bmatrix} = \mathbf{S} \begin{bmatrix} x \\ y \\ z \\ 1 \end{bmatrix}
\tag{5.15}
$$

and then converting to cylindrical polar coordinates (the z'-coordinate remains unchanged)

$$
r' = \sqrt{x'^2 + y'^2}
\tag{5.16}
$$

$$
\theta' = \arctan2(y', x')
\tag{5.17}
$$

where $\arctan2(y', x')$ is the standard C++ math library function that calculates the arctangent of y'/x', taking into account the quadrant that θ lies in, which depends on the signs of x' and y'.

The position that a point in the myocardium moves to at time $t = n\tau$ is

$$
\mathbf{T}(\mathbf{x}, n\tau) = \mathbf{x} + \sum_{h=1}^{n} \mathbf{u}^h(\mathbf{Sx})
\tag{5.18}
$$

where $\mathbf{u}^h(\mathbf{Sx} = \mathbf{x}' = [x', y', z']^T)$ is defined by a CFFD

$$
\mathbf{u}^h(\mathbf{x}') = \sum_{i=0}^{n_{r'}} \sum_{j=0}^{n_{\theta'}} \sum_{k=0}^{n_{z'}} \beta^3 \left(\frac{r' - r'_{i,j,k}}{\delta_{r'}} \right) \beta^3 \left(f_{\theta'}(\theta', \theta'_{i,j,k}, \delta_{\theta'}) \right) \beta^3 \left(\frac{z' - z'_{i,j,k}}{\delta_{z'}} \right) \phi'_{i,j,k}
\tag{5.19}
$$

Here $\phi'_{i,j,k}$ is the control point displacement vector at position $[r'_{i,j,k}, \theta'_{i,j,k}, z'_{i,j,k}]$ (in cylindrical coordinates) and $\delta_{r'}$, $\delta_{\theta'}$, and $\delta_{z'}$ are the control point spacings in the r'-, θ'-, and z'-direction respectively. $f_{\theta'}(\theta', \theta'_{i,j,k}, \delta_{\theta'})$ is a function which measures the relative angular distance between θ' and $\theta'_{i,j,k}$ and whose range is restricted to be in the interval [-2, 2). The coordinate systems involved and the relationship between
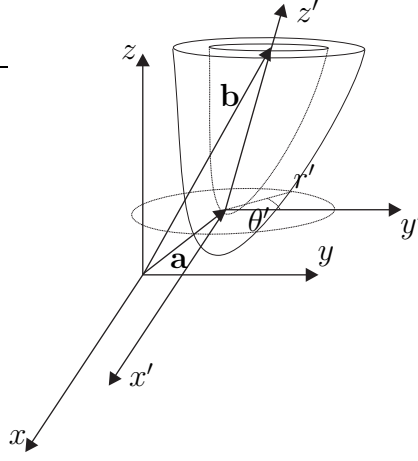
Figure 5.3: The three coordinate systems involved in computing the deformation of the myocardium using cylindrical free-form deformations. The xyz-coordinates system is the global coordinate system and is the coordinate system of the MR images. The $x'y'z'$ coordinate system is defined with respect to the line that joins the apex to the base of the LV. And the $r'\theta'z'$ coordinate system is defined with respect to the axes of the $x'y'z'$ coordinate system.

them are shown in figure 5.3 and an example of a CFFD control point grid aligned with the LA of the LV is shown in figure 5.4.

The strain can be obtained by first computing the Jacobian matrix of the deformation described by the cylindrical free-form deformations and using equation 4.20. Expressing the displacement of a point $\mathbf{x}'$ at time $t = n\tau$

$$\mathbf{u}(\mathbf{x}', n\tau) = \mathbf{T}(\mathbf{x}', n\tau) - \mathbf{x}' \tag{5.20}$$

in terms of its x'-, y'-, and z'-components we obtain

$$
\begin{aligned}
u_{x'}(\mathbf{x}', n\tau) &= \sum_{h=1}^{n} u_{x'}^{h}(\mathbf{x}') \\
&= \sum_{h=1}^{n} \sum_{i=0}^{n_{r'}} \sum_{j=0}^{n_{\theta'}} \sum_{k=0}^{n_{z'}} \beta^3 \left(\frac{r' - r'_{i,j,k}}{\delta_{r'}} \right) \beta^3 \left(f_{\theta'}(\theta', \theta'_{i,j,k}, \delta_{\theta'}) \right) \beta^3 \left(\frac{z' - z'_{i,j,k}}{\delta_{z'}} \right) \times \\
&\quad (\mu_{i,j,k}^{h} \widehat{\mathbf{e}}_{r'}.\widehat{\mathbf{e}}_{x'} + \nu_{i,j,k}^{h} \widehat{\mathbf{e}}_{\theta'}.\widehat{\mathbf{e}}_{x'} + \xi_{i,j,k}^{h} \widehat{\mathbf{e}}_{z'}.\widehat{\mathbf{e}}_{x'})
\end{aligned} \tag{5.21}
$$
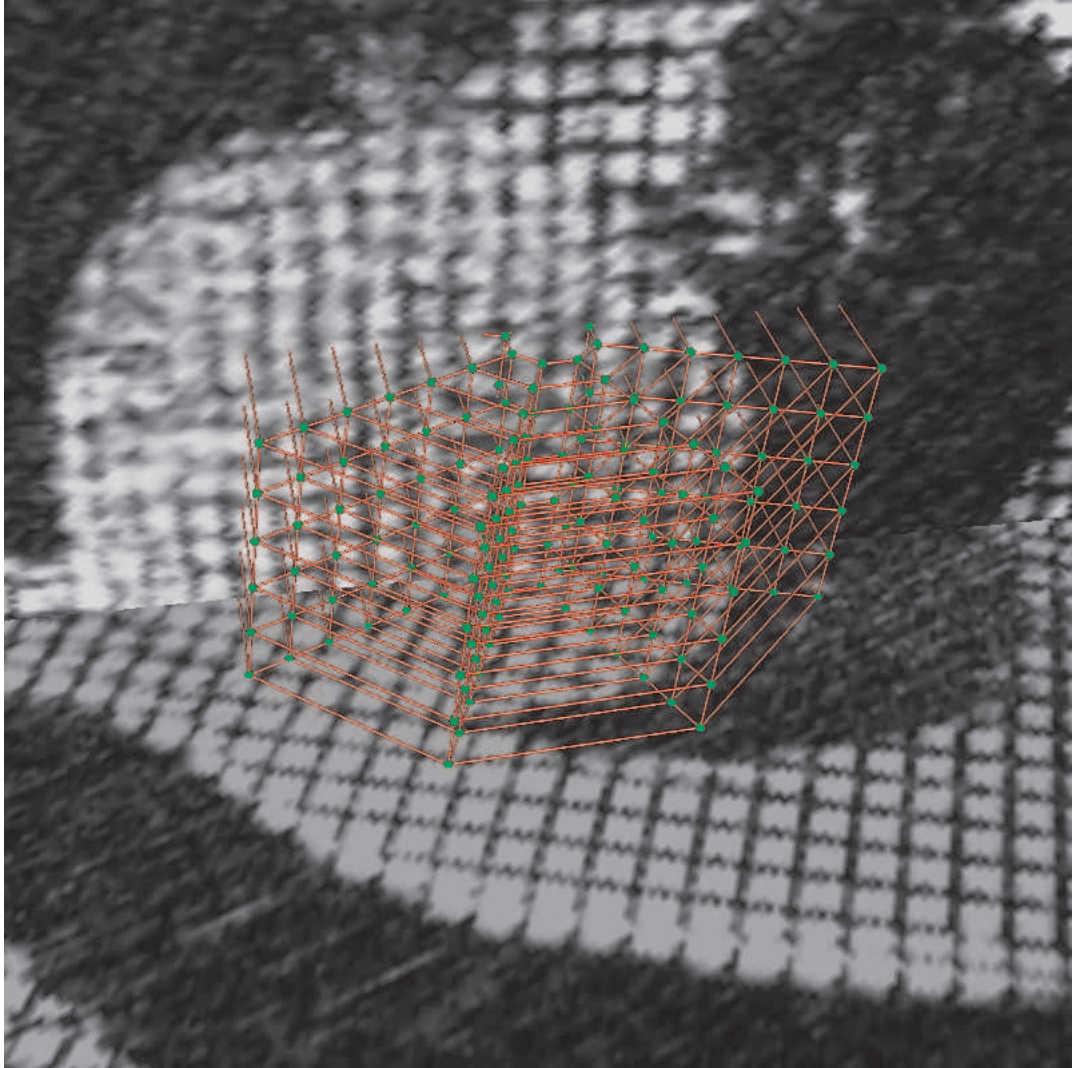
Figure 5.4: This figures shows the control point grid of a CFFD aligned with the LA of the LV.

$$u_{y'}(\mathbf{x}', n\tau) = \sum_{h=1}^{n} u_{y'}^{h}(\mathbf{x}')$$

$$= \sum_{h=1}^{n} \sum_{i=0}^{n_{r'}} \sum_{j=0}^{n_{\theta'}} \sum_{k=0}^{n_{z'}} \beta^3 \left(\frac{r' - r'_{i,j,k}}{\delta_{r'}} \right) \beta^3 \left(f_{\theta'}(\theta', \theta'_{i,j,k}, \delta_{\theta'}) \right) \beta^3 \left(\frac{z' - z'_{i,j,k}}{\delta_{z'}} \right) \times$$

$$(\mu_{i,j,k}^{h} \widehat{\mathbf{e}}_{r'}.\widehat{\mathbf{e}}_{y'} + \nu_{i,j,k}^{h} \widehat{\mathbf{e}}_{\theta'}.\widehat{\mathbf{e}}_{y'} + \xi_{i,j,k}^{h} \widehat{\mathbf{e}}_{z'}.\widehat{\mathbf{e}}_{y'}) \tag{5.22}$$

$$u_{z'}(\mathbf{x}', n\tau) = \sum_{h=1}^{n} u_{z'}^{h}(\mathbf{x}')$$

$$= \sum_{h=1}^{n} \sum_{i=0}^{n_{r'}} \sum_{j=0}^{n_{\theta'}} \sum_{k=0}^{n_{z'}} \beta^3 \left(\frac{r' - r'_{i,j,k}}{\delta_{r'}} \right) \beta^3 \left(f_{\theta'}(\theta', \theta'_{i,j,k}, \delta_{\theta'}) \right) \beta^3 \left(\frac{z' - z'_{i,j,k}}{\delta_{z'}} \right) \times$$

$$(\mu_{i,j,k}^{h} \widehat{\mathbf{e}}_{r'}.\widehat{\mathbf{e}}_{z'} + \nu_{i,j,k}^{h} \widehat{\mathbf{e}}_{\theta'}.\widehat{\mathbf{e}}_{z'} + \xi_{i,j,k}^{h} \widehat{\mathbf{e}}_{z'}.\widehat{\mathbf{e}}_{z'}) \tag{5.23}$$

where $\mu_{i,j,k}^{h}$, $\nu_{i,j,k}^{h}$, and $\xi_{i,j,k}^{h}$ are the components of the control point displacement vectors in the r'-, θ'-, and z'-directions respectively, $\widehat{\mathbf{e}}_{r'}$, $\widehat{\mathbf{e}}_{\theta'}$, $\widehat{\mathbf{e}}_{z'}$ are unit vectors in the r'-, θ'-, and z'-directions respectively, and $\widehat{\mathbf{e}}_{x'}$, $\widehat{\mathbf{e}}_{y'}$, and $\widehat{\mathbf{e}}_{z'}$ are unit-vectors in the x'-, y'-, and z'-directions respectively.

The components of the Jacobian matrix, $\mathbf{J}'(\mathbf{x}', n\tau)$, of the deformation field (in the $x'y'z'$ coordinate system) can then be found by using the chain rule for differentiation. For example

$$\frac{\partial u_{x'}(\mathbf{x}', n\tau)}{\partial y'} = \sum_{h=1}^{n} \sum_{i=0}^{n_{r'}} \sum_{j=0}^{n_{\theta'}} \sum_{k=0}^{n_{z'}} \left[\frac{d\beta^3}{du} \frac{du}{dy'} \beta^3 \left(f_{\theta'}(\theta', \theta'_{i,j,k}, \delta_{\theta'}) \right) + \right.$$

$$\left. \beta^3 \left(\frac{r' - r'_{i,j,k}}{\delta_{r'}} \right) \frac{d\beta^3}{df_{\theta'}} \frac{df_{\theta'}}{dy'} \right] \beta^3 \left(\frac{z' - z'_{i,j,k}}{\delta_{z'}} \right) (\mu_{i,j,k}^{h} \widehat{\mathbf{e}}_{r'}.\widehat{\mathbf{e}}_{x'} + \nu_{i,j,k}^{h} \widehat{\mathbf{e}}_{\theta'}.\widehat{\mathbf{e}}_{x'} + \xi_{i,j,k}^{h} \widehat{\mathbf{e}}_{z'}.\widehat{\mathbf{e}}_{x'})$$

where

$$u = \frac{r' - r'_{i,j,k}}{\delta_{r'}} \tag{5.24}$$

and the first derivative of β^3 is given in equation 4.25. Using equations 5.16 and 5.17 we obtain

$$\frac{\partial u_{x'}(\mathbf{x}', n\tau)}{\partial y'} = \sum_{h=1}^{n} \sum_{i=0}^{n_{r'}} \sum_{j=0}^{n_{\theta'}} \sum_{k=0}^{n_{z'}} \left[\frac{1}{\delta_{r'}} \frac{d\beta^3}{du} \frac{y}{r'} \beta^3 \left(f_{\theta'}(\theta', \theta'_{i,j,k}, \delta_{\theta'}) \right) + \right.$$

$$\left. \frac{1}{\delta_{\theta'}} \beta^3 \left(\frac{r' - r'_{i,j,k}}{\delta_{r'}} \right) \frac{d\beta^3}{df_{\theta'}} \frac{x'}{r'^2} \right] \beta^3 \left(\frac{z' - z'_{i,j,k}}{\delta_{z'}} \right) (\mu_{i,j,k}^{h} \widehat{\mathbf{e}}_{r'}.\widehat{\mathbf{e}}_{x'} + \nu_{i,j,k}^{h} \widehat{\mathbf{e}}_{\theta'}.\widehat{\mathbf{e}}_{x'} + \xi_{i,j,k}^{h} \widehat{\mathbf{e}}_{z'}.\widehat{\mathbf{e}}_{x'})$$

The other components of the Jacobian matrix of the deformation field can be computed in a similar way. The Jacobian matrix of the deformation field in the xyz-coordinate system is then

$$\mathbf{J}(\mathbf{x}, n\tau) = \mathbf{J}'(\mathbf{x}', n\tau)\mathbf{S}[1, 2, 3; 1, 2, 3] \tag{5.25}$$

where $\mathbf{S}[1, 2, 3; 1, 2, 3]$ is the sub-matrix formed from the first three rows and columns of the matrix in equation 5.14.

5.2.2 Combined Nonrigid Registration of SA and LA Images

The estimation of the deformation field $\mathbf{T}(\mathbf{x}, t)$ proceeds in a similar way to that given in section 4.1.1. Since we are only interested in recovering the motion field within the myocardium we use segmented images of the myocardium at end-diastole as the images to register to. We also set the control point displacement vectors which cannot affect the motion field in the myocardium to be passive and do not consider them during the optimization process as shown in figure 5.5. This not only allows us to produce more accurate results but also to do the registration more quickly. The motion field reconstruction is achieved as shown in figure 4.6 by registering the volume images taken during the cardiac cycle to the segmented volume images taken at end-diastole.

5.3 Results

5.3.1 Cardiac Motion Simulator Data

In this subsection we present validation results using cardiac motion simulator data. In the following subsection we will present results on data acquired from normal human volunteers. As in chapter 4 we conducted experiments on the nine sets of
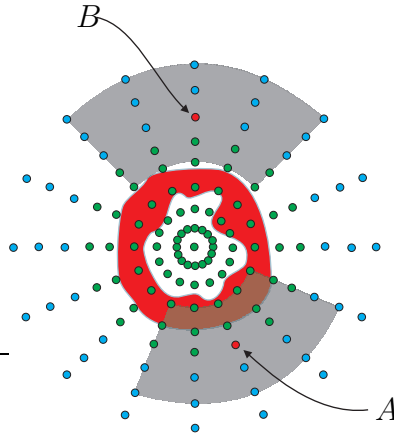
Figure 5.5: This figure shows a SA view of the heart segmented at end-diastole. Control points which cannot affect the deformation field in the myocardium are marked passive. For example point B is marked as passive while point A remains active.

images A_1–A_3, B_1–B_3, C_1–C_3. For each set of images the deformation of the myocardium was computed using the method presented in section 5.2. The relative errors, $\rho(t)$ (equation 4.18), and the RMS errors, $\delta(t)$ (equation 4.19), in the displacement vectors of points in the myocardium estimated from the transformation $\mathbf{T}(\mathbf{x}, t)$ was then computed. The relative errors in the computed displacement vectors are plotted in figures 5.6(a), 5.6(b), and 5.6(c), and the RMS errors in the computed displacement vectors are plotted in figures 5.7(a), 5.7(b), and 5.7(c).

As can be seen from a comparison of figures 4.10 and 5.6, and figures 4.11 and 5.7 the registration algorithm based on cylindrical free-form deformations has performed slightly worse than the algorithm based on Cartesian free-form deformations. This result clearly needs to be explained.

Figure 5.8 shows plots of the relative error in the computed displacement field for image set C_1 for the same SA slices as those shown in figure 4.17. As can be seen in the figure the relative errors are larger near the epicardium and the endocardium for both FFDs and CFFDs. This is to be expected as the deformation of the myocardium near the borders is more difficult to estimate than within the borders. But in the images on the right the CFFDs can be seen to have performed worse in the apical and basal slices than the FFDs but performed slightly better in
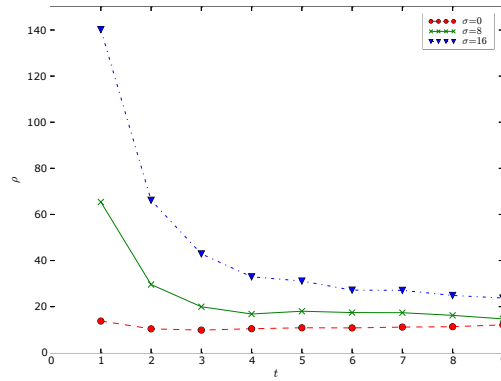
(a) Image set A
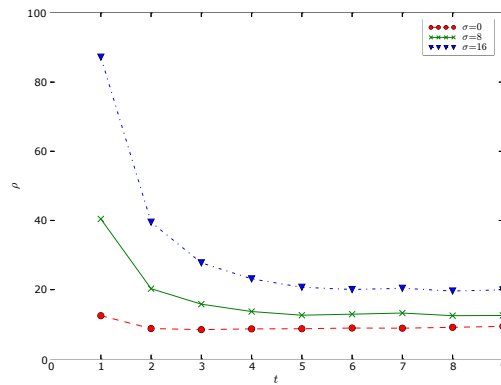
(b) Image set B
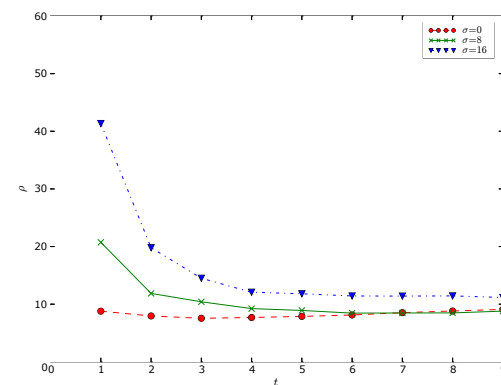
(c) Image set C

Figure 5.6: This figure shows the variation of the relative error in the estimated displacements for the three different types of motion generated from the LV simulator and for different amounts of Gaussian noise added to the images.
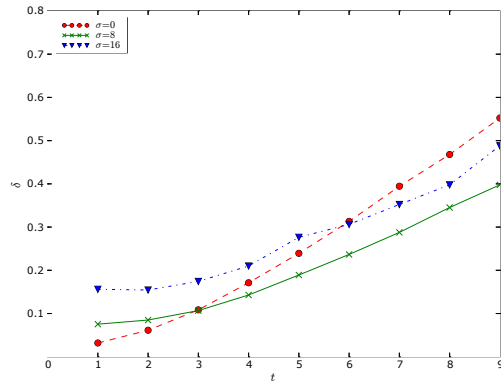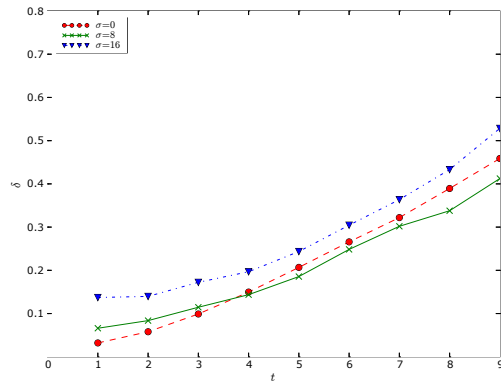
(a) Image set A
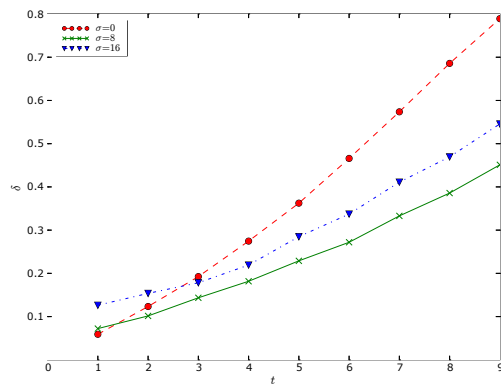
(b) Image set B

(c) Image set C

Figure 5.7: This figure shows the variation of the RMS error in the estimated displacements for the three different types of motion generated from the LV simulator and for different amounts of Gaussian noise added to the images.

the mid-ventricular slice than the FFDs, especially near the epicardium. This is due to the fact that the only the mid-ventricular part of the LV resembles a cylinder.

The canine simulator images were also used to test the performance of the cylindrical free-form registration algorithm in estimating strains. The derived radial, circumferential, and longitudinal strain maps corresponding to the ones shown in figure 4.14 are presented in figure 5.9, while the differences between the true and estimated strains are shown in figure 5.10. Tensor ellipsoid plots showing the principal strain directions are shown in figure 5.11. As can be seen from the figures the estimated strain maps, although similar to the true ones, are not as accurate as the ones estimated using Cartesian FFDs.

5.3.2 Human Data

We also used the data from section 4.2.2 to reconstruct the deformation fields in the hearts of a group of normal volunteers. For each of the volunteers the deformation field within the myocardium was calculated using the method presented in section 5.2 for all times between end-diastole and end-systole. The control point spacings in the radial, circumferential, and longitudinal directions were 8 mm, $\pi/4$, and 10 mm respectively. As in chapter 4, to test the performance of the method, tag-intersection points in four different imaging planes (basal SA slice, mid-ventricular SA slice, apical SA slice, and horizontal LA slice) were tracked manually by a human observer. The RMS error between the estimated and observed displacements of the tag-intersection points are given in figures 5.12(a), 5.12(b), 5.12(c), and 5.12(d) for apical SA, mid-ventricular SA, basal SA, and HLA slices respectively. Comparison of these figures with the corresponding ones for the FFD (figures 4.20(a), 4.20(b), 4.20(c), and 4.20(d) respectively) show that, again, the CFFDs have not performed as well as FFDs. However, comparing figures 4.20(b) and 5.12(b) shows that for 7 of the 11 volunteers the CFFDs performed better than the Cartesian FFDs in tracking the motion of the myocardium, for 1 volunteer the performance was the same, and
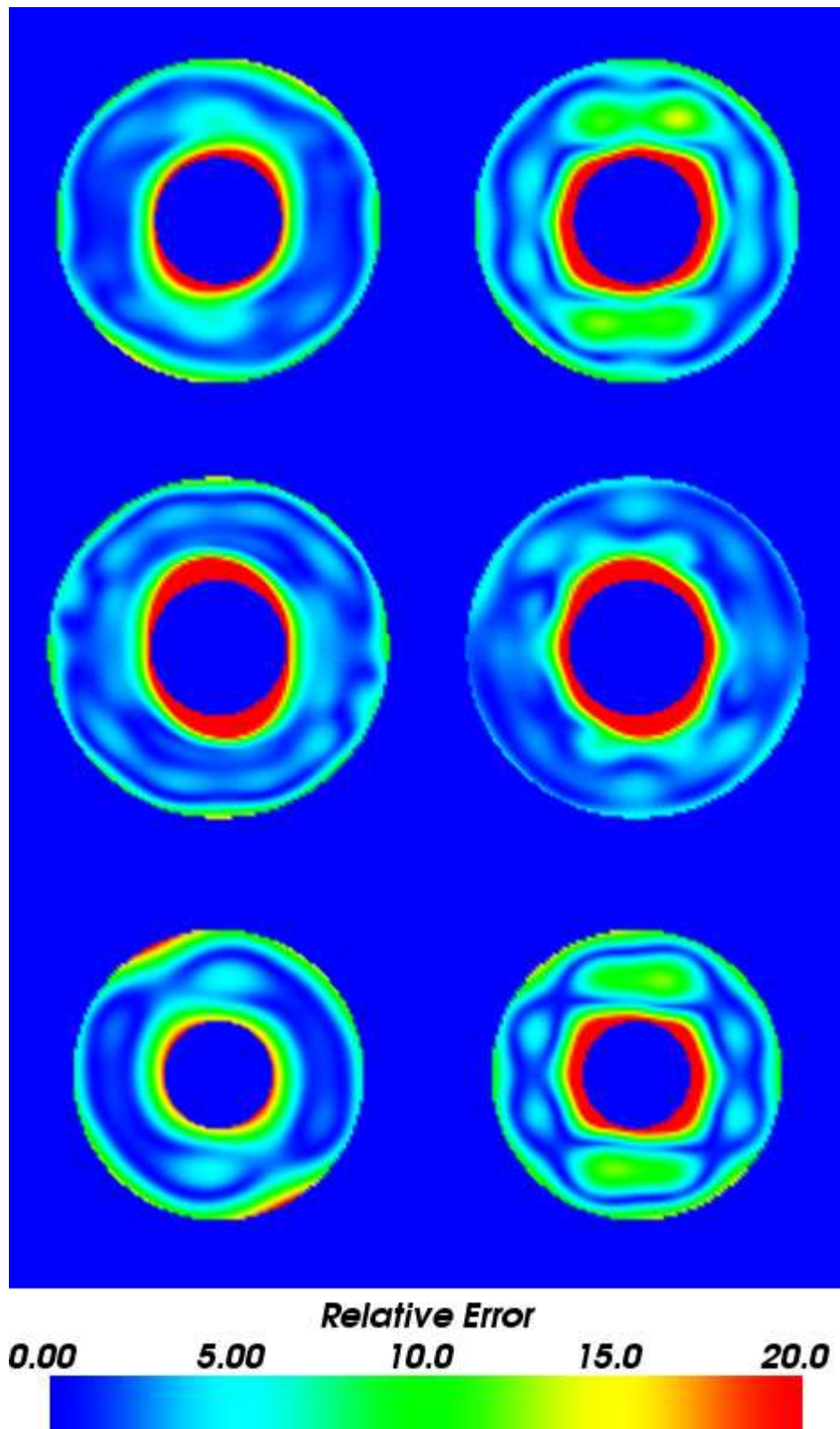
Figure 5.8: This figure shows a comparison of the relative errors in the displacements computed using FFDs (left) and CFFDs (right) for image set C_1. The positions of the SA slices shown here are the same as those in figure 4.17.
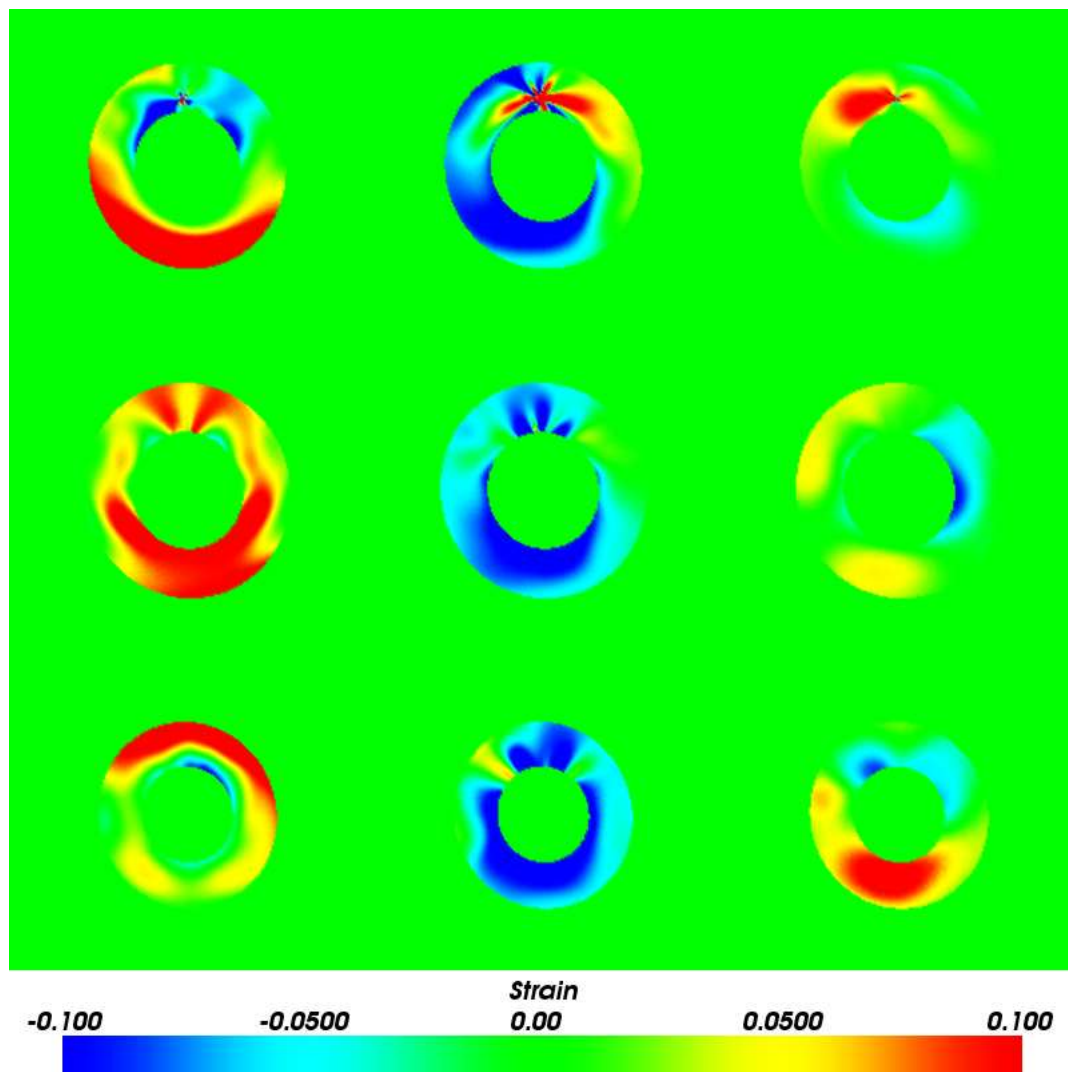
Figure 5.9: This figure shows plots of the radial, circumferential, and longitudinal strains in the myocardium computed from the cylindrical free-form deformations obtained from the registration algorithm for the simulator images generated from the k-parameter values in figure 4.12. The strain maps shown here should be compared with the true strain maps in figure 4.14.
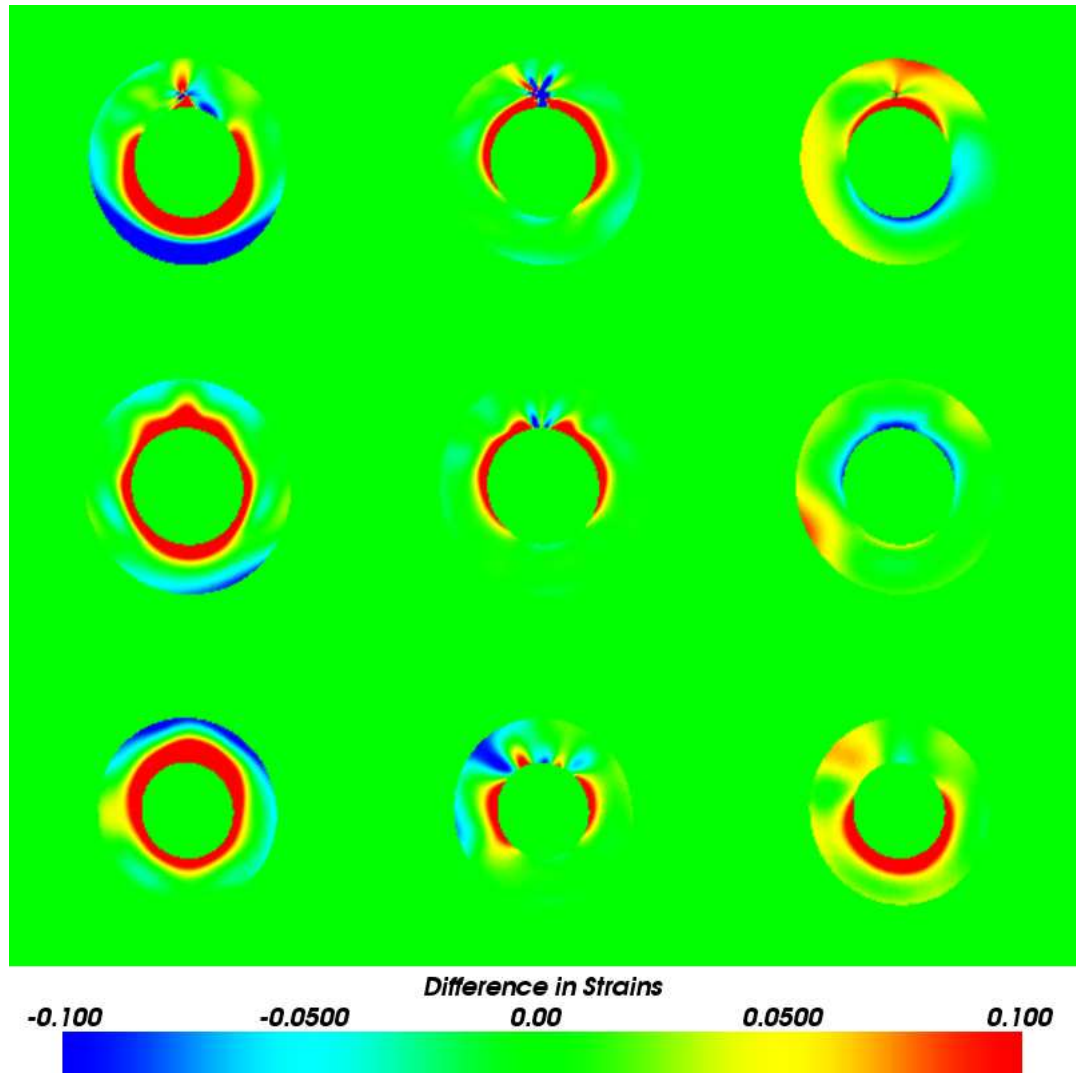
Figure 5.10: This figure shows the differences between the true (figure 4.14) and estimated (figure 5.9) strain maps.
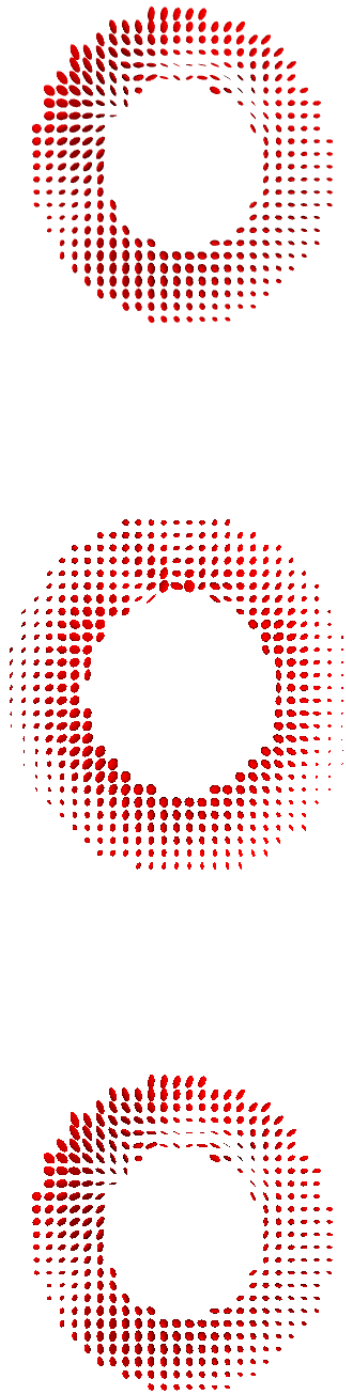
Figure 5.11: This figure shows plots of the strain in the myocardium computed from the cylindrical free-form deformations obtained from the registration algorithm for the simulator images generated from the k-parameter values in figure 4.12. The strain maps shown here should be compared with the true strain maps in figure 4.17.

(a) Apical SA Slice

(b) Mid-ventricular SA Slice

(c) Basal SA Slice

(d) Horizontal LA Slice
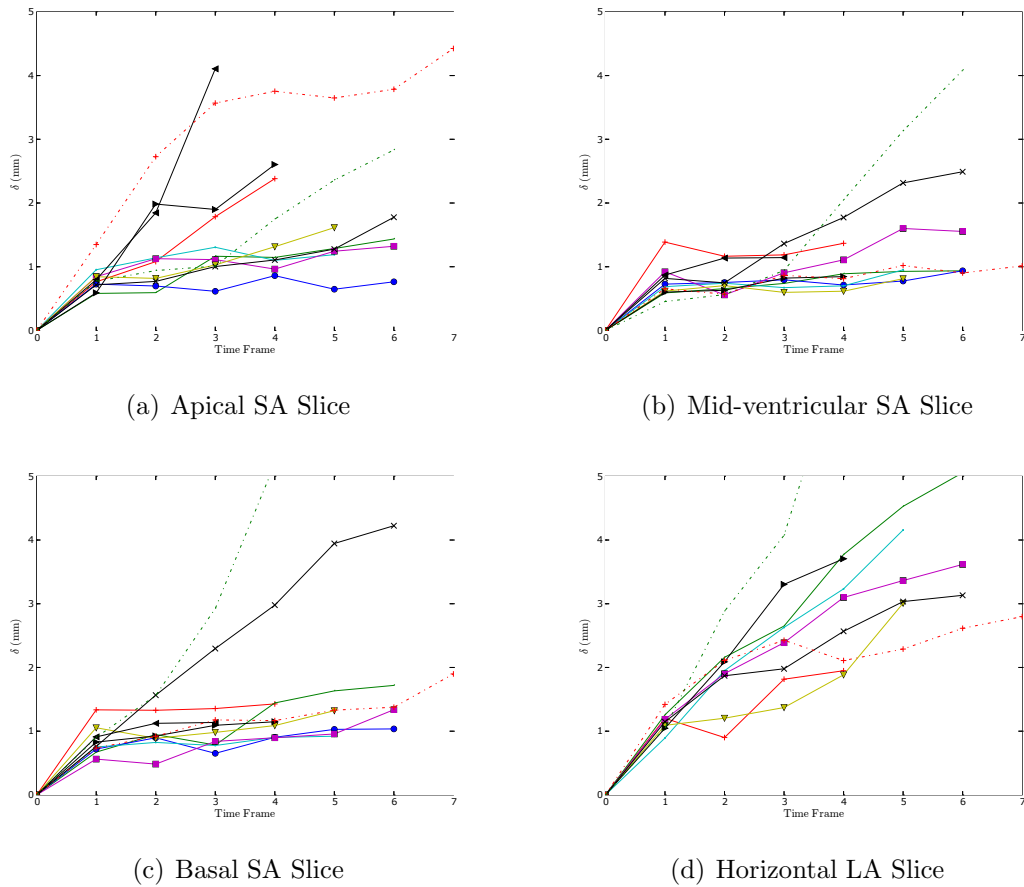
Figure 5.12: These graphs show the variation of the RMS error in the estimated in-plane displacements obtained from the registration algorithm as compared with the manual tracking of tag intersection points in different slices for the 11 volunteers.

for the remaining 3 the CFFDs performed worse. So, the CFFDs have performed slightly better than the Cartesian FFDs in tracking the motion of the myocardium in the mid-ventricular region of the LV. This can again be explained by the fact that the shape of the LV near the mid-ventricle resembles a cylinder and the CFFDs are able to track the motion of the LV more accurately in this region than the Cartesian FFDs.

Increasing the control point spacing in the radial and circumferential directions had a deterimental effect on the performance of the motion tracking algorithm as shown in figure 5.13.

We also visualized the tag tracking in the form of virtual tag grids in figure 5.14. Here a grid has been overlaid on SA and LA views of the heart at end-diastole and
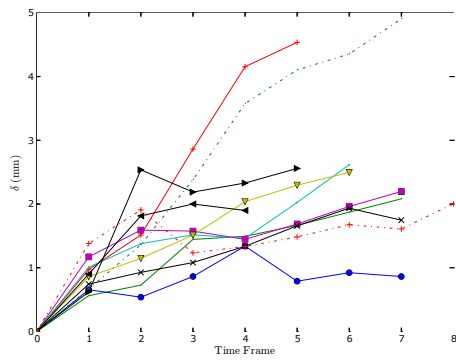
(a) Apical SA Slice
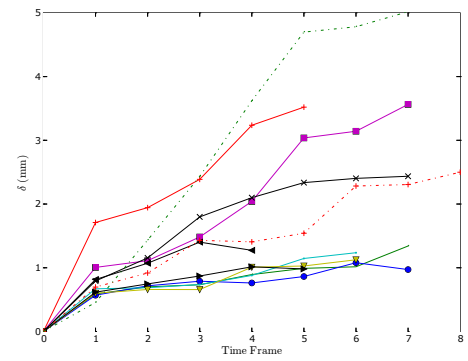
(b) Mid-ventricular SA Slice
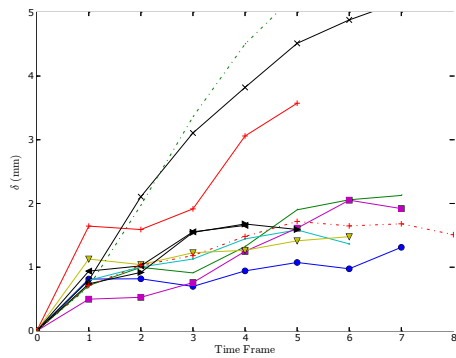
(c) Basal SA Slice
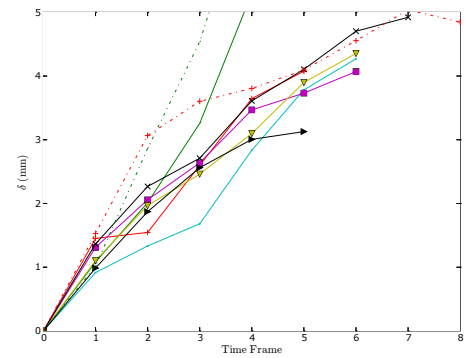
(d) Horizontal LA Slice

Figure 5.13: These graphs show the variation of the RMS error in the estimated in-plane displacements obtained from the registration algorithm as compared with the manual tracking of tag intersection points in different slices for the 11 volunteers. In this figure control point spacings of 4 mm and $\pi/8$ were used in the radial and circumferential directions respectively.

been allowed to deform with the calculated transformations as the heart contracts.

From the output transformations we also computed the radial, circumferential, and longitudinal strains in different regions of the myocardium. A bullseye plot of the average radial, circumferential, and longitudinal strains computed at end-systole for the 11 volunteers is shown in figure 5.15. While figures 5.16, 5.17, and 5.18 show the variation of the radial, circumferential, and longitudinal strains over time. These should be compared with the corresponding bullseye plots (figure 4.28) and graphs showing the variation in strain over time (figures 4.29, 4.30, and 4.31). The results are similar to those obtained in chapter 4. The radial strain is the greatest in the anterolateral part of the myocardium while the circumferential strain is uniform around the center of the LV and increases towards the apex. The estimation of the longitudinal strain is again made difficult by the relatively small number of LA slices acquired for the study.

5.4 Summary

In this chapter we investigated the use of a cylindrical free-form deformation (CFFD) for describing the motion of the myocardium of the LV. We validated our method using a cardiac motion simulator. The results presented showed that the CFFD performed slightly worse than the registration algorithm based on Cartesian FFDs except for the mid-ventricular region of the LV where its accuracy is slightly better than that of Cartesian FFDs for both simulated data and human volunteer data. The radial and circumferential strain maps computed for the human volunteer data are also comparable to those reported in other studies [111, 43].

The results presented in this chapter show that the coordinate system used can have a significant impact on the accuracy of image registration in tracking the motion of the heart. In a patient study tagged MR images may only be one of the many different imaging modalities used to obtain a comprehensive view of the anatomy and function of the heart. If, for example, tagged MR images are only acquired
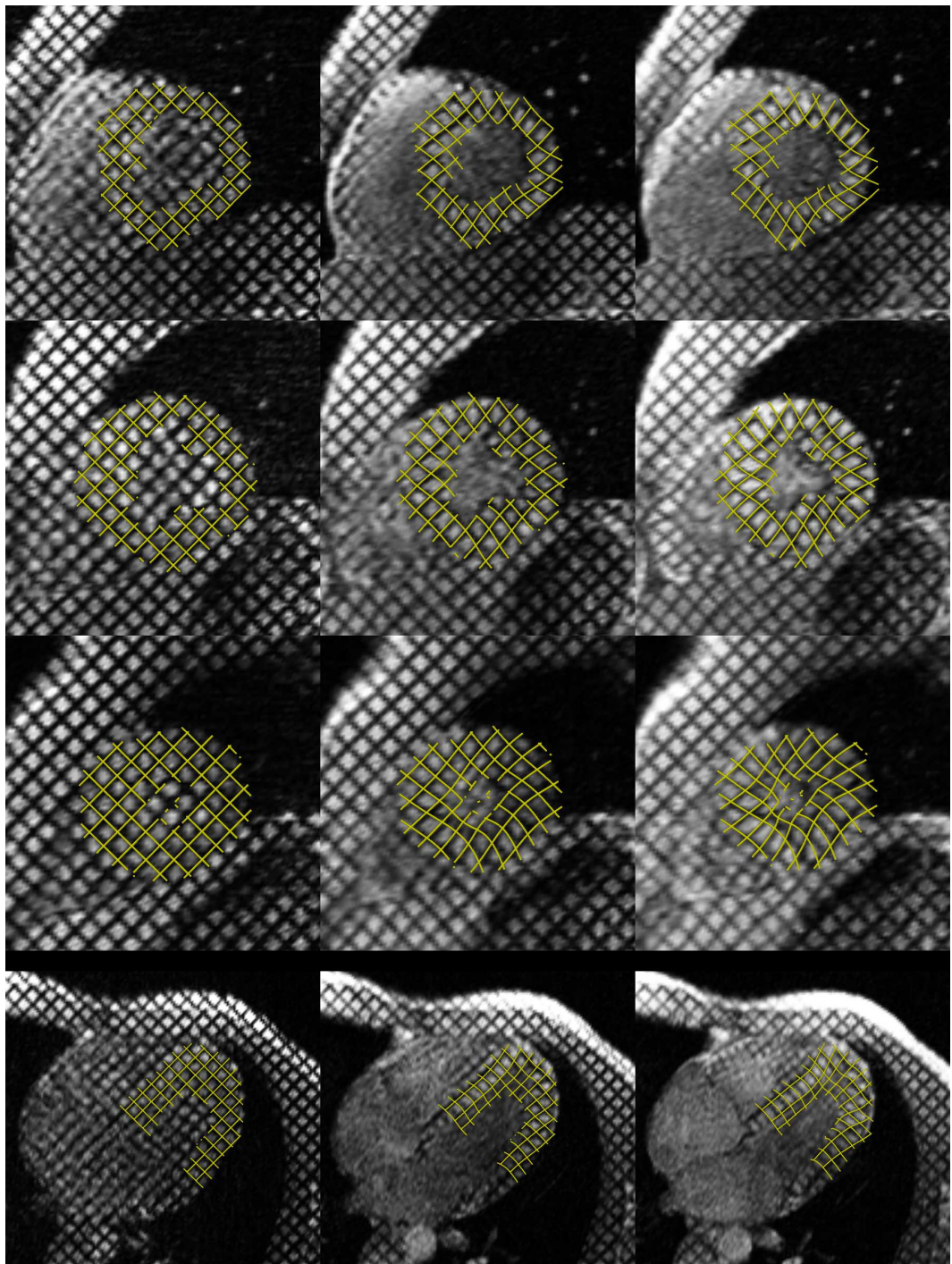
Figure 5.14: This figure shows a series of tagged images taken from one of the volunteers. A virtual tag grid has been placed on the tag pattern at end-diastole and allowed to deform with time according to the deformation field calculated. As time progresses the virtual tag grid can be seen to follow the underlying tag pattern and so we can say that the deformation field has been reconstructed accurately. The first three rows show basal, mid-ventricular, and apical SA images respectively. The fourth row shows a horizontal LA image. The first, second, and third columns correspond to end-diastole, mid-systole, and end-systole respectively. Animations of these virtual tag grids can be found on the accompanying CD.

Figure 5.15: This figure (from left to right) shows bullseye plots of the average radial, circumferential, and longitudinal strains in the myocardium computed at end-systole for the 11 volunteers.

in the mid-ventricular region of the LV, CFFDs may prove to be more suitable for performing motion analysis in this region of the LV.

A limitation of the registration techniques presented in this and the previous chapter for cardiac motion tracking is that deformation parameters can only be computed for discrete time instants (namely the times at which the images have been acquired). In the following chapter we investigate the use of 4D FFDs for cardiac motion tracking. 4D FFDs are parameterized by a temporal variable in addition to the three spatial variables and ensure computed deformation parameters are temporally smooth as well as being spatially smooth.

(a) Basal Septal   (b) Basal Anterior   (c) Basal Lateral   (d) Basal Inferior

(e) Mid Septal   (f) Mid Anterior   (g) Mid Lateral   (h) Mid Inferior

(i) Apical Septal   (j) Apical Anterior   (k) Apical Lateral   (l) Apical Inferior
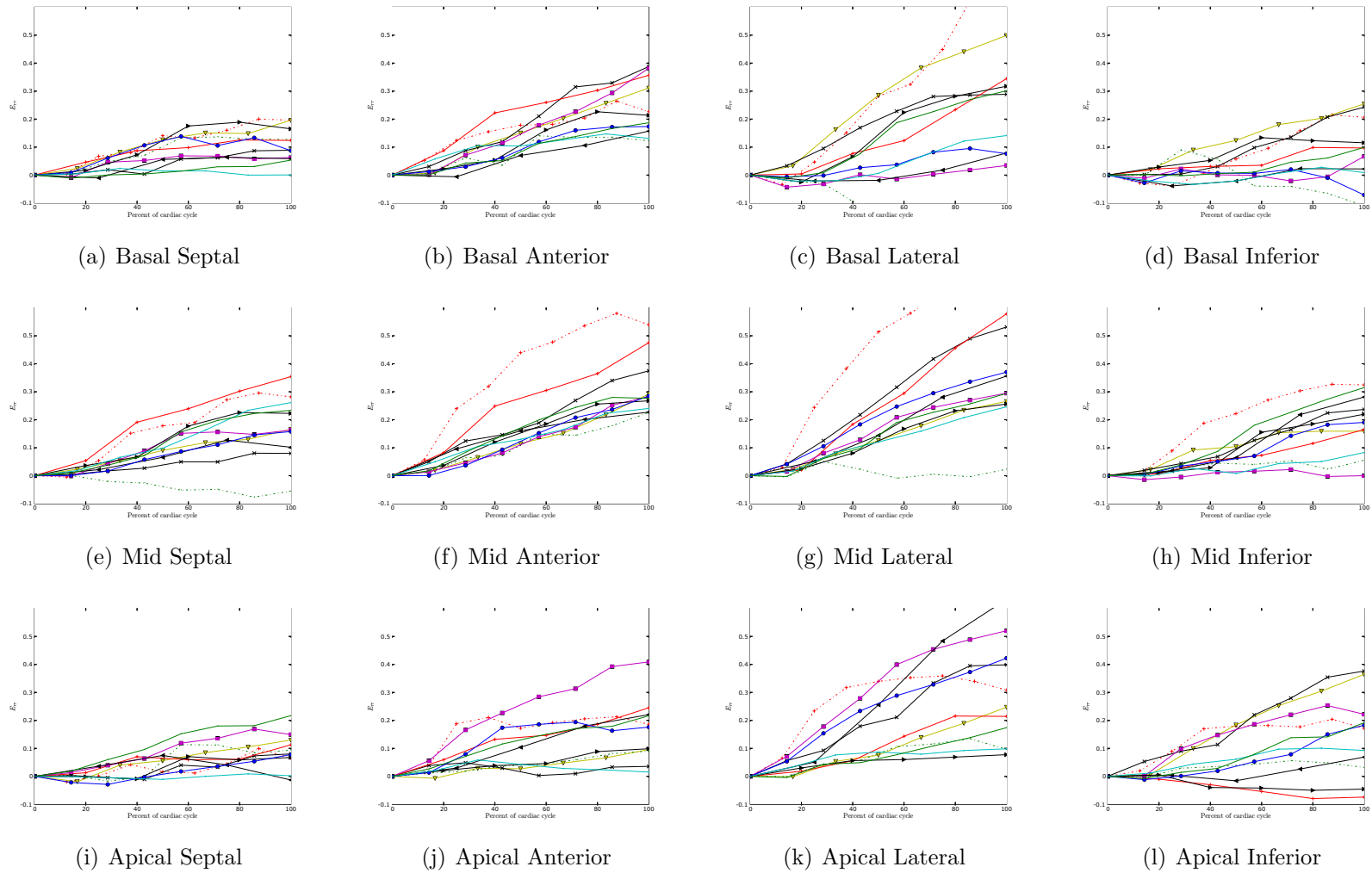
Figure 5.16: This figure shows plots of the radial strain in the different regions of the heart computed from the free-form deformations obtained from the registration algorithm for the 11 volunteers.

(a) Basal Septal   (b) Basal Anterior   (c) Basal Lateral   (d) Basal Inferior

(e) Mid Septal   (f) Mid Anterior   (g) Mid Lateral   (h) Mid Inferior

(i) Apical Septal   (j) Apical Anterior   (k) Apical Lateral   (l) Apical Inferior
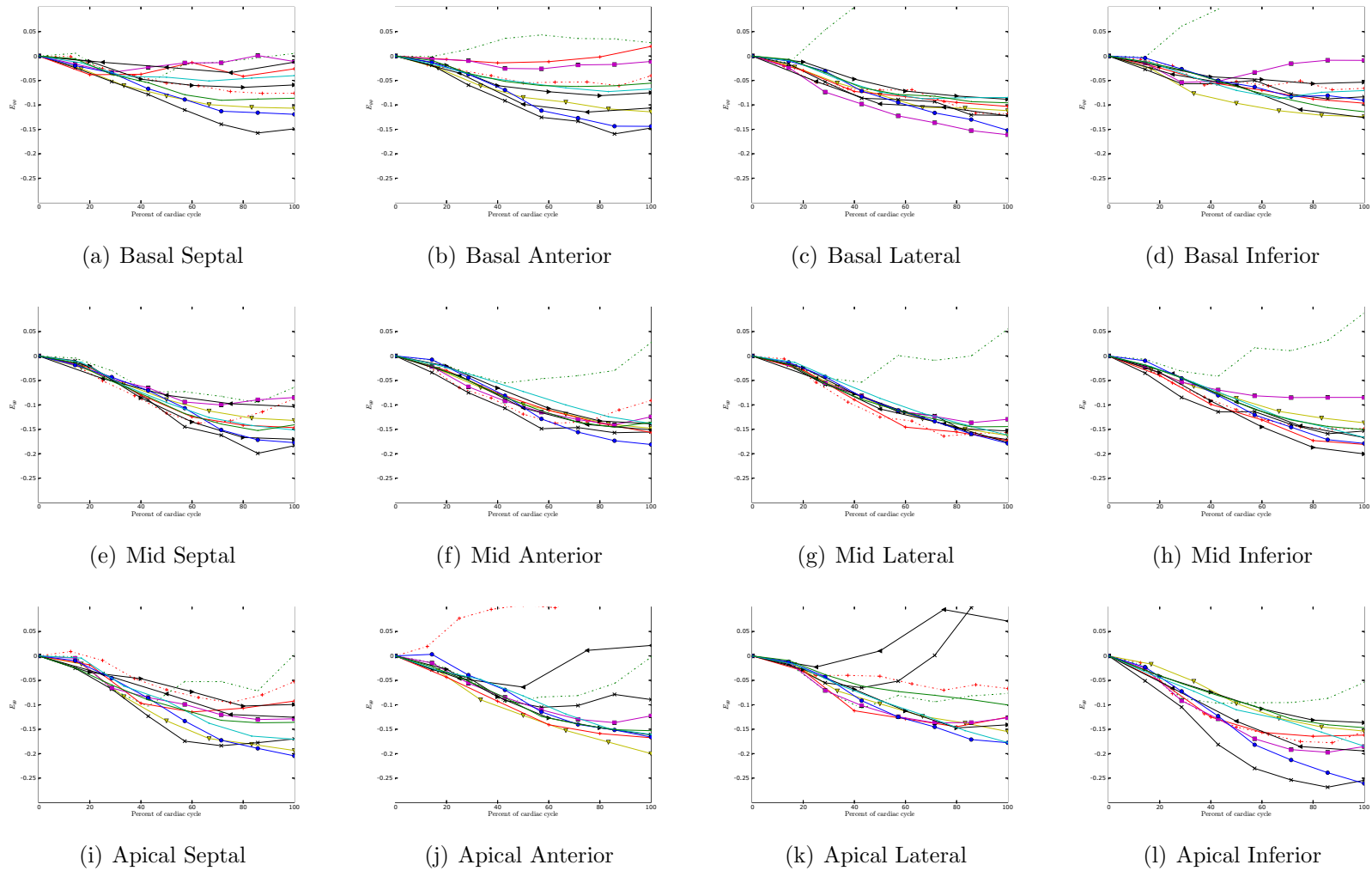
Figure 5.17: This figure shows plots of the circumferential strain in the different regions of the heart computed from the free-form deformations obtained from the registration algorithm for the 11 volunteers.

(a) Basal Septal

(b) Basal Anterior

(c) Basal Lateral

(d) Basal Inferior

(e) Mid Septal

(f) Mid Anterior

(g) Mid Lateral

(h) Mid Inferior

(i) Apical Septal

(j) Apical Anterior

(k) Apical Lateral

(l) Apical Inferior
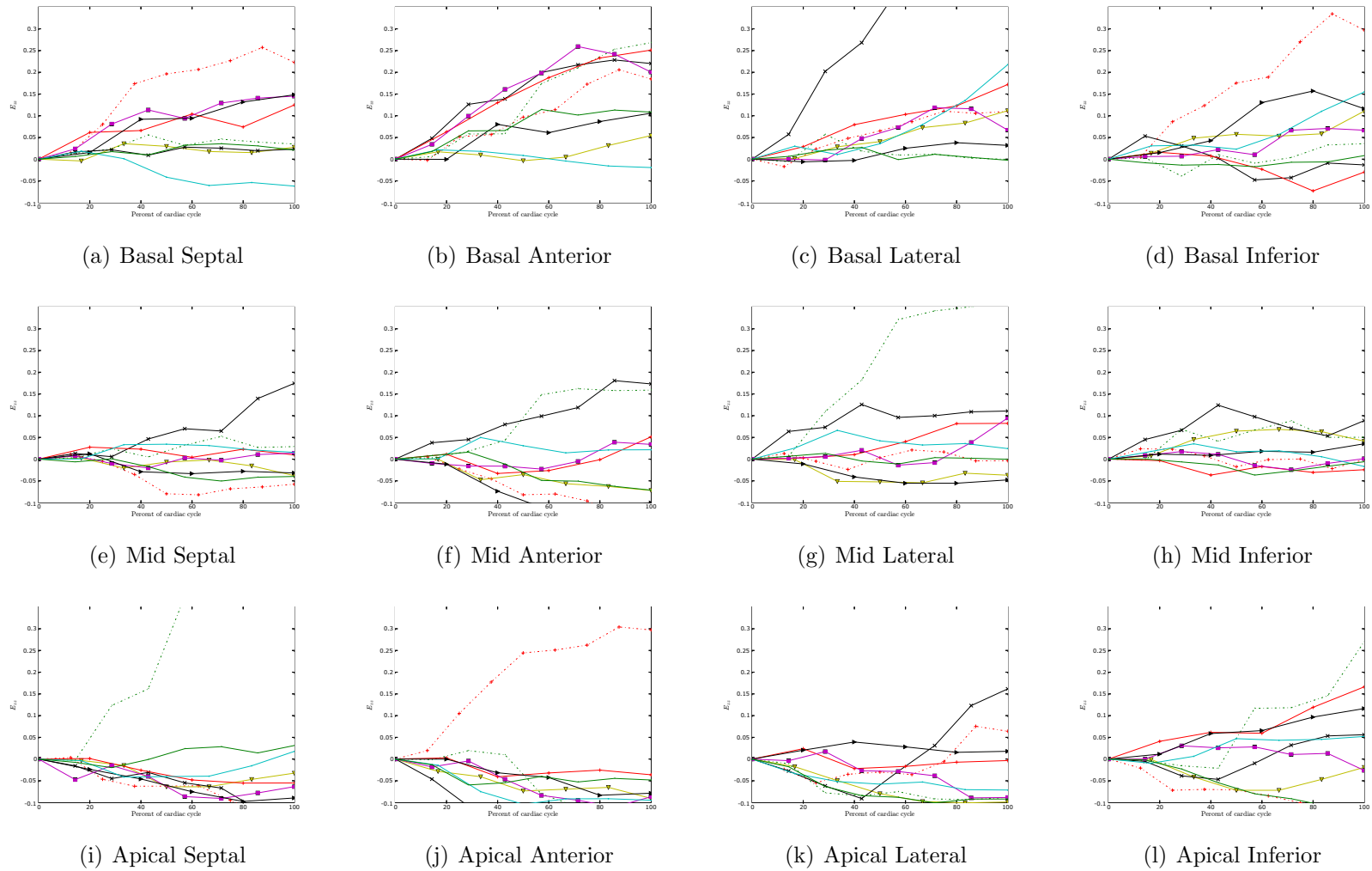
Figure 5.18: This figure shows plots of the longitudinal strain in the different regions of the heart computed from the free-form deformations obtained from the registration algorithm for the 11 volunteers.

Chapter 6

Cardiac Motion Tracking in Tagged MR Images Using a 4D B-Spline Motion Model and Nonrigid Image Registration

In the previous two chapters we presented methods for cardiac motion tracking in tagged MR images using nonrigid image registration and transformation models based on Cartesian and cylindrical coordinate systems. The transformation models used in both of these methods suffer from the same limitation—deformation parameters can only be evaluated at discrete time instants and they are not temporally smooth.

In this chapter we present a method for tracking the motion of the heart in tagged MR images using nonrigid image registration by maximization of NMI with a *four dimensional* (4D) B-spline transformation model. We track the motion of the myocardium of the left ventricle (LV) by registering a sequence of images taken during systole to a set of reference images taken at end-diastole. Registration is achieved by optimizing the mutual informations between the images being registered and the reference images. The transformation used to register the sequence

of images is a 4D B-spline transform. This allows us to describe the deformation of the LV in a way that is both spatially and temporally smooth. The advantage of using a 4D B-spline transform is that strains, displacements, and velocities can be calculated at any arbitrary time between end-diastole and end-systole. The ability to evaluate deformation parameters at arbitrary time instants is important practically as deformation fields obtained from different volunteers can be compared more easily.

This chapter is organized as follows. In section 6.1 we detail the 4D image registration method developed for cardiac motion tracking using tagged MR images. As in the previous two chapters we have validated our method using a cardiac motion simulator and data acquired from a group of normal volunteers and the results obtained are presented in section 6.2. Finally, in section 6.3 we summarize our work. The work presented in this chapter has been published in [30].

6.1 Registration of 4D Tagged MR Images

The method proposed in this chapter is to pose the problem of tracking the motion of the heart as a 4D registration problem. In order to measure through-plane motion we again need to acquire images with tag planes in the SA and LA directions. We represent the 4D images in which the tag planes are perpendicular to the SA and LA image planes as S4D$(\mathbf{x}, t)$ and L4D$(\mathbf{x}, t)$ respectively.

To track the motion of the heart we need to find a transformation, $\mathbf{T}(\mathbf{x}, t)$, which describes how a particular material point at position $\mathbf{x}$ in the myocardium at time $t = 0$ moves over time. In chapters 4 and 5 we estimated this transformation in a sequence of registration steps in which the volume images, $S_{n\tau}$ and $L_{n\tau}$, taken during systole were registered simultaneously to the segmented volume images, S_{seg} and L_{seg} respectively. In this chapter we propose to estimate $\mathbf{T}(\mathbf{x}, t)$ by registering the 4D volume images S4D$(\mathbf{x}, t)$ and L4D$(\mathbf{x}, t)$ simultaneously to the 4D volume
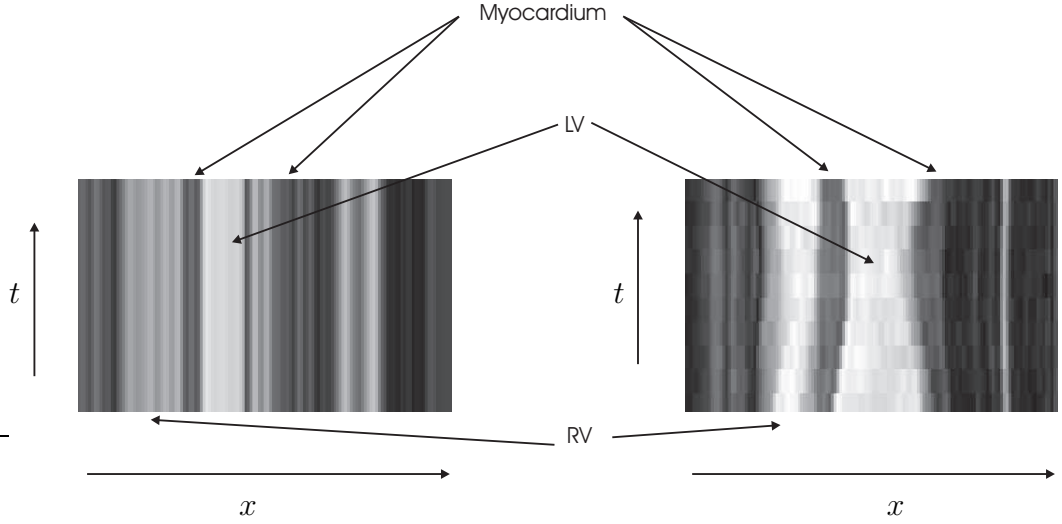
Figure 6.1: These images show one slice from a 4D image in which the horizontal axis represents the x-direction and the vertical axis represents time (untagged images have been used for clarity). The regions corresponding to the LV, RV, and myocardium are also indicated. To reconstruct the deformation field in the myocardium the image on the right, in which the LV is moving, is registered to the image on the left, in which the LV is stationary.

images $\mathrm{S4D_{seg}}(\mathbf{x}, t)$ and $\mathrm{L4D_{seg}}(\mathbf{x}, t)$ respectively, where

$$\mathrm{S4D_{seg}}(\mathbf{x}, t) = \mathrm{S_{seg}}(\mathbf{x}) \tag{6.1}$$

$$\mathrm{L4D_{seg}}(\mathbf{x}, t) = \mathrm{L_{seg}}(\mathbf{x}) \tag{6.2}$$

and $\mathrm{S_{seg}}$ and $\mathrm{L_{seg}}$ are the segmented volume images of the myocardium at end-diastole. The 4D registration which needs to be performed is illustrated in figure 6.1 for the SA direction.

Performing this registration yields a transformation, $\mathbf{T}(\mathbf{x}, t)$, which maps points in the 4D images, $\mathrm{S4D_{seg}}(\mathbf{x}, t)$ and $\mathrm{L4D_{seg}}(\mathbf{x}, t)$, in which the myocardium is stationary, to their corresponding positions in the images $\mathrm{S4D}(\mathbf{x}, t)$ and $\mathrm{L4D}(\mathbf{x}, t)$, in which the myocardium is moving. The transformation used to effect the registration is represented as a 4D B-spline FFD

$$\mathbf{T}(\mathbf{x}, t) = \mathbf{x} + \mathbf{u}(\mathbf{x}, t) \tag{6.3}$$

176

where

$$
\mathbf{u}(\mathbf{x}, t) \;=\; \sum_{l=0}^{n_t} \sum_{i=0}^{n_x} \sum_{j=0}^{n_y} \sum_{k=0}^{n_z} \beta^3\left(\frac{t - t_l}{\delta_t}\right) \beta^3\left(\frac{x - x_{i,j,k}}{\delta_x}\right) \beta^3\left(\frac{y - y_{i,j,k}}{\delta_y}\right) \times
$$

$$
\beta^3\left(\frac{z - z_{i,j,k}}{\delta_z}\right) \phi_{i,j,k,l} \tag{6.4}
$$

and the $\phi_{i,j,k,l}$ are the 3D displacement vectors at the positions of the $(n_x + 1)(n_y + 1)(n_z + 1)(n_t + 1)$ control points, δ_x, δ_y, δ_z are the control point spacings in the x-, y-, z-directions respectively, t_l are the time instants at which the images haven been acquired in constructing the 4D images, and δ_t is the time interval between the control points in the temporal direction. The x-, y-, and z-axes of the 4D FFD are aligned with the x-, y-, and z-axes of the segmented SA image S4D$_{\text{seg}}$ as in chapter 4. In chapter 4 the deformation field at a particular time point was computed by summing a sequence of FFDs over time (equations 4.4 and 4.5). In equation 6.4 the deformation is computed by blending the displacement vectors in the temporal direction in addition to the spatial directions and ensures temporal smoothness of the deformation field.

Again, we set the control point displacement vectors which cannot affect the deformation field within the myocardium to be zero and do not consider them during the optimization process. This is done in exactly the same way as shown in figure 4.4.

6.1.1 Combined Nonrigid Registration of SA and LA Images

A suitable similarity function must now be found which measures the degree to which the 4D images, S4D and L4D, have been registered with the segmented 4D images, S4D$_{\text{seg}}$ and L4D$_{\text{seg}}$ respectively. The NMI between the segmented 4D SA volume image, S4D$_{\text{seg}}$, and the transformed 4D SA volume image, $\mathbf{T}$(S4D), so that it has been registered to the segmented image with the current estimate of the

transformation $\mathbf{T}(\mathbf{x}, t)$ is

$$N(\text{S4D}_{\text{seg}}; \mathbf{T}(\text{S4D})) = \frac{H(\text{S4D}_{\text{seg}}) + H(\mathbf{T}(\text{S4D}))}{H(\text{S4D}_{\text{seg}}, \mathbf{T}(\text{S4D}))} \tag{6.5}$$

A similar equation for the LA images can be written as

$$N(\text{L4D}_{\text{seg}}; \mathbf{T}(\text{L4D})) = \frac{H(\text{L4D}_{\text{seg}}) + H(\mathbf{T}(\text{L4D}))}{H(\text{L4D}_{\text{seg}}, \mathbf{T}(\text{L4D}))} \tag{6.6}$$

Equations 6.5 and 6.6 can then be weighted according to the number of voxels in the segmented SA and LA volume images and summed to yield a similarity function similar to the ones used in chapters 4 and 5. This approach would be suitable for 4D image registration of images in which there are no tags present (such as untagged anatomical images of the LV or images of the brain). However, tagged MR image analysis is complicated by the fact that as the LV contracts tag planes can move from their initial position in a direction perpendicular to the tag plane direction and become aligned with an adjacent tag plane at a later time. During the optimization procedure the transformation estimate can become trapped at a local maximum. This happens because locally the initial transformation estimate (the identity transformation) is already at its optimum according to the intensity based similarity criterion used. In addition the intensities of voxels in the images, S4D and L4D, varies over time.

To account for these complications we evaluate the following similarity measure in which each time frame in the transformed 4D images, $\mathbf{T}(\text{S4D})$ and $\mathbf{T}(\text{L4D})$, is compared with the corresponding time frame in the stationary 4D images, $\mathbf{T}(\text{S4D}_{\text{seg}})$ and $\mathbf{T}(\text{L4D}_{\text{seg}})$

$$
\begin{aligned}
\mathcal{C} = {} & \sum_{l=0}^{n} w_{\text{S}} \frac{H(\text{S4D}_{\text{seg}}(\mathbf{x}, l\tau)) + H(\mathbf{T}(\text{S4D}(\mathbf{x}, l\tau)))}{H(\text{S4D}_{\text{seg}}(\mathbf{x}, l\tau), \mathbf{T}(\text{S4D}(\mathbf{x}, l\tau)))} + \\
& w_{\text{L}} \frac{H(\text{L4D}_{\text{seg}}(\mathbf{x}, l\tau)) + H(\mathbf{T}(\text{L4D}(\mathbf{x}, l\tau)))}{H(\text{L4D}_{\text{seg}}(\mathbf{x}, l\tau), \mathbf{T}(\text{L4D}(\mathbf{x}, l\tau)))}
\end{aligned}
\tag{6.7}
$$

where w_S and w_L are the weights given in equations 4.9 and 4.10, and $n + 1$ is the total number of time frames.

6.1.2 Optimization Procedure

To stop the transformation, $\mathbf{T}(\mathbf{x}, t)$, from getting trapped at local maxima we use a two-stage optimization procedure. In the first stage we separate the optimization of the control point displacement vectors in the spatial and temporal directions. We consider each value of the control point index l (in the temporal direction) in turn, from $l = 1$ to $l = n_t$, and optimize only the subset of control point displacement vectors for which the temporal index is equal to the value being considered. As modifying a control point displacement vector while keeping the control point index l (in the temporal direction) constant changes the displacement field $\mathbf{u}(\mathbf{x}, t)$ only within the time interval $[t_{\min}(l), t_{\max}(l))$ where

$$t_{\min}(l) = t_l - 2\delta_t \tag{6.8}$$

$$t_{\max}(l) = t_l + 2\delta_t \tag{6.9}$$

the similarity measure, $\mathcal{C}$, need only be evaluated for those time frames which fall within the time interval $[t_{\min}(l), t_l)$. We denote the similarity measure evaluated within this time interval as $\mathcal{C}[t_{\min}, t_l)$. The subset of control point displacement vectors are optimized so that $\mathcal{C}[t_{\min}, t_l)$ is maximized using a gradient ascent technique similar to the one in algorithm 1. After optimizing the control point displacement vectors for index l we use the recursive filtering technique of Unser *et al* [167] to interpolate the motion field so that

$$\mathbf{T}(\mathbf{x}_{i,j,k}, t_m) = \begin{cases} \mathbf{T}(\mathbf{x}_{i,j,k}, t_l) & \text{for } m > l \\ \mathbf{T}(\mathbf{x}_{i,j,k}, t_m) & \text{for } m \leq l \end{cases} \tag{6.10}$$

This provides a good initial estimate of the transformation field at time $t = t_{l+1}$. We then repeat the optimization of the control point displacement vectors for each index $> l$. This is similar to the approach we took in chapters 4 and 5 and ensures that the registration algorithm does not get trapped at a local maximum during the second stage of the optimization procedure.

In the second stage all the control point displacement vectors are optimized simultaneously so as to maximize the similarity measure (equation 6.7). A gradient ascent algorithm is used during the second stage of the optimization also.

6.2   Results

6.2.1   Cardiac Motion Simulator Data

We repeated the experiments conducted in chapters 4 and 5 on the simulator images A_1–A_3, B_1–B_3, C_1–C_3 by reconstructing the motion fields within the myocardium using the method presented in section 6.1. The control point spacings in the spatial direction were the same as those chosen in chapter 4 and the control point spacing in the temporal direction was chosen to be equal to the time between two consecutive time frames. We then computed the relative, $\rho(t)$ (equation 4.18), and RMS errors, $\delta(t)$ (equation 4.19), in the reconstructed motion fields. The relative errors in the reconstructed motion fields are plotted in figures 6.2(a), 6.2(b), and 6.2(c), while the RMS errors are plotted in figures 6.3(a), 6.3(b), and 6.3(c).

Comparison of figures 6.2 and 6.3 with figures 4.10 and 4.11 respectively show that the 4D registration algorithm presented in this chapter performs marginally better than the algorithm used in chapter 4 when there is no noise present in the images. The 4D tracking algorithm is not as robust to the presence of noise in the images as indicated by the $\sigma = 8$ and $\sigma = 16$ curves.

The canine simulator images were also used to test the performance of the 4D registration algorithm in estimating strain fields. To compute the strain the Jaco-
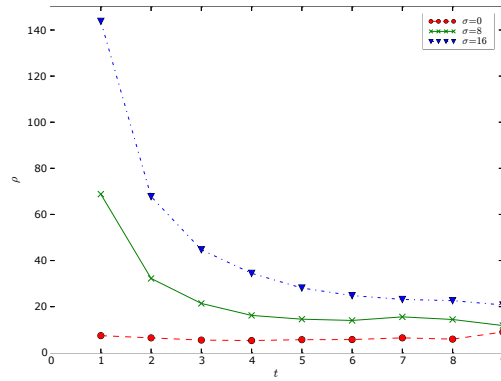
(a) Image set A
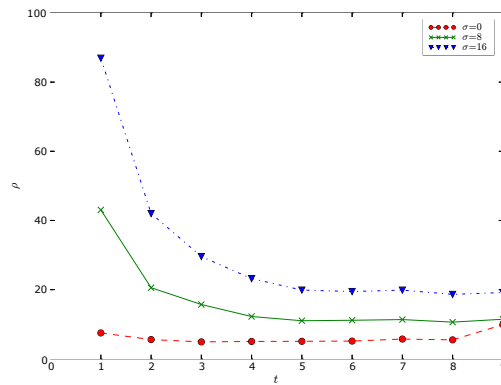
(b) Image set B
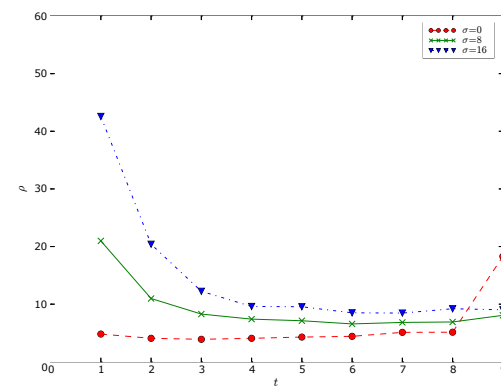
(c) Image set C

Figure 6.2: This figure shows the variation of the relative error in the estimated displacements for the three different types of motion generated from the LV simulator and for different amounts of Gaussian noise added to the images.
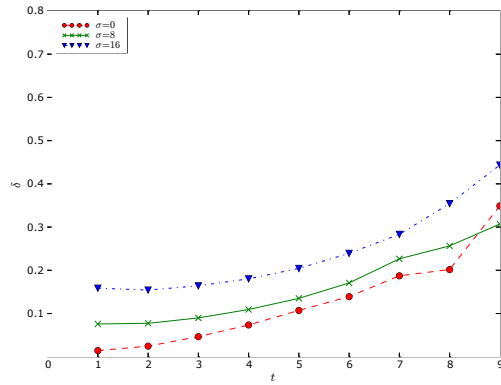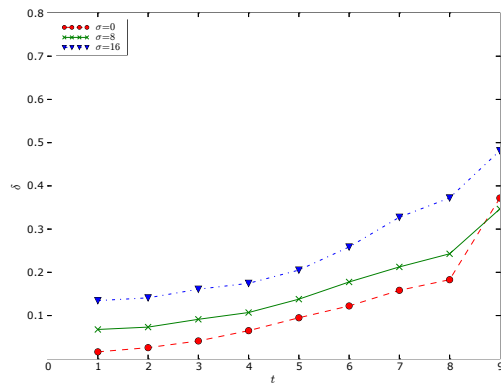
(a) Image set A
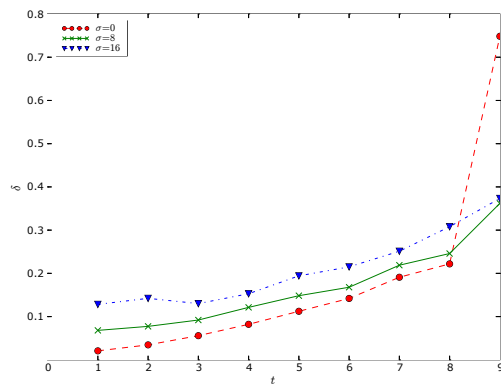
(b) Image set B

(c) Image set C

Figure 6.3: This figure shows the variation of the RMS error in the estimated displacements for the three different types of motion generated from the LV simulator and for different amounts of Gaussian noise added to the images.

bian matrix of the deformation field $\mathbf{u}(\mathbf{x}, t) = [u_x(\mathbf{x}, t), u_y(\mathbf{x}, t), u_z(\mathbf{x}, t)]^T$ must be calculated. The Lagrangian strain tensor can then be expressed in terms of the Jacobian matrix (equation 4.20). The components of the Jacobian matrix can be computed easily by differentiating 6.4 with respect to x, y, and z. For example

$$\frac{\partial u_x(\mathbf{x}, t)}{\partial y} = \frac{1}{\delta_y} \sum_{l=0}^{n_t} \sum_{i=0}^{n_x} \sum_{j=0}^{n_y} \sum_{k=0}^{n_z} \beta^3 \left(\frac{t - t_l}{\delta_t} \right) \beta^3 \left(\frac{x - x_{i,j,k}}{\delta_x} \right) \frac{d\beta^3}{dv} \beta^3 \left(\frac{z - z_{i,j,k}}{\delta_z} \right) \mu_{i,j,k,l}$$
(6.11)

where the $\mu_{i,j,k,l}$ are the x-components of the control point displacement vectors, and v and $d\beta^3/dv$ are given in equations 4.24 and 4.25 respectively.

The computed radial, circumferential, and longitudinal strains for the canine simulator images are shown in figure 6.4 and the differences between the true and estimates strain maps are shown in figure 6.5. Tensor ellipsoid plots of the strain are shown in figure 6.6.

6.2.2   Human Data

We also repeated the experiments on human volunteer data and reconstructed the deformation fields within the hearts of a group of normal volunteers. For each of the volunteers the deformation field within the myocardium was calculated using the method presented in section 6.1 for all times between end-diastole and end-systole. As in the previous chapters we tested the performance of the method by comparing the displacements of tag-intersection points in four different imaging planes computed using the 4D FFD with those measured by a human observer. The RMS error between the estimated and observed displacements of the tag-intersection points are given in figure 6.7(a), 6.7(b), 6.7(c), and 6.7(d) for apical SA, mid-ventricular SA, basal SA, and HLA slices respectively. Comparison of these figures with the corresponding figures in chapter 4 (figures 4.20(a), 4.20(b), 4.20(c), and 4.20(d) respectively) show that the 4D registration algorithm has performed not as well as the 3D registration algorithm in chapter 4. The 4D registration algorithm is not as robust as the 3D registration algorithm to the presence of noise in the images. We
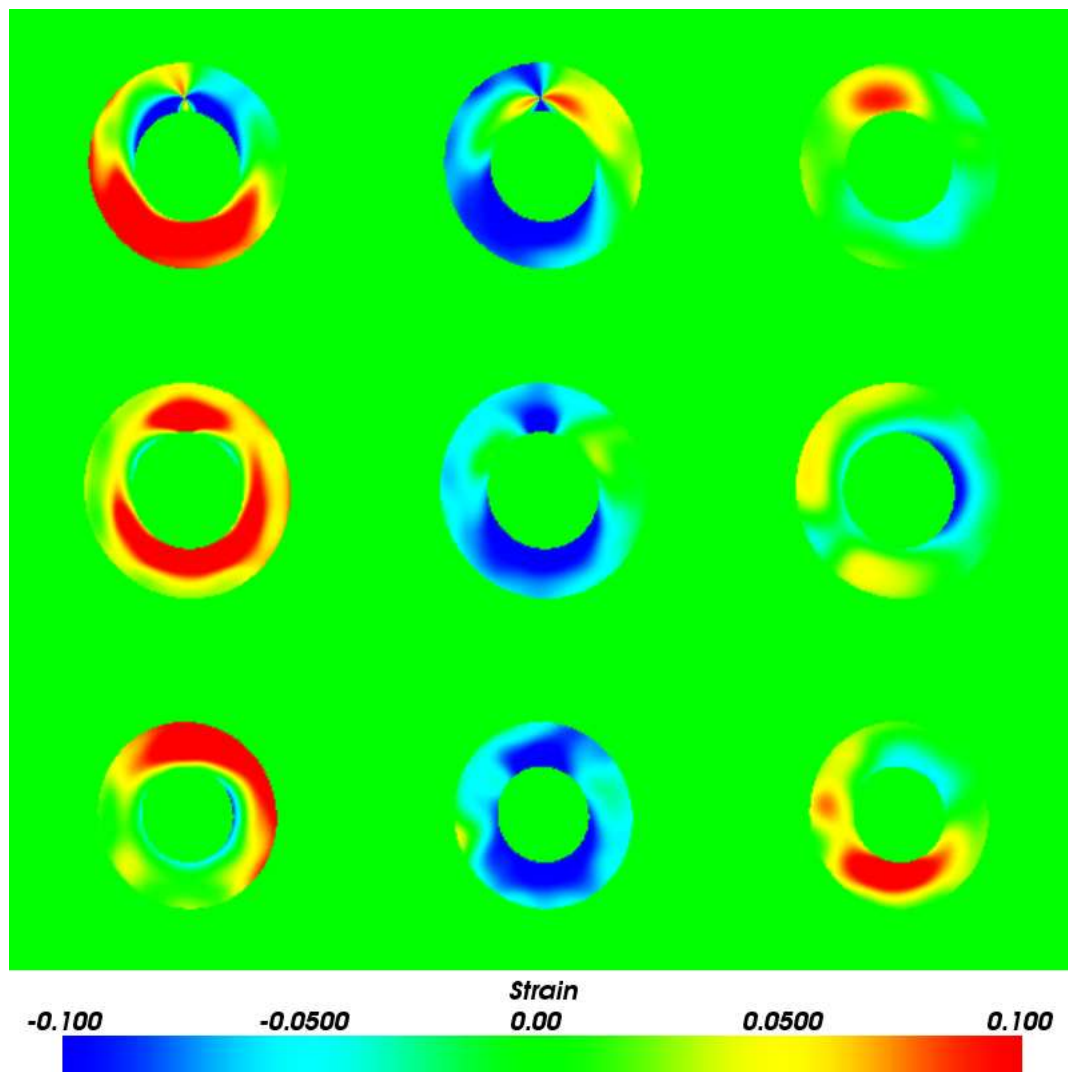
Figure 6.4: This figure shows plots of the radial, circumferential, and longitudinal strains in the myocardium computed from the 4D free-form deformations obtained from the registration algorithm for the simulator images generated from the k-parameter values in figure 4.12. The strain maps shown here should be compared with the true strain maps in figure 4.14.
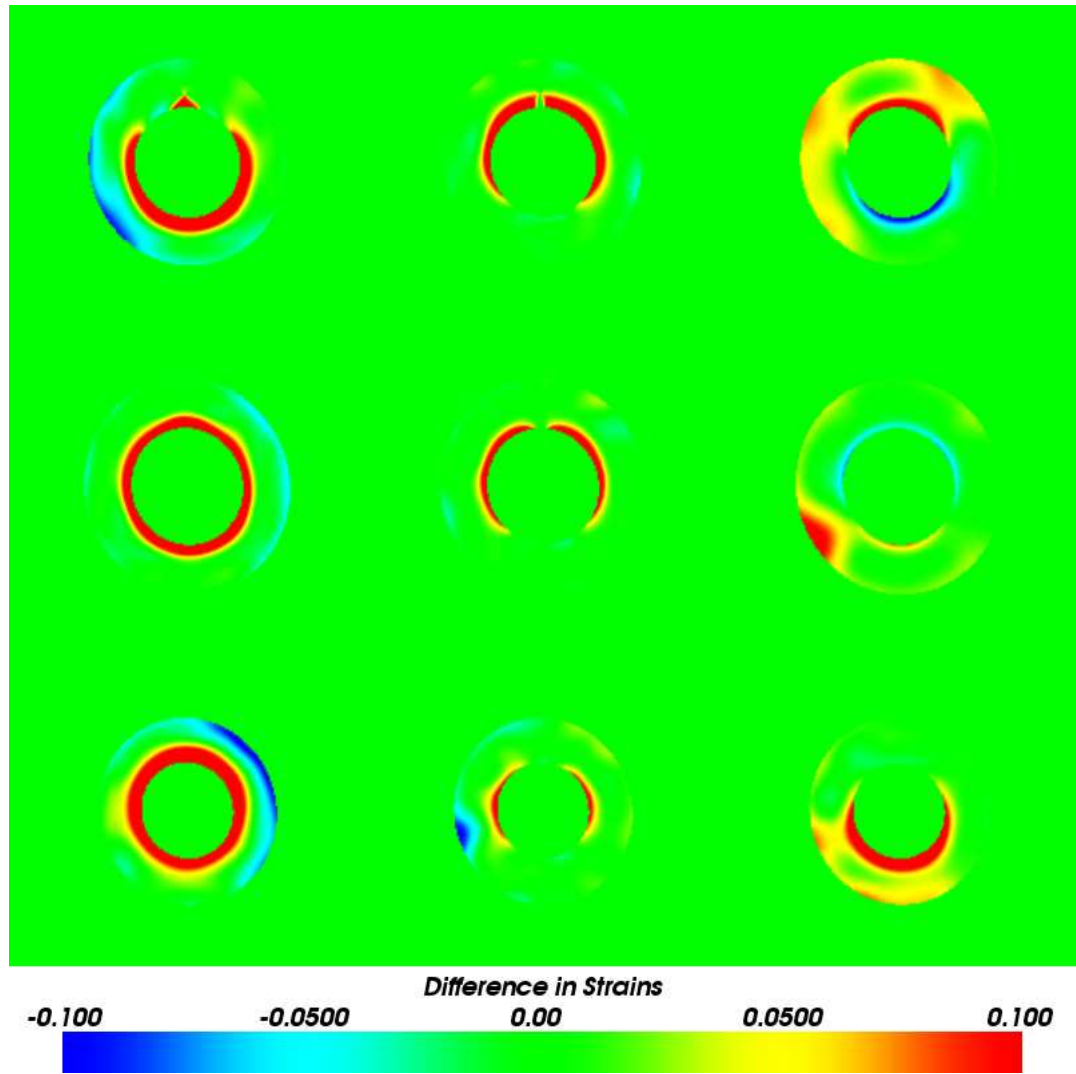
Figure 6.5: This figure shows the differences between the true (figure 4.14) and estimated (figure 6.4) strain maps.

Figure 6.6: This figure shows plots of the strain in the myocardium computed from the 4D free-form deformations obtained from the registration algorithm for the simulator images generated from the k-parameter values in figure 4.12. The strain maps shown here should be compared with the true strain maps in figure 4.17.

(a) Apical SA Slice

(b) Mid-ventricular SA Slice

(c) Basal SA Slice

(d) Horizontal LA Slice
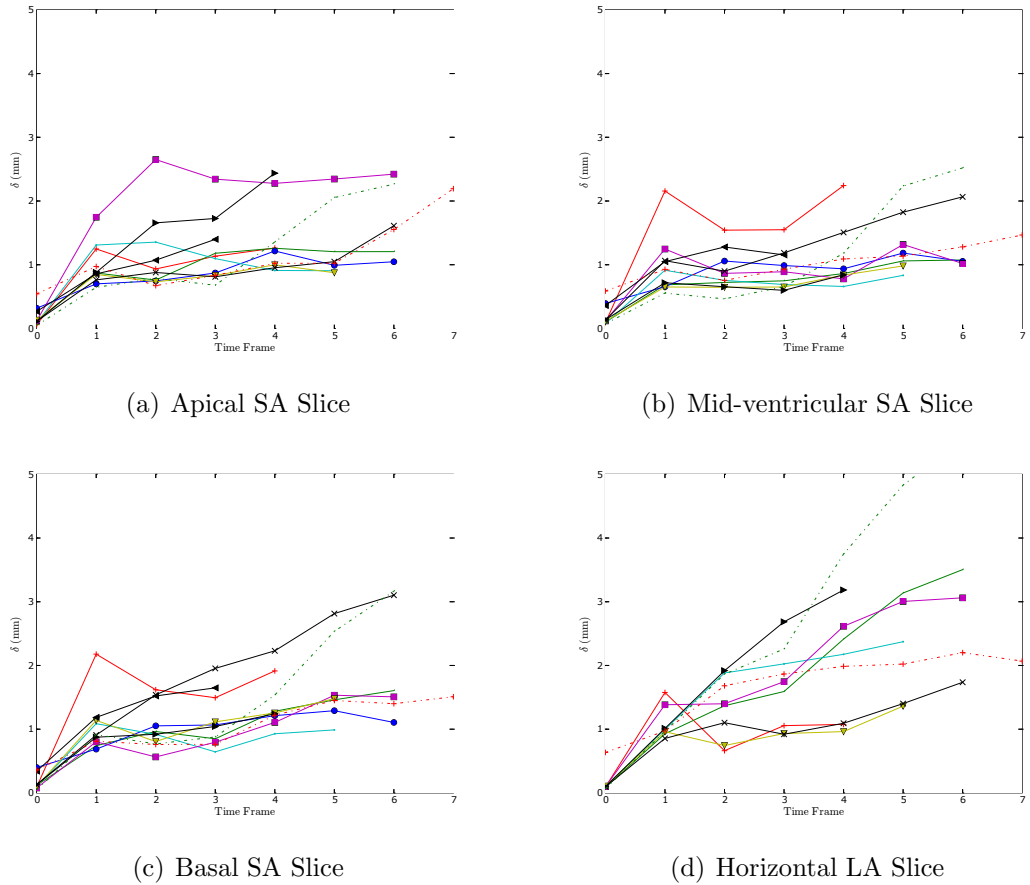
Figure 6.7: These graphs show the variation of the RMS error in the estimated in-plane displacements obtained from the registration algorithm as compared with the manual tracking of tag intersection points in different slices for the 11 volunteers.

also see from the graphs that the errors in the displacements of the tag-intersection points are not zero at time $t = 0$. This happens because the control point displacement vectors at later times influence the deformation field at time $t = 0$. As we have not constrained the deformation field produced by the 4D FFD to remain zero at the start of the cardiac cycle during the optimization process, small errors result in the computed deformation field at time $t = 0$.

Figure 6.8 shows a visualization of the tag tracking in the form of virtual tag grids. Looking at the circled areas in the figure we see that there are certain regions in the myocardium where the registration algorithm has not been able to accurately track the motion of the myocardium—in the basal SA and LA slices two tag lines have been mapped to the same tag line in the end-diastolic image. Thus the two-step

optimization procedure we are using is not able to recover the deformation field in the myocardium accurately in all cases and manual intervention may be necessary.

From the output transformations we also computed the radial, circumferential, and longitudinal strains in different regions of the myocardium. A bullseye plot of the average radial, circumferential, and longitudinal strains computed at end-systole for the 11 volunteers is shown in figure 6.9. While figures 6.10, 6.11, and 6.12 show the variation of the radial, circumferential, and longitudinal strains over time in different regions of the heart. These should be compared with the corresponding bullseye and strain plots in chapter 4.

6.3   Summary

In this chapter we presented a 4D registration algorithm for cardiac motion tracking. The experiments we conducted on simulator data showed that the 4D registration algorithm is able to track the motion of the myocardium slightly more accurately than the methods presented in chapters 4 and 5 when there is no noise present in the images. In real MR images, where noise is present, the registration algorithm is not as accurate in recovering the deformation field as the methods presented in chapters 4 and 5. Two difficulties are encountered which are limitations of the optimization procedure used. Firstly, we have not constrained the 4D FFD to be zero at the start of the cardiac cycle; and secondly, the optimization procedure can sometimes map two tag lines in a particular image taken during the cardiac cycle to a single tag line in the image taken at end-diastole. One way of solving this problem might be to interpolate a 4D FFD from the output deformation field computed in chapter 4. The interpolated 4D FFD could then be provided as an input to the registration algorithm. The input transformation obtained in this way would provide a good estimate of the deformation field and so stop the optimization procedure from getting trapped at local maxima.

Although a good estimate of the initial 4D deformation field could be obtained
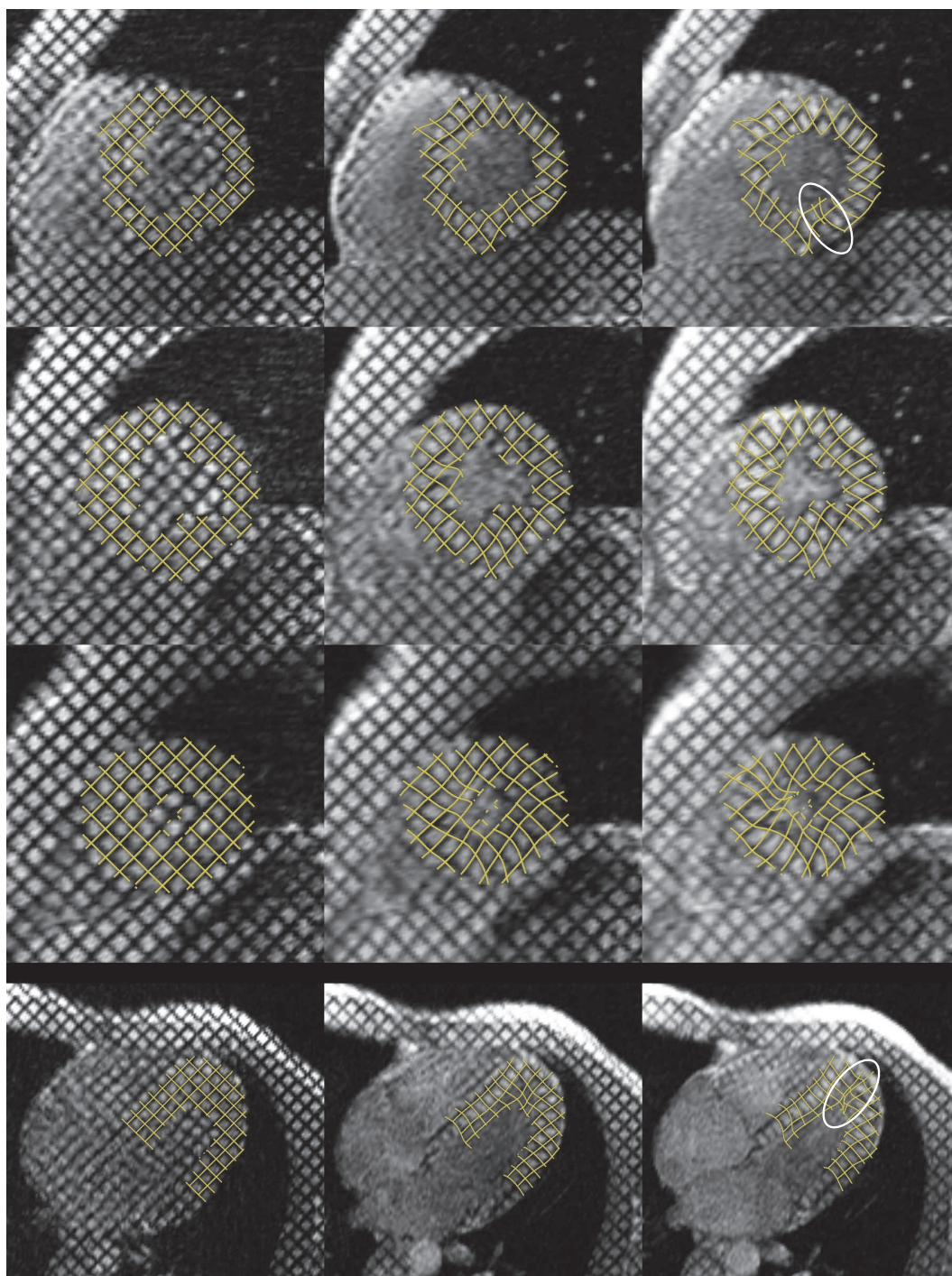
Figure 6.8: This figure shows a series of tagged images taken from one of the volunteers. A virtual tag grid has been placed on the tag pattern at end-diastole and allowed to deform with time according to the deformation field calculated. As time progresses the virtual tag grid can be seen to follow the underlying tag pattern and so we can say that the deformation field has been reconstructed accurately. The first three rows show basal, mid-ventricular, and apical SA images respectively. The fourth row shows a horizontal LA image. The first, second, and third columns correspond to end-diastole, mid-systole, and end-systole respectively. Animations of these virtual tag grids can be found on the accompanying CD.

Figure 6.9: This figure (from left to right) shows bullseye plots of the average radial, circumferential, and longitudinal strains in the myocardium computed at end-systole for the 11 volunteers.

in this way, a more efficient procedure would be to make use of prior information about the expected types of motion of the LV to re-parameterize the 3D FFDs used in chapter 4 in terms of the major modes of variation in the deformation fields. The motion tracking can be performed much more quickly as the re-parameteriziation of the FFDs in terms of the major modes reduces the dimensions of the parameter search space during optimization. In the next chapter we show how such a statistical model of deformation can be built.

(a) Basal Septal (b) Basal Anterior (c) Basal Lateral (d) Basal Inferior

(e) Mid Septal (f) Mid Anterior (g) Mid Lateral (h) Mid Inferior

(i) Apical Septal (j) Apical Anterior (k) Apical Lateral (l) Apical Inferior
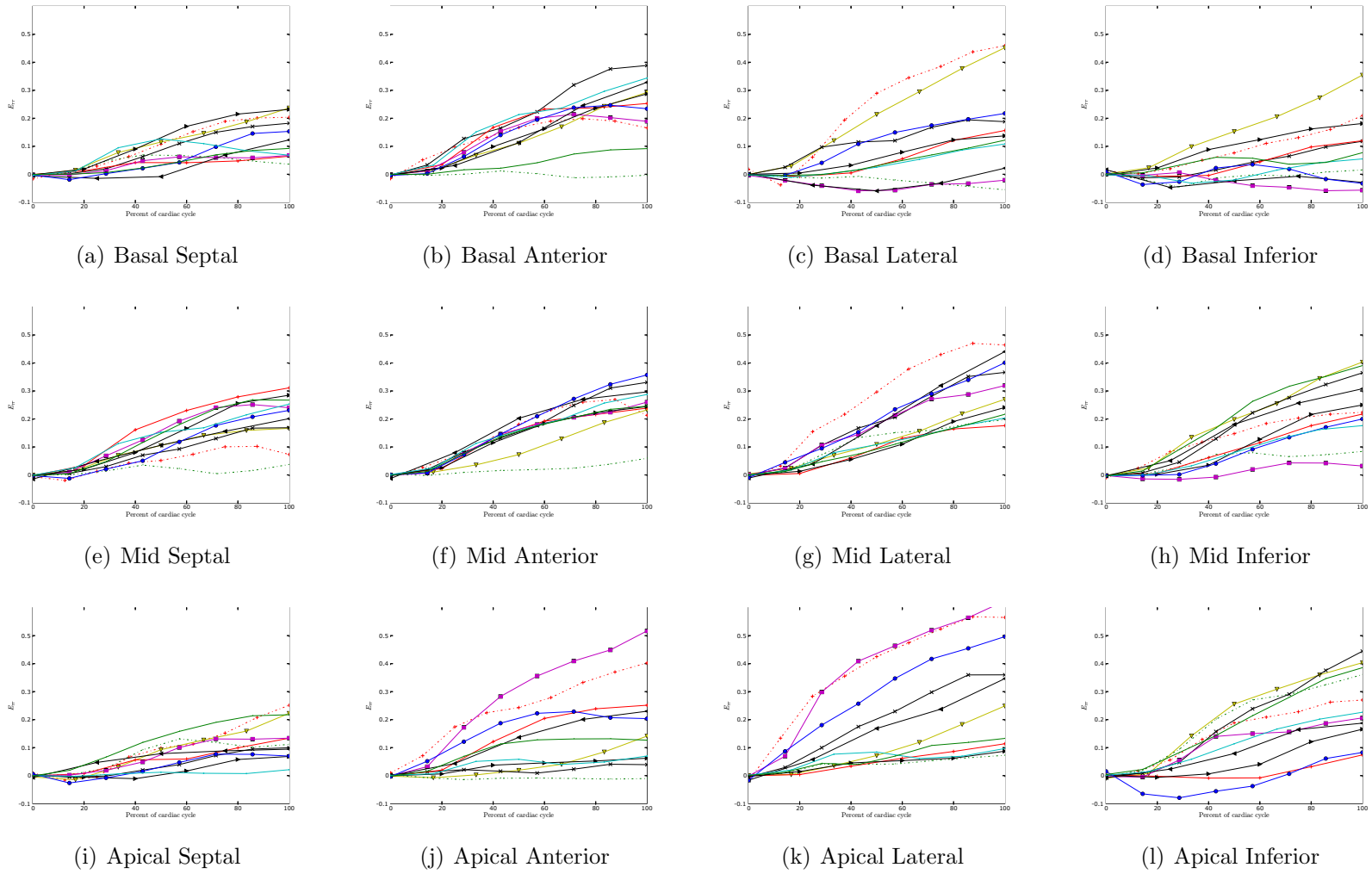
Figure 6.10: This figure shows plots of the radial strain in the different regions of the heart computed from the free-form deformations obtained from the registration algorithm for the 11 volunteers.

(a) Basal Septal   (b) Basal Anterior   (c) Basal Lateral   (d) Basal Inferior

(e) Mid Septal   (f) Mid Anterior   (g) Mid Lateral   (h) Mid Inferior

(i) Apical Septal   (j) Apical Anterior   (k) Apical Lateral   (l) Apical Inferior
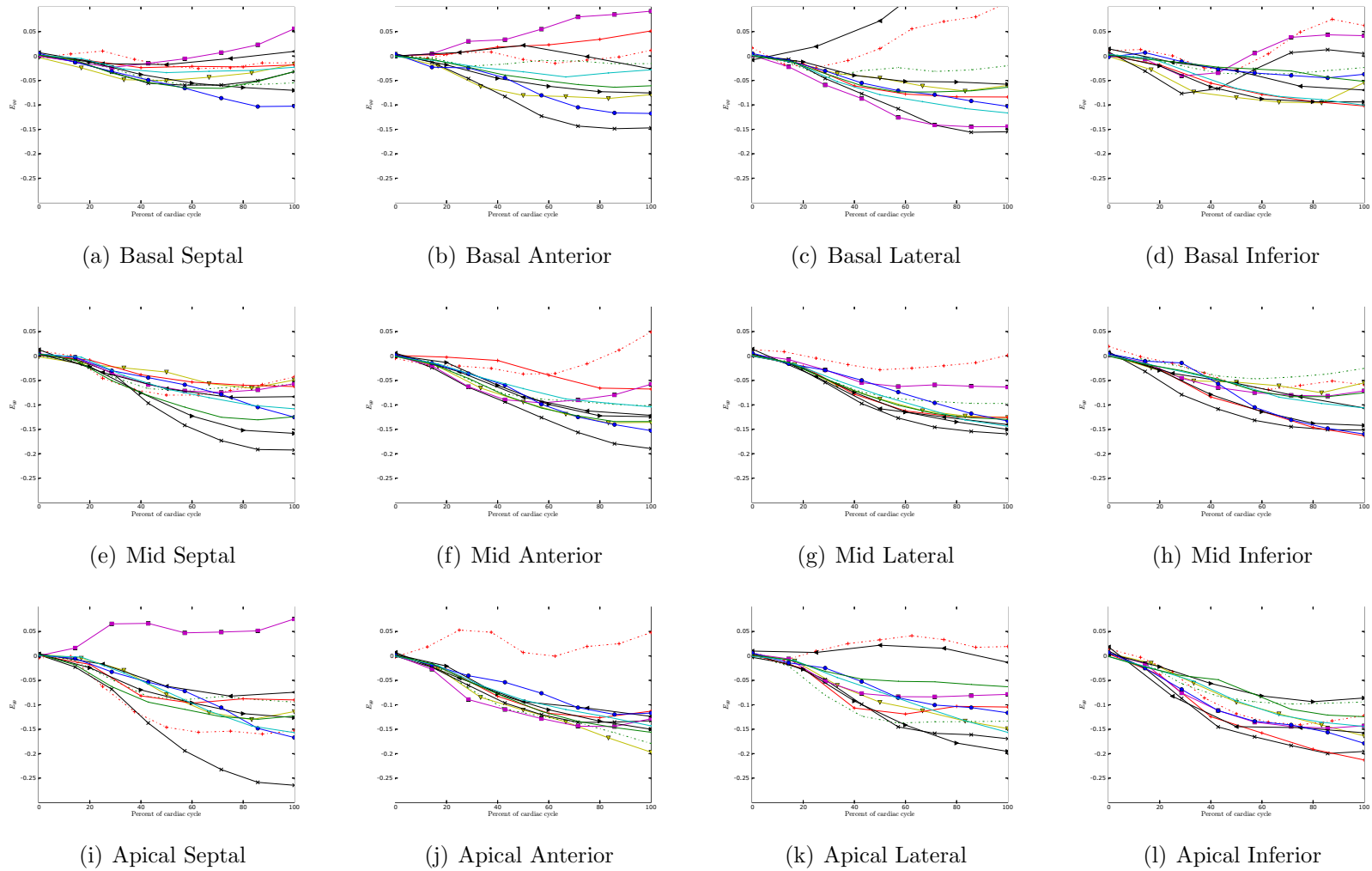
Figure 6.11: This figure shows plots of the circumferential strain in the different regions of the heart computed from the free-form deformations obtained from the registration algorithm for the 11 volunteers.

(a) Basal Septal   (b) Basal Anterior   (c) Basal Lateral   (d) Basal Inferior

(e) Mid Septal   (f) Mid Anterior   (g) Mid Lateral   (h) Mid Inferior

(i) Apical Septal   (j) Apical Anterior   (k) Apical Lateral   (l) Apical Inferior
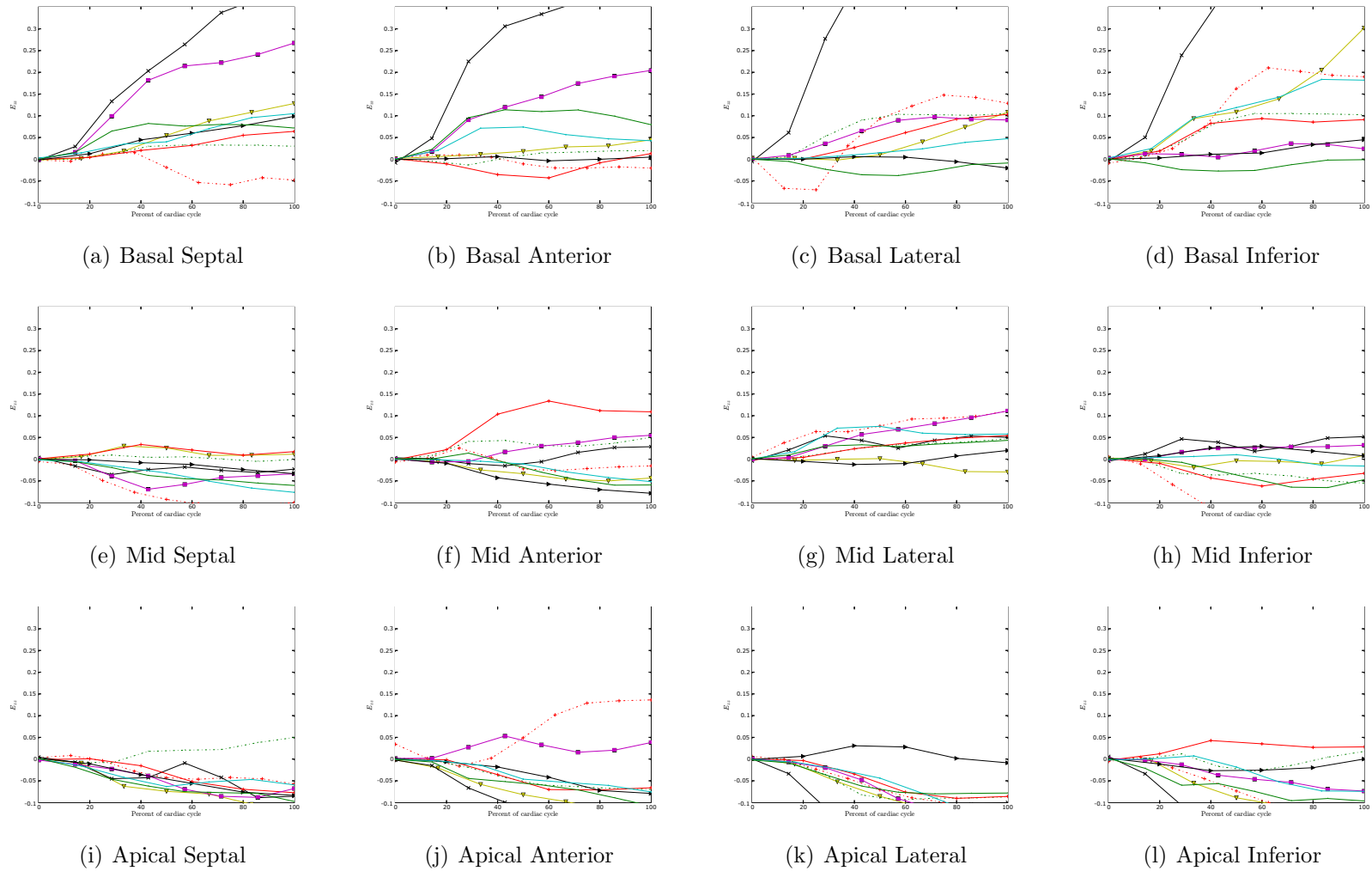
Figure 6.12: This figure shows plots of the longitudinal strain in the different regions of the heart computed from the free-form deformations obtained from the registration algorithm for the 11 volunteers.

Chapter 7

Construction of a Statistical Model for Cardiac Motion Analysis Using Nonrigid Image Registration

In this chapter we present a new technique for tracking the movement of the myocardium using a statistical motion model constructed from the motion fields in the hearts of several healthy volunteers. The key idea is to reduce the dimensions of the parameter space which needs to be searched in order to track the motion of the heart using the statistical model. To build the statistical model we track the motion of the myocardium in a group of volunteers using the nonrigid registration technique developed in chapter 4. We then map the motion fields obtained into a common reference coordinate system. A principal component analysis (PCA) is performed on the motion fields to extract the major modes of variation in the fields between the successive time frames. The modes of variation obtained are used to re-parameterize the FFDs and build our statistical motion model. The results of using our model to track the motion of the heart in normal volunteers are also presented.

This chapter is organized as follows. Section 7.1 begins with a brief review of re-

lated work on statistical shape models and statistical deformation models, section 7.2 describes how we have built our motion model of the heart, section 7.3 explains the model-based motion tracking, and section 7.4 presents our results for normal volunteers. Finally, section 7.5 summarizes the work presented in this chapter. The work presented in this chapter has been published in [32].

7.1 Related Work

7.1.1 Statistical Shape and Deformation Models

The key idea of statistical shape models (Cootes *et al* [38]) is to build a model of a particular class of shape given a set of examples of this shape. By examining the statistics of the example shapes and their variability the model can be just as flexible as a deformable model and yet be specific to the class of structures it represents. The specificity of the derived statistical shape model increases the robustness of image interpretation with the model even in the presence of noise or occlusion.

A statistical shape model is constructed from a set of labelled points derived from a set of images containing the example shapes. These points are usually chosen manually. The $N + 1$ shapes are represented in form of shape vectors, $\mathbf{X}_0, \cdots, \mathbf{X}_N$, where each shape vector $\mathbf{X}_i$ consists of a concatenation of $M + 1$ landmarks

$$\mathbf{x}_{ij} = [x_{ij}, y_{ij}, z_{ij}]^T, j = 0 \ldots M \tag{7.1}$$

describing the contour or surface of the shape of interest:

$$\mathbf{X}_i = [\mathbf{x}_{i0}^T, \mathbf{x}_{i1}^T, \ldots, \mathbf{x}_{iM}^T]^T = [x_{i0}, y_{i0}, z_{i0}, x_{i1}, y_{i1}, z_{i1}, \ldots, x_{iM}, y_{iM}, z_{iM}]^T \tag{7.2}$$

Since the example shapes may have arbitrary orientations and scales they must first be aligned so that the variability in the shape vectors resulting from these changes in pose and scale can be eliminated. Cootes *et al* describe an iterative

procedure for the alignment of the shapes in which the weighted sum of squares distances between equivalent points on different shapes is minimized. The weight assigned to a particular point is computed by measuring the variance in the distance of that point from the other points in the shape over the class of shapes involved. A point which tends to move a great deal with respect to the other points in the shape is given a low weight, while a point which is stationary with respect to the other points in the shape is given a high weight. The shape vectors $\mathbf{X}_i$ are assumed to have been aligned in this way.

Each shape vector $\mathbf{X}_i$ can be thought of as a point in a $3(M + 1)$ dimensional space and that the N points lie within some region of this space called the *allowable shape domain*. Any point within the allowable shape domain represents a plausible shape from the class of shapes being considered. Cootes *et al* assume that the allowable shape domain is approximately ellipsoidal and proceed to build the statistical shape model based on this assumption by performing a *principal component analysis* (PCA) on the example shape vectors [55]. The basic idea behind PCA is to transform the set of coordinate variables describing the shape vectors into a new set of coordinate variables which are uncorrelated with respect to each other. This is done as described in the following paragraphs.

The center of the allowable shape domain is the mean shape vector

$$\langle \mathbf{X} \rangle = \frac{1}{N + 1} \sum_{i=0}^{N} \mathbf{X}_i \tag{7.3}$$

and the deviation of each shape from the mean is:

$$d\mathbf{X}_i = \mathbf{X}_i - \langle \mathbf{X} \rangle \tag{7.4}$$

The covariance matrix, $\mathbf{S}$, of the mean corrected shape vectors is then computed using:

$$\mathbf{S} = \frac{1}{N + 1} \sum_{i=0}^{N} d\mathbf{X}_i d\mathbf{X}_i^T \tag{7.5}$$

Since $\mathbf{S}$ is a symmetric matrix it can be written in the form

$$\mathbf{S} = \mathbf{\Phi}\mathbf{\Lambda}\mathbf{\Phi}^T \qquad (7.6)$$

where $\mathbf{\Phi}$ is an orthogonal matrix and $\mathbf{\Lambda}$ is a diagonal matrix. This implies that:

$$\mathbf{\Phi}^T\mathbf{S}\mathbf{\Phi} = \mathbf{\Lambda} \qquad (7.7)$$

The above equation can be thought of as rotation in $3(M+1)$ dimensions which transforms the vector of correlated coordinate variables $d\mathbf{X}$ into a vector of uncorrelated coordinate variables $d\mathbf{Y}$. The components of the vector $d\mathbf{Y}$ are related to the components of the vector $d\mathbf{X}$ by:

$$d\mathbf{Y} = \mathbf{\Phi}^T d\mathbf{X} \qquad (7.8)$$

Equation 7.6 also implies that

$$\mathbf{S}\mathbf{\Phi} = \mathbf{\Phi}\mathbf{\Lambda} \qquad (7.9)$$

which is equivalent to

$$\mathbf{S}\phi_i = \lambda_i\phi_i \qquad (7.10)$$

where the ϕ_i are the $3(M+1)$ column vectors of $\mathbf{\Phi}$ and the λ_i the $3(M+1)$ diagonal elements of $\mathbf{\Lambda}$. The elements of the matrix $\mathbf{\Phi}$ can be found by solving for the eigenvectors and eigenvalues of the matrix $\mathbf{S}$.

Any shape, $\mathbf{X}$, in the training set can be rewritten in terms of the eigenvectors of the covariance matrix

$$\mathbf{X} = \langle\mathbf{X}\rangle + \sum_{j=0}^{3M-1} p_j\phi_j \qquad (7.11)$$

which is also written as:

$$\mathbf{X} = \langle\mathbf{X}\rangle + \mathbf{\Phi}\mathbf{p} \qquad (7.12)$$

$\mathbf{p}$ is called the parameter vector for the shape vector $\mathbf{X}$. The components p_j can be

found easily by making use of the fact that the ϕ_j are orthogonal to each other:

$$p_j = \phi_j^T(\mathbf{X} - \langle \mathbf{X} \rangle) = \phi_j^T d\mathbf{X} \tag{7.13}$$

The eigenvectors of the covariance matrix correspond to the axes of the $3(M + 1)$ dimensional ellipsoid, and the axes with the largest eigenvalues represent the transformed coordinate variables with the largest variances. In many cases most of the variation in the shape vectors can be described by a relatively small number of transformed variables, so that the the allowable shape domain can be approximated by an ellipsoid in a lower dimensional space. The number of dimensions, L, needed to approximate a particular shape vector can be chosen so that the sum of variances of the first L transformed variables is greater than or equal to a sufficiently large proportion, f, of the total variance λ_T:

$$\sum_{i=0}^{L} \lambda_i \geq f\lambda_T = f\sum_{i=0}^{3M} \lambda_i \tag{7.14}$$

The class of shapes under investigation can be reparameterized in terms of the major modes of variation given by the eigenvectors ϕ_i and new examples can also be generated from within the allowable shape domain by choosing a shape vector such that the components of the parameter vector, $\mathbf{p}$, are restricted to lie in a suitable range:

$$\mathbf{X} \approx \langle \mathbf{X} \rangle + \mathbf{\Phi}\mathbf{p} \tag{7.15}$$

A typical choice is 3 standard deviations for each mode, j, of variation:

$$-3\sqrt{\lambda_j} \leq p_j \leq 3\sqrt{\lambda_j} \tag{7.16}$$

The re-parameterization of the shape vector in terms of the major modes of variation provides a systematic way of generating new examples of the class of shapes under consideration. Cootes *et al* call the reparameterized shape models *active shape*

models (ASMs). ASMs have been used widely for image segmentation tasks [93, 59, 150] as well as for locating structures in brain and heart images and shape analysis [37, 160].

Active appearance models (AAMs) [36] are an extension of ASMs which attempt to model the intensities of pixels within the boundaries of the shape models. These have been used to segment images of the heart in MRI and ultrasound images of the heart [110, 18, 109].

The concept of *statistical deformation models* (SDMs) [75, 58] is closely related to the idea of statistical shape models, however the key difference is that the PCA is used to analyze motion fields rather than shape landmarks. This concept has been successfully applied for modelling of anatomical variability of neurological structures across a population of subjects.

7.2 Construction of a Statistical Model of Cardiac Motion

There are three main parts to the construction of our motion model. Firstly, in section 7.2.1, we define the notation used to describe the motion fields for all times between end-diastole and end-systole for the different subjects. Secondly, in section 7.2.2, the motion fields obtained are mapped into a common coordinate system so that a comparison across subjects may be performed. Finally, in section 7.2.3, we build our motion model by performing a principal component analysis (PCA) of the motion fields in the common coordinate system for all the volunteer subjects to obtain the most dominant modes of motion between any two consecutive time frames.

7.2.1 Myocardial Motion Analysis

The method we use to track the motion of the heart is described in chapter 4. In this section we define the notation used to describe the construction of the statistical motion model.

For a single subject, S, consider a point in the myocardium at end-diastole, $\mathbf{x}_0' = [x_0', y_0', z_0']^T$, which moves to another point $\mathbf{x}_{n\tau}' = [x_{n\tau}', y_{n\tau}', z_{n\tau}']^T$ at time $n\tau$. The transformation which gives the position that a point in the myocardium has moved to at time $n\tau$ is written as

$$\mathbf{T}^S(\mathbf{x}_0', n\tau) = \mathbf{x}_0' + \sum_{h=1}^{n} \mathbf{u}^{S,h}(\mathbf{x}_0') \tag{7.17}$$

where $\mathbf{u}^{S,h}$ are the FFDs computed in chapter 4. The actual motion fields are given by:

$$\mathbf{u}^S(\mathbf{x}_0', n\tau) = \mathbf{T}^S(\mathbf{x}_0', n\tau) - \mathbf{x}_0' = \sum_{h=1}^{n} \mathbf{u}^{S,h}(\mathbf{x}_0') \tag{7.18}$$

The FFDs, $\mathbf{u}^{S,h}$, which describe the motion between two successive time frames are used to construct our statistical motion model.

7.2.2 Transformation of Myocardial Motion Fields

To make an objective comparison of the cardiac motion fields derived from different subjects requires their alignment in a common coordinate system. For this purpose we use a technique developed by Rao *et al* [134, 133] which aligns cardiac MR images from different subjects into a common spatial coordinate system and also transforms the motion fields from these subjects into a common spatial coordinate system.

7.2.2.1 Temporal Alignment of Motion Fields

Typically, the length of the cardiac cycles will vary from subject to subject. Furthermore, in prospectively gated MR imaging acquisitions, the trigger delay and temporal resolution of the acquired images can vary from acquisition to acquisi-

tion. To compensate for the temporal misalignment resulting from these factors, we manually determine an affine temporal mapping which aligns the end-diastolic and end-systolic time points of each subject S with the corresponding time points in a reference subject R. Using this temporal mapping we can align and re-sample the motion fields from different subjects into a common temporal coordinate system.

Suppose that the end-systolic time frames for subjects S and R are n_S and n_R respectively. To simplify the discussion assume also that the end-diastolic time frames are 0 for both subjects and the time interval between end-diastole and end-systole is the same for both volunteers, i.e., $n_S \tau_S = n_R \tau_R$. The sequence of FFDs describing the motion fields for subjects S and R have n_S and n_R levels respectively. We need to re-sample the sequence of FFDs describing the motion field for subject S so that it has the same number levels as subject R. This is achieved by linear interpolation. For example the control point displacement vectors of the sequence of FFDs of subject S re-sampled so that it has n_R levels can be computed easily from the following equation

$$\mathbf{u}^S(\mathbf{x}', n\tau_R) = (1 - \alpha)\mathbf{u}^S(\mathbf{x}', n_a\tau) + \alpha\mathbf{u}^S(\mathbf{x}', (n_a + 1)\tau) \qquad (7.19)$$

where

$$n_a = \left\lfloor \frac{n}{n_R} n_S \right\rfloor \qquad (7.20)$$

$$\alpha = \frac{n}{n_R} n_S - n_a \qquad (7.21)$$

and $n \in \{1, 2, \ldots, n_R - 1\}$. When $n = n_R$

$$\mathbf{u}^S(\mathbf{x}', n_R\tau_R) = \mathbf{u}^S(\mathbf{x}', n_S\tau_S) \qquad (7.22)$$

7.2.2.2 Spatial Alignment of Motion Fields

We now have a set of transformations for each subject which have the same number of levels and which cover the same portion of the cardiac cycle (in our case this is from end-diastole to end-systole). However, each motion field is still defined in its own intrinsic spatial coordinate system. To map the motion fields into a common spatial coordinate system we also need to calculate a mapping between the end-diastolic anatomy of subject S and the reference subject R. We use this mapping to transform the myocardial motion fields $\mathbf{u}^S(\mathbf{x}, n\tau_R)$ into the coordinate system of R. The transformation between subjects R and S can be obtained using a registration of the end-diastolic images of both subjects. This yields a mapping $\mathbf{F}$ between the coordinate systems of subjects R and S which are represented by (x, y, z) and (x', y', z') respectively:

$$\mathbf{F} : (x, y, z) \longmapsto (x'(x, y, z), y'(x, y, z), z'(x, y, z)) \tag{7.23}$$

We are now in a position to transform the motion fields of the subject S defined in the coordinate system (x', y', z') into the coordinate system of R, (x, y, z). If the motion vector at a point with position vectors $\mathbf{x}'_0 = [x'_0, y'_0, z'_0]^T$ in the coordinate system of S is equal to $\mathbf{u}^S$, this will transform to a vector $\tilde{\mathbf{u}}^S$ at the location $\mathbf{x}_0 = [x_0, y_0, z_0]^T$ in the coordinate system of R, where:

$$\mathbf{x}_0 = \mathbf{F}^{-1}(\mathbf{x}'_0) \tag{7.24}$$

In order to determine $\tilde{\mathbf{u}}^S$, consider a path

$$\mathcal{L} : \mathbf{x}(\theta), \theta \in [0, 1] \tag{7.25}$$

defined in the coordinate system of R that represents the transformed motion vector, i.e.,

$$\mathbf{x}(0) \quad = \quad \mathbf{x}_0 \tag{7.26}$$

$$\mathbf{x}(1) \quad = \quad \mathbf{F}^{-1}(\mathbf{x}'_0 + \mathbf{u}^S) \tag{7.27}$$

Integrating the differential elements of the path from $\theta = 0$ to $\theta = 1$ gives:

$$\tilde{\mathbf{u}}^S = \mathbf{x}(1) - \mathbf{x}(0) = \int_0^1 \frac{d\mathbf{x}(\theta)}{d\theta} \, d\theta \tag{7.28}$$

Writing $\mathbf{x}'(\theta)$ as the path $\mathcal{L}$ defined in the coordinate system of S and by using the chain rule for differentiation the components of $d\mathbf{x}'(\theta)/d\theta$ are

$$\frac{dx'}{d\theta} \quad = \quad \frac{\partial x'}{\partial x}\frac{dx}{d\theta} + \frac{\partial x'}{\partial y}\frac{dy}{d\theta} + \frac{\partial x'}{\partial z}\frac{dz}{d\theta} \tag{7.29}$$

$$\frac{dy'}{d\theta} \quad = \quad \frac{\partial y'}{\partial x}\frac{dx}{d\theta} + \frac{\partial y'}{\partial y}\frac{dy}{d\theta} + \frac{\partial y'}{\partial z}\frac{dz}{d\theta} \tag{7.30}$$

$$\frac{dz'}{d\theta} \quad = \quad \frac{\partial z'}{\partial x}\frac{dx}{d\theta} + \frac{\partial z'}{\partial y}\frac{dy}{d\theta} + \frac{\partial z'}{\partial z}\frac{dz}{d\theta} \tag{7.31}$$

These can be written in matrix form as

$$\frac{d\mathbf{x}'(\theta)}{d\theta} = J(\mathbf{x}(\theta))\frac{d\mathbf{x}(\theta)}{d\theta} \tag{7.32}$$

where

$$J(\mathbf{x}(\theta)) = \left.\begin{bmatrix} \frac{\partial x'}{\partial x} & \frac{\partial x'}{\partial y} & \frac{\partial x'}{\partial z} \\ \frac{\partial y'}{\partial x} & \frac{\partial y'}{\partial y} & \frac{\partial y'}{\partial z} \\ \frac{\partial z'}{\partial x} & \frac{\partial z'}{\partial y} & \frac{\partial z'}{\partial z} \end{bmatrix}\right|_{\mathbf{x}=\mathbf{x}(\theta)} \tag{7.33}$$

Multiplying both sides of equation 7.32 by $J^{-1}(\mathbf{x}(\theta))$ we obtain

$$\frac{d\mathbf{x}(\theta)}{d\theta} = J^{-1}(\mathbf{x}(\theta))\frac{d\mathbf{x}'(\theta)}{d\theta} \tag{7.34}$$

and substituting into equation 7.28 we finally get:

$$\tilde{\mathbf{u}}^S = \int_0^1 J^{-1}(\mathbf{x}(\theta)) \frac{d\mathbf{x}'(\theta)}{d\theta} \, d\theta \qquad (7.35)$$

This integral can then be approximated by dividing the interval $[0, 1]$ into n_θ subintervals of length $\delta\theta$,

$$\tilde{\mathbf{u}}^S \simeq \sum_{k=0}^{n_\theta - 1} J^{-1}(\mathbf{x}^{(k)})(\mathbf{x}'^{(k+1)} - \mathbf{x}'^{(k)}) \qquad (7.36)$$

where $\mathbf{x}'^{(k)} = \mathbf{x}'_0 + k\delta\theta\mathbf{u}^S$ and $\mathbf{x}^{(k)} = \mathbf{F}^{-1}(\mathbf{x}'^{(k)})$. Figure 7.1 illustrates how equation 7.36 is evaluated using the recursion formula $\mathbf{f}$ given by:

$$\mathbf{f}(\mathbf{x}'^{(0)}) \;=\; \mathbf{x}_0 \qquad (7.37)$$

$$\mathbf{f}(\mathbf{x}'^{(k+1)}) \;=\; \mathbf{f}(\mathbf{x}'^{(k)}) + J^{-1}(\mathbf{f}(\mathbf{x}'^{(k)}))(\mathbf{x}'^{(k+1)} - \mathbf{x}'(k)),$$

$$k = 0, \ldots, n_\theta - 1 \qquad (7.38)$$

7.2.3 Principal Component Analysis of Myocardial Motion Fields

The motion fields for each subject at this stage have been re-sampled temporally so that the transformations describing them have the same number of levels and they have also been mapped into the common coordinate system of subject R (the ˜ is used to signify this fact):

$$\tilde{\mathbf{T}}^S(\mathbf{x}, n\tau) = \mathbf{x} + \sum_{h=1}^{n} \tilde{\mathbf{u}}^{S,h}(\mathbf{x}) \qquad (7.39)$$

In our application we apply a PCA directly to the free-form deformations, $\tilde{\mathbf{u}}^{S,h}$, describing the cardiac motion fields [140, 139]. Suppose that we have $N+1$ free-form
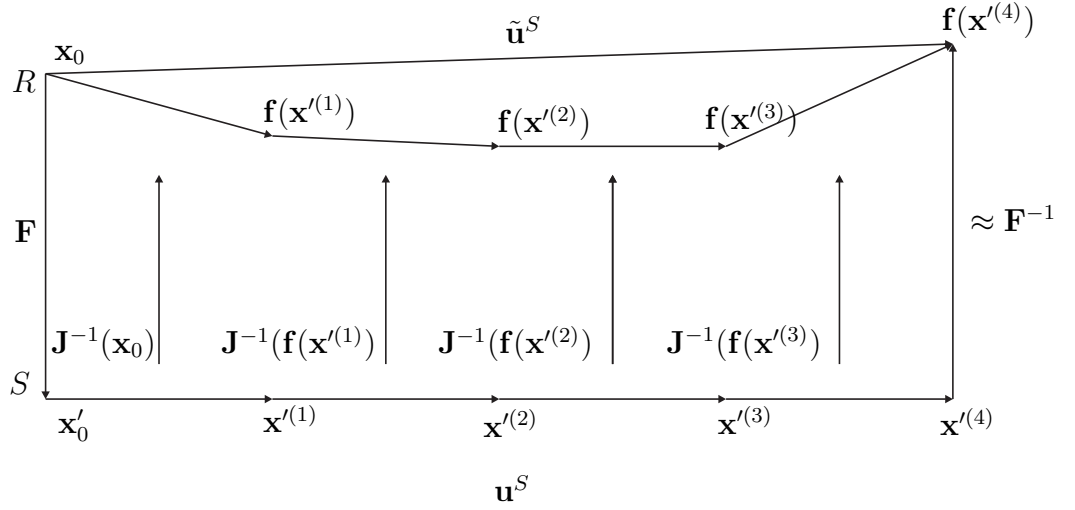
Figure 7.1: This figure (from [133]) illustrates how the motion vector $\mathbf{u}^S$ in the coordinates system of the subject S is transformed into the coordinate system of R. The transformation $\mathbf{F}$ is used to transform the point $\mathbf{x}_0$ into the coordinate system of S. The motion vector at the transformed point $\mathbf{x}'_0$ is then divided into n_θ subintervals (here $n_\theta = 4$). The vector $\mathbf{x}'^{(1)} - \mathbf{x}'^{(0)}$ is then transformed by the Jacobian matrix of the transformation $\mathbf{F}$ evaluated at $\mathbf{x}_0$ to find the transformed vector in the coordinate system of R. The transformed vector is then appended to $\mathbf{x}_0$ to obtain the position $\mathbf{f}(\mathbf{x}'^{(1)})$ at which the Jacobian matrix is evaluated and then used to transform the interval $\mathbf{x}'^{(2)} - \mathbf{x}'^{(1)}$. The subsequent intervals are transformed in a similar way and appended to yield the final transformed vector $\tilde{\mathbf{u}}^S$.

deformations described as vectors:

$$\tilde{\mathbf{X}}_0, \tilde{\mathbf{X}}_1, \cdots, \tilde{\mathbf{X}}_N \tag{7.40}$$

For each subject, the vector $\tilde{\mathbf{X}}_i$ corresponds to a concatenation of $M + 1 = (n_x + 1) \times (n_y + 1) \times (n_z + 1)$ 3D control point displacement vectors

$$\tilde{\mathbf{X}}_i = [\tilde{\mathbf{d}}_0^T, \tilde{\mathbf{d}}_1^T, \cdots, \tilde{\mathbf{d}}_M^T]^T \tag{7.41}$$

describing the motion of the myocardium between two particular time frames. The goal of SDMs is to approximate the distribution of $\tilde{\mathbf{X}}$ using a parameterized linear model of the form

$$\tilde{\mathbf{X}} = \left\langle \tilde{\mathbf{X}} \right\rangle + \tilde{\mathbf{\Phi}}\tilde{\mathbf{p}} \tag{7.42}$$

where $\left\langle \tilde{\mathbf{X}} \right\rangle$ is the average of the control point displacement vectors (or average

motion field) for all $N + 1$ subjects

$$\left\langle \tilde{\mathbf{X}} \right\rangle = \frac{1}{N+1} \sum_{i=0}^{N} \tilde{\mathbf{X}}_i \qquad (7.43)$$

and $\tilde{\mathbf{p}}$ is the model parameter vector. The columns of the matrix $\tilde{\mathbf{\Phi}}$ are formed from the eigenvectors of the covariance matrix $\tilde{\mathbf{S}}$:

$$\tilde{\mathbf{S}} = \frac{1}{N} \sum_{i=0}^{N} \left(\tilde{\mathbf{X}}_i - \left\langle \tilde{\mathbf{X}} \right\rangle \right) \left(\tilde{\mathbf{X}}_i - \left\langle \tilde{\mathbf{X}} \right\rangle \right)^T \qquad (7.44)$$

From this, we can calculate the principal modes of variation of the control point displacement vectors (or the associated FFD) as the eigenvectors $\tilde{\phi}_i$ and corresponding eigenvalues $\tilde{\lambda}_i$ (sorted so that $\tilde{\lambda}_i \geq \tilde{\lambda}_{i+1}$) of $\tilde{\mathbf{S}}$. If $\tilde{\mathbf{\Phi}}$ contains the $L < \min\{M + 1, N + 1\}$ eigenvectors corresponding to the largest nonzero eigenvalues, we can approximate any motion field within the population group under investigation using equation 7.42 where $\tilde{\mathbf{\Phi}} = (\tilde{\phi}_0 | \tilde{\phi}_2 | \cdots | \tilde{\phi}_{L-1})$ and $\tilde{\mathbf{p}}$ is a L dimensional vector given by $\tilde{\mathbf{p}} = \tilde{\mathbf{\Phi}}^T \left(\tilde{\mathbf{X}} - \left\langle \tilde{\mathbf{X}} \right\rangle \right)$. The vector $\tilde{\mathbf{p}}$ defines the parameters of the statistical motion model. By varying these parameters we can generate different instances of a FFD which describes the class of motion fields under analysis using equation 7.42.

There are two different ways in which we can perform a statistical analysis of the motion fields $\tilde{\mathbf{u}}^{S,h}$. We can either treat the motion fields between any two time frames separately and perform a separate PCA of the motion fields for each time interval. Alternatively, we can pool all motion fields for all subjects and for all times and perform only a single PCA to build a statistical model of cardiac motion. These two ways of performing the PCA are illustrated in figures 7.2(a) and 7.2(b) respectively. In the following we will discuss both methods.
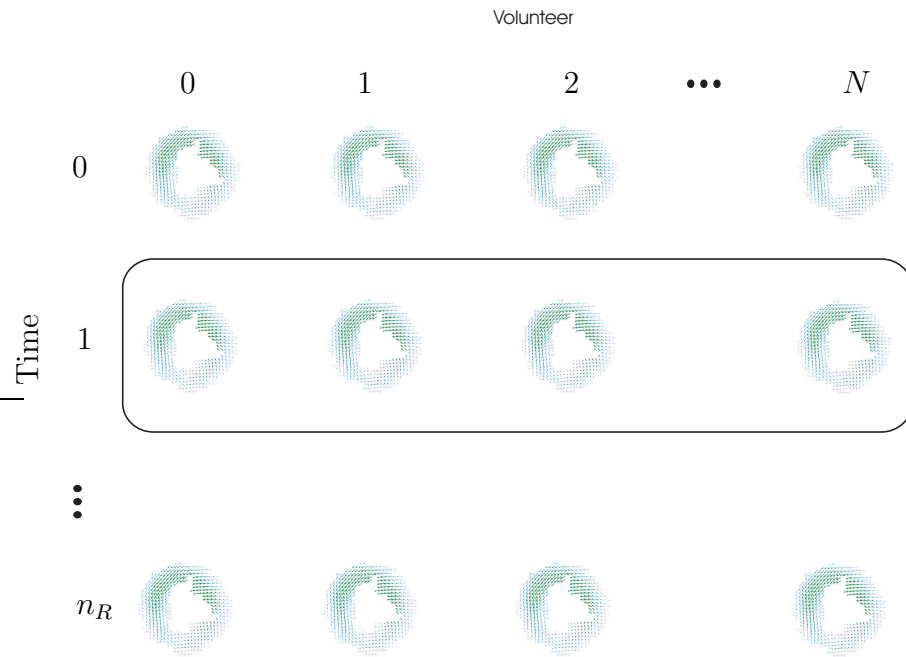
(a) Time Dependent PCA
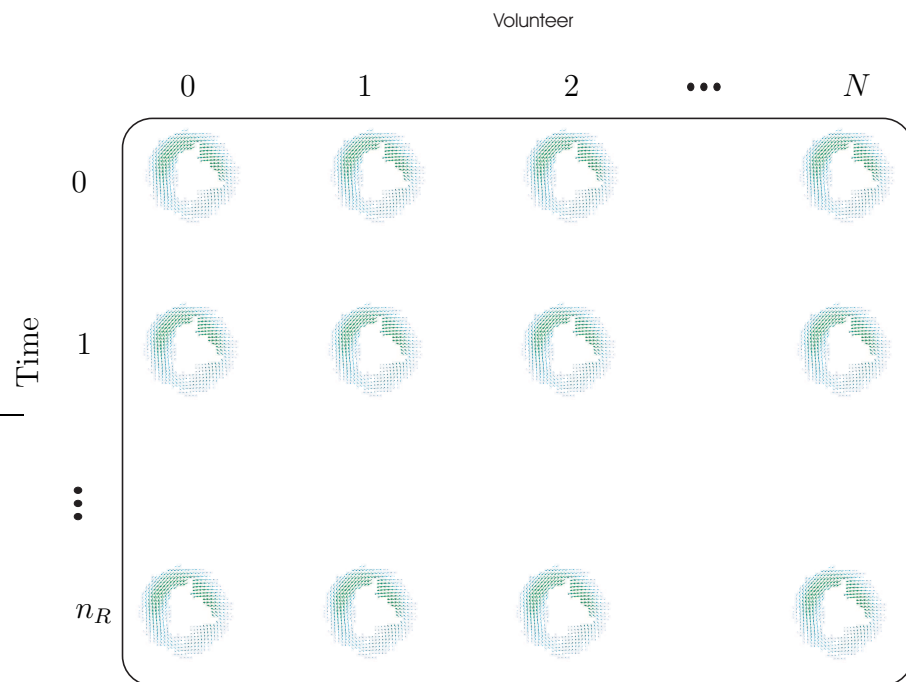
(b) Time Independent PCA

Figure 7.2: The two ways in which the PCA can be performed when building the statistical motion model. The motion fields between any two time frames can be treated separately and a set of PCAs can be performed for each time interval (a), or alternatively the motion fields for all subjects and for all time frames can be pooled together and a single PCA can be performed.

7.2.3.1 Building Separate Statistical Motion Models For Each Phase of the Cardiac Cycle

Between any two times we have a set of FFDs describing the motion of the heart between those two times. For example between $t = 0$ and $t = \tau$ these are given by the first levels of $\tilde{\mathbf{u}}^{S_i}$ for the different subjects S_i:

$$\tilde{\mathbf{u}}^{S_0,1}, \tilde{\mathbf{u}}^{S_1,1}, \dots, \tilde{\mathbf{u}}^{S_N,1} \tag{7.45}$$

These motion fields are described by a set of control point displacement vectors for each subject

$$\tilde{\mathbf{X}}^{S_0,1}, \tilde{\mathbf{X}}^{S_1,1}, \dots, \tilde{\mathbf{X}}^{S_N,1} \tag{7.46}$$

where subject S_0 is the same as subject R.

We perform a PCA on these control point vectors to obtain the major modes of variation in the motion of the heart between time frames 0 and 1 (i.e. at the beginning of the contraction). These are described by a set of eigenvectors, $\tilde{\boldsymbol{\Phi}}^1$ and eigenvalues, $\tilde{\boldsymbol{\Lambda}}^1$. Similarly we can perform a PCA on the control point vectors describing the motion of the heart between all other successive time frames. This yields n_R sets of eigenvectors and eigenvalues describing the major modes of variation between those successive time frames. The eigenvectors and values obtained

$$\tilde{\boldsymbol{\Phi}}^h, \tilde{\boldsymbol{\Lambda}}^h \quad \text{where } h \in \{1, 2, \dots n_R\} \tag{7.47}$$

are then used to parameterize our statistical motion model. The advantage of this method is that by restricting the PCA to the motion fields at a particular time instant the tracking will use only those variations in motion specific to the time instant in question.

Figure 7.3 shows the first mode of variation in the transformed motion fields for the start of the cardiac cycle.
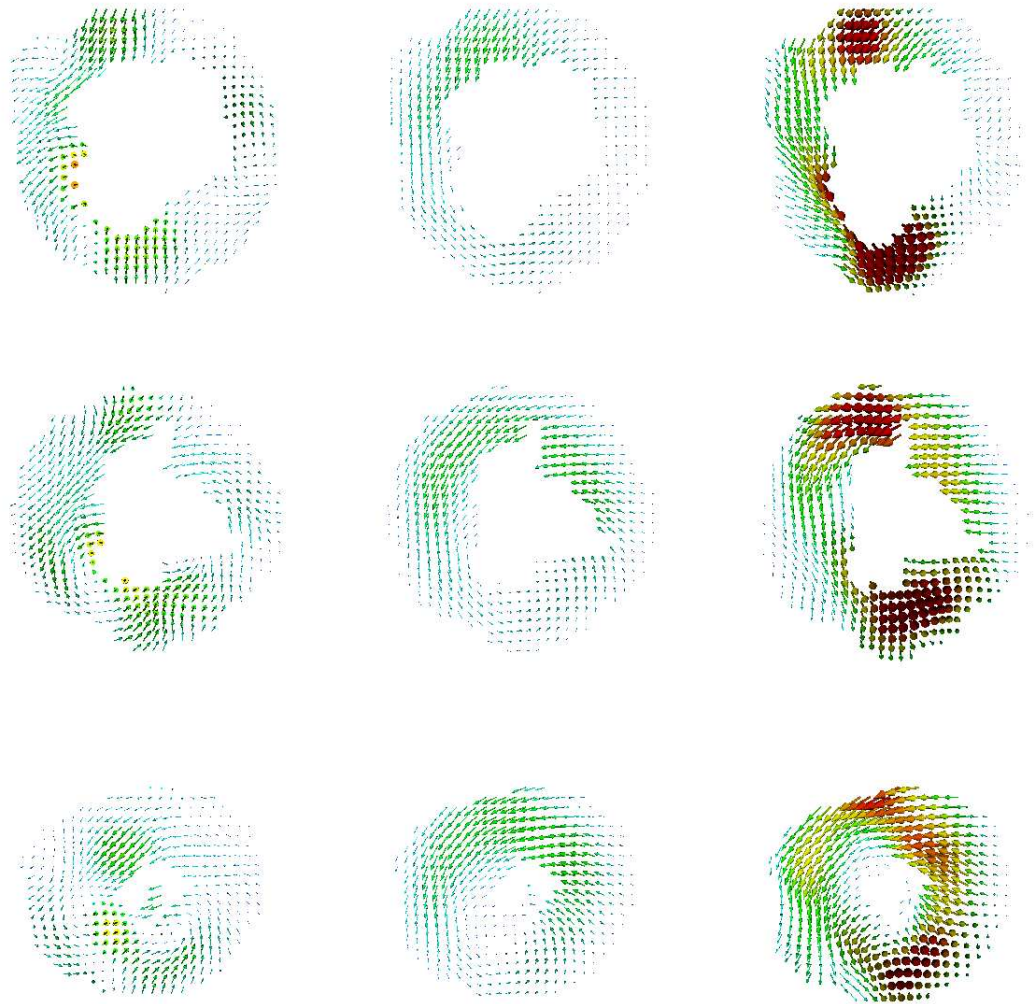
Figure 7.3: Arrow plots showing the first mode of variation in the computed deformation fields in the reference coordinate system of one volunteer at the start of the cardiac cycle. The variation in the deformation fields are shown, from top to bottom, in the basal, mid-ventricular and apical SA slices respectively. The second column represents the mean deformation field; and the first and third columns correspond to the subtraction and addition respectively of three standard deviations in the first mode of variation of the deformation field.

7.2.3.2 Building a Single Statistical Motion Model for the Entire Cardiac Cycle

Pooling the cardiac motion fields, $\tilde{\mathbf{u}}^{S_i,h}$, for all subjects and between all time frames and performing a PCA on these motion fields yields a single set of eigenvectors, $\tilde{\boldsymbol{\Phi}}$, and eigenvalues, $\tilde{\boldsymbol{\Lambda}}$ for all time frames. Our model now consists of a sequence of FFDs with n_R levels but with each level being parametrized by the single set of eigenvectors $\tilde{\boldsymbol{\Phi}}$. The eigenvectors $\tilde{\boldsymbol{\Phi}}$ contain information about both the intra- and intersubject variation in the cardiac motion. The model can be used to track the motion of the heart by registering the sequence of SA and LA images taken during systole to the SA and LA images taken at end-diastole by optimizing the model parameter vectors $\tilde{\mathbf{p}}$ at each level. The advantage of this method is that it does not require a temporal alignment of the cardiac cycle of the subject whose heart motion is being tracked, but the disadvantage of this method is that it does not take into account the variation in the motion of the heart over time. Figure 7.4 shows the first mode of variation in the deformation field over the entire cardiac cycle.

7.3 Model-based Nonrigid Registration for Cardiac Motion Tracking

To use the statistical motion model for tracking the motion in a particular reference subject R we need to construct the statistical motion model in the coordinate system of that subject. In our current implementation we are using an affine transformation to model the mapping $\mathbf{F}$. As a result of this $J^{-1}(\mathbf{x}^{(k)})$ will be constant and the expression in equation 7.36 reduces to:

$$\tilde{\mathbf{d}}^S \simeq J^{-1}(\mathbf{d}^S) \tag{7.48}$$
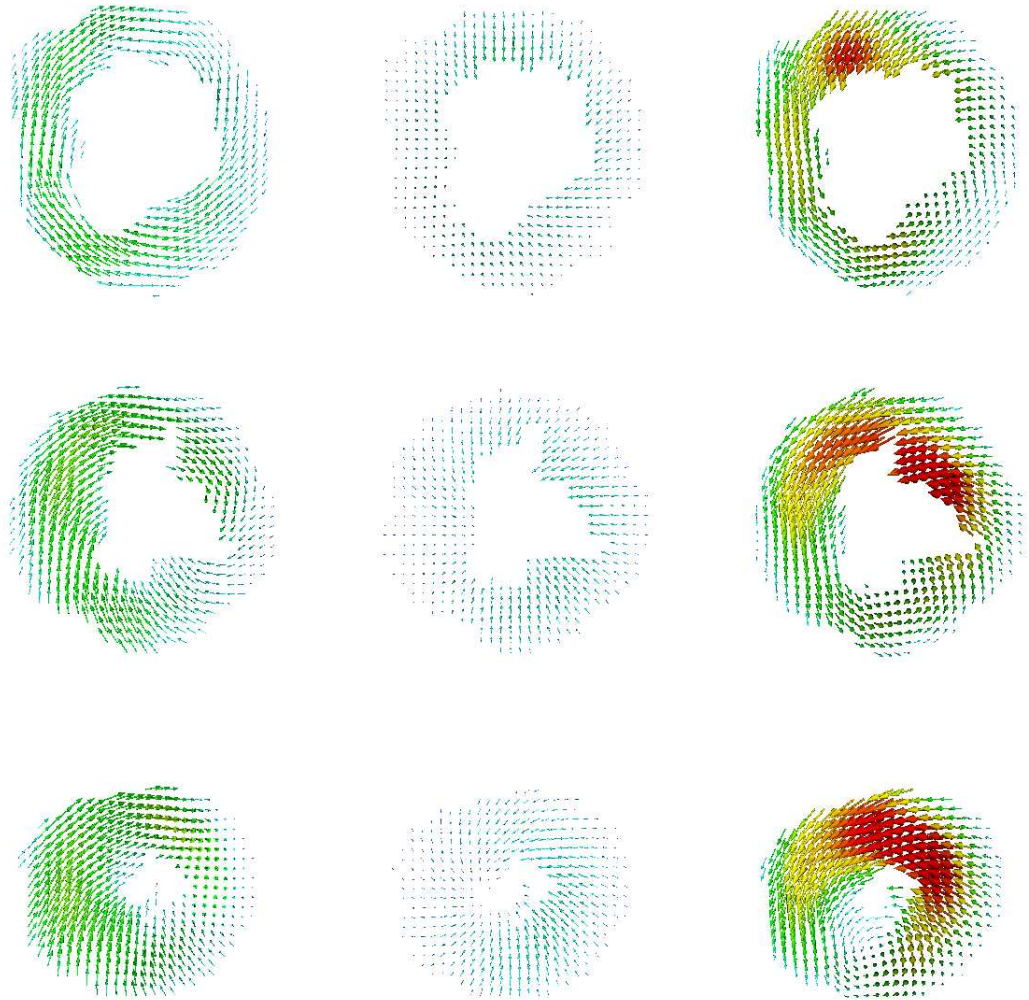
Figure 7.4: Arrow plots showing the first mode of variation in the computed deformation fields in the reference coordinate system of one volunteer over the entire cardiac cycle. The variation in the deformation fields are shown, from top to bottom, in the basal, mid-ventricular and apical SA slices respectively. The second column represents the mean deformation field; and the first and third columns correspond to the subtraction and addition respectively of three standard deviations in the first mode of variation of the deformation field.

Applying this technique to each of the motion fields of the subject gives us a set of transformed motion fields $\tilde{\mathbf{u}}^S(\mathbf{x})$ from which we calculate the statistical motion model as described in the previous section. Using this statistical motion model we can re-parameterize the FFD model used for the motion tracking in section 7.2.1 via the modes of variation learned from the motion fields:

$$
\mathbf{u}^{S,h}(\mathbf{x}) = \sum_{i=0}^{n_x}\sum_{j=0}^{n_y}\sum_{k=0}^{n_z} \beta^3\left(\frac{x - x_{i,j,k}}{\delta_x}\right) \beta^3\left(\frac{y - y_{i,j,k}}{\delta_y}\right) \beta^3\left(\frac{z - z_{i,j,k}}{\delta_z}\right) \times \\
\left(\left\langle \tilde{\mathbf{X}}^h \right\rangle + \tilde{\boldsymbol{\Phi}}^h \mathbf{p}^h\right)_{i,j,k} \tag{7.49}
$$

Here, the control points of the FFD are represented as a linear combination of the principal modes of variation. Rather than optimizing the location of the control points, one can optimize the parameter vector $\mathbf{p}^h$ which controls the modes of the FFD but provides a much smaller number of degrees of freedom than the number of control points. This can significantly reduce the number of degrees of freedom for the motion tracking and the associated computational complexity, while constraining the registration to statistically likely types of motion.

To track the motion of the heart in a subject we use exactly the same procedure given in figure 4.6 for all time frames between end-diastole and end-systole except that now the free-form deformations are controlled by the parameter vector.

7.4 Results

Tagged MR data from 17 healthy volunteers was acquired with a Siemens Sonata 1.5 T scanner and a Philips Gyroscan Intera 1.5 T scanner consisting of series of SA and LA slices. A cine breath-hold sequence with a SPAMM tag pattern was used with imaging being done at end expiration. The image voxel sizes were typically $1.40 \times 1.40 \times 7$ mm, with the distance between slices being 10 mm. We tracked the movement of the myocardium in all volunteers and transformed the motion fields obtained into a common coordinate system as described in sections 7.2.1 and 7.2.2.

Two separate statistical models of the motion of the heart were then built. In the first model (section 7.2.3.1), each level in the multi-level free form transformation used for tracking the heart was parametrized by a separate set of eigenvectors describing the major modes of variation in the motion of the heart at the corresponding time frame. We refer to this as the time-dependent motion model. In the second model (section 7.2.3.2), each level in the multi-level free form transformation used for tracking the heart was parametrized by a single set of eigenvectors describing the major modes of variation in the motion of the heart over the entire cardiac cycle. We refer to this as the time-independent model.

Figure 7.5 shows a plot of the variance and cumulative variance explained by the principal modes of the time-dependent motion model at the start of the cardiac cycle. While figure 7.6 shows the corresponding plot for the time-independent motion model. The first 12 principal modes of the time-dependent model explained 95% of the total variance in the volunteer motion fields, while the first 49 principal modes of the time-independent model explained 95% of the total variance in the motion fields.

To validate the quality of the statistical motion models, we have used both the time-dependent and time-independent motion models to track the motion of the heart in 8 healthy volunteers for all time frames between end-diastole and end-systole. For this purpose we have constructed both motion models without using the motion fields of the volunteer hearts which were tracked. To compare how well the motion tracking had been performed using the two models an observer manually tracked the motion of tag intersection points in 4 different imaging planes for the volunteers. The estimated displacements of the tag intersection points obtained from our statistical motion models were then compared with the true displacements measured by the human observer. The results of the motion tracking for the two models are shown in figures 7.7 and 7.8 respectively for the different volunteers. Here we have plotted the RMS error in the displacement of tag intersection points as a function of time.
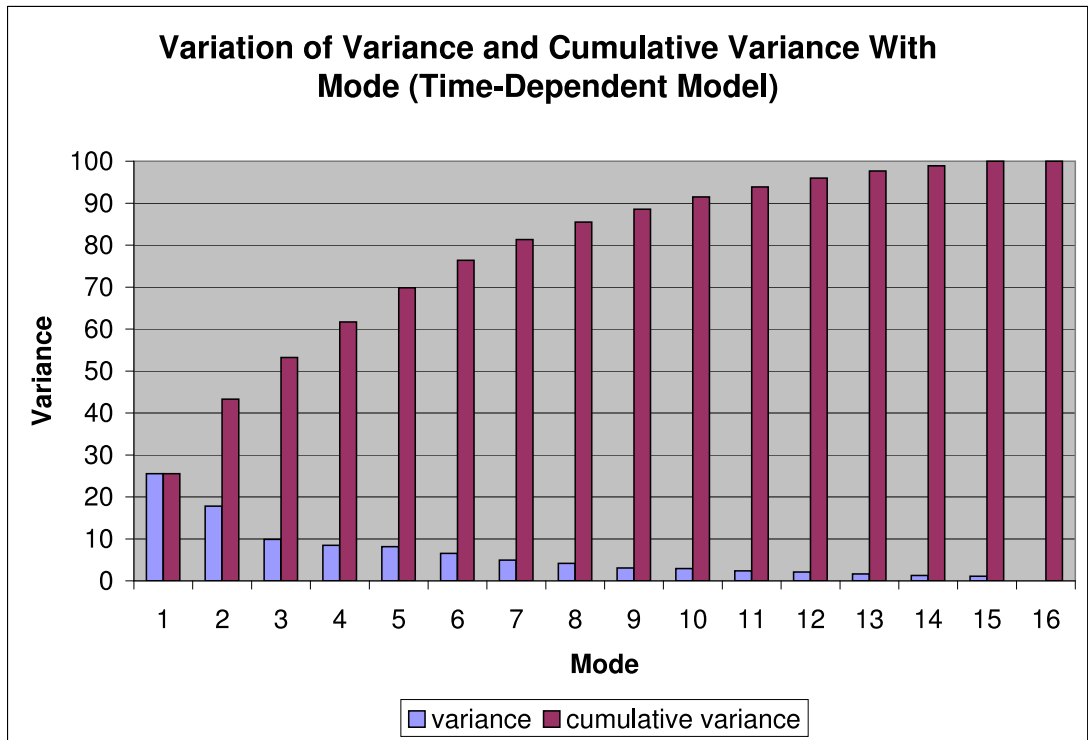
Figure 7.5: Plot of the variance and cumulative variance in the motion fields explained by the principal modes of the time-dependent statistical deformation model at the start of the cardiac cycle.
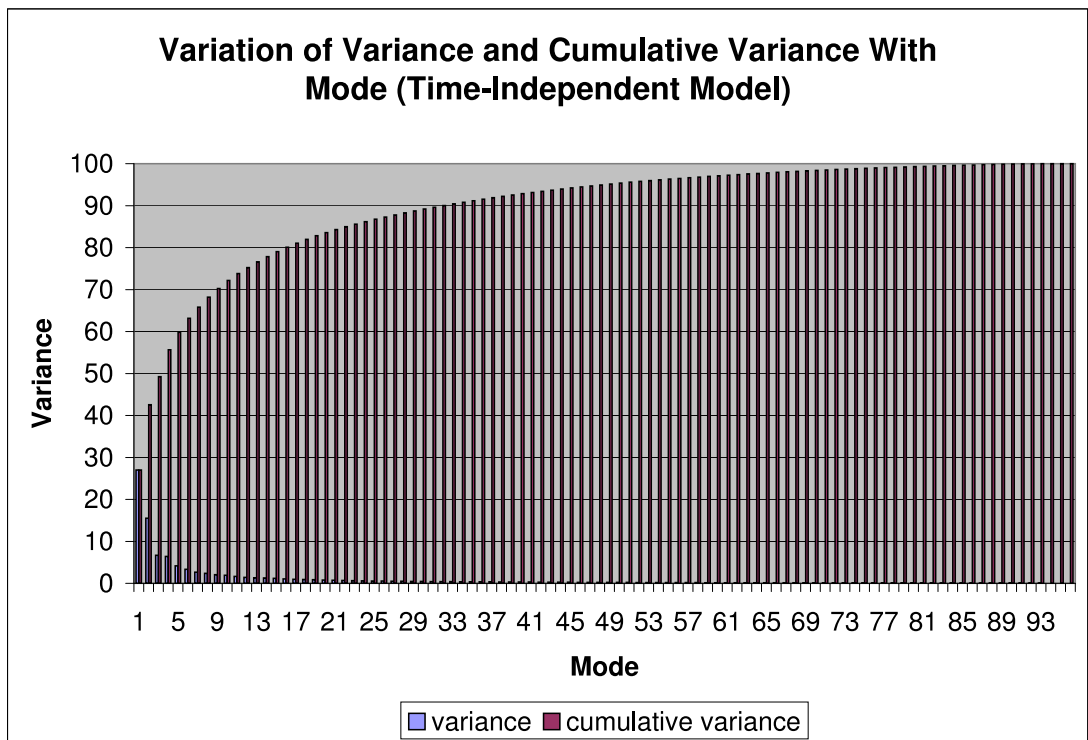
Figure 7.6: Plot of the variance and cumulative variance in the motion fields explained by the principal modes of the time-independent statistical deformation model.
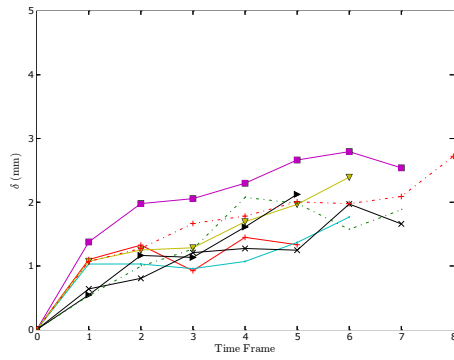
(a) Apical SA Slice
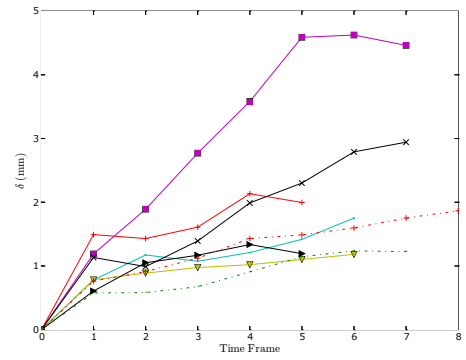
(b) Mid-ventricular SA Slice
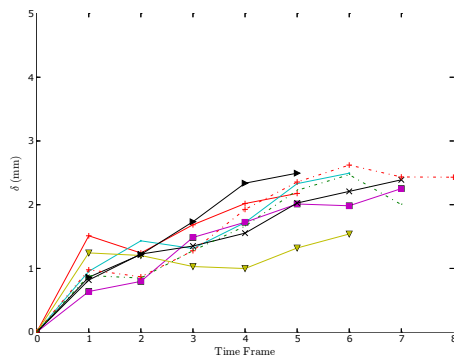
(c) Basal SA Slice
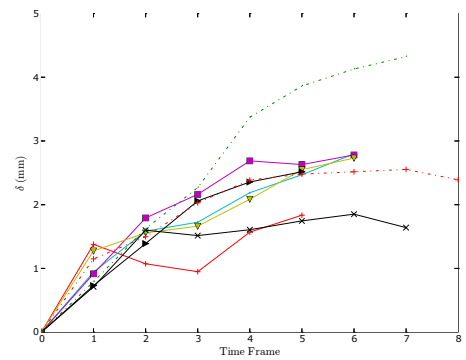
(d) Horizontal LA Slice

Figure 7.7: These graphs show the variation of the RMS error in the estimated in-plane displacements obtained from the registration algorithm as compared with the manual tracking of tag intersection points in different slices for the 11 volunteers using the time-dependent statistical deformation model.
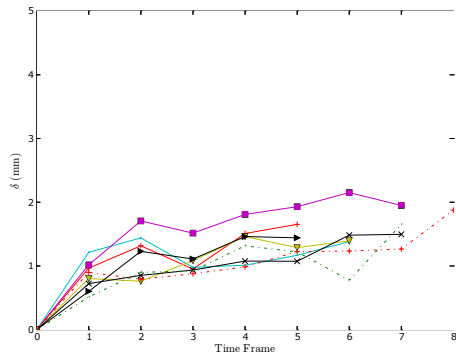
(a) Apical SA Slice
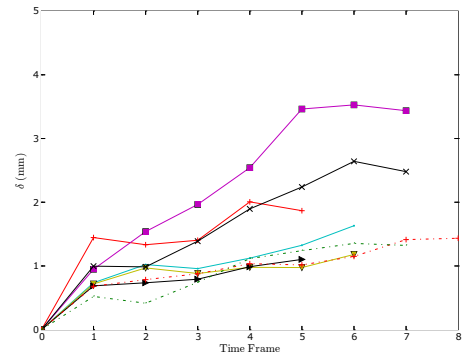
(b) Mid-ventricular SA Slice
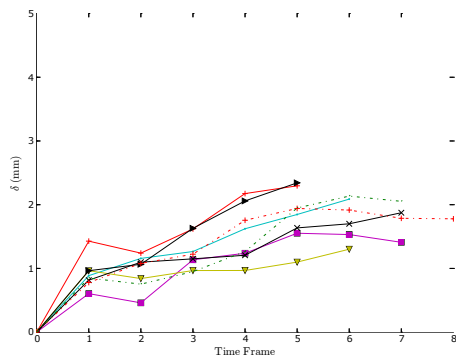
(c) Basal SA Slice
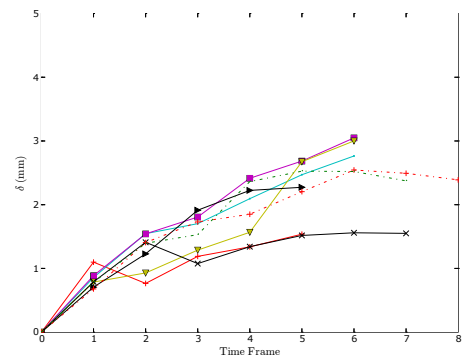
(d) Horizontal LA Slice

Figure 7.8: These graphs show the variation of the RMS error in the estimated in-plane displacements obtained from the registration algorithm as compared with the manual tracking of tag intersection points in different slices for the 11 volunteers using the time-independent statistical deformation model.

Figures 7.9 and 7.10 show the performance of the motion tracking visually for a volunteer using the time-dependent and time-independent models.

As can be seen from a comparison of figures 7.7 and 7.8 the time-independent motion model is able to track the motion of the myocardium much more easily than the time-dependent model. This is because the FFDs from which the time-dependent model has been constructed are a subset of the FFDs from which the time-independent motion model has been constructed.

7.5 Summary

In this chapter we have introduced a new technique for tracking the movement of the myocardium using a statistical model derived from the motion fields in the hearts of several healthy volunteers. To build the statistical model we have tracked the motion of the myocardium in tagged MR images of 17 volunteers using a non-rigid registration technique based on free-form deformations and mapped the motion fields obtained into a common reference coordinate system. A principal component analysis (PCA) was then performed on the motion fields to extract the major modes of variation in the fields between the successive time frames. The free-form deformations were then reparameterized in terms of the major modes of variation learned from the statistical model. This can significantly reduce the number of degrees of freedom for the registration algorithm and the associated computational complexity, while constraining the motion tracking to statistically likely types of motion.
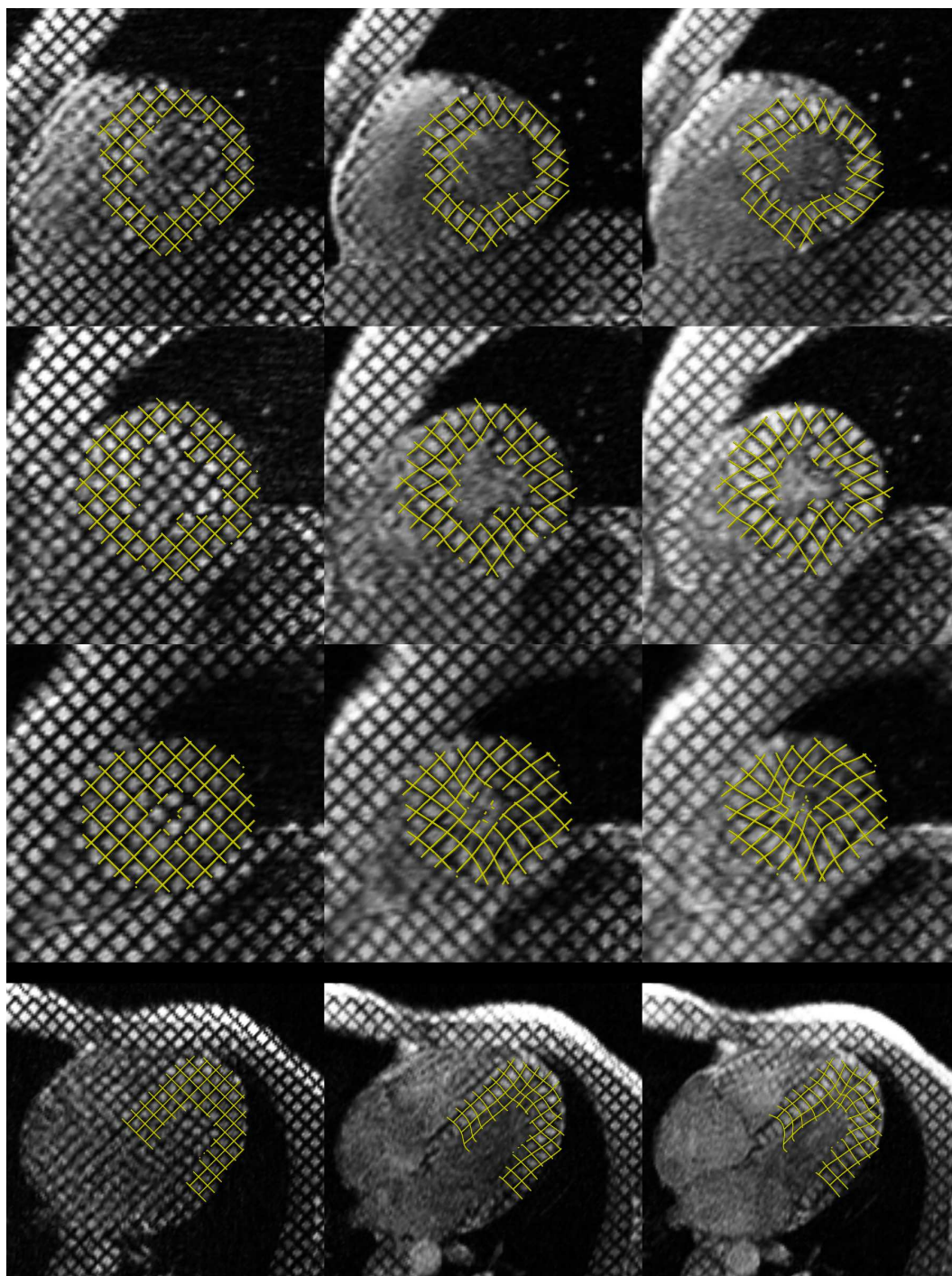
Figure 7.9: This figure shows a series of tagged images taken from one of the volunteers. A virtual tag grid has been placed on the tag pattern at end-diastole and allowed to deform with time according to the deformation field calculated using the time-dependent statistical deformation model. The first three rows show basal, mid-ventricular, and apical SA images respectively. The fourth row shows a horizontal LA image. The first, second, and third columns correspond to end-diastole, mid-systole, and end-systole respectively. Animations of these virtual tag grids can be found on the accompanying CD.
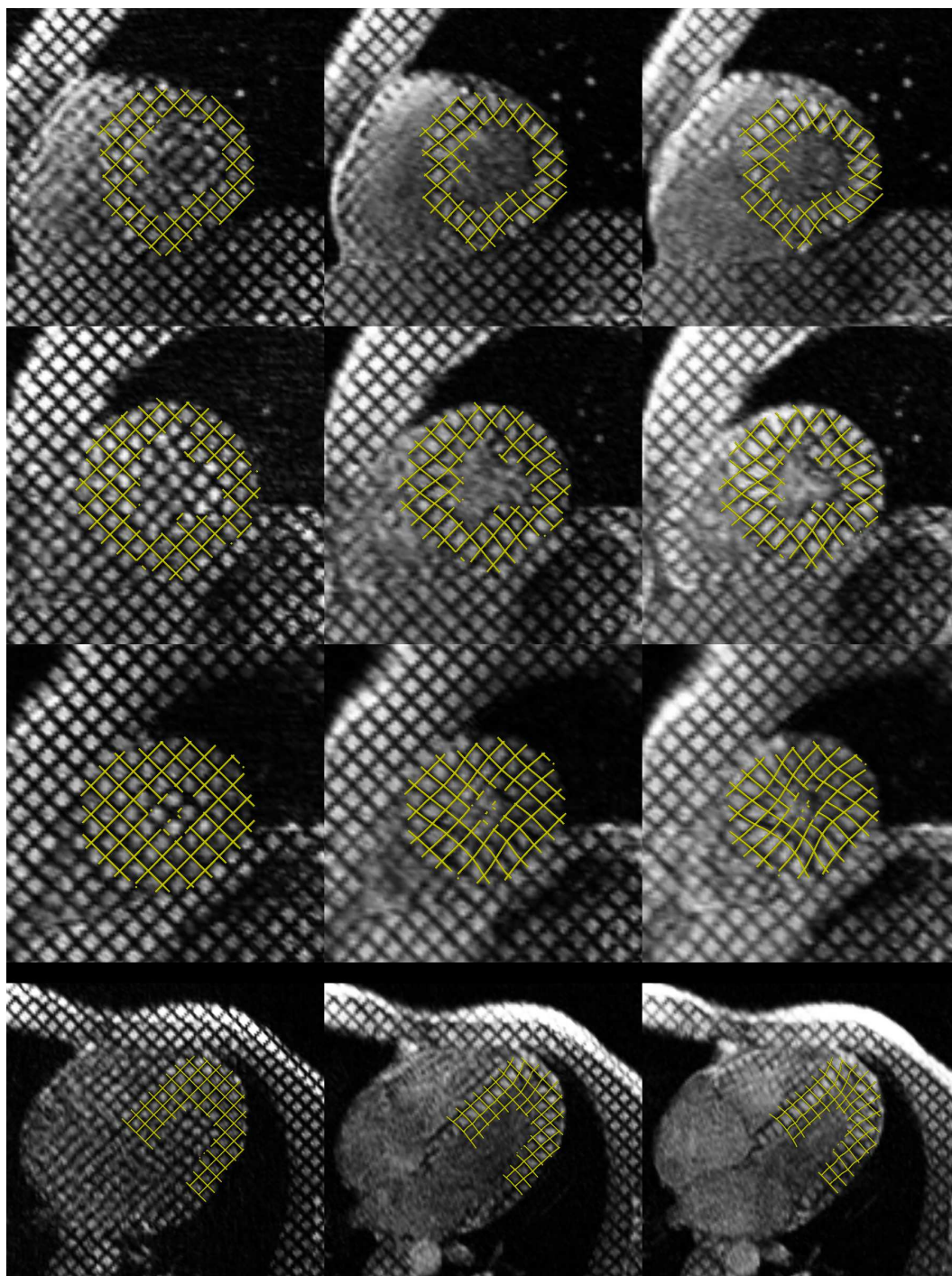
Figure 7.10: This figure shows a series of tagged images taken from one of the volunteers. A virtual tag grid has been placed on the tag pattern at end-diastole and allowed to deform with time according to the deformation field calculated using the time-independent statistical deformation model. The first three rows show basal, mid-ventricular, and apical SA images respectively. The fourth row shows a horizontal LA image. The first, second, and third columns correspond to end-diastole, mid-systole, and end-systole respectively. Animations of these virtual tag grids can be found on the accompanying CD.

Chapter 8

Conclusions and Outlook

Cardiac motion analysis is a challenging endeavor. The principal contributions of this thesis have been the development of nonrigid image registration techniques for cardiac motion tracking in tagged MR images. In contrast to existing techniques no assumptions need to be made on the nature of the tag pattern in the images, and tag localization and deformation field reconstruction are performed simultaneously. Our main contributions have been:

- In chapter 4 a technique for cardiac motion tracking in tagged MR images using nonrigid image registration and free-form deformations was developed. The method presented was validated using a motion simulator and strain patterns from a group of normal volunteers were derived.

- In chapter 5 the use of a cylindrical free-form deformation model for cardiac motion tracking using nonrigid image registration was investigated. The cylindrical free-form deformations were found to be not as accurate as Cartesian free-form deformations in being able to capture the motion of the myocardium in the apical and basal regions of the LV. However, cylindrical free-form deformations performed slightly better than Cartesian free-form deformations in the mid-ventricular region of the LV as the configuration of the control points defining the deformation conform more closely with the shape of the

LV in that region. Thus, in certain cases, it might be more suitable to use cylindrical free-form deformations for cardiac motion tracking.

- In chapter 6 a 4D registration method for motion tracking using 4D free-form deformations was developed. The advantages of using such a transformation model is that deformation parameters can be computed at any arbitrary time instant between end-diastole and end-systole allowing comparisons of motion fields between different subjects to be made more easily. However, several issues which are related to the two-step optimization procedure used still need to be solved before the developed 4D registration algorithm can be used routinely in clinical practice.

- In chapter 7 a statistical motion model was constructed. The motion fields in a group of volunteers were mapped into the coordinate system of a reference subject. A PCA of the motion fields was then performed to extract the major modes of variation in the motion fields. Two different types of PCA were performed, a time-dependent PCA and a time-independent PCA. The free-form deformations describing the motion of the heart were then reparameterized using the major modes of variation in the deformation fields. The reduced number of dimensions in the parameter space which needs to be searched to find the optimal free-form deformation to register the images taken during systole to the end-diastolic image significantly reduces the computational complexity of the motion reconstruction problem. However the statistical model that we have constructed may have difficulties in tracking the motion of patients' hearts as the images used in constructing our models were derived from a group of normal volunteers.

8.1 Discussion

8.1.1 General Limitations of MR Tagging

A limitation of the proposed methods is that, if there is a sufficiently large motion between two time frames, the motion tracking algorithms may become confused and report no motion at all. This can happen if the number of slices acquired and the temporal resolution of the images is not sufficient to capture the deformation of the myocardium accurately. For example, we can imagine a hypothetical case in which the motion of the LV between two successive time frames is such that the tag planes at time $i\tau$ have been displaced by a rigid translation motion equal to the tag spacing in the direction perpendicular to the tag planes. This would mean that the tag planes at $(i+1)\tau$ would be aligned with the tag planes at $i\tau$, and so no motion of the LV would be detected.

It is also possible to argue that this is a limitation of the imaging protocol used and not of the method itself, since we can acquire images with a higher spatial and temporal resolution to ensure that there is sufficient information in the images to accurately recover the motion of the myocardium.

There are a number of other factors related to the image acquisition that have an influence on the accuracy and robustness of the motion field reconstruction:

- As the tags fade during the cardiac cycle due to $T1$ relaxation, the motion reconstruction is limited by the duration of time over which the tags are visible. In the images we have acquired, we have been able to track the motion of the myocardium accurately from end-diastole to end-systole during which the tags are clearly visible. With the use of other tag sequences such as CSPAMM [53], which slow the process of tag fading but at the expense of an increased acquisition time, it may be possible to track the motion of the myocardium over the entire cardiac cycle.

- The tag spacing and spatial resolution of the images acquired have a direct

influence on the accuracy of the estimated strain fields, especially in the endo-cardial region of the myocardium. A smaller tag spacing enables the regional characteristics of the deformation field to be measured with a greater accuracy but would also require the acquisition of images with a higher temporal resolution.

- Another problem stems from the fact that the complete analysis of 3D cardiac motion requires the acquisition of images during several different breath-holds. Thus, to reconstruct an accurate representation of the deformation field within the myocardium the subject must lie completely still and hold their breath always in the same position of the respiratory cycle. In particular, for patients this may be difficult and the longer the image acquisition takes, the more likely it is that the patient will have moved during that time, and the greater the chance of errors being introduced into the deformation field reconstruction.

- Another important consideration is the configuration of imaging planes used to recover the deformation field within the myocardium. A sufficient number of planes must be chosen so as to cover the region of interest adequately. Each configuration will have an effect on the accuracy of the motion field reconstruction as well as the implementation of the tracking algorithm and in particular, the interpolation scheme used. These issues must be weighed against the cost and time required to acquire the images in a real clinical environment.

It is important to realize that the points listed above are limitations of tagged MRI rather than that of any particular motion tracking method.

8.2 Future Work

We have shown that reliable estimates of strain can be obtained by using image registration based motion tracking. Future clinical research could be aided by building

a database of strain patterns seen in normal volunteers. One could build such a database by recruiting a of group of volunteers whose motion fields could be reconstructed and mapped into a common coordinate system. The benefit of using such a database would be that quantitative comparisons could be made with motion and strain patterns seen in an abnormal heart. It would also be interesting to compare the strain results obtained from registration with those obtained from other methods such as HARP.

There are a number of other interesting possibilities for future research. From the work presented in chapter 5 we have seen that the coordinate system used in defining the free-form deformations can have a significant impact on the accuracy of motion tracking using image registration. A possibility for future research is to investigate the use of free-form deformations defined using lattices of other topologies [96]. Incorporating knowledge of the fiber structure and orientation which can be obtained from diffusion tensor MR imaging [164] into the transformation model may also increase the speed and accuracy of image registration.

In the following two subsections we present some initial investigations on two further research topics of interest: motion tracking in untagged MR images and the combined analysis of cardiac motion and blood flow in the LV.

8.2.1 Motion Analysis in Untagged MR Images

As we have made no assumptions about the nature of the tag pattern in the MR images acquired, or even its presence, one can ask the following question: Is there sufficient texture in untagged images to enable the deformation field to be reconstructed from these images? To investigate this possibility we also acquired untagged images of the LV for the volunteer data sets used in chapters 4, 5, and 6. These images were acquired shortly before the tagged images were acquired so that the movement of the volunteer between image acquisitions could be minimized. The image acquisition geometry for the tagged and untagged images was the same. We

then reconstructed the motion of the heart using the 4D registration algorithm presented in chapter 6; once using the untagged MR images and once using the tagged MR images. We labelled the two transformations $\mathbf{T}_{\text{TrueFISP}}$ and $\mathbf{T}_{\text{SPAMM}}$ respectively for each volunteer.

A cylindrical coordinate system was defined whose longitudinal axis passed through the center of the LV and was perpendicular to the SA imaging planes. The myocardium in each SA slice was divided into 16 sectors around the center of the LV and the average radial, circumferential, and longitudinal displacements were computed in each sector using the two transformations, $\mathbf{T}_{\text{TrueFISP}}$ and $\mathbf{T}_{\text{SPAMM}}$. Scatter plots of the radial, circumferential, and longitudinal displacements were drawn to evaluate how well $\mathbf{T}_{\text{TrueFISP}}$ and $\mathbf{T}_{\text{SPAMM}}$ were correlated. The results are shown in figure 8.1.

Linear regression analysis was then performed on the scatter plots of the motion fields, the results of which are presented in table 8.1. As can be seen there is a good correlation between the radial and longitudinal displacements computed from $\mathbf{T}_{\text{TrueFISP}}$ and $\mathbf{T}_{\text{SPAMM}}$, but there is less of an agreement between the circumferential displacements. In figure 8.2 we show the motion fields computed from $\mathbf{T}_{\text{TrueFISP}}$ and $\mathbf{T}_{\text{SPAMM}}$. The first and second rows show arrow plots of the displacement fields in a mid-ventricular SA slice for one of the volunteers using $\mathbf{T}_{\text{TrueFISP}}$ and $\mathbf{T}_{\text{SPAMM}}$ respectively. As can be seen the motion fields are very similar but there are regions where not all of the twisting motion has been captured in $\mathbf{T}_{\text{TrueFISP}}$. These regions are indicated by the circles in the third column. In the third and fourth rows, virtual tag grids have been placed on the SA tagged MR image sequences and have been deformed over time by $\mathbf{T}_{\text{TrueFISP}}$ and $\mathbf{T}_{\text{SPAMM}}$ respectively. From the third row we see that there is a good agreement in the motion fields computed from the two sets of images since the virtual tag grid follows the tag pattern in the images.

The results presented in figures 8.1 and 8.2, and table 8.1 show that there is a correlation between the radial and longitudinal displacements computed from the tagged and untagged MR images. Figure 8.1(b) also indicates that not all of twisting
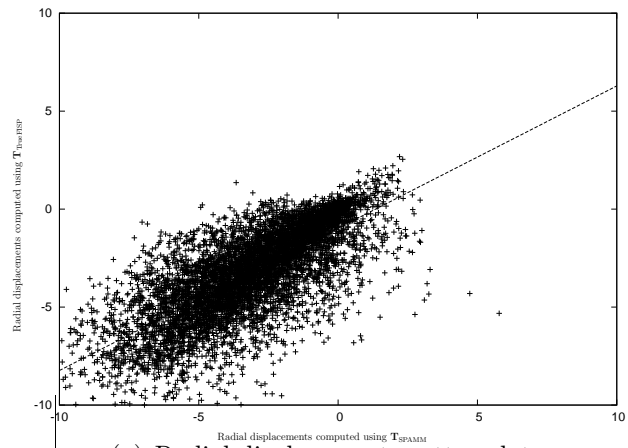
(a) Radial displacement scatter plot
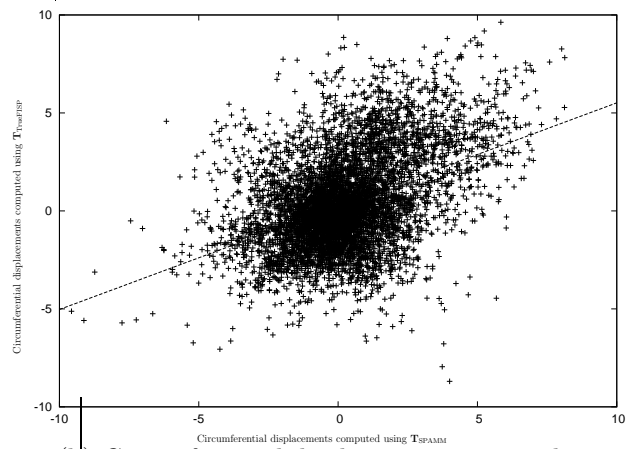
(b) Circumferential displacement scatter plot
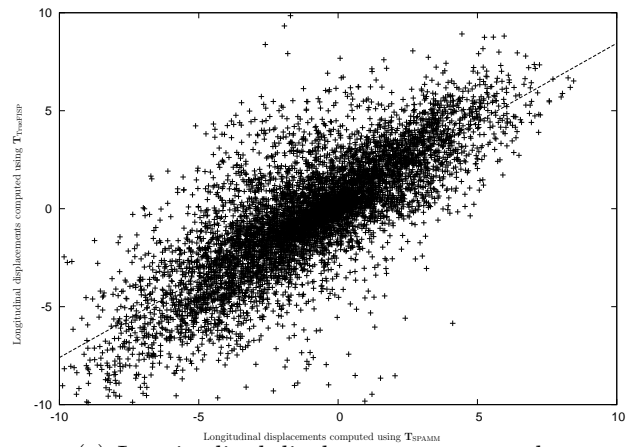
(c) Longitudinal displacement scatter plot

Figure 8.1: Scatter plots showing the correlation between the radial, circumferential, and longitudinal displacements computed using $\mathbf{T}_{\text{TrueFISP}}$ and $\mathbf{T}_{\text{SPAMM}}$. Results of linear regression analysis on these plots are given in table 8.1.

	Line of Best Fit	Correlation Coefficient
Radial	$y = 0.73x - 0.97$	0.74
Circumferential	$y = 0.53x + 0.24$	0.43
Longitudinal	$y = 0.80x + 0.42$	0.78

Table 8.1: The results of linear least squares fitting for the radial, circumferential, and longitudinal displacements computed using $\mathbf{T}_{\text{TrueFISP}}$ and $\mathbf{T}_{\text{SPAMM}}$.
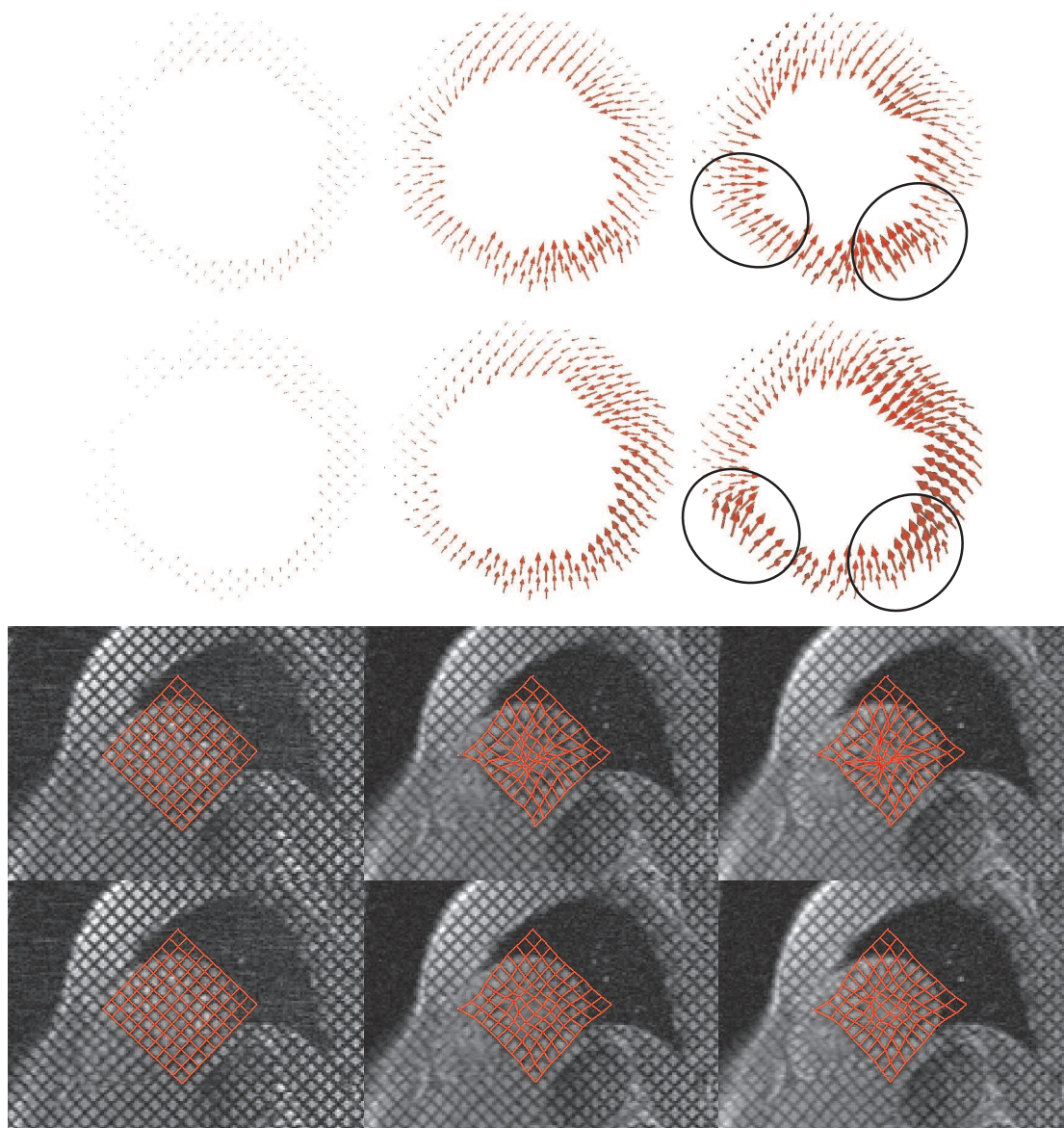
Figure 8.2: The first and second rows show the computed motion fields in a mid-ventricular SA slice for one of the volunteers using $\mathbf{T}_{\text{TrueFISP}}$ and $\mathbf{T}_{\text{SPAMM}}$ respectively. The columns, from left to right, correspond to end-diastole, mid-systole, and end-systole. Regions of the myocardium which show a discrepancy in the computed motion fields are indicated by the circles in the third column. In the third and fourth rows, virtual tag grids have been placed on the SA tagged MR image sequences and have been deformed over time by $\mathbf{T}_{\text{TrueFISP}}$ and $\mathbf{T}_{\text{SPAMM}}$ respectively.

motion can be detected from the untagged images. These results show that there is some promise in using image registration techniques for recovering the deformation field within the myocardium using untagged MR images and it would be fruitful to further investigate whether the strain patterns computed are still clinically useful. The statistical motion models that we have developed may also improve the accuracy of the motion patterns extracted from untagged MR images using image registration.

8.2.2 Combined Analysis of Cardiac Motion and Blood Flow

Another avenue for further research is the combined analysis of cardiac motion and blood flow. The LV wall motion directly affects the efficiency with which blood can be pumped out to the rest of the body and it would be clinically useful to determine whether there is any relationship between the blood flow patterns in the LV and the motion of the LV wall.

In the following we present some initial results which we have obtained on the combined visualization and analysis of cardiac motion and blood flow in the LV. To do this horizontal LA untagged MR images of the LV from a normal healthy volunteer were acquired and used to reconstruct the deformation field within the myocardium with a 3D version of the motion tracking algorithm presented in chapter 6. Phase contrast MR images were also acquired from the same volunteer and used to reconstruct the flow field in the LV. The flow and motion fields were then visualized together using vector plots. The radial strain in the myocardium was then calculated and compared with the variation of the average speed of the blood in the LV over time.

Figure 8.3 shows a visualization of the flow and motion fields together using arrow plots. The first row shows the time period from early-systole to end-systole. As can be seen in the figure the free wall of the LV contracts much more than the septum. At the same time that this contraction occurs, blood is pumped out of the left ventricle through the aorta with a high velocity. Immediately afterwards the

atrio-ventricular valve opens, and blood rushes in from the left atrium into the LV, which can be seen in the second row of the figure. Again the free wall of LV expands much more than the septum. The final row shows late-diastole when left ventricular filling has almost been completed. A large vortex is also seen near the end of the cycle.

Figure 8.4 shows a plot of the radial strain over time. The lateral wall of the LV experiences the greatest strain. We also computed the average radial strain in the myocardium as well as the mean squared speed of the blood in the LV. These results are shown in figures 8.5 and 8.6. Time frames 0 and 18 correspond to the start and the end of the cardiac cycle respectively, while time frame 7 corresponds to end-systole. As can be seen in the figures the radial strain increases from 0 and reaches a maximum of 0.5 at end-systole. During this time the mean squared speed of the blood increases as blood is pushed out of the outflow tract and decreases to a minimum at end-systole. After end-systole the strain decreases as the LV relaxes and when the atrio-ventricular valve opens, the blood flow velocity increases again as blood pours in from the left atrium.

These results show that simple global relationships between the blood flow and the motion in the LV can be derived. Further work needs to be done on investigating the relationship between local flow features and local strain patterns in the myocardium. To do this would require the acquisition of 4D data sets of the blood flow in the LV in addition to the 4D cardiac MR images. A further possibility would be to predict blood flow patterns within the LV from the motion of the ventricular wall by building a *computation fluid dynamics* (CFD) model.

8.2.3 Conclusions

We have shown that image registration is a viable technique for cardiac motion analysis. Clinically useful parameters such as strain can be computed directly from the output transformations obtained from image registration. No user interaction is
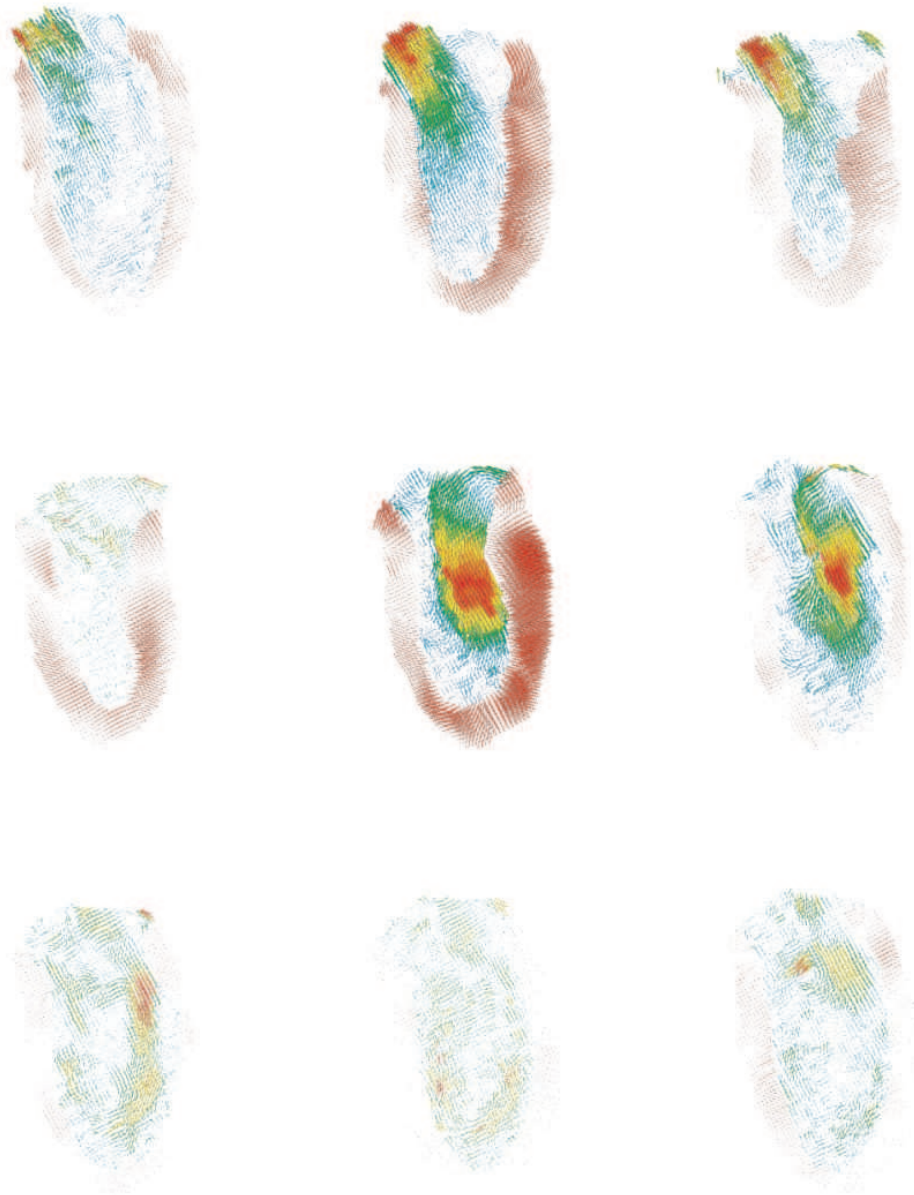
Figure 8.3: The first row shows the contraction of the left-ventricle and the flow out of the aorta during the time period from early-systole to end-systole. The second row shows the filling of the left ventricle which occurs just after end-systole. The final row shows late-diastole when left ventricular filling has almost been completed.
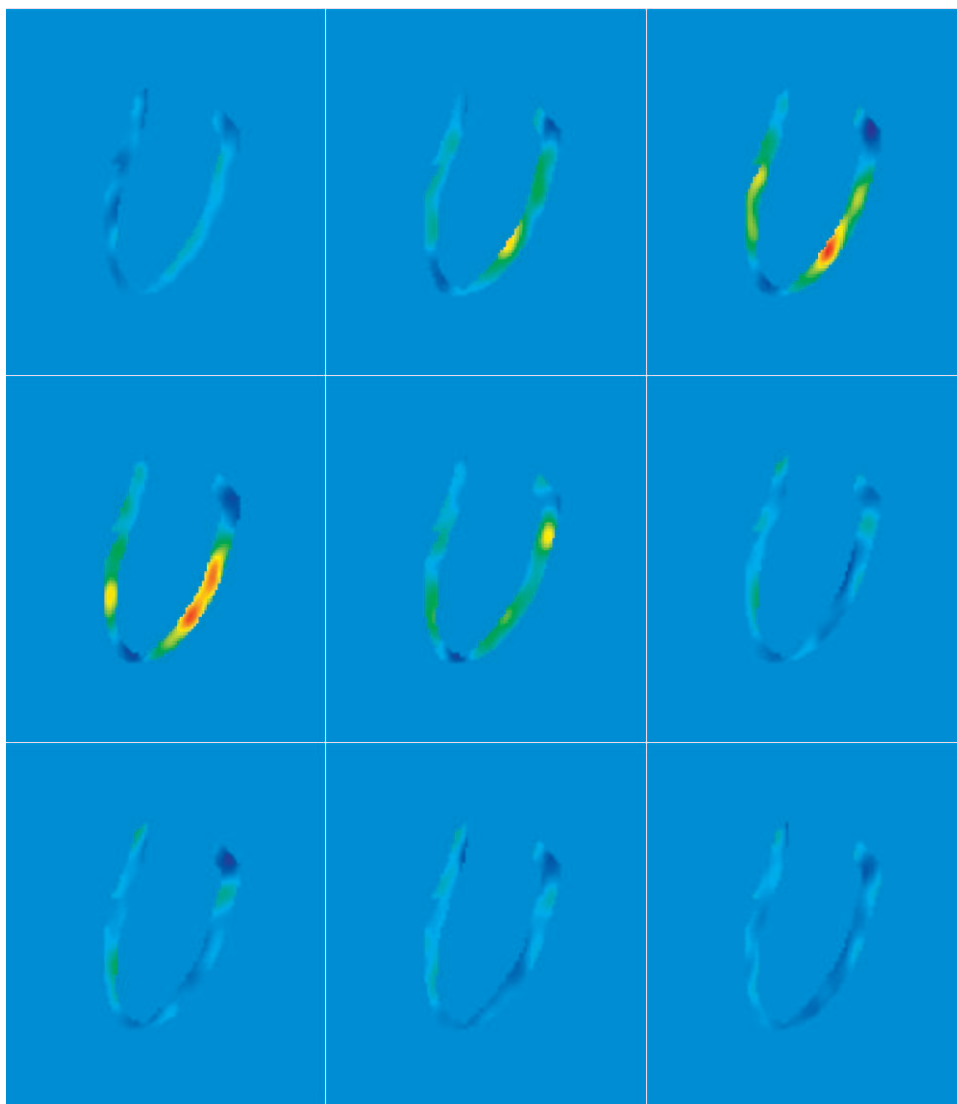
Figure 8.4: Plot of the radial strain in the myocardium. Blue colors correspond to negative values in the strain and red to positive values.
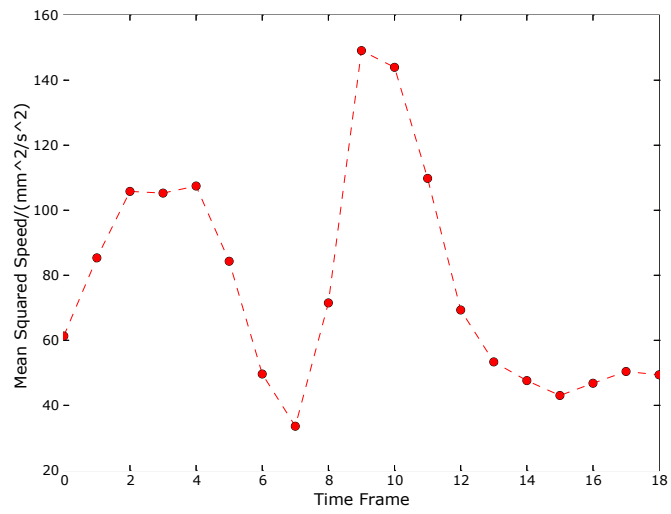
Figure 8.5: Plot of the variation of the mean squared speed of the blood in the LV over time.
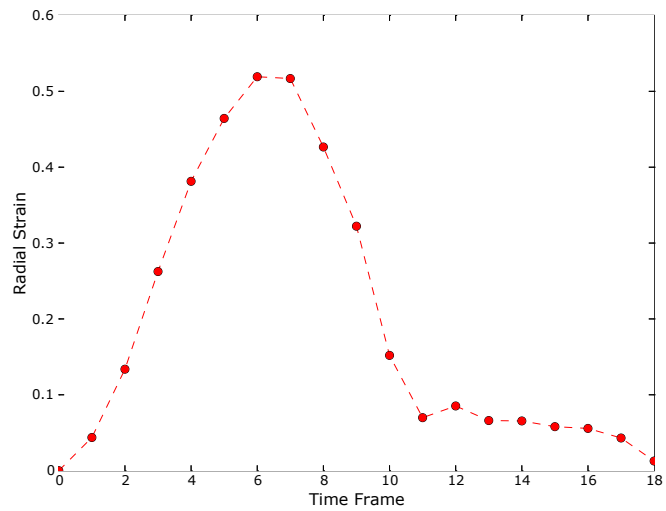
Figure 8.6: Plot of the variation of the average radial strain in the myocardium over time.

required during the motion field reconstruction, enabling clinicians and researchers to make more effective use of their time in investigating the relationship between CVDs and cardiac motion. It is likely that image registration will play an increasingly important role in cardiac motion analysis.

Publications

Articles in Journals

- R. Chandrashekara, R. H. Mohiaddin, and D. Rueckert. Analysis of 3D myocardial motion in tagged MR images using nonrigid image registration. *IEEE Transactions on Medical Imaging*, 23(10):1245–1250, October 2004. [29]

- A. Rao, R. Chandrashekara, G. I. Sanchez-Ortiz and R. Mohiaddin and P. Aljabar and J. V. Hajnal and B. K. Puri and D. Rueckert. Spatial Transformation of motion and deformation fields using nonrigd registration. *IEEE Transactions on Medical Imaging*, 23(9):1065–1076, September 2004. [133]

Articles in Conference Proceedings

- R. Chandrashekara, R. H. Mohiaddin, and D. Rueckert. Cardiac motion tracking in tagged MR images using a 4D B-spline motion model and nonrigid image registration. In Proceedings of the 2004 IEEE International Symposium on Biomedical Imaging: From Nano to Macro, Arlington, VA, USA, April 2004. IEEE. [30]

- R. Chandrashekara, A. Rao, G. I. Sanchez-Ortiz, R. H. Mohiaddin, and D. Rueckert. Construction of a statistical model for cardiac motion analysis using nonrigid image registration. In C. Taylor and J. Alison Noble, editors, Information Processing in Medical Imaging, pages 599–610, Ambleside, UK,

July 2003. Springer. [32]

- R. Chandrashekara, R. H. Mohiaddin, and D. Rueckert. Analysis of myocardial motion and strain patterns using a cylindrical B-spline transformation model. In N. Ayache and H. Delingette, editors, Surgery Simulation and Soft Tissue Modeling, pages 88–99, Juan-Les Pins, France, June 2003. Springer. [28]

- A. Rao, G. I. Sanchez-Ortiz, R. Chandrashekara, M. Lorenzo-Valdés, R. Mohiaddin, and D. Rueckert. Construction of a cardiac motion atlas from MR using nonrigid registration. In *Proceedings of the Second International Workshop on Functional Imaging and Modeling of the Heart*, pages 141–150, Lyon, France, June 5–6 2003. [135]

- A. Rao, G. I. Sanchez-Ortiz, R. Chandrashekara, M. Loreonzo-Valdés, R. Mohiaddin and D. Rueckert. Comparison of cardiac motion acrosss subjects using nonrigid registration. In *Proceedings of the Fifth International Conference on Medical Image Computing and Computer Assisted Intervantion*, pages 722–729, Springer, 2002. [134]

- R. Chandrashekara, R. H. Mohiaddin, and D. Rueckert. Analysis of myocardial motion in taggedMR images using nonrigid image registration. In Alex Houston and Reyer Zwiggelaar, editors, Proceedings of Medical Image Understanding and Analysis 2002, pages 1–4, Portsmouth, UK, July 2002. [26]

- D. Rueckert, M. Lorenzo-Valdés, R. Chandrashekara, G. I. Sanchez-Ortiz, and R. Mohiaddin. Non-rigid registration of cardiac MR: Application to motion modelling and atlas-based segmentation. In *Proceedings of the 2002 IEEE International Symposium on Biomedical Imaging*, pages 481–484, 7–10 July 2002. [141]

- R. Chandrashekara, R. H. Mohiaddin, and D. Rueckert. Analysis of myocardial motion in tagged MR images using nonrigid image registration. In M.

Sonka and J. Michael Fitzpatrick, editors, Proceedings of the SPIE International Symposium on Medical Imaging: Image Processing, volume 4684, pages 1168–1179, San Diego, California USA, February 2002. SPIE. [25]

- R. Chandrashekara, R. H. Mohiaddin, and D. Rueckert. Interactive visualization and analysis of myocardial motion using tagged MRI. In Silvia D. Olabarriaga, Wiro J. Niessen, and Frans Gerritsen, editors, Proceedings of the Workshop on Interactive Medical Image Visualization and Analysis, pages 37–40, Utrecht, The Netherlands, October 2001. [24]

Abstracts

- R. Chandrashekara, R. H. Mohiaddin, and D. Rueckert. Combined visualization and analysis of blood flow and motion in the left ventricle. In Proceedings of the International Workshop on Flow and Motion, In press, Zurich, Switzerland, 11–13 July 2004. [31]

- R. Chandrashekara, R. H. Mohiaddin, and D. Rueckert. Estimation of myocardial strain parameters from tagged MR images using nonrigid registration via cylindrical FFDs. In Proceedings of the International Society for Magnetic Resonance in Medicine, page 706, Toronto, Canada, 10–16 July 2003. [27]

Bibliography

[1] M. Abe, Y. Kazatani, H. Fukuda, H. Tatsuno, H. Habara, and H. Shinbata. Left ventricular volumes, ejection fraction, and regional wall motion calculated with gated technetium-99m tetrofosmin SPECT in reperfused acute myocardial infarction at super-acute phase: Comparison with left ventriculography. *Journal of Nuclear Cardiology*, 7(6):569–574, 2000.

[2] I. Adachi, K. Morita, M. B. Imran, M. Konno, T. Mochizuki, N. Kubo, Y. Itoh, C. Kato, E. Tsukamoto, and N. Tamaki. Heterogeneity of myocardial wall motion and thickening in the left ventricle evaluated with quantitative gated SPECT. *Journal of Nuclear Cardiology*, 7(4):296–300, 2000.

[3] American Heart Association. Heart disease and stroke statistics – 2004 update. http://www.americanheart.org/, Dallas, Texas, 2004.

[4] A. A. Amini, Y. Chen, R. W. Curwen, V. Mani, and J. Sun. Coupled B-snake grids and constrained thin-plate splines for analysis of 2D tissue deformations from tagged MRI. *IEEE Transactions on Medical Imaging*, 17(3):344–356, June 1998.

[5] A. A. Amini, Y. Chen, M. Elayyadi, and P. Radeva. Tag surface reconstruction and tracking of myocardial beads from SPAMM-MRI with parametric B-spline surfaces. *IEEE Transactions on Medical Imaging*, 20(2):94–103, February 2001.

[6] A. A. Amini, R. W. Curwen, R. T. Constable, and J. C. Gore. MR physics-based snake tracking and dense deformations from tagged MR cardiac images. In *Proceedings of the AAAI Symposium on Applications of Computer Vision to Medical Image Processing*, pages 126–129, Stanford, USA, 1994.

[7] A. A. Amini, R. W. Curwen, and J. C. Gore. Snakes and splines for tracking non-rigid heart motion. In Bernard Buxton and Roberto Cipolla, editors, *Proceedings of the Fourth European Conference on Computer Vision*, volume 1065 of *Lecture Notes in Computer Science*, pages 251–261, Cambridge, UK, April 1996. Springer.

[8] T. Arts, W. C. Hunter, A. Douglas, A. M. M. Muijtjens, and R. S. Reneman. Description of the deformation of the left ventricle by a kinematic model. *Biomechanics*, 25(10):1119–1127, 1992.

[9] K. S. Arun, T. S. Huang, and S. D. Blostein. Least-squares fitting of two 3-D point sets. *IEEE Transactions on Pattern Analysis and Machine Intelligence*, 9:698–700, May 1987.

[10] L. Axel. Tagged cardiovascular magnetic resonance of systole. In W. J. Manning and D. J. Pennell, editors, *Cardivascular Magnetic Resonance*, chapter 4, pages 41–47. Churchill Livingstone, 2002.

[11] L. Axel and L. Dougherty. Heart wall motion: Improved method of spatial modulation of magnetization for MR imaging. *Radiology*, 172(2):349–360, 1989.

[12] L. Axel and L. Dougherty. MR imaging of motion with spatial modulation of magnetization. *Radiology*, 171(3):841–845, 1989.

[13] B. D. Bolster, Jr., E. R. McVeigh, and E. A. Zerhouni. Myocardial tagging in polar coordinates with use of striped tags. *Radiology*, 177(3):769–772, December 1990.

[14] R. Bajcsy and S. Kovačič. Multiresolution elastic matching. *Computer Vision, Graphics, and Image Processing*, 46(1):1–21, April 1989.

[15] D. S. Berman and G. Germano. Evaluation of ventricular ejection fraction, wall motion, wall thickening, and other parameters with gated myocardial perfusion single-photon emission computed tomography. *Journal of Nuclear Cardiology*, 4(2):S169–S171, 1997.

[16] P. J. Besl and N. D. McKay. A method for registration of 3D shapes. *IEEE Transactions on Pattern Analysis and Machine Intelligence*, 14:239–256, 1992.

[17] F. L. Bookstein. Principal warps: Thin-plate splines and the decomposition of deformations. *IEEE Transactions on Pattern Analysis and Machine Intelligence*, 11(6):567–585, June 1989.

[18] J. G. Bosch, S. C. Mitchell, B. P. F. Lelieveldt, F. Nijland, O. Kamp, M. Sonka, and J. H. C. Reiber. Automatic segmentation of echocardiographic sequences by active appearance motion models. *IEEE Transactions on Medical Imaging*, 21(11):1374–1383, November 2002.

[19] A. Boudraa, M. Arzi, J. Sau, J. Champier, S. Hadj-Moussa, J. E. Besson, D. Sappey-Marinier, R. Itti, and J. J. Mallet. Automated detection of the left ventricular region in gated nuclear cardiac imaging. *IEEE Transactions on Biomedical Engineering*, 43:430–436, April 1996.

[20] J. J. Bray, P. A. Cragg, A. D. C. Macknight, and R. G. Mills. *Lecture Notes on Human Physiology*. Blackwell Science, fourth edition, 1999.

[21] P. J. Burt and E. H. Adelson. The Laplacian pyramid as a compact image code. *IEEE Transactions on Communications*, 31(4):532–540, April 1983.

[22] C. R. Maurer, Jr. and J. M. Fitzpatrick. A review of medical image registration. In R. J. Maciunas, editor, *Interactive Image-Guided Neurosurgery*, pages 17–44. Thieme Medical Publishers, 1993.

[23] M. D. Cerqueira, N. J. Weissman, V. Dilsizian, A. K. Jacobs, S. Kaul, W. K. Laskey, D. J. Pennell, J. A. Rumberger, T. J. Ryan, and M. S. Verani. Standardized myocardial segmentation and nomenclature for tomographic imaging of the heart. *Journal of Cardiovascular Magnetic Resonance*, 4(2):203–210, 2002.

[24] R. Chandrashekara, R. H. Mohiaddin, and D. Rueckert. Interactive visualization and analysis of myocardial motion using tagged MRI. In Silvia D. Olabarriaga, Wiro J. Niessen, and Frans Gerritsen, editors, *Proceedings of the Workshop on Interactive Medical Image Visualization and Analysis*, pages 37–40, Utrecht, The Netherlands, October 2001.

[25] R. Chandrashekara, R. H. Mohiaddin, and D. Rueckert. Analysis of myocardial motion in tagged MR images using nonrigid image registration. In M. Sonka and J. Michael Fitzpatrick, editors, *Proceedings of the SPIE International Symposium on Medical Imaging: Image Processing*, volume 4684, pages 1168–1179, San Diego, California USA, February 2002. SPIE.

[26] R. Chandrashekara, R. H. Mohiaddin, and D. Rueckert. Analysis of myocardial motion in tagged MR images using nonrigid image registration. In Alex Houston and Reyer Zwiggelaar, editors, *Proceedings of Medical Image Understanding and Analysis 2002*, pages 1–4, Portsmouth, UK, July 2002.

[27] R. Chandrashekara, R. H. Mohiaddin, and D. Rueckert. Analysis of myocardial motion and strain patterns using a cylindrical B-spline transformation model. In N. Ayache and H. Delingette, editors, *Surgery Simulation and Soft Tissue Modeling*, pages 88–99, Juan-Les Pins, France, June 2003. Springer.

[28] R. Chandrashekara, R. H. Mohiaddin, and D. Rueckert. Estimation of myocardial strain parameters from tagged MR images using nonrigid registration via cylindrical FFDs. In *Proceedings of the International Society for Magnetic Resonance in Medicine*, page 706, Toronto, Canada, 10–16 July 2003.

[29] R. Chandrashekara, R. H. Mohiaddin, and D. Rueckert. Analysis of 3D myocardial motion in tagged MR images using nonrigid image registration. *IEEE Transactions on Medical Imaging*, 23(10):1245–1250, October 2004.

[30] R. Chandrashekara, R. H. Mohiaddin, and D. Rueckert. Cardiac motion tracking in tagged MR images using a 4D B-spline motion model and nonrigid image registration. In *Proceedings of the 2004 IEEE International Symposium on Biomedical Imaging: From Nano to Macro*, Arlington, VA, USA, April 2004. IEEE.

[31] R. Chandrashekara, R. H. Mohiaddin, and D. Rueckert. Combined visualization and analysis of blood flow and motion in the left ventricle. In *Proceedings of the International Workshop on Flow and Motion*, pages 112–113, Zurich, Switzerland, 11–13 July 2004.

[32] R. Chandrashekara, A. Rao, G. I. Sanchez-Ortiz, R. H. Mohiaddin, and D. Rueckert. Construction of a statistical model for cardiac motion analysis using nonrigid image registration. In C. Taylor and J. Alison Noble, editors, *Information Processing in Medical Imaging*, pages 599–610, Ambleside, UK, July 2003. Springer.

[33] G. E. Christensen, R. D. Rabbitt, and M. I. Miller. Deformable templates using largest deformation kinematics. *IEEE Transactions on Image Processing*, 5(10):1435–1447, October 1996.

[34] A. Collignon, F. Maes, D. Delaere, D. Vandermeulen, P. Suetens, and G. Marchal. Automated multimodality image registration based on information theory. In Y. Bizais, C. Barillot, and R. Di Paola, editors, *Information Processing in Medical Imaging*, pages 263–274. Kluwer Academic Publishers, Dordrecht, 1995.

[35] T. F. Cootes, C. Beeston, G. J. Edwards, and C. J. Taylor. A unified framework for atlas matching using active appearance models. In *Proceedings of the*

16th International Conference on Information Processing in Medical Imaging, pages 322–333, 1999.

[36] T. F. Cootes, G. J. Edwards, and C. J. Taylor. Active appearance models. *IEEE Transactions on Pattern Analysis and Machine Intelligence*, 23(6):681–685, June 2001.

[37] T. F. Cootes, A. Hill, C. J. Taylor, and J. Haslam. Use of active shape models for locating structures in medical images. *Image and Vision Computing*, 12(6):355–365, July/August 1994.

[38] T. F. Cootes, C. J. Taylor, D. H. Cooper, and J. Graham. Active shape models—their training and application. *Computer Vision and Image Understanding*, 61(1):38–59, 1995.

[39] C. Corsi, G. Saracino, A. Sarti, and C. Lamberti. Left ventricular volume estimation for real-time three-dimensional echocardiography. *IEEE Transactions on Medical Imaging*, 21(9):1202–1208, September 2002.

[40] C. Costa and L. Moura. Automatic detection of LV contours in nuclear medicine using geometrical information and a neural net. In *Computers in Cardiology*, pages 557–560, 1995.

[41] T. M. Cover and J. A. Thomas. *Elements of Information Theory*. John Wiley & Sons, Inc., 1991.

[42] P. E. Danielsson. Euclidean distance mapping. *Computer Graphics and Image Processing*, 14:227–248, 1980.

[43] J. Declerck, N. Ayache, and E. R. McVeigh. Use of a 4D planispheric transformation for the tracking and the analysis of LV motion with tagged MR images. In *SPIE Medical Imaging, vol. 3660*, San Diego, CA, USA, February 1999.

[44] J. Declerck, T. S. Denney, C. Ozturk, W. O'Dell, and E. R. McVeigh. Left ventricular motion reconstruction from planar tagged MR images: A comparison. *Physics in Medicine and Biology*, 45:1611–1632, 2000.

[45] J. Declerck, J. Feldmar, and N. Ayache. Definition of a four-dimensional continuous planispheric transformation for the tracking and the analysis of left-ventricle motion. *Medical Image Analysis*, 2(2):197–213, 1998.

[46] J. Declerck, J. Feldmar, M. L. Goris, and F. Betting. Automatic registration and alignment on a template of cardiac stress and rest reoriented SPECT images. *IEEE Transactions on Medical Imaging*, 16(6):727–737, December 1997.

[47] T. Delzescaux, F. Frouin, A. De Cesare, S. Phillip-Foliguet, R. Zeboudj, M. Janier, A. Todd-Pokropek, and A. Hermant. Adaptive and self-evaluating registration method for mycoardial perfusion assessment. *Magnetic Resonance Materials in Physics, Biology and Medicine*, 13:28–39, 2001.

[48] A. P. Dempster, N. M. Laird, and D. B. Rubin. Maximum likelihood from incomplete data via the EM algorithm. *Journal of the Royal Statistical Society. Series B (Methodological)*, 39(1):1–38, 1977.

[49] X. Deng and T. S. Denney, Jr. Three-dimensional myocardial strain reconstruction from tagged MRI using a cylindrical B-spline model. *IEEE Transactions on Medical Imaging*, 23(7):861–867, July 2004.

[50] J. D'hooge, B. Bijnens, J. Thoen, F. Van de Werf, G. R. Sutherland, and P. Suetens. Echocardiographics strain and strain-rate imaging: A new tool to study regional myocardial function. *IEEE Transactions on Medical Imaging*, 21(9):1022–1030, September 2002.

[51] L. Dougherty, J. C. Asmuth, A. S. Blom, L. Axel, and R. Kumar. Validation of an optical flow method for tag displacement estimation. *IEEE Transactions on Medical Imaging*, 18(4):359–363, April 1999.

[52] A. Fenster, D. B. Downey, and H. N. Cardinal. Three-dimensional ultrasound imaging. *Physics in Medicine and Biology*, 46(5):67–99, May 2001.

[53] S. E. Fishcer, G. C. McKinnon, S. E. Maier, and P. Boesiger. Improved myocardial tagging contrast. *Magnetic Resonance in Medicine*, 30(2):191–200, August 1993.

[54] J. M. Fitzpatrick, D. L. G. Hill, and C. R. Maurer, Jr. Image registration. In Milan Sonka and J. Michael Fitzpatrick, editors, *Handbook of Medical Imaging*, volume 2, pages 447–513. SPIE Press, 2000.

[55] B. Flury and H. Riedwyl. *Multivariate Statistics: A Practical Approach*. Chapman and Hall, 1988.

[56] A. F. Frangi, W. J. Niessen, and M. A. Viergever. Three-dimensional modeling for functional analysis of cardiac images: A review. *IEEE Transactions on Medical Imaging*, 20(1):2–25, January 2001.

[57] A. F. Frangi, D. Rueckert, J. A. Schnabel, and W. J. Niessen. Automatic construction of multiple-object three-dimensional statistical shape models: Application to cardiac modeling. *IEEE Transactions on Medical Imaging*, 21(9):1151–1166, September 2002.

[58] J. C. Gee and R. K. Bajcsy. Elastic matching: Continuum mechanical and probabilistic analysis. In A. W. Toga, editor, *Brain Warping*, pages 183–197. Academic Press, 1999.

[59] G. Gerig, M. Styner, and G. Szekely. Statistical shape models for segmentation and structural analysis. In *Proceedings of the International Symposium on Biomedical Imaging*, pages 18–21, July 2002.

[60] A. Giachetti. On-line analysis of echocardiographic image sequences. *Medical Image Analysis*, 2(3):261–284, 1998.

[61] A. Goshtasby. Registration of images with geometric distortions. *IEEE Transactions on Geoscience and Remote Sensing*, 26(1):60–64, January 1988.

[62] R. A. Greenbaum, S. Y. Ho, D. G. Gibson, A. E. Becker, and R. H. Anderson. Left ventricular fibre architecture in man. *British Heart Journal*, 45(3):248–263, March 1981.

[63] S. N. Gupta and J. L. Prince. On variable brightness optical flow for tagged MRI. In *Information Processing in Medical Imaging*, pages 323–334. Kluwer, June 1995.

[64] M. A. Guttman, J. L. Prince, and E. R. McVeigh. Tag and contour detection in tagged MR images of the left ventricle. *IEEE Transactions on Medical Imaging*, 13(1), March 1994.

[65] M. A. Guttman, E. A. Zerhouni, and E. R. McVeigh. Analysis and visualization of cardiac function from MR images. *IEEE Computer Graphics and Applications*, 17:30–38, January 1997.

[66] D. A. Herzka, M. A. Guttman, and E. R. McVeigh. Myocaridal tagging with SSFP. *Magnetic Resonance in Medicine*, 49:329–340, 2003.

[67] K. T. Hickey, R. R. Sciacca, S. Bokhari, O. Rodriguez, R. Chou, T. L. Faber, C. D. Cooke, E. V. Garcia, K. Nichols, and S. R. Bergmann. Assessment of cardiac wall motion and ejection fraction with gated pet using N-13 ammonia. *Clinical Nuclear Medicine*, 29(4):243–248, April 2004.

[68] D. L. G. Hill, P. G. Batchelor, M. Holden, and D. J. Hawkes. Medical image registration. *Physics in Medicine and Biology*, 46(3):1–45, March 2001.

[69] S. G. Hoggar. *Mathematics for Computer Graphics*. Cambridge University Press, 1993.

[70] B. K. P. Horn and B. G. Schunck. Determining optical flow. *Artificial Intelligence*, 17:185–203, August 1981.

[71] E. W. Hsu and C. S. Henriquez. Myocardial fiber orientation mapping using reduced encoding diffusion tensor imaging. *Journal of Cardiovascular Magnetic Resonance*, 3(4):339–347, 2001.

[72] J. Huang, D. Abendschein, V. G. Dávila-Román, and A. A. Amini. Spatiotemporal tracking of myocardial deformations with a 4-D B-spline model from tagged MRI. *IEEE Transactions on Medical Imaging*, 18(10):957–972, October 1999.

[73] L. Ibáñez, W. Schroeder, L. Ng, and J. Cates. *The Insight Segmentation and Registration Toolkit*. Kitware, 2003.

[74] M. P. Jolly, N. Duta, and G. Funka-Lea. Segmentation of the left ventricle in cardiac MR images. In *Proceedings of the International Conference on Computer Vision*, pages 501–508, July 7–14 2001.

[75] S. C. Joshi. *Large Deformation Diffeomorphisms and Gaussian Random Fields for Statisitical Characterization of Brain Sub-Manifolds*. PhD thesis, Washington University, 1998.

[76] H. Kanai, H. Hasegawa, N. Chuhachi, Y. Koiwa, and M. Tanaka. Noninvasive evaluation of local myocardial thickening and its color-coded imaging. *IEEE Transactions on Ultrasonics, Ferroelectrics, and Frequency Control*, 44(4):752–768, July 1997.

[77] M. Kass, A. Witkin, and D. Terzopoulos. Snakes: Active contour models. *International Journal of Computer Vision*, 1(4):321–331, 1988.

[78] A. M. Katz. *Physiology of the Heart*. Raven Press, third edition, 2000.

[79] M. R. Kaus, J. von Berg, W. Niessen, and V. Pekar. Automated segmentation of the left ventricle in cardiac MRI. In R. E. Ellis and T. M. Peters,

editors, *Proceedings of the Sixth International Conference on Medical Image Computing and Computer Assisted Intervention*, volume 2878 of *Lecture Notes in Computer Science*, pages 432–439. Springer-Verlag, 2003.

[80] A. Khorsand, S. Graf, C. Pirich, G. Wagner, D. Moertl, H. Frank, K. Kletter, H. Sochor, G. Maurer, E. Schuster, and G. Porenta. Image analysis of gated cardiac PET to assess left ventricular volumes and contractile function. In *Computers in Cardiology*, pages 311–314, 2000.

[81] G. J. Klein, B. W. Reutter, and R. H. Huesman. Four-dimensional affine registration models for respiratory-gated pet. *IEEE Transactions on Nuclear Science*, 48(3):756–760, June 2001.

[82] C. M. Kramer, N. Reichek, V. A. Ferrari, T. Theobald, J. Dawson, and L. Axel. Regional heterogeneity of function in hypertrophic cardiomyopathy. *Circulation*, 90(1):186–194, July 1994.

[83] S. Kumar and D. Goldgof. Automatic tracking of SPAMM grid and the estimation of deformation parameters from cardiac MR images. *IEEE Transactions on Medical Imaging*, 13(1):122–132, March 1994.

[84] P. C. Lauterbur. Image formation by induced local interactions: Examples employing nuclear magnetic resonance. *Nature*, 242:190–191, 1973.

[85] M. J. Ledesma-Carbayo, J. Kybic, M. Sühling, P. Hunziker, M. Desco, A. Santos, and M. Unser. Cardiac ultrasound motion detection by elastic registration exploiting temporal coherence. In *Proceedings of the International Symposium on Biomedical Imaging*, pages 585–588, 2002.

[86] S. Lee, G. Wolberg, K. Chwa, and S. Y. Shin. Image metamorphosis with scattered feature constraints. *IEEE Transactions on Visualization and Computer Graphics*, 2(4):337–354, December 1996.

[87] S. Lee, G. Wolberg, and S. Y. Shin. Scattered data interpolation with multi-level B-splines. *IEEE Transactions on Visualization and Computer Graphics*, 3(3):228–244, July–September 1997.

[88] B. P. F. Lelieveldt, R. J. van der Geest, M. Ramze Rezaee, J. G. Bosch, and J. H. C. Reiber. Anatomical model matching with fuzzy implicit surfaces for segmentation of thoracic volume scans. *IEEE Transactions on Medical Imaging*, 18(3):218–230, March 1999.

[89] M. Leoncini, G. Marcucci, R. Sciagrà, F. Frascarelli, A. M. Traini, D. Mondanelli, M. Magni, L. Bini, F. Bellandi, A. Mennuti, and R. P. Dabizzi. Nitrate-enhanced gated technetium 99m sestamibi SPECT for evaluating regional wall motion at baseline and during low-dose dobutamine infusion in patients with chronic coronary artery disease and left ventricular dysfunction: Comparison with twodimensional echocardiography. *Journal of Nuclear Cardiology*, 7:426–431, 2000.

[90] W. Liang, S. C. DeJong, C. R. McKay, and M. Sonka. Automated detection of left ventricular borders from intracardiac ultrasound images. In *Computer in Cardiology*, pages 265–268, 1996.

[91] Z. Liang and P. C. Lauterbur. *Principles of Magnetic Resonance Imaging—A Signal Processing Perspective*. IEEE Press, 2000.

[92] W. E. Lorensen and H. E. Cline. Marching cubes: A high resolution 3D surface reconstruction algorithm. In *Proceedings of the 14th Annual Conference on Computer Graphics and Interactive Techniques*, volume 21, pages 163–169. ACM, July 1987.

[93] C. Lorenz and N. Krahnstover. 3D statistical shape models for medical image segmentation. In *Proceedings of the Second International Conference On 3D Digital Imaging and Modeling*, pages 414–423, October 1999.

[94] M. Lorenzo-Valdés, G. I. Sanchez-Ortiz, R. Mohiaddin, and D. Rueckert. Atlas-based segmentation and tracking of 3D cardiac MR images using non-rigid registration. In T. Dohi and R. Kikinis, editors, *Proceedings of the Fifth International Conference on Medical Image Computing and Computer Assisted Intervention*, volume 2488 of *Lecture Notes in Computer Science*, pages 642–650, Tokyo, Japan, September 2002. Springer.

[95] M. Lorenzo-Valdés, G. I. Sanchez-Ortiz, R. Mohiaddin, and D. Rueckert. Segmentation of 4D cardiac MR images using a probabilistic atlas and the EM algorithm. In R. E. Ellis and T. M. Peters, editors, *Proceedings of the Sixth International Conference on Medical Image Computing and Computer Assisted Intervention*, volume 2878 of *Lecture Notes in Computer Science*, pages 440–450, Montreal, Canada, November 2003. Springer.

[96] R. MacCracken and K. I. Joy. Free-form deformations with lattices of arbitrary topology. In *Proceedings of the 23rd Annual Conference on Computer Graphics and Interactive Techniques*, pages 181–188. ACM, 1996.

[97] G. E. Mailloux, F. Langlois, P. Y. Simard, and M. Bertrand. Restoration of the velocity field of the heart from two-dimensional echocardiograms. *IEEE Transactions on Medical Imaging*, 8(2):143–153, June 1989.

[98] J. B. A. Maintz and M. A. Viergever. A survey of medical image registration. *Medical Image Analysis*, 2:1–36, 1998.

[99] T. Mäkelä, P. Clarysse, O. Sipilä, N. Pauna, Q. C. Pham, T. Katila, and I. E. Magnin. A review of cardiac image registration methods. *IEEE Transactions on Medical Imaging*, 21(9):1011–1021, September 2002.

[100] T. Mäkelä, Q. C. Pham, P. Clarysse, J. Nenonen, J. Lötjönen, O. Sipilä, H. Hänninen, K. Lauerma, J. Knuuti, T. Katila, and I. E. Magnin. A 3-D model-based registration approach for the PET, MR, and MCG cardiac data fusion. *Medical Image Analysis*, 7(3):377–389, September 2003.

[101] J. F. Mangin, V. Frouin, I. Bloch, B. Bendriem, and J. Lopez-Krahe. Fast nonsupervised 3D registration of PET and MR images of the brain. *Journal of Cerebral Blood Flow and Metabolism*, 14(5):749–762, 1994.

[102] D. Manke, P. Rösch, K. Nehrke, and P. Börnert O. Dössel. Model evaluation and calibration for prospective respiratory motion correction in coronary MR angiography based on 3-D image registration. *IEEE Transactions on Medical Imaging*, 21(9):1132–1141, September 2002.

[103] W. J. Manning and D. J. Pennell, editors. *Cardiovascular Magnetic Resonance*. Churchill Livinstone, 2002.

[104] P. Mansfield and I. L. Pykett. Biological and medical imaging by NMR. *Journal of Magnetic Resonance*, 29:355–373, 1978.

[105] S. Masood, J. Gao, and G. Z. Yang. Virtual tagging: Numerical considerations and phantom validation. *IEEE Transactions on Medical Imaging*, 21(9):1123–1131, September 2002.

[106] K. McLeish, D. L. G. Hill, D. Atkinson, J. M. Blackall, and R. Razavi. A study of the motion and deformation of the heart due to respiration. *IEEE Transactions on Medical Imaging*, 21(9):1142–1150, September 2002.

[107] E. R. McVeigh and E. Atalar. Cardiac tagging with breath-hold cine MRI. *Magnetic Resonance in Medicine*, 28:318–327, 1992.

[108] F. G. Meyer, R. T. Constable, A. J. Sinusas, and J. S. Duncan. Tracking myocardial deformation using phase contrast MR velocity fields: A stochastic approach. *IEEE Transactions on Medical Imaging*, 15(4):453–465, August 1996.

[109] S. C. Mitchell, J. G. Bosch, B. P. F. Lelieveldt, R. J. van der Geest, J. H. C. Reiber, and M. Sonka. 3D active appearance models: Segmentation of car-

diac MR and ultrasound images. *IEEE Transactions on Medical Imaging*, 21(9):1167–1178, September 2002.

[110] S. C. Mitchell, B. P. F. Lelieveldt, R. J. van der Geest, J. H. C. Reiber, and M. Sonka. Multistage hybrid active appearance model matching: Segmentation of left and right ventricles in cardiac MR images. *IEEE Transactions on Medical Imaging*, 20(5):415–423, May 2001.

[111] C. C. Moore, E. R. McVeigh, and E. A. Zerhouni. Quantitative tagged magnetic resonance imaging of the normal human left ventricle. *Topics in Magnetic Resonance Imaging*, 11(6):359–371, 2000.

[112] T. J. Mosher and M. B. Smith. A DANTE tagging sequence for the evaluation of translational sample motion. *Magnetic Resonance in Medicine*, 15:334–339, 1990.

[113] W. G. O'Dell, C. C. Moore, W. C. Hunter, E. A. Zerhouni, and E. R. McVeigh. Three-dimensional myocardial deformations: Calculation with displacement field fitting to tagged MR images. *Radiology*, 195(3):829–835, June 1995.

[114] World Health Organization. World health report. http://www.who.int/whr/2003/en, 2003.

[115] N. F. Osman, W. S. Kerwin, E. R. McVeigh, and J. L. Prince. Cardiac motion tracking using cine harmonic phase (HARP) magnetic resonance imaging. *Magnetic Resonance in Medicine*, 42:1048–1060, 1999.

[116] N. F. Osman, E. R. McVeigh, and J. L. Prince. Imaging heart motion using harmonic phase MRI. *IEEE Transactions on Medical Imaging*, 19(3):186–202, March 2000.

[117] C. Ozturk and E. R. McVeigh. Four-dimensional B-spline based motion analysis of tagged MR images: Introduction and *in vivo* validation. *Physics in Medicine and Biology*, 45:1683–1702, 2000.

[118] L. C. Palmon, N. Reichek, S. B. Yeon, N. R. Clark, D. Brownson, E. Hoffman, and L. Axel. Intramural myocardial shortening in hypertensive left ventricular hypertrophy with normal pump function. *Circulation*, 89(1):122–131, January 1994.

[119] L. Pan, J. A. C. Lima, and N. F. Osman. Fast tracking of cardiac motion using 3D-HARP. In C. Taylor and J. A. Noble, editors, *Proceedings of the 18th International Conference on Information Processing in Medical Imaging*, volume 2732 of *Lecture Notes in Computer Science*, pages 611–622, Ambleside, UK, July 2003. Springer-Verlag Heidelberg.

[120] X. Papademetris, A. J. Sinusas, D. P. Dione, and J. S. Duncan. Estimation of 3D left ventricular deformation from echocardiography. *Medical Image Analysis*, 5(1):17–28, March 2001.

[121] J. Park, D. Metaxas, and L. Axel. Analysis of left ventricular wall motion based on volumetric deformable models and MRI-SPAMM. *Medical Image Analysis*, 1(1):53–71, 1996.

[122] J. Park, D. Metaxas, A. A. Young, and L. Axel. Deformable models with parameter functions for cardiac motion analysis from tagged MRI data. *IEEE Transactions on Medical Imaging*, 15(3):278–289, June 1996.

[123] N. J. Pelc, R. J. Herfkens, A. Shimakawa, and D. Enzmann. Phase contrast cine magnetic resonance imaging. *Magnetic Resonance Quarterly*, 7(4):229–254, 1991.

[124] C. A. Pelizzari, G. T. Y. Chen, D. R. Spelbring, R. R. Weichselbaum, and C. T. Chen. Accurate three-dimensional registration of CT/PET, and/or MR images of the brain. *Journal of Computer Assisted Tomography*, 13:20–26, 1989.

[125] D. Perperidis, A. Rao, M. Lorenzo-Valdés, R. Mohiaddin, and D. Rueckert. Spatio-temporal alignment of 4D cardiac MR images. In I. E. Magnin, J. Montagnat, P. Clarysse, J. Nenonen, and T. Katila, editors, *Proceedings of the Second International Workshop on Functional Imaging and Modeling of the Heart*, volume 2674 of *Lecture Notes in Computer Science*, pages 205–214, Lyon, France, June 2003. Springer-Verlag Heidelberg.

[126] D. Perperidis, A. Rao, R. Mohiaddin, and D. Rueckert. Non-rigid spatio-temporal alignment of 4D cardiac MR images. In J. C. Gee, J. B. A. Maintz, and M. W. Vannier, editors, *Proceedings of the Second International Workshop on Biomedical Image Registration*, volume 2717 of *Lecture Notes in Computer Science*, pages 191–200, Philadelphia, USA, June 2003. Springer-Verlag Heidelberg.

[127] C. Petitjean, N. Rougon, F. Preteux, P. Cluzel, and P. Grenier. Measuring myocardial deformation from MR data using information-theoretic nonrigid registration. In G. Goos, J. Hartmanis, and J. van Leeuwen, editors, *Proceedings of the Second International Workshop on Functional Imaging and Modeling of the Heart*, volume 2674 of *Lecture Notes in Computer Science*, pages 162–172, Lyon, France, June 2003. Springer.

[128] J. P. W. Pluim, J. B. A. Maintz, and M. A. Viergever. Image registration by maximization of combined mutual information and gradient information. *IEEE Transactions on Medical Imaging*, 19(8):809–814, August 2000.

[129] J. P. W. Pluim, J. B. A. Maintz, and M. A. Viergever. Mutual-information-based registration of medical images: A survey. *IEEE Transactions on Medical Imaging*, 22(8), August 2003.

[130] J. P. W. Pluim, J. B. Antoine Maintz, and M. A. Viergever. f-information measures in medical image registration. In M. Sonka and K. M. Hanson, editors, *Proceedings of the SPIE International Symposium on Medical Imaging:*

Image Processing, volume 4322, pages 579–587, San Diego, California USA, 2001. SPIE.

[131] J. L. Prince and E. R. McVeigh. Optical flow for tagged MR images. In *Proceedings of the 1991 International Conference on Acoustics, Speech, and Signal Processing*, pages 2441–2444, 1991.

[132] J. L. Prince and E. R. McVeigh. Motion estimation from tagged MR images. *IEEE Transactions on Medical Imaging*, 11(2):238–249, June 1992.

[133] A. Rao, R. Chandrashekara, G. I. Sanchez-Ortiz, R. Mohiaddin, P. Aljabar, J. V. Hajnal, B. K. Puri, and D. Rueckert. Spatial transformation of motion and deformation fields using nonrigid registration. *IEEE Transactions on Medical Imaging*, 23(9):1065–1076, September 2004.

[134] A. Rao, G. I. Sanchez-Ortiz, R. Chandrashekara, M. Lorenzo-Valdés, R. Mohiaddin, and D. Rueckert. Comparison of cardiac motion across subjects using nonrigid registration. In *Proceedings of the Fifth International Conference on Medical Image Computing and Computer Assisted Intervention*, pages 722–729. Springer, 2002.

[135] A. Rao, G. I. Sanchez-Ortiz, R. Chandrashekara, M. Lorenzo-Valdés, R. Mohiaddin, and D. Rueckert. Construction of a cardiac motion atlas from MR using nonrigid registration. In *Proceedings of the Second International Workshop on Functional Imaging and Modeling of the Heart*, pages 141–150, Lyon, France, June 5–6 2003.

[136] M. Rayner and S. Petersen. European cardiovascular disease statistics. http://www.heartstats.org/, 2000.

[137] N. Reichek. MRI myocardial tagging. *Journal of Magnetic Resonance Imaging*, 10:609–616, 1999.

[138] D. Rueckert, M. J. Clarkson, D. L. G. Hill, and D. J. Hawkes. Non-rigid registration using higher-order mutual information. In K. M. Hanson, editor, *Proceedings of the SPIE International Symposium on Medical Imaging: Image Processing*, pages 438–447, San Diego, California USA, 2000. SPIE.

[139] D. Rueckert, A. F. Frangi, and J. A. Schanbel. Automatic construction of 3-D statistical deformation models of the brain using nonrigid registration. *IEEE Transactions on Medical Imaging*, 22(8):1014–1025, August 2003.

[140] D. Rueckert, A. F. Frangi, and J. A. Schnabel. Automatic construction of 3D statistical deformation models using non-rigid registration. In Wiro J. Niessen and Max A. Viergever, editors, *Proceedings of the Fourth International Conference on Medical Image Computing and Computer Assisted Intervention*, pages 77–84, Utrecht, The Netherlands, October 2001. Springer.

[141] D. Rueckert, M. Lorenzo-Valdés, R. Chandrashekara, G. I. Sanchez-Ortiz, and R. Mohiaddin. Non-rigid registration of cardiac MR: Application to motion modelling and atlas-based segmentation. In *Proceedings of the 2002 IEEE International Symposium on Biomedical Imaging*, pages 481–484, 7–10 July 2002.

[142] D. Rueckert, L. I. Sonoda, C. Hayes, D. L. G. Hill, M. O. Leach, and D. J. Hawkes. Nonrigid registration using free-form deformations: Application to breast MR images. *IEEE Transactions on Medical Imaging*, 18(8):712–721, August 1999.

[143] S. Ryf, K. V. Kissinger, M. A. Spiegel, P. Börnert, W. J. Manning, P. Boesiger, and M. Stuber. Spiral MR myocardial tagging. *Magnetic Resonance in Medicine*, 51:237–242, 2004.

[144] S. Ryf, M. A. Spiegel, M. Gerber, and P. Boesiger. Myocardial tagging with 3D-CSPAMM. *Journal of Magnetic Resonance Imaging*, 16:320–325, 2002.

[145] G. Saab, R. A. deKemp, H. Ukkonen, T. D. Ruddy, G. Germano, and R. S. B. Beanlands. Gated fluorine 18 fluorodeoxyglucose positron emission tomography: Determination of global and regional left ventricular function and myocardial tissue characterization. *Journal of Nuclear Cardiology*, 10(3):297–303, 2003.

[146] M. F. Santarelli, V. Postitano, P. Marcheschi, L. Landini, P. Marzullo, and A. Benassi. Multimodal cardiac image fusion by geometrical features registration and warping. In *Computers in Cardiology*, pages 277–280. IEEE, 23–26 September 2001.

[147] J. A. Schnabel, D. Rueckert, M. Quist, J. M. Blackall, A. D. Castellano-Smith, T. Hartkens, G. P. Penney, W. A. Hall, H. Liu, C. L. Truwit, F. A. Gerritsen, D. L. G. Hill, and D. J. Hawkes. A generic framework for non-rigid registration based on non-uniform multi-level free-form deformations. In Wiro J. Niessen and Max A. Viergever, editors, *Proceedings of the Fourth International Conference on Medical Image Computing and Computer Assisted Intervention*, pages 573–581, Utrecht, The Netherlands, October 2001. Springer.

[148] W. J. Schroeder, J. A. Zarge, and W. E. Lorensen. Decimation of triangle meshes. In *Proceedings of the 19th Annual Conference on Computer Graphics and Interactive Techniques*, volume 26, pages 65–70, July 1992.

[149] T. W. Sederberg and S. R. Parry. Free-form deformation of solid geometric models. In *Proceedings of the 13th Annual Conference on Computer Graphics and Interactive Techniques*, volume 20, pages 151–160. ACM, August 1986.

[150] D. Shen, Y. Zhan, and C. Davatzikos. Segmentation of prostate boundaries from ultrasound images using statistical shape model. *IEEE Transactions on Medical Imaging*, 22(4):539–551, April 2003.

[151] P. Shi, A. J. Sinusas, R. T. Constable, E. Ritman, and J. S. Duncan. Point-tracked quantitative analysis of left ventricular surface motion from 3d image sequences. *IEEE Transactions on Medical Imaging*, 19(1):36–50, January 2000.

[152] M. A. Spiegel, R. Luechinger, J. Schwitter, and P. Boesiger. Ringtag: Ring-shaped tagging for myocardial centerline assessment. *Investigative Radiology*, 38(10):669–678, October 2003.

[153] M. Stuber, M. B. Scheidegger, S. E. Fischer, E. Nagel, F. Steinemann, O. M. Hess, and P. Boesiger. Alterations in the local myocardial motion pattern in patients suffering from pressure overload due to aortic stenosis. *Circulation*, 100:361–368, 1999.

[154] M. Stuber, M. A. Spiegel, S. E. Fischer, M. B. Scheidegger, P. G. Danias, E. M. Pedersen, and P. Boesiger. Single breath-hold slice-following CSPAMM myocardial tagging. *Magnetic Resonance Materials in Physics, Biology and Medicine*, 9:85–91, 1999.

[155] C. Studholme, D. L. G. Hill, and D. J. Hawkes. Automated three-dimensional registration of magnetic resonance and positron emission tomography brain images by multiresolution optimization of voxel similarity measures. *Medical Physics*, 24(1):25–35, 1997.

[156] C. Studholme, D. L. G. Hill, and D. J. Hawkes. An overlap invariant entropy measure of 3D medical image alignment. *Pattern Recognition*, 32(1):71–86, 1998.

[157] B. Sturm, K. A. Powell, S. S. Halliburton, and R. D. White. Image fusion of 4d cardiac CTA and MR images. In *30th Applied Imagery Pattern Recognition Workshop*, pages 21–24, 10–12 October 2001.

[158] P. Suetens. *Fundamentals of Medical Imaging*. Cambridge University Press, 2002.

[159] T. S. Dennney, Jr. and J. L. Prince. Reconstruction of 3D left ventricular motion from planar tagged cardiac MR images: An estimation theoretic approach. *IEEE Transactions on Medical Imaging*, 14(4):1–11, December 1995.

[160] X. Tao, J. L. Prince, and C. Davatzikos. Using a statistical shape model to extract sulcal curves on the outer cortex of the human brain. *IEEE Transactions on Medical Imaging*, 21(5):513–524, May 2002.

[161] Texas Heart Institute. Coronary artery disease. http://www.tmc.edu/thi/cad.html, 2004.

[162] P. Thévenaz and M. Unser. Optimization of mutual information for multiresolution image registration. *IEEE Transactions on Image Processing*, 9(12):2083–2099, December 2000.

[163] F. A. Tibayan, D. T. M. Lai, T. A. Timek, P. Dagum, D. Liang, G. T. Daughters, N. B. Ingels, and D. C. Miller. Alterations in left ventricular torsion in tachycardia-induced dilated cardiomyopathy. *The Journal of Thoracic and Cardiovascular Surgery*, 124(1):43–49, July 2002.

[164] W. Y. I. Tseng, T. G. Reese, R. M. Weisskoff, T. J. Brady, and V. J. Wedeen. Myocardial fiber shortening in humans: Initial results of mr imaging. *Radiology*, 216:128–139, 2000.

[165] Y. Tseng and J. Hwang. 3D heart border delineation and motion estimation using ultrasound transthoracic images for assisted heart diseases diagnoses. In *Proceedings of the International Conference on Image Processing*, volume 3, pages 543–546, 26–29 October 1997.

[166] T. G. Turkington, T. R. DeGrado, M. W. Hanson, and R. Edward Coleman. Alignment of dynamic cardiac PET images for correction of motion. *IEEE Transactions on Nuclear Science*, 44(2):235–242, April 1997.

[167] M. Unser, A. Aldroubi, and Murray Eden. Fast B-spline transforms for continuous image representation and interpolation. *IEEE Transactions on Pattern Analysis and Machine Intelligence*, 13(3):277–285, March 1991.

[168] P. Vaduganathan, Z. He, G. W. Vick III, J. J. Mahmarian, and M. S. Verani. Evaluation of left ventricular wall motion, volumes, and ejection fraction by gated myocardial tomography with technetium 99m-labeled tetrofosmin: A comparison with cine magnetic resonance imaging. *Journal of Nuclear Cardiology*, 6(1):3–10, 1999.

[169] P. van Dijk. Direct cardiac NMR imaging of heart wall and blood flow velocity. *Journal of Computer Assisted Tomography*, 8:429–436, 1984.

[170] Paul A. Viola. *Alignment by Maximization of Mutual Information*. PhD thesis, Massachusetts Institute of Technology, June 1995.

[171] E. Waks, J. L. Prince, and A. S. Douglas. Cardiac motion simulator for tagged MRI. In *Proceedings of the IEEE Workshop on Mathematical Methods in Biomedical Image Analysis*, pages 182–191, June 1996.

[172] X. Wang, L. He, Y. Tang, and W. G. Wee. A divide and conquer deformable contour method with a model based searching algorithm. *IEEE Transactions on Systems, Man, and Cybernetics—Part B: Cybernetics*, 33(5):738–751, October 2003.

[173] S. Webb, editor. *The Physics of Medical Imaging*. Institute of Physics Publishing, 1988.

[174] I. Wolf, M. Hastenteufel, R. De Simone, M. Vetter, G. Glombitza, S. Mottl-Link, C. F. Vahl, and H. Meinzer. ROPES: A semiautomated segmentation method for accelerated analysis of three-dimensional echocardiographic data. *IEEE Transactions on Medical Imaging*, 21(9), September 2002.

[175] C. Xu and J. L. Prince. Snakes, shapes, and gradient vector flow. *IEEE Transactions on Image Processing*, 7(3):359–369, March 1998.

[176] H. Yamagishi, K. Akioka, K. Hirata, Y. Sakanoue, I. Toda, M. Yoshiyama, M. Teragaki, K. Takeuchi, J. Yoshikawa, and H. Ochi. Dobutamine-stress electrocardiographically gated positron emission tomography for detection of viable but dysfunctional myocardium. *Journal of Nuclear Cardiology*, 6(6):626–632, 1999.

[177] X. Ye, J. A. Noble, and D. Atkinson. 3-D freehand echocardiography for automatic left ventricle reconstruction and analysis based on multiple acoustic windows. *IEEE Transactions on Medical Imaging*, 21(9), September 2002.

[178] F. Yeung, S. F. Levinson, D. Fu, and K. J. Parker. Feature-adaptive motion tracking of ultrasound image sequences using a deformable mesh. *IEEE Transactions on Medical Imaging*, 17(6):945–956, December 1998.

[179] A. A. Young. Model tags: Direct three-dimensional tracking of heart wall motion from tagged magnetic resonance images. *Medical Image Analysis*, 3(4):361–372, 1999.

[180] A. A. Young, D. L. Kraitchman, L. Dougherty, and L. Axel. Tracking and finite element analysis of stripe deformation in magnetic resonance tagging. *IEEE Transactions on Medical Imaging*, 14(3):413–421, September 1995.

[181] E. A. Zerhouni, D. M. Parish, W. J. Rogers, A. Yang, and E. P. Shapiro. Human heart: Tagging with MR imaging — a method for noninvasive assessment of myocardial motion. *Radiology*, 169(1):59–63, 1988.

[182] Y. Zhu, M. Drangova, and N. J. Pelc. Fourier tracking of myocardial motion using cine-PC data. *Magnetic Resonance in Medicine*, 35(4):471–480, April 1996.

[183] Y. Zhu, M. Drangova, and N. J. Pelc. Estimation of deformation gradient and strain from cine-PC velocity data. *IEEE Transactions on Medical Imaging*, 16(6):840–851, December 1997.

[184] Y. Zhu and N. J. Pelc. A spatiotemporal model of cyclic kinematics and its applications to analyzing nonrigid motion with MR velocity images. *IEEE Transactions on Medical Imaging*, 18(7):557–569, July 1999.